Effects of Additives on the Molecular-Level Behavior of Disordered Pharmaceuticals

A dissertation submitted to the faculty of
The University of Minnesota

By
Kweku Konadu Amponsah-Efah

In partial fulfilment of the requirements for the degree of
Doctor of Philosophy

Raj Suryanarayanan
(Advisor)

December 2020

Acknowledgements

I am grateful to Dr. Raj Suryanarayanan, for his support, and for providing me with many opportunities for professional development. I also thank my committee members – Dr. Ronald Siegel, Dr. Timothy Weidman, Dr. Renee Frontiera and Dr. Jorge Vinals – for critically reviewing my preliminary exam proposal and thesis. All were encouraging and offered invaluable advice when I took their courses or discussed my data with them.

Sincere thanks also to various experts who either collaborated with us or contributed substantially to the thesis; Dr. Borries Demeler, Dr. Jan Thoen, Dr. Christ Glorieux, Dr. Reed Eisenhart, Dr. Letitia Yao, Dr. Michelle Miller and Dr. Sam Erb were helpful with experimental design and data interpretation. Dr. Courtney Aldrich provided access to his ITC instrument and Evan Alexander helped with the experiments. Dr. Wenqian Xu and Dr. Andrey Yakovenko assisted us at the Argonne National Labs. Beckman Coulter (facilitated by Whitney Heyvaert) generously supported the analytical ultracentrifugation experiments. I am also thankful for financial support from the Bighley Graduate Student Fellowship and the National Science Foundation (NSF CMMI-1662039).

The faculty, staff and graduate students at the Department of Pharmaceutics were warm and welcoming. Sury lab members created a nice atmosphere to work in: Naveen Thakral, Seema Thakral, Pinal Mistry, Mehak Mehta, Michelle Fung, Sampada Koranne, Subarna Samanta, Krishna Kumar, Naga Duggirala, Anasuya Sahoo, Alpana Thorat, Jayesh Sonje,

Navpreet Kaur, Tony Lee, Bhushan Munjal and Karlis Berzins. Candice McDermott, Jody Tracy, Katie James and Amanda Hokanson assisted our department administratively.

Many friends helped in different ways. It is impossible to mention everyone's name, but Davin Rautiola, Krutika Jain, Carolyn Reinhart, Saikat Banerjee, Evan Alexander, Amani Lee, Chenguang Wang, Vidur Sarma, Wei-Jhe Sun, Saif Rahman, Jiangnan Dun, Shenye Hu, Minjee Kim, Afroz Mohammed, Gautham Gampa, Monica Ohnsorg and Nidhi Sharda are a few that come to mind as I write this section. Frederick and Adwoa Osei-Yeboah were an incredibly strong support. The leaders and the entire congregation of South East Christian Church always looked out for me, especially on holidays. Thank you all so much.

Finally, I express my heartfelt gratitude to my family – Kofi, Iris, Kojo, KD and Nanna – for their unconditional love. Even though we were geographically separated, I could count on your support. I will forever be indebted to you all.

Dedicated to KD

ABSTRACT

Amorphous solid dispersions (ASDs) can improve the oral bioavailability of poorly water-soluble drugs. However, the physical instability of the amorphous form, denoted by the propensity to recrystallize, is a major barrier to the use of ASDs. The overarching goal of this thesis was to understand the mechanisms by which two major classes of additives – antiplasticizers (various polymers) and plasticizers (mainly glycerol) – affect the physical stability of amorphous formulations, in the dry solid form, as well as in aqueous solution. In the first project, we investigated the impact of the strength of drug–polymer interactions, on the dissolution performance of ASDs. With ketoconazole and three polymers as model compounds, we observed that the interactions that stabilize amorphous drugs in the solid state, can also be relevant and important in sustaining the level of supersaturation in aqueous solution. The second project explored the use of analytical ultracentrifugation as a novel technique for characterizing drug–polymer interactions in aqueous buffers. It was possible to quantify the "free" versus "bound" fractions of drug in aqueous solution, and to semi-quantitatively assess the impact of interactions on the dissolution performance of ASDs. The third and fourth projects evaluated the effects of glycerol on the molecular mobility and physical stability of amorphous itraconazole (ITZ), in the "solid" state. It is well-known that small molecule plasticizers, such as water or glycerol, increase the molecular mobility and accelerate the crystallization of amorphous drugs. In the case of amorphized ITZ, however, glycerol at low concentrations did not cause physical instability. Rather, the smectic state (one of the intermediate liquid-crystalline phases of ITZ) was selectively stabilized. The mechanism by which glycerol stabilized the smectic state was investigated with high resolution techniques (synchrotron diffractometry, differential and adiabatic scanning calorimetry, and spectroscopy). The results revealed that additives with fast dynamics, can drive weak first-order (or second-order) intermediate liquid-crystalline phase transitions, to strong first-order transitions, by a possible coupling of the additive concentration to the order parameter. We also demonstrated that the stabilized smectic state can perform the dual role of maintaining good physical stability while achieving adequate dissolution performance.

TABLE OF CONTENTS

LIST OF FIGURES

SUPPLEMENTARY FIGURES

LIST OF TABLES

SUPPLEMENTARY TABLES

1 INTRODUCTION

1.1 BACKGROUND AND MOTIVATION

Advances in combinatorial chemistry and high throughput screening methods, have led to an explosion in the number of chemical compounds that are potential drug candidates[1,2]. With every lead molecule identified, efforts are intensified to market the drug as a solid oral dosage form (e.g. as tablets or capsules) because of convenience to patients, safety, high compliance rates and low manufacturing costs. When given orally, the solid drug must first *dissolve* in the aqueous environment of the gastro-intestinal (GI) tract, before being *absorbed* into the bloodstream[3]. Aqueous solubility and GI membrane permeability, therefore, form the basis for the Biopharmaceutics Classification System (BCS)[3]. There are four main BCS classes, with each class having an almost equal number of drugs that are currently marketed[4]. In the research and development pipeline, however, only 5-10% of compounds have high solubility and high permeability (BCS class I compounds). The majority (60-70%) have poor solubility but adequate permeability (BCS class II)[4]. Research into strategies that could overcome the solubility challenge, is therefore a key focus in the pharmaceutical sciences[5].

There are several approaches to enhance the aqueous solubility of poorly-soluble drugs: particle size reduction (e.g. micronization and nanosizing), formation of salts (for drugs with ionizable functional groups), formation of co-crystals (for drugs with hydrogen bond donor or acceptor groups), use of solubilizing carriers (e.g. lipids as self-emulsifying delivery systems; cyclodextrins or surfactants as complexation agents) and

amorphization[4,6–9]. Of these approaches, amorphous systems have gained much attention over the last few decades as a result of extensive fundamental research, advances in large-scale manufacturing methods such as hot-melt extrusion technology, and the experience gained through launch of commercial products.[10,11]

Amorphous materials lack the long-range lattice periodicity of the corresponding crystalline compounds. The disordered molecules can therefore readily interact with the (mainly aqueous) GI fluid, without the need to overcome the crystal lattice energy barrier, leading to high apparent aqueous solubility. However, the high energetic state is also a thermodynamic driving force for crystallization both in the dry, solid state as well as in aqueous solution. To overcome this challenge, the drug is dispersed (as an amorphous solid dispersion) in a carrier that can prevent or retard drug crystallization. An amorphous solid dispersion (ASD) can thus be defined as a molecular-level mixture of a drug with one or more inert carriers, to form a homogeneous phase[4,5,12]. With amorphous formulations, solubility increases as high as a thousand-fold relative to the crystalline drug solubility, have been reported[13,14].

The two key characteristics of any successfully designed ASD are (i) physical stability during processing and storage, and (ii) optimal dissolution performance[15]. Academic and industrial research in the early years focused on understanding the factors that affect the physical stability of ASDs under "dry" conditions[16]. Both thermodynamic (e.g. heat of fusion, configurational entropy, surface energy)[17,18] and kinetic (e.g. diffusivity and

molecular mobility)[19] factors have been shown to influence amorphous drug crystallization.

The behavior of amorphous systems in aqueous media, however, tends to be more complex, with many interdependent factors affecting the concentration-time profiles[16]. Even though many reports show *in vitro* dissolution enhancement of ASDs, compared to the crystalline or neat amorphous drugs, the exact mechanisms by which polymers stabilize the amorphous drugs in solution are poorly understood[11,16]. Thus, polymer selection for ASD formulation remains largely empirical. Research efforts geared towards understanding the physical chemistry of ASDs and their supersaturated solutions, with a broader goal of linking the solid state behavior to *in vitro* dissolution profiles and *in vivo* performance, are thus required[11].

From the perspective of aqueous solubility enhancement, the amorphous form is the most widely-used disordered form. However, it is also highly unstable. Intermediate between the amorphous (completely disordered) and the crystalline (fully ordered) states, are a number of mesomorphic states[20]. With free energy levels intermediate between the energy levels of the amorphous and crystalline states, mesomorphic forms may give rise to an increased drug dissolution rate relative to the crystalline form, while maintaining better physical stability than the amorphous form. An organic compound having a rod-like or disc-like shape, may form mesomorphic (also called liquid crystalline, LC) phases[20]. Many small molecule drugs have these characteristics, such that if they do possess LC phases,

the dual advantage of good physical stability and optimal dissolution may be realized[21]. Yet, mesomorphic compounds are not given adequate attention in the pharmaceutical sciences[21,22].

Polymers are the main carriers for ASDs. Other excipients such as small-molecule plasticizers, surfactants and acidity modifiers may also be included in ASD formulations, to aid processing or to improve drug dissolution[23]. The polymeric additives for ASDs are typically already used in the pharmaceutical industry as excipients, and there is a wealth of information on their properties[12]. The effects of non-polymeric additives on the physical stability of amorphous drugs have, however, not been adequately investigated.

The central goal of the thesis was therefore to gain fundamental insight into the mechanisms by which additives stabilize disordered pharmaceuticals, in the solid state, and in aqueous solution. In the solid state, we investigated how glycerol, a small molecule plasticizer, affects the thermodynamic behavior and physical stability of itraconazole. Itraconazole was of interest because it can exist either as an amorphous compound, or as a liquid crystal. In aqueous solution, we investigated the impact of drug–polymer interactions, on the dissolution performance of amorphous solid dispersions.

1.2 THEORETICAL BACKGROUND AND LITERATURE REVIEW

1.2.1 Pharmaceutical solid forms: crystalline and amorphous

The majority of small-molecule active pharmaceutical ingredients (APIs) are crystalline solids. The crystalline form, possessing long-range orientational and positional order in three dimensions, is usually the most thermodynamically stable[25]. Amorphous materials on the other hand, lack long-range order, even though they often possess a limited degree of short-range order. The disordered state is characterized by higher free energy, compared to the corresponding crystalline form, which may lead to an enhanced dissolution rate and consequently an increase in bioavailability.

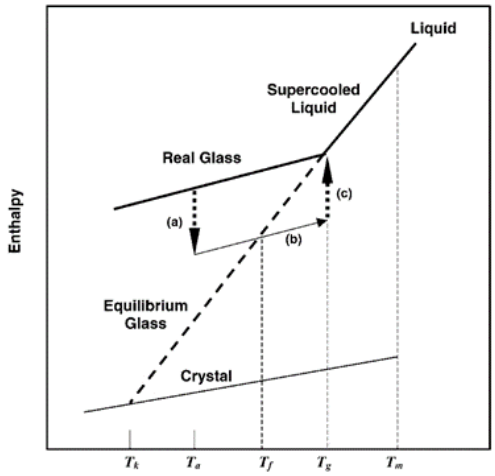

Figure 1.1. Schematic depicting the variation in enthalpy as a function of temperature. T_m is the equilibrium melting point, T_g is the glass transition temperature, T_f is the fictive temperature, T_a is the annealing temperature, and T_k is the Kauzmann (or zero mobility) temperature. Figure reproduced from Kawakami and Pikal[26].

Figure 1.1 is a schematic representation of enthalpy as a function of temperature, for crystalline and amorphous materials[26]. The vertical axis could also depict entropy, or specific volume. When a crystalline solid is heated, the enthalpy or volume does not increase much with respect to temperature, until the melting temperature (T_m) is reached. At T_m, there is a sharp discontinuity in the enthalpy, indicating a first-order solid-to-liquid phase transition. When the isotropic melt is cooled very slowly, the liquid usually crystallizes at $T < T_m$. However, with rapid cooling rates, the liquid may fail to crystallize resulting in the supercooled liquid (or the amorphous) state. Although the supercooled liquid is a nonequilibrium state relative to the crystalline state, it is an equilibrium state with respect to structural changes with temperature[26]. In other words, the supercooled liquid is in "structural equilibrium".

Upon further cooling, the timescale for structural rearrangement within the supercooled liquid eventually becomes too slow to keep up with the cooling rate. The temperature at which the supercooled liquid eventually falls out of structural equilibrium, is the glass transition temperature (T_g). At $T < T_g$, the amorphous material is in the glassy state. The state defined by an extension of the supercooled liquid line at $T < T_g$, represents the glassy state that would have been in structural equilibrium. When the real glass is stored isothermally at an annealing temperature $T_a < T_g$, the enthalpy, entropy and specific volume approach this extrapolated "equilibrium glassy state" asymptotically, in a process referred to as aging. The fictive temperature, T_f, is conceptually the temperature at which the equilibrium supercooled liquid would have the same properties as the aged glass. At

T_f, the property of interest (enthalpy, specific volume, or configurational entropy) when extrapolated along the glass line, intersects the extrapolated equilibrium supercooled liquid line[27]. The fictive temperature can thus be used to define the structure(s) of different glasses. The Kauzmann temperature, T_k, also known as the temperature of zero mobility, marks the theoretical lower limit of excess entropy.

1.2.2 Pharmaceutical solid forms: mesomorphic forms (liquid crystals)

Crystalline and amorphous materials, as introduced in Section 1.2.1, are in the solid and super-viscous liquid states, respectively. Some materials however show a series of transitions between the solid and the liquid states, as temperature is varied. The new phases have mechanical, optical and structural properties between those of the crystalline solid and the corresponding isotropic liquid. The intermediate phases are thus termed *liquid crystalline (LC) phases*, *mesomorphic phases* or *mesophases*. Mesophases are indefinitely stable at defined temperatures and pressures[28], and thus considered a fourth state of matter (besides the well-known *solid*, *liquid*, and *gaseous* states). Mesophases, observed above the melting point during heating are termed *enantiotropic*, whereas those occurring below the melting point on supercooling of the crystal, are *monotropic*[28]. In general, transitions between the various mesophases, which occur at defined temperatures, are reversible, with little hysteresis between heating and cooling cycles[28].

1.2.2.1 Thermotropic and lyotropic liquid crystals

Liquid crystals (LCs) are generally divided into two broad categories: (i) thermotropic LCs and (ii) lyotropic LCs. Thermotropic LCs are formed by heating a solid, or cooling an isotropic liquid, or by heating or cooling a thermodynamically stable mesophase[28]. Organic molecules with rod-like (calamitic or prolate) or disc-like (discotic or oblate) shapes typically form thermotropic mesophases. The minimum number of components necessary to form a thermotropic mesophase is one (i.e. only the mesogen is needed); and the degrees of freedom that need to be specified, according to the Gibbs phase rule is one (usually temperature). On the other hand, lyotropic LCs are formed by dissolving compounds having amphiphilic character in a suitable protic solvent, such as water or glycerol, under appropriate conditions of concentration and temperature[28]. Lyotropic LCs require a minimum of two components to form, such that both composition and temperature must be specified to describe the mesophases.

Additives (commonly referred to in the literature, as guest molecules) are sometimes incorporated into liquid crystals (host molecules), to form LC binary mixtures[29]. The goal for researching such host-guest mixtures, is often to explore unusual phase sequences of the host LC. Many novel LC phases resulting from binary mixtures have been identified, which have found practical application for electronic displays and thermal sensors[29]. When the guest molecule is a non-mesogenic solvent, it is important to note that such binary mixtures are not lyotropic systems. Polymer-dispersed liquid crystals (PDLCs) are another class of host-guest systems, in which LCs are dispersed in amorphous polymers. Many

large-area displays, commonly used as road signs and advertisements boards, as well as electrically switchable windows, are PDLCs[29].

1.2.2.2 Thermotropic mesophases

Thermotropic mesophases are generally grouped based on their degree of anisotropy, as well as their molecular orientation[28]. The average direction, along which the molecules point, is termed the director of the phase, ***n***. The most common phases are the nematic (N) and smectic (Sm) phases. Upon cooling from the isotropic liquid, the nematic (N) phase is first encountered, where rod-like molecules align parallel to each other, with their long axes all pointing roughly in the same direction[28]. Molecules in the nematic phase rotate about their long axes, and to some degree about their short axes. When cooled further, the molecules in the nematic phase may subsequently separate out into layers, resulting in the smectic (Sm) phase. The N phase therefore has only ***orientational order***, whereas the Sm phase has both ***orientational*** and ***translational (or positional) order***.

Smectic phases therefore have at least two directions; the *director* and the *layer normal*. Multiple smectic phases exist (labeled A, B, C… G, etc.) depending on the relationship between the two directions. In the simplest smectic phase (the smectic A phase), the director and layer normal are collinear. In the smectic C phase, the director is tilted, making an angle with the layer normal. Other subtle variations in smectic phases lead to smectic sub-classes (eg. SmA_1, SmA_2, SmA_d, etc)[28].

1.2.2.3 Orientational and translational order parameters

Order parameters "quantify" the quality of orientation and layering. The degree to which rod-like molecules are aligned along the director, is termed the ***orientational order parameter*** of the phase, which is defined as:

$$S = \frac{1}{2}\langle 3cos^2\theta - 1\rangle$$

where θ is the angle between the long axis of each individual rod-like molecule, and the director $\boldsymbol{n}$. An S value of 0 indicates no order (isotropic liquid) and 1 indicates perfect orientational order. Translational order refers to a distribution function, $D(r)$, which is a measure of the probability of finding the center of mass of a molecule at position r with respect to a test molecule at $r = 0$. To quantify the quality of layering (i.e., the extent to which the molecules are organized into layers), McMillan[30–32] introduced the ***translational (positional) order parameter,*** Σ, defined as the amplitude of the density wave that originates from the one-dimensional periodic layers[28,30]. The translational order parameter also takes values ranging from 0 (no positional order) to 1 (perfect positional order). Thus, the more the molecules are segregated into well-defined layers, the higher the translational order parameter.

1.2.3 Phase transitions in rod-like liquid crystals

Liquid crystalline materials show a rich variety of phase transitions[33]. Calorimetric studies provide information on the energy effects. Complementary structural information can be obtained from X-ray and molecular-mobility studies[20].

1.2.3.1 General classification of phase transitions – first and second order transitions

Phase transitions in liquid crystals can be first-order, or second-order[33]. In first-order transitions, there are discontinuities in the first derivative of the free energy with respect to other thermodynamic variables. Solid-to-liquid, and liquid-to-gas transitions are typically first-order. First-order transitions also involve a latent heat. The magnitude of the latent heat, and the presence (or absence) of pretransitional heat capacity effects, are used to sub-classify first-order transitions as strong or weak transitions. Second-order phase transitions are continuous in the first derivative but exhibit discontinuity in the second derivative of the free energy. The heat capacity (C_p), exhibits either a discontinuous jump (mean-field behavior) or a divergence (critical fluctuation behavior)[20]. **Table 1.1** gives a summary of the characteristic behavior of enthalpy (H) and the specific heat capacity (C_p) as a function of temperature (T), near the transition temperatures (T_{tr}) for first-order, and second-order phase transitions[33].

1.2.3.2 Liquid crystalline phase transitions

The most extensively studied transitions in calamitic LCs are the isotropic-to-nematic (I-N) and the nematic-to-smectic A (N-SmA) transitions[34]. Direct transition from the isotropic to the smectic phase (I-Sm) is relatively less common, and not as well-studied[35].

Isotropic-Nematic Transition: Thermodynamic behavior in the vicinity of the I-N transition, is often described by the Landau–de Gennes model, based on an expansion of

the excess free energy as a function of the orientational order parameter S[36,37]. For calamitic LCs, the I-N transition is mostly a first-order (or weakly first-order) transition.

Nematic-Smectic Transition: According to McMillan[31,38], the N-SmA transition is generally a second-order (continuous) transition, even though it may also be first-order. It becomes first-order, when a coupling exists between the translational and the orientational order parameters[31,38].

Isotropic-Smectic Transition: Direct transition from the isotropic (I) to the smectic (Sm) phase has been described based on the Landau–de Gennes theory, as a prototype symmetry breaking transition (a strongly first-order transition)[35,39].

Table 1.1. Variation of enthalpy (H) and specific heat capacity (C_p) with temperature for liquid crystalline phase transitions.
H_L = latent heat, δH = pretransitional enthalpy increase, CP = critical point. The heat capacity and enthalpy of the vertical axes increase upwards. Temperature (horizontal axes) increases to the right. Marks on the horizontal axes indicate the transition temperatures. Figures are reproduced from reference [33].

	Transition	Enthalpy (H) profile	Heat capacity (C_p) profile	Description and features
1	**Strong First Order**	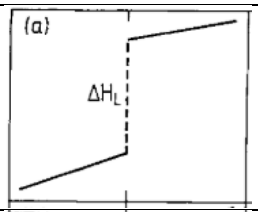	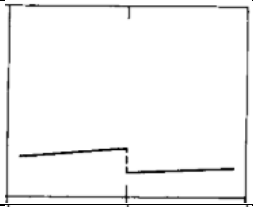	Large latent heat. C_p almost temperature-independent
2	**Weak First Order**, with pretransitional fluctuation behavior	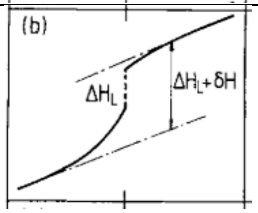	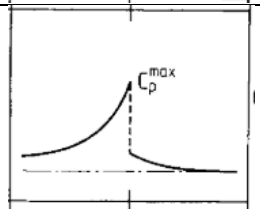	Small latent heat. Substantial pretransitional temperature variation in H. Anomalous pretransitional increase in C_p
3	**Mean-field second-order**. CP is the critical point on the enthalpy curve for the Landau second-order transition temperature.	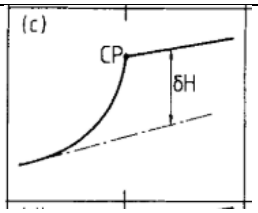	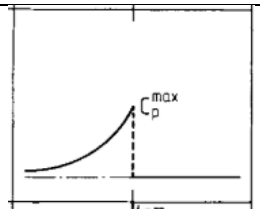	Rapid variation of H below T_{tr} due to changes in long-range order with temperature. Rapid change of C_p below T_{tr}; discontinuous C_p jump at T_{tr}.
4	**Critical fluctuation-dominated second order** with a diverging specific heat capacity at the critical temperature	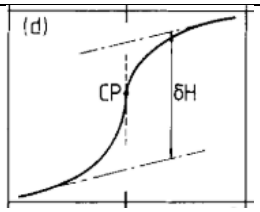	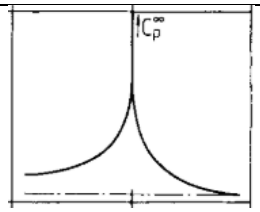	Pretransitional enthalpy variation; anomalies in C_p above and below T_{tr}. Divergence of C_p to infinity
5	**Critical fluctuation-dominated second order** with a large but finite specific heat capacity at the critical temperature	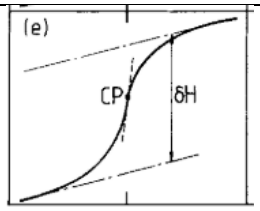	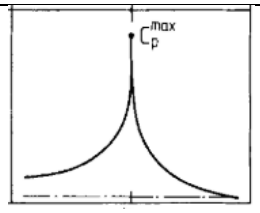	Pretransitional enthalpy variation; anomalies in C_p above and below T_{tr}. C_p has a large but finite value

1.2.3.3 Thermal characterization of phase transitions in liquid crystals

Differential scanning calorimetry (DSC) is an ideal survey technique for locating different phases and determining the major thermal features associated with phase transitions. However, DSC is not suited for making detailed quantitative measurements of latent heats, making it difficult to distinguish first- and second- order transitions[20,33]. It is also impossible to identify weak first-order transitions with significant pretransitional heat capacity variations using DSC alone. The main problem of the DSC, in this regard, stems from the requirement of rapid scan rates[20,33].

Adiabatic scanning calorimetry (ASC) provides greater accuracy and resolution, allowing detailed study of the phase transitions in liquid crystals. ASC continuously measures, with high precision, the evolution of the heat capacity C_p and the enthalpy H of a sample as a function of temperature while maintaining thermal equilibrium within the sample. The basic measurement principle is as follows: a constant power P is supplied to the sample and the resulting change in temperature T is measured as a function of time t[20,33]. The heat capacity is calculated from the relation:

$$C_p = \frac{P}{T(t)}$$

The enthalpy as a function of temperature, $H(T)$, can also be obtained from the relation:

$$H(T) = H(T_0) + P[t(T) - t(T_0)]$$

where T_0 is the starting temperature, and $t(T_0)$ is the start time for a run. Continuous determination of $H(T)$, provides a unique tool for confirming the order of phase transitions.

If the enthalpy shows a jump at a certain temperature, a latent heat is present, and the transition is discontinuous (first-order). However, if such a jump is absent, the transition is continuous (or second-order).

1.2.3.4 Theoretical analysis of heat capacity data of phase transitions

When the heat capacity $C_p(T)$ and/or enthalpy $H(T)$ data has been acquired experimentally, an essential second step is the theoretical analysis to gain insight into the basic physical model that explains the thermal properties of the phase transitions[20]. The magnitude of the latent heat ΔH_L, relative to the pretransition enthalpy δH, indicates how close the system is to either an ***isolated critical point*** (the critical point is the end point of a phase equilibrium curve), or to a ***tricritical point*** (the point in a phase diagram, at which three-phase coexistence – the triple point – terminates). The liquid-to-gas transition, for example, is at an isolated critical point. The SmA_d-to-SmA_2 transition was also shown to be an isolated critical point[40]. At a tricritical point, a first-order phase transition can change into a second-order transition (and *vice versa*). This unusual effect, has been shown, in the N-SmA transition of some liquid crystals[33,41].

The variation of certain physical properties near the phase transition point of a system, can be defined in terms of critical exponents[20]. There are many different kinds of critical exponents. The critical exponent α, relates the specific heat capacity C_p, to reduced temperature $\tau = \frac{T-T_c}{T_c}$, [where T_c (critical temperature) is the temperature at which the

transition occurs] *via* the relation, $C_p = A|\tau|^{-\alpha} + B$. In the latter expression, A and B are the critical amplitude and background term, respectively[20].

The critical exponent can be determined by analyzing adiabatic scanning calorimetry heat capacity data, measured above and below the phase transition. Different *universality classes* have unique theoretical α values. For example, when $\alpha = 0.5$, the transition is at a tricritical point; $\alpha = 0$ indicates mean field behavior. The critical exponent from heat capacity data, can be related to the order parameter from x-ray experiments, using the Rushbrooke scaling relation ($\alpha + 2\beta + \gamma$; where β is the order parameter exponent, and γ is from susceptibility) or the hyperscaling relation ($2 - \alpha = dv$; where v is the correlation length exponent)[20].

To summarize, adiabatic scanning calorimetry heat capacity data analysis is thus useful for (i) locating phase transitions, (ii) establishing the global behavior at critical points, (iii) testing the consistency of independent experimental quantities, and (iv) testing the level of agreement with theoretical models.

1.2.4 Potential benefits of pharmaceutical liquid crystals

Despite being widely used in optics and electronic displays, liquid crystals are not extensively studied in the pharmaceutical literature[29]. Pharmaceutical compounds that have been reported to have LC phases include fenoprofen, nafcillin sodium, cromolyn sodium, folic acid, ritonavir, nafoxidin hydrochloride, itraconazole, salvarsan,

neosalvarsan, palmitolyl propranolol hydrochloride, penbutolol sulfate, ciclosporin, cholesteryl myristate[22]. The majority form lyotropic LC phases, and find use in topical preparations such as creams and lotions because of their interactions with phospholipids[29]. Thermotropic LC drugs are relatively less common. Thus, not much has been documented about their structure/property relationships, and their pharmaceutical benefits[42].

1.2.5 Molecular mobility

In the context of amorphous (supercooled) materials, molecular mobility refers to the molecular movement that results from the constant rearrangement towards structural equilibrium. There are two main groups of motions – global motions (characterized by α-relaxation times) and local motions (characterized by β-, γ, δ relaxation times). Global motions, the slower of the two groups, are co-operative and responsible for the glass transition[19]. Local motions, which are non-cooperative, result from movements of branch chains (in the case of large polymers), or movements of the entire molecule[43,44].

In the supercooled state, α-relaxation times are very short (typically <100 s) and the temperature-dependence is often well-described by the Vogel-Fulcher-Tammann equation[45]:

$$\tau_\alpha = \tau_0 exp\left(\frac{DT_0}{T - T_0}\right) \tag{1.1}$$

where τ_0, T_0 and D are fitting parameters: τ_0 is the relaxation time of the unrestricted material, D is the strength parameter, an indicator of the kinetic fragility of the material, and T_0 is the temperature of zero mobility (theoretical Kauzmann temperature).

In the glassy region, α-relaxation times become extremely slow, with an Arrhenius-like temperature dependence[46,47]. Local motions on the other hand, become more prominent, exhibiting Arrhenius temperature dependences[46,47].

1.2.6 Polymeric additives

A wide range of polymers have been used for ASD formulations. Based on comprehensive reviews by Leuner & Dressman (2000)[12], and Liu & Edgar (2016)[48], the common polymeric excipients have been categorized in **Table 1.2.** Several novel polymers have also been developed specifically for ASDs, including carboxyl-containing cellulosic materials[49], and amphiphilic block copolymers such as Soluplus® (polyvinyl caprolactam–polyvinyl acetate–polyethylene glycol graft copolymer)[50]. The novel polymers tend to have bifunctional character, as matrices for solid solutions and as active solubilizers through micelle formation in water. Soluplus®, the most well-known and earliest example of such "novel" polymers, was also designed to be self-plasticizing such that it would be easily used in hot-melt extrusion[51].

Table 1.2. Polymers used in ASDs.

Polymer types	General classification	Examples
Synthetic Polymers	Hydrophilic polymers	Polyvinylpyrrolidone (PVP) Polyethylene Glycols (PEG)
	Hydrophobically modified polymers	Polyvinylpyrrolidone vinyl acetate (PVPVA) Polyvinyl acetate phthalate (PVAP)
	Methacrylate-based polymers	Polyhydroxyethyl methacrylate (PHEMA) Eudragit® (copolymers derived from esters of acrylic and methacrylic acid)
Cellulose Derivatives	pH Independent Cellulose Esters and Ethers	Cellulose acetate Cellulose butyrate Cellulose acetate phthalate Hydroxypropyl methyl cellulose phthalate (HPMCP)
	pH responsive cellulose derivatives	Carboxymethyl cellulose acetate butyrate Cellulose acetate phthalate Hydroxypropyl methyl cellulose Phthalate Hydroxypropyl methyl cellulose acetate succinate (HPMCAS)

1.2.6.1 Mechanisms by which polymers stabilize amorphous drugs

The main mechanisms by which polymers stabilize amorphous solid dispersions, in the dry "solid" state, include (i) reduction in molecular mobility of the drug, (ii) specific interactions with functional groups of the drug (iii) increase in the glass transition temperature (T_g) of the system (antiplasticization), and (iv) the polymer as a "physical" barrier to crystallization (i.e. polymer dilution). Though often investigated as separate phenomena, in reality, all four mechanisms are interrelated. For example, specific drug–polymer interactions result in reduced molecular mobility, which could further manifest as an increase in the T_g of the system[52].

1.2.6.1.1 Reduction in molecular mobility

Because molecular mobility precedes or accompanies crystallization, the two phenomena may be coupled[19]. Thus, an additive that restricts mobility of the amorphous drug, can potentially suppress drug recrystallization; the converse also holds true. As an example, in the supercooled liquid region, polyacrylic acid (PAA) reduced the molecular mobility of acetaminophen to a greater extent than an equal amount of polyvinylpyrrolidone (PVP)[53]. The acetaminophen-PAA ASDs were thus more physically stable than the acetaminophen-PVP ASDs[53]. Reduced drug mobility due to the presence of the polymer, has also been linked to improved physical stability of ASDs in the glassy region[54].

The extent of coupling between molecular mobility and crystallization, in both the supercooled and glassy states, can be obtained by comparing the timescales of various kinds of molecular motions (global or local mobility) to the timescales of crystallization, using a logarithmic correlation plot[19]. In the supercooled region, high coupling values have been obtained for ASDs prepared from several drug–polymer systems such as nifedipine-PVP[55], itraconazole-HPMCAS[56], celecoxib-PVP[57], and indomethacin-PVP[58], thereby, further underscoring the relevance of molecular mobility in physical stabilization.

1.2.6.1.2 Specific drug–polymer interactions

In general, the strengths (inferred from theoretical bond energies) of intermolecular interactions can be rank-ordered as: ionic interactions (~1000 kJ/mol) > hydrogen-bonding (~100 kJ/mol) > dipole-dipole interactions (~10 kJ/mol)[59]. Several studies have

highlighted a general correlation between the strength of drug–polymer interactions, and the physical stability of ASDs upon storage[52,60–63]. Strong interactions between drug–polymer pairs have been linked to increased crystallization inhibition. Examples include ionic interactions (ketoconazole–polyacrylic acid[52], lapatinib–hydroxypropyl methyl cellulose phthalate[60], and acetaminophen – polyacrylic acid) as well as hydrogen bonding (indomethacin–PVP[61,62], nifedipine–PVP[63], and celecoxib–PVP). Strong drug–polymer interactions cause the movements of the drug molecules to be restricted, thereby leading to reduced crystallization. The effect of interactions can be easily assessed in ASDs with low polymer content (<5% w/w), where the T_g of the system is not raised relative to the T_g of the neat drug[52].

1.2.6.1.3 Antiplasticization

Polymers with high glass transition temperatures (T_g), when miscible with the drug, can result in single-phase ASDs with T_g values higher than that of the neat drug. When the T_g of the ASD is sufficiently raised by the polymer, molecular mobility can be substantially reduced, at pharmaceutically-relevant storage temperatures (in the glassy region). An increase in T_g is often considered an indicator of reduction in molecular mobility. The extent of antiplasticization (or plasticization) is often quantified by mathematical models based on the free volume theory, such as the Gordon-Taylor[64] equation.

1.2.6.1.4 Polymer as a physical barrier to drug diffusion

The polymer may also prevent drug crystallization, by simply forming a physical barrier around the drug molecules, thereby reducing drug diffusion. This is usually suggested as the main mechanism when specific drug–polymer interactions are absent, the T_g of the system is not affected relative to the neat drug, and there is no measurable difference in molecular mobility. As an example, three polymers – PVP, HPMC and HPMCAS – were found to be equally effective in reducing the crystallization rate of felodipine from amorphous solid dispersions (at comparable polymer loading)[65]. There was no correlation between the nucleation rate and either the T_g of the ASDs relative to the neat drug, or the presence of drug–polymer hydrogen bonding. The authors reasoned, therefore, that the polymers simply increased the kinetic barrier to nucleation[65]. Similarly, small amounts of PVP (up to 10% w/w) in dispersions resulted in marked increases in the crystallization induction times of sucrose[66]. The polymer caused very little change to the T_g of sucrose, in the concentration range where significant inhibition of crystallization occurred[66]. Similar effects have been reported, where polymer dilution inhibited crystal growth and disrupted crystallite morphology[67,68].

1.2.7 Plasticizers

Plasticizers are materials (typically low molecular weight, low viscosity, low T_g liquids), generally added to polymers or amorphous compounds, to increase plasticity/flexibility, or to reduce brittleness[69]. Plasticizers are incorporated in ASDs to facilitate manufacturing processes such as hot melt extrusion or to alter the physicochemical properties of the final

product[51]. Common plasticizers include polyalcohols (e.g. glycerol), citrate esters (e.g. triethyl citrate), fatty acid esters (glycerol monostearate, stearyl alcohol), glycol derivatives (polyethylene glycol, propylene glycol), vitamin E TPGS, mineral and castor oils, etc[51]. Surfactants such as polysorbate 80, sodium lauryl sulfate and docusate sodium, have also been evaluated as plasticizers for polymer systems. Water, a universal plasticizer, may also inadvertently be introduced into amorphous formulations, from the atmosphere or during processing. Despite their importance in processing, plasticizers are known to accelerate drug crystallization, which is an undesired effect[51,70]. Nonetheless, some plasticizers, at low concentrations, may counterintuitively exert an anti-plasticization effect[71].

1.2.7.1 Mechanisms of plasticization

The *lubricity*, *gel*, *viscosity* and *free volume* theories are the main theories that explain plasticization[72]. The theories were developed based on polymer models, but the principles also apply to small molecules. Other quantitative models have also been developed from computational methods[72].

According to the ***lubricity theory***, plasticizers reduce intermolecular friction between the host molecules, causing the molecules to slip over each other more easily. The reduced internal resistance to sliding, leads to increased molecular movement[72]. The ***gel theory*** considers the polymer as having a rigid three-dimensional "honeycomb" structure, with lose attachments/interactions between the polymer molecules. The plasticizer reduces the

number of points of attachment, (i.e. reduces the polymer-to-polymer interactions) causing the rigid polymer structures to be deformed or disaggregated[72,73]. The ***free volume theory,*** postulated by Fox and Flory[74], indicates that between atoms and molecules, there is nothing but free volume (defined as the difference between the volume observed at absolute zero temperature, and the volume measured for the real crystal, glass or liquid, at a given temperature)[74]. The free volume gives enough "room" for the host molecules to move. Plasticizers typically increase the free volume of the system, leading to additional flexibility and ease of movement to the host molecules. Many mathematical models, based on the free volume additivity rule have been developed, which correlate the glass transition temperature (T_g) of the plasticized systems, with the individual T_gs of the host compound and the plasticizer[74]. The extent to which a plasticizer reduces the T_g, is usually a measure of the plasticizer efficiency[75].

1.2.8 Dissolution of amorphous solid dispersions

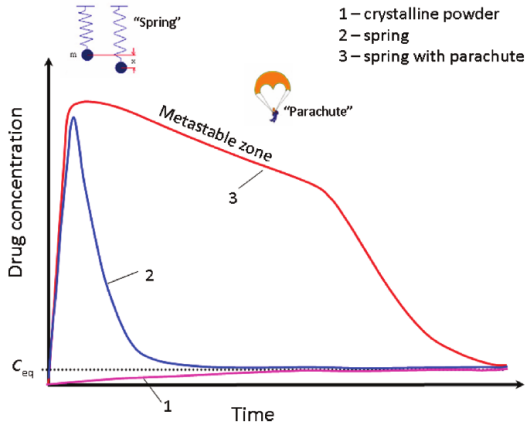

Figure 1.2. The spring and parachute concept, to describe achieving high apparent solubility for poorly-soluble drugs. Figure reproduced from Babu and Nangia[76]

The dissolution of amorphous systems is usually described by the "spring and parachute" concept[4,77]. When introduced into an aqueous medium, the neat amorphous compound rapidly dissolves, yielding a highly supersaturated solution (the spring in **Figure 1.2**). The peak solubility occurs due to a combination of factors, such as the higher free energy, reduced particle size, randomization of molecules, larger surface area and the higher wettability of the amorphous drug[4]. The high supersaturation however becomes a driving force for crystallization, leading to a rapid concentration decline.

The initial dissolution rate of an ASD may be drug-controlled or polymer-controlled[16]. Drug-controlled dissolution typically occurs when the ASD has a low polymer content. A drug-rich layer forms at the dissolving surface, which crystallizes rapidly, preventing further drug release. When the ASD has high polymer content, drug release is independent of the drug properties, and thus referred to as polymer-controlled dissolution. These mechanisms mainly apply to hydrophilic polymers.

For the ASD to maintain the peak drug concentration (i.e. for the metastable zone/ "parachute" in **Figure 1.2** to be prolonged), the amorphous-to-crystalline phase transformation must be inhibited by the polymer. The mechanisms of stabilization in the "solid" state (explained in section 1.2.6.1), may also be relevant in aqueous solution. Thus, the polymer may prevent drug concentration decline, by maintaining specific interactions

with the functional groups of the drug, by reducing mobility of the drug molecules, or by acting as a physical barrier to drug aggregation.

Drug–polymer interactions formed in the dry ASD (ionic interactions, hydrogen bonding, and other weaker intermolecular attractive forces) can, in principle, be disrupted by competing polymer–water interactions, especially when the polymer is substantially hydrophilic. Of the main types of interactions, hydrogen bonding may be the most susceptible to disruption by water molecules[78]. Comparatively, drug–polymer hydrophobic associations may be more stable in aqueous media. Thus, amphiphilic polymers with high hydrophobic content have been found to maintain drug supersaturation for longer durations[79,80]. Measures of molecular movement in solution (i.e. Brownian motion) such as diffusion or sedimentation, can reveal the impact of heterogeneous interactions. Diffusion measurements in particular, have been used to characterize ligand-protein interactions in aqueous media[78]. The polymer may also act as a physical barrier to crystallization in solution, by changing the hydrodynamic boundary layer of the crystal surface, thereby decreasing the rate of molecular migration to the crystal. Adsorption of the polymer to any crystal nuclei formed, can also prevent further crystal growth[81].

1.2.9 Characterizing drug–polymer interactions in aqueous solution

Analytical methods routinely used for characterizing ligand–protein, or protein–excipient interactions in solution, may be used for drug–polymer interaction studies. The most commonly used are spectroscopy (e.g. FTIR, Raman, vibrational optical activity, NMR,

fluorescence) and calorimetry (e.g. isothermal titration calorimetry)[78]. The biggest challenge with using any of the techniques for characterization of drug–polymer interactions in water, is the poor aqueous solubility of the model drug compounds, which leads to weak signals.

1.2.9.1 Analytical ultracentrifugation

An analytical ultracentrifuge is simply a high-speed (up to 60,000 rev/min) centrifuge, with an appropriate detecting system for simultaneously recording solute migration in solution. AUC experiments are generally in two classes: (1) sedimentation velocity (SV-AUC) and (2) sedimentation equilibrium (SE-AUC), the key difference being the strength of the centrifugal field applied. SV-AUC experiments typically utilize higher centrifugal fields, and shorter run times. In SV-AUC, the centrifugal field causes the solute to migrate from the meniscus to the base of the AUC cell. The migration of molecules as a function of time is characterized by the sedimentation coefficient, s, which is the velocity per unit centrifugal force:

$$s = \frac{1}{\omega^2 r}\frac{dr}{dt} = \frac{m}{f} \tag{1.2}$$

where $\omega^2 r$ is the centrifugal field, r the radius, t time of sedimentation, m the buoyant molecular mass and f the frictional coefficient. The sedimentation coefficient is expressed in the unit of seconds, but usually reported in Svedbergs, S, where 1 S = 10^{-13} seconds. The sedimentation coefficient is also governed by the famous Svedberg equation,

$$s = \frac{M(1 - \overline{v} \cdot \rho_s)}{N \cdot f} \tag{1.3}$$

where M is the molar mass, $\overline{v}$ the partial specific volume of the solute, ρ_s the density of the solvent, f is the friction coefficient and N Avogadro's number. Assuming validity of Stoke's law, the Svedberg equation can be manipulated to obtain particle sizes (or more precisely, Stokes-equivalent diameters) *via* the relation:

$$d_p = \sqrt{\frac{18\eta_s s}{(\rho_p - \rho_s)}} \tag{1.4}$$

where d_p is the particle diameter (Stoke's equivalent diameter), η_s is the dynamic viscosity of solvent and ρ_p is the particle density.

Experimentally observed sedimentation coefficients vary with temperature and solution density. Thus, s-values are usually converted to a standard state of 20 °C in water, at infinite dilution (denoted $s_{20,w}$). When the measured $s_{20,w}$ value is compared with the $s_{20,w}$ predicted theoretically for a smooth compact sphere of the same mass and density, the frictional ratio, f/f_0 is obtained[82]. The frictional ratio characterizes the shape of the molecule. Additional details of the basic theory of Analytical Ultracentrifugation can be found in excellent literature references[83].

1.3 CHAPTER DESCRIPTIONS AND HYPOTHESES

1.3.1 Chapter 2

In an earlier report, the influence of the strength of drug–polymer interactions on the molecular mobility and physical stability of amorphous solid dispersions formulated with ketoconazole (KTZ) and each of the three polymers – (i) poly(acrylic acid), (PAA) (ii) poly hydroxy methyl methacrylate, (PHEMA) and (iii) poly vinyl pyrrolidone, (PVP) – was investigated[52]. Ionic, as well as hydrogen-bonding interactions were characterized between KTZ and PAA and hydrogen bonding was characterized between KTZ and PHEMA. There were no specific interactions between KTZ and PVP. The drug–polymer interaction strengths, as well as the physical stability of the ASDs, were rank-ordered as KTZ-PAA > KTZ-PHEMA > KTZ-PVP. The interactions, molecular mobility and crystallization measurements were conducted in the dry "solid" form, without any organic or aqueous solvents. An unanswered question, however, was if the interactions observed in the "solid" state, would be maintained in aqueous solution, and if such interactions would translate to improved dissolution performance. In Chapter 2, the work was extended into aqueous solution, using the same model systems. The hypothesis was:

> ***Strong drug–polymer interactions in the solid state, can translate into interactions in aqueous solution, resulting in an increased extent and duration of supersaturation.***

Potential interactions in water were investigated with two-dimensional NMR and isothermal titration calorimetry. Crystallization (monitored with synchrotron X-ray diffractometry) and dissolution tests (USP apparatus IV) were used to gauge the ASD performance in water.

1.3.2 Chapter 3

A link between strength of interactions in the dry ASD, and the strength of interactions in aqueous media was shown, with ketoconazole ASDs in Chapter 2. It was our intention to extend this study to other model systems, to determine if the hypothesis could be generalized. Model drugs of interest included indomethacin[58,61], nifedipine[63] and griseofulvin[84]. In each of the literature sources cited, the solid-state interactions of the drugs with various polymers had been characterized, and there was a good correlation between the drug–polymer interaction strengths and the physical stability of the ASDs. Our approach was to investigate whether the drug–polymer interactions persist in aqueous media, using two-dimensional NMR and isothermal titration calorimetry. However, we encountered a significant challenge; the low aqueous solubility of these compounds caused very low signal strengths, below the limit of quantification of the analytical techniques. This challenge highlighted the need for other analytical techniques that could characterize drug–polymer interactions at the molecular-level, in aqueous media, with enough analytical signal sensitivity.

We therefore explored the use of analytical ultracentrifugation (AUC) for the characterization of drug–polymer interactions, in Chapter 3. We used the principle of co-sedimentation, to infer interactions. Our hypothesis was as follows:

> ***Drug–polymer interactions in solution will cause the sedimentation behavior of a drug, in the presence of a polymer, to change and approach the sedimentation behavior of the neat polymer.***

To test this hypothesis, we selected three drug–polymer pairs (that had been shown by other techniques, to interact in aqueous solution) as model systems, and investigated their sedimentation patterns with analytical ultracentrifugation.

1.3.3 Chapters 4 and 5

Chapters 4 and 5, are two parts of an investigation into the effect of glycerol, on the liquid crystalline phase transitions of itraconazole. Itraconazole (ITZ) is a thermotropic liquid crystal with isotropic, nematic and smectic A phases. When glycerol, a plasticizer, was incorporated into ITZ by solvent evaporation, unusual effects were observed:

(i) the mesophase sequence was altered in a glycerol-concentration dependent manner.

(ii) drug crystallization was not observed for more than 2 years, when the ITZ-glycerol mixtures were stored in the glassy region.

The goal was therefore to understand the mechanism by which glycerol modulated the mesomorphic sequence and the physical stability of ITZ. The hypothesis to be tested for both chapters was:

Additives with fast dynamics, can accelerate the development of smectic order in itraconazole, by a coupling of the additive concentration to the translational and orientational order parameters of the neat drug.

In Chapter 4, we investigated the thermal behavior of neat ITZ as well as the ITZ-glycerol mixtures, using differential and adiabatic scanning calorimetry (DSC and ASC). The transition temperatures and total enthalpy changes were located with DSC. Then, the critical behavior and the order of the mesomorphic transitions were established with ASC. Finally, in Chapter 5, the structural packing arrangement, molecular mobility, physical stability and dissolution behavior of the samples were investigated using synchrotron X-ray diffractometry and spectroscopy (IR and NMR).

2 The Influence of the Strength of Drug–Polymer Interactions on the Dissolution Performance of Amorphous Solid Dispersions

2.1 OVERVIEW

In an earlier report, ionic interactions between ketoconazole (KTZ), a weakly basic drug, and poly(acrylic acid) (PAA), an anionic polymer, resulted in a dramatic decrease in molecular mobility as well as reduced crystallization propensity of amorphous solid dispersion (ASD) in the solid state. On the other hand, weaker dipole–dipole interactions between KTZ and polyvinylpyrrolidone (PVP) resulted in ASDs with higher crystallization propensity (Mistry *et al*, Mol Pharm. 2015;12(9):3339-3350). In this work, we investigated the behavior of the ketoconazole (KTZ) solid dispersions in aqueous media. *In vitro* dissolution tests showed that the PAA ASD maintained the level of supersaturation for a longer duration, than the PVP ASD at low polymer contents (4 to 20% w/w polymer). Additionally, the PAA ASDs were more resistant to drug crystallization in aqueous medium, when measured with synchrotron X-ray diffractometry. Two-dimensional ^{1}H NOESY NMR cross peaks between ketoconazole and PAA confirmed the existence of drug–polymer interactions in D_2O. The interaction was accompanied by a reduced drug diffusivity as monitored by 2D DOSY NMR, and enthalpy-driven when characterized by isothermal titration calorimetry (ITC). On the other hand, drug–polymer interactions were not detected between ketoconazole and PVP in aqueous solution, with NOESY, DOSY or ITC. The results suggest that the interactions that stabilize ASDs in the solid state, can also be relevant and important in sustaining supersaturation in aqueous solution.

2.2 INTRODUCTION

The rate and extent of drug absorption following oral administration is influenced by solubility in the gastro-intestinal (GI) fluid and permeability through the GI membrane[8]. Advances in combinatorial chemistry and high through-put screening methods have led to an increase in target specificity and hydrophobicity of drug candidates[1,85]. With more than 70% of drugs under development having high permeability but poor aqueous solubility (BCS Class II compounds), strategies that enable increased apparent aqueous solubility, have become important[8,86]. One strategy is to use amorphous solid dispersions (ASDs), which refer to molecular-level mixtures of drug and polymer, formulated with the aim of improving oral bioavailability. From a formulation perspective, the first step towards stabilization of ASDs is to prevent drug crystallization in the solid state, during storage, and polymers have proven effective in that regard[87]. The ability of the polymer to raise the glass transition temperature (T_g) of the dispersion[88], to reduce molecular mobility[19], and to act as a physical barrier to molecular aggregation[65–68], have all been linked to crystallization inhibition in the solid state.

If the drug is retained in the amorphous state until used by the patient, but crystallizes rapidly following oral administration, the potential solubility advantage may be negated. Adequate supersaturation in the GI fluid must be maintained for a period, long enough to translate to enhancement in absorption and consequently bioavailability. Therefore, in addition to stabilizing the drug in the dry solid dispersion, polymers must help maintain drug supersaturation in solution. To gauge the extent and duration of solubility

enhancement, amorphous formulations are usually evaluated using *in vitro* dissolution tests. The physicochemical properties (such as the degree of lipophilicity and ionizability) of both the polymer and the drug, viscosity of the diffusion layer, the drug-to-polymer ratio of the formulated ASD, and the nature and strength of drug–polymer interactions are all key factors that can influence the degree of supersaturation, as well as the drug concentration in solution as a function of time.

The strength of intermolecular interactions can be rank-ordered as ionic interactions > hydrogen bonding > dipole-dipole (non-specific) interactions[59]. Several studies have highlighted a general correlation between the strength of drug–polymer interactions, and the physical stability of ASDs upon storage[52,60–63]. Strong drug–polymer interactions may prevent drug crystallization in the solid state by increasing miscibility, improving phase homogeneity and/or decreasing molecular mobility[52,63,89,90]. In an aqueous environment, however, the role of the type and strength of drug–polymer interactions on the dissolution enhancement, is not as clear. On the one hand, it is believed that when the strong solid state interactions persist in aqueous solution, the initial dissolution rate of the drug increases, and the level of supersaturation is sustained for a much longer duration[91]. Specific interactions that are resistant to disruption by water molecules, would thus be most beneficial. On the other hand, it has also been suggested that strong solid-state drug–polymer interactions may be detrimental to ASD performance in aqueous solution. As an example, drug–polymer hydrogen bonding in the solid state, was posited to cause a reduction in the dissolution rate, for ASDs with low polymer content[92]. There is a need for

studies that comprehensively characterize interactions in the solid state as well as in aqueous solutions, to enable rational selection of polymers during the development of ASDs.

We demonstrated in an earlier report, that the weakly basic drug ketoconazole (KTZ) exhibited ionic as well as strong hydrogen bonding interactions with poly(acrylic acid) (PAA), when formulated as an ASD[52]. As a result, there was a dramatic reduction in the molecular mobility of the system, and a consequent reduction in crystallization rate, both in the supercooled[52] and glassy states[93]. In contrast, poly (2-hydroxyethyl methacrylate) (PHEMA) and polyvinylpyrrolidone (PVP), showed weaker hydrogen bonding and dipole–dipole interactions with KTZ, respectively. The strength of drug–polymer interactions, reduction in molecular mobility, and the enhancement in physical stability followed the same rank order: PAA>PHEMA>PVP. The pronounced physical stabilization afforded by PAA raised the question: *Is the KTZ-PAA interaction, observed in the solid state, retained in aqueous medium following dissolution of the dispersion? If so, does the interaction prolong supersaturation?* To extend our work, we hypothesize that strong drug–polymer interactions in the solid state can translate to interactions in solution, thereby facilitating sustained supersaturation.

Our first objective was to evaluate the performance of the amorphous dispersions in aqueous media. Two complementary approaches were taken. (i) *In vitro* dissolution tests provided a measure of the drug concentration in solution and the duration of

supersaturation. (ii) The extent of drug crystallization as a function of time, monitored following wetting of the dispersion, provided a measure of the ability of the dispersion to resist crystallization. Our second objective was to identify and characterize the drug–polymer interactions in aqueous solution. Two-dimensional nuclear Overhauser effect spectroscopy (2D-NOESY) was used to probe the spatial proximity of drugs and polymers in solution[94]. The impact of interactions on drug diffusivity was assessed with diffusion ordered spectroscopy (DOSY)[95–98]. Finally, the thermodynamic "binding" signature and the strength of the interactions was measured with isothermal titration calorimetry (ITC)[99].

2.3 EXPERIMENTAL SECTION

2.3.1 Materials

Crystalline ketoconazole was obtained from Laborate Pharmaceuticals (Haryana, India). PAA (Mw ≈ 1800 g/mol) was purchased from Sigma-Aldrich (Missouri, USA), PVP-K12 (Mw ≈ 2000−3000 g/mol) was obtained from BASF (New Jersey, USA), and PHEMA (Mw ≈ 3700) was obtained from Polymer Source (Quebec, Canada). All solvents and chemicals were of analytical grade. The structures of all the compounds used are given in **Figure 2.1**.

(a) Ketoconazole (KTZ)

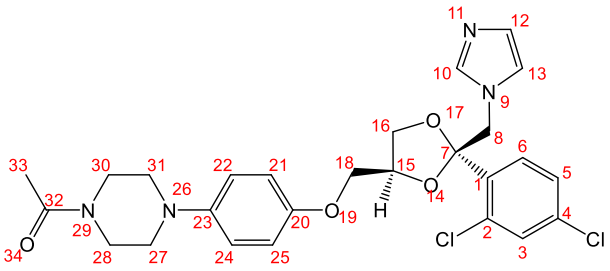

(b) Polyacrylic acid (PAA)

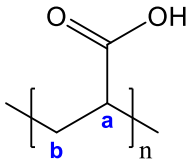

(c) Polyvinylpyrrolidone (PVP)

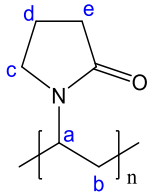

(d) Poly(2-hydroxyethyl methacrylate) (PHEMA)

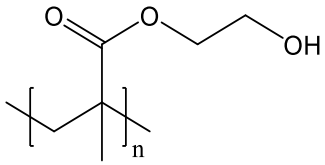

Figure 2.1. Structures of the model drug (KTZ) and polymers (PAA, PVP and PHEMA).

2.3.2 Preparation of amorphous systems

Neat amorphous KTZ was prepared by melting crystalline KTZ at 160°C and rapidly cooling in liquid nitrogen. The glass was gently ground using a mortar and pestle to obtain the free-flowing powder. Solid dispersions of KTZ with polymer contents ranging between 4 and 40% w/w, were prepared by solvent evaporation, followed by melt-quenching. The drug and polymer were dissolved in methanol, and the solvent was rapidly evaporated (IKA-HB10 digital system rotary evaporator, Werke GmbH and Co., Staufen, Germany) at 50 °C under reduced pressure. The powder was further dried under reduced pressure, at room temperature, for ~24 hours, to remove residual solvent before melt-quenching. As controls, physical mixtures were prepared by geometrically mixing neat amorphous KTZ with each polymer (4 to 40% w/w polymer content). All powders were sifted through 250 µm pore-size sieves, before use. Additional details of the preparation methods, as well as baseline characterization of the samples by differential scanning calorimetry, infra-red spectroscopy, thermal gravimetry, and Karl-Fischer titration have been reported elsewhere[52,100].

2.3.3 *In vitro* powder dissolution testing

Dissolution tests were conducted in aqueous phosphate buffer (pH 7.4), using a flow-through cell with a 22.6 mm internal diameter (USP Apparatus 4, Sotax Ltd) attached to a UV analyzer (Specord 210 Plus). A glass bead (5 mm diameter) was placed at the bottom of the cell to prevent the powder from entering the inlet tubing. The bottom cone of the

cell was filled with 1 mm diameter glass beads. A glass microfiber filter (Whatman®, 25 mm diameter, 0.7 µm pore size) prevented the undissolved powder from escaping from the top of the cell.

An accurately weighed quantity of the powder sample (50 mg drug equivalent) was distributed throughout the 1 mm glass beads of the flow-through cell. The dissolution medium, maintained at 37 °C, was pumped through the cell at a flow rate of 4 mL/min. The flow-through cell was operated in the open-loop mode, wherein fresh dissolution medium from the reservoir continuously passed through the cells. At pre-determined timepoints, the UV absorbance of the filtered sample was measured *in line* at 225 nm, against a reference cell containing the blank dissolution medium. The absorbance readings were converted to dissolved drug concentration values, using a calibration curve.

Experiments were run in triplicate and the mean and standard deviation values (as error bars) are presented. From each concentration-time dissolution profile, the area under the curve from the start of experiment to the last time point $(AUC)_{(0\rightarrow t)}$, the maximum concentration (C_{max}), and the time to reach the maximum concentration (T_{max}) were determined. The ratio [$AUC_{(0\rightarrow t)}$, sample]/[$AUC_{(0\rightarrow t)}$, crystalline KTZ], was used to quantify the extent of dissolution enhancement. The dissolution enhancement factors were compared using the student's t-test. A p-value ≤ 0.05 was used to assess statistical significance. All dissolution data analyses were performed with OriginLab® software.

2.3.4 Synchrotron X-ray diffractometry

Approximately 20 mg of each sample was accurately weighed in a DSC pan (T-zero®, TA Instruments, DE) and 25 μL of phosphate buffer (pH 7.4) was added to uniformly wet the sample. The pan was hermetically sealed, mounted on a custom-made holder, and exposed to synchrotron radiation at pre-defined time intervals, for approximately 4 hours. Measurements were performed in triplicate using fresh amorphous sample for each run. Details of the experimental set-up and data analyses procedures were presented earlier[100]. Diffraction patterns are presented as one-dimensional scattering intensity (I) versus scattering wavevector ($Q = 4\pi sin\,\theta/\lambda$) plots, where θ is the angle of incidence and λ is the wavelength. The crystallinity at each time point was quantified using equation (2.1), where I_c is the intensity of the crystalline contribution (total area of all crystalline peaks) and I_a is the intensity of the amorphous contribution (area of the amorphous halo)[101]. The peak areas were obtained by profile fitting (Jade®, Materials Data Inc, CA).

$$Crystallinity\ index = \frac{I_c}{I_c + I_a} \tag{2.1}$$

2.3.5 Solution NMR

Sample preparation for solution NMR experiments

Two methods were used to prepare drug–polymer mixtures for the NMR experiments. In the first method, an accurately weighed amount of polymer was dissolved in D_2O. The polymer solution (1 mL) was then added to an excess of KTZ (~20 mg) in a glass vial, shaken in a vortex mixer at room temperature for approximately 40 minutes, filtered (0.45

μm PTFE filter), and transferred to 5 mm NMR tubes for data acquisition. The concentration of KTZ in the filtrate was confirmed by HPLC (USP 25 Assay method for Ketoconazole Solution).

In the second approach, D_2O acidified to pH 2.5 with concentrated hydrochloric acid, was used as solvent. Stock solutions of ketoconazole and each polymer were separately prepared in the solvent. Aliquots of the drug and polymer stock solutions were pipetted into a vial, and diluted with an appropriate amount of solvent, such that the final drug and polymer concentrations were 5 and 20 mg/mL respectively. Spectra of the drug–polymer mixtures prepared using both methods were qualitatively similar, except for minor differences that could be explained by expected solution pH variations. Data presented within the text, are from the second method of preparation.

As controls, spectra of the neat drug and neat polymer solutions in acidified D_2O, were also acquired. Of note, KTZ did not dissolve in D_2O (with or without organic co-solvents), at concentrations high enough for detection. PHEMA was also not soluble in D_2O at relevant concentrations.

One-dimensional proton nuclear magnetic resonance spectroscopy (1D ^{1}H NMR)

1D ^{1}H-NMR experiments were performed on either a Bruker Avance III HD 500 MHz 2-channel spectrometer equipped with a 5 mm Prodigy TCI cryoprobe with z-axis gradients in the magnet, or on a Bruker AV 400 spectrometer. Spectral assignments were made,

based on standard 2D methods such as COSY, HSQC and HMBC experiments (data not shown), and compared with published data for KTZ[102,103], PVP[96] and PAA[104]. Spectra were processed with the Bruker Topspin software (version 3.2).

Two-dimensional proton nuclear Overhauser effect spectroscopy (^{1}H/^{1}H NOESY)

Experiments were performed on a Bruker Avance III HD 500 MHz 2-channel spectrometer equipped with a 5 mm Prodigy TCI cryoprobe with z-axis gradients in the magnet. Spectra were recorded using standard NOESY pulse sequence with water suppression using excitation sculpting, from the Bruker pulse-program library. All measurements were carried out at ambient temperature, ~25 °C. In a typical experiment, data were acquired with 2048 data points in F2, 256 increments in F1, and 16 scans per increment, over a spectral width of 12 ppm, with NOE mixing time of 1 s, and a relaxation delay of 2 s. Data analysis was done with the Topspin 3.2 software package.

Two-dimensional diffusion ordered spectroscopy (2D DOSY)

Experiments were performed on a Bruker Avance III (500 MHz) instrument with a 5 mm broadband fluorine observe (BBFO) probe, at ambient temperature (~25 °C). The longitudinal eddy current delay bipolar gradient pulse sequence acquired in 2D (ledbpgp2s) was employed for self-diffusion coefficient measurements. Gradient strength was incremented in steps along a linear ramp from 2 to 95% of the maximum strength of ~60 Gauss cm^{-1}. Gradient lengths and diffusion times were optimized for each sample, in order to achieve sufficient signal attenuation. The relaxation delay was 2 s and a total of 16 scans was used for each sample. Data was analyzed with the Topspin 3.2 software. The diffusion

coefficient (D) for each species was determined from a fit of selected resonances to equation (2.2).

$$I = I_0 * \exp\left[-D * (2\pi\gamma g\delta)^2 * \left(\Delta - \frac{\delta}{3}\right) * 1e4\right] \quad (2.2)$$

where I is the recorded signal intensity as a function of gradient strength g, I_0 the unattenuated signal intensity, γ the gyromagnetic ratio of ^{1}H, δ the length of the gradient pulse (2 ms), and Δ the diffusion time (~100 ms).

2.3.6 Isothermal titration calorimetry (ITC)

The objective of the ITC experiment was to obtain a quantitative measure of the drug–polymer interaction strength in aqueous solution. To make this possible, the drug solution concentration had to be high, such that an accurately measurable heat (> 0.5 µcal, for the largest heat) would be absorbed/released[105]. High KTZ concentrations (40 mM) could be prepared in acidic solvent (pH 1.1 buffer), but not in neutral buffers.

Sample preparation for ITC experiments

KTZ solution (40 mM) was prepared in buffer (pH 1.1 ± 0.1; comprising 106 mM HCl and 50 mM KCl), and filtered (0.45 µm PTFE), immediately before each ITC experiment. Solutions of each polymer (3 mM, calculated based on the weight-average molecular weight of the polymer) were separately prepared, using the same buffer (pH 1.1 ± 0.1).

ITC experimental details

Experiments were performed on a Microcal^{TM} Auto-ITC$_{200}$ system (Malvern Instruments, MA) which has a 200 µL sample cell and an identical reference cell. The sample cell was filled with the polymer solution and titrated with sequential injections of the drug solution at a constant stirring rate of 750 rpm. Control experiments were performed by (i) titrating the drug solution into blank buffer and (ii) titrating the buffer into the polymer solution. Unless otherwise stated, the sample chamber was maintained at 25 °C. The first injection was a 0.4 µL aliquot to remove the effect of solute diffusion across the syringe tip during the equilibration period. This first/initial injection was not considered for analysis. Subsequently, 4 µL injections were made into the sample cell for an experimental run time of 150 minutes. The duration of each injection was 20 s, and the time interval between successive injections was 180 s. To extend the run time, experiments were performed in an automated "continued injection" mode, wherein, when full, 30 µL of solution was withdrawn from the sample cell and discarded, to make room for more sequential injections of the titrant. This process of withdrawing solution from the sample cell and continuing the titrations was repeated for up to six experiments. Microcal origin® concat (add-on) software was used to concatenate experiments and to correct for concentration and baseline offsets.

ITC data analysis

The heat (Q) measured over time (t) was integrated to obtain the incremental heat ΔQ, which was normalized to the molar concentration of injectant, and plotted as a function of

the molar ratio between drug and polymer. Data processing, peak integration and fitting to the standard binding model was done with the Affinimeter® ITC software (Software for Science, Spain)[106]. Additional details of the ITC data analysis procedure and the fitting model are provided in the Supplementary Information.

2.4 RESULTS AND DISCUSSION

Ketoconazole (KTZ, **Figure 2.1a**) is weakly basic, with pKa values of 6.5 and 2.9[107]. As an ionizable compound, KTZ exhibits pH-dependent aqueous solubility, being practically insoluble at pH > 4, but highly soluble in acidic media (pH < 2.5), at room temperature[107]. The speciation profile of ketoconazole, as a function of pH, is given in **Figure S1**. PAA and PVP are water-soluble over a wide pH range, whereas PHEMA is a "water-swellable" hydrogel, with limited aqueous solubility[108] (see **Figure 2.1b-d**). The carboxylic acids within the monomer unit of PAA exhibit pH-dependent ionization (pKa 4.5), being substantially unionized at pH < 2.5, and almost completely ionized at pH > 6.5[109]. PVP on the other hand, is a relatively 'neutral' polymer [110,111].

In our earlier reports[52,93], significant differences in the drug–polymer interaction strength, molecular mobility, and the drug crystallization propensity were observed, when ASDs formulated with each of the three polymers, at low (4 – 40% w/w) polymer contents, were characterized. Since low excipient contents in ASDs offer the advantage of reducing the

pill burden, it was of interest, to evaluate the behavior of the ASDs having such low polymer contents, in aqueous media.

2.4.1 Powder dissolution

Figure 2.2 shows the dissolution profiles of neat ketoconazole, as well as the solid dispersions. Crystalline KTZ yielded a concentration of ~3 µg/mL in solution, about the same as its reported equilibrium solubility of 2 µg/mL (pH 7.8, 37 °C)[112]. Neat amorphous KTZ, however, showed an initial rapid rise in concentration to ~18 µg/mL, a six-fold increase compared to the concentration of crystalline KTZ, but still far below the estimated "amorphous solubility" of 57 µg/mL (pH 10, 37 °C)[113]. The increased drug concentration from amorphous KTZ persisted for approximately 40 minutes before declining. The rapid rise and decline in concentration, is the classical "spring" effect exhibited by amorphous materials in aqueous solution[4,77].

(a) KTZ-PAA ASDs

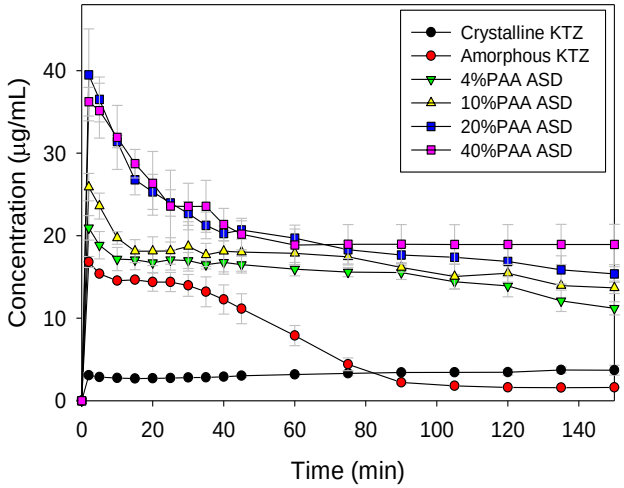

(b) KTZ-PVP ASDs

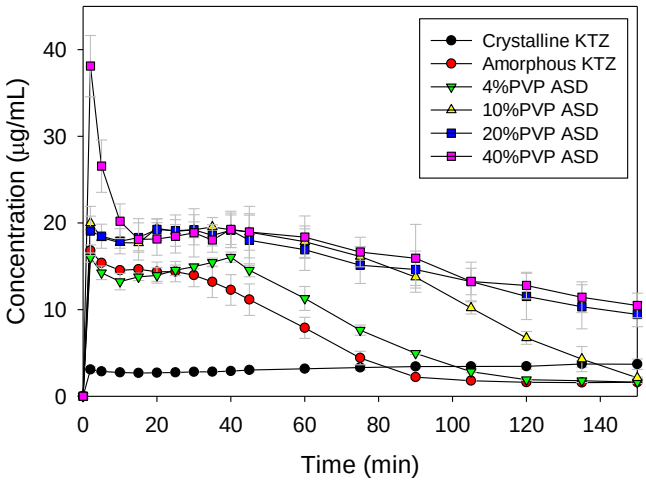

Figure 2.2. Dissolution profiles of crystalline KTZ, amorphous KTZ, and ASDs formulated with (a) PAA and (b) PVP at polymer contents ranging between 4 and 40% w/w (mean ± standard dev; n = 3). Experiments were in performed in pH 7.4 phosphate buffer at 37°C. Profiles of KTZ-PHEMA ASDs, are presented in the supplementary information (**Figure S2a**)

Dissolution profiles of the PAA ASDs are shown in **Figure 2.2a**. At the lowest polymer loading (4% w/w PAA), the drug concentration increased rapidly to ~20 µg/mL, and leveled off, with a slight decline. As the polymer content of the dispersion increased (with 10 and 20% PAA), progressively higher maximum drug concentration (C_{max}, see **Figure S3a**) levels were reached rapidly, though these could not be sustained. The acidic microenvironment created around the weakly basic drug particles, by the rapidly dissolving polymer, PAA, increased the drug solubility, resulting in the high C_{max} values. As recently shown, a 2 to 3 unit decrease in the microenvironmental pH of the dissolving particles could double the initial dissolution rate of KTZ[114]. The high degree of supersaturation however becomes a driving force for crystallization, manifesting as the decline that follows the initial surge in drug concentration[115]. Nonetheless, at all polymer contents, the PAA ASDs maintained ~six-fold higher drug concentration levels by the end of the experimental runs, compared to crystalline KTZ. The supersaturation, observed after 40 min, is very likely sustained by a different mechanism, since the pH of the dissolution medium in the bulk phase did not reduce significantly (due to the buffer capacity, as well as the constant flow of fresh dissolution medium). We hypothesize that drug–polymer interactions in solution, will be relevant. Of note, an increase in PAA content from 20 to 40% w/w (**Figure 2.2a)**, did not translate to any solubility enhancement.

Dissolution profiles of the PVP ASDs, shown in **Figure 2.2b**, differ in two main aspects, when compared to the profiles of the PAA ASDs. Firstly, the ASDs containing less than 40% PVP, do not show the initial spike in drug concentration within the first 40 minutes.

This is understandable, since PVP, being a relatively "neutral" polymer, does not lower the pH of the microenvironment of the dissolving drug particles as much as PAA does. Thus, the effect of rapid polymer dissolution driving an increased supersaturation is observed, mainly at higher (>40%) polymer contents. The second general feature identified from the dissolution profiles of the KTZ–PVP ASDs (**Figure 2.2b**) is, that the drug concentration levels drop after ~40 minutes, an indication that PVP is not as effective as PAA, at inhibiting drug crystallization. The profile of the ASD with 4% PVP content, was quite similar to that of neat amorphous KTZ, and a polymer content of at least 20% w/w was required to sustain the KTZ supersaturation for practically useful timescales.

The PHEMA ASDs exhibited slightly different dissolution characteristics (see **Figure S2a**). The C_{max} values at all polymer contents, were not significantly different from the C_{max} of neat amorphous ketoconazole. The level of supersaturation was, however, sustained much longer in the PHEMA ASDs, at all polymer contents, than in the PVP ASDs. Both effects – i.e. low C_{max} values and the sustained supersaturation – can be explained by the "diffusion-controlled" mechanism of drug release, proffered for ASDs formulated with hydrogels[116,117]. When the ASD is introduced into the aqueous medium, the polymer immediately imbibes water and swells, trapping the drug molecules and preventing the rapid surge in drug concentration, resulting in the low C_{max}. With time, however, the dissolved drug slowly diffuses out of the gel-like polymer matrix at a steady rate, thus sustaining the level of supersaturation.

The dissolution profiles of the ASDs are replotted in **Figure 2.3**, to enable a better comparison of the polymer effect. Pronounced differences were observed at low polymer contents (4 – 20% polymer) where supersaturation was sustained for a longer duration in the PAA and PHEMA ASDs.

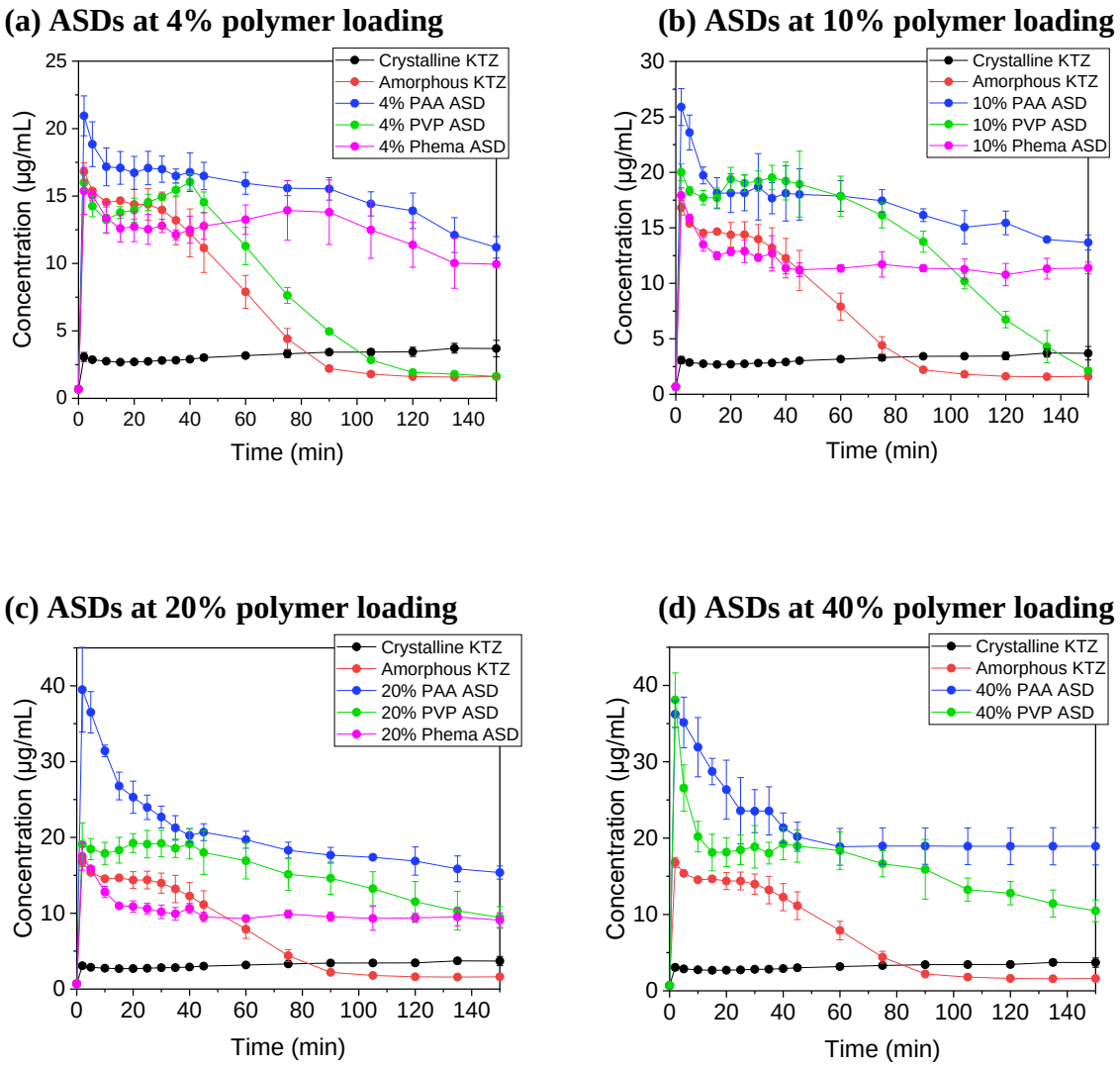

Figure 2.3. Comparison of dissolution profiles of ASDs formulated at different polymer contents. (a) 4% w/w polymer, (b) 10% w/w polymer, (c) 20% w/w polymer, (d) 40% w/w polymer content.

As controls, binary physical mixtures (PMs) of neat amorphous KTZ and each polymer were subjected to the same dissolution testing experiments (PAA and PVP PMs in **Figure 2.4**, PHEMA PMs in **Figure S2b**). Generally, at all polymer contents, the physical mixtures achieved similar or even higher C_{max} values when compared to the ASDs (see **Figure S3a**). Interestingly, the KTZ-PVP physical mixture at 40% polymer content, showed the highest C_{max} of ~80 µg/mL. In spite of the high C_{max} values, however, the drug concentration levels declined rapidly for all the physical mixtures, regardless of the polymer type. This latter observation is in line with the current state of knowledge, that intimate mixing of the drug and polymer at the molecular-level, greatly helps in sustaining the level of supersaturation[118].

(a) KTZ-PAA Physical Mixtures

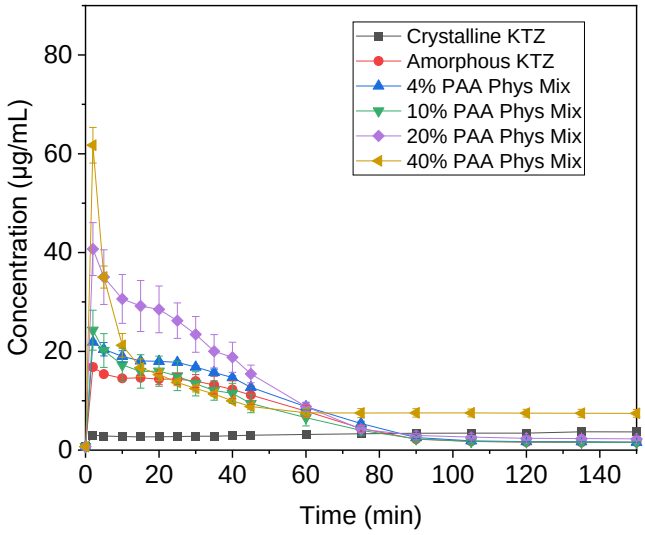

(b) KTZ-PVP Physical Mixtures

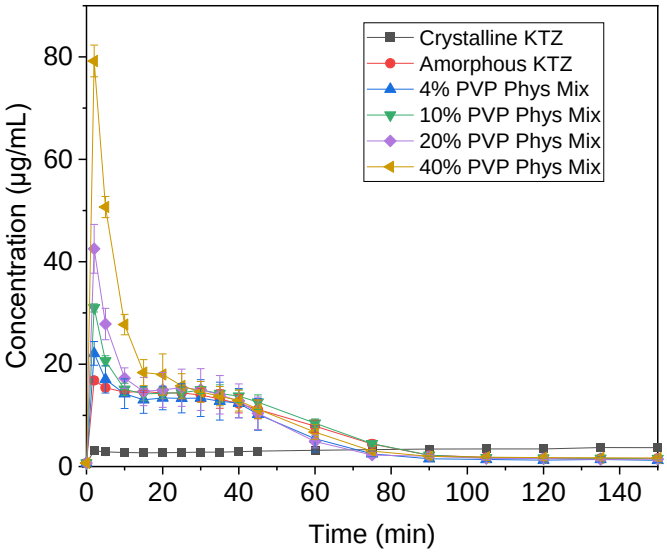

Figure 2.4. Dissolution profiles of crystalline KTZ, amorphous KTZ, and physical mixtures formulated with (a) PAA and (b) PVP, at polymer contents ranging between 4 and 40% w/w (mean ± standard dev; n = 3). Experiments were in performed in pH 7.4 phosphate buffer at 37°C. Profiles of KTZ-PHEMA physical mixtures, are presented in the supplementary information (**Figure S2b**)

The composite effect of the extent and duration of supersaturation was quantified with the area under the dissolution curve (AUC). The $AUC_{(0\rightarrow150min)}$ of each formulation was normalized with the $AUC_{(0\rightarrow150min)}$ of crystalline KTZ, and the resulting dissolution enhancement factors (AUC ratios) are presented in **Figure 2.5**. Alternatively, for each sample, the total amount of KTZ dissolved after 150 min, is plotted in **Figure S2.3b**. The AUC ratios, or the total drug dissolved, allow the dissolution behaviors of the different amorphous systems to be compared. For example, at low (4-20 % w/w) polymer contents, the dissolution enhancement from the PAA ASDs was significantly higher than the enhancement from the PVP ASDs. The AUC ratios also allow the effects of polymer type and polymer loading to be compared. A similar level of dissolution enhancement (an AUC ratio of 4.7) could be achieved with either 4% PAA or 20% PVP, revealing the superiority of PAA in maintaining KTZ in solution. The dissolution enhancement for the PHEMA ASDs, however, did not change significantly, with increasing polymer content.

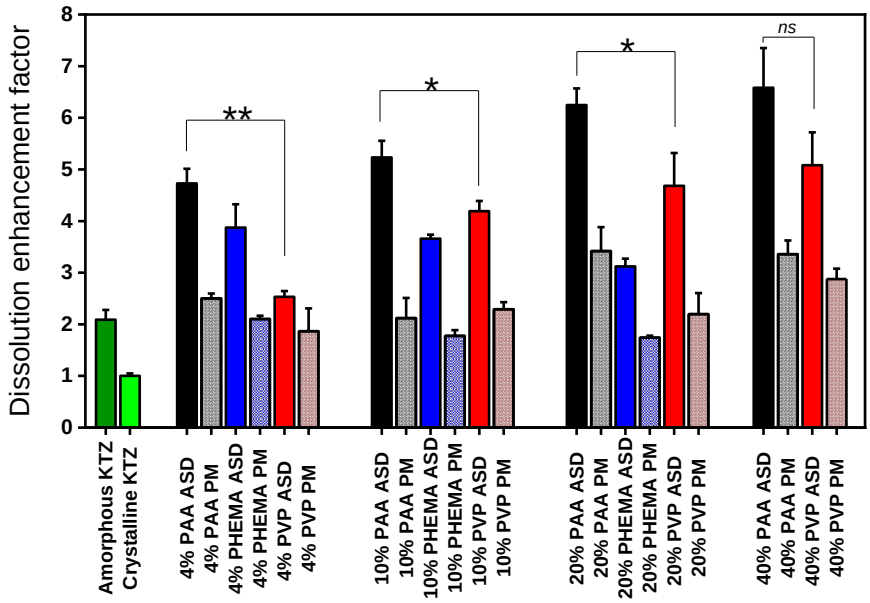

Figure 2.5. Dissolution enhancement factors, obtained from dissolution profiles of amorphous solid dispersions (ASDs) and physical mixtures (PMs), prepared with different polymers (PAA, PHEMA or PVP) at polymer contents ranging between 4 and 40% w/w. Enhancement factors of crystalline and amorphous KTZ are included for comparison. Student's t-test performed between selected ASDs at the same polymer loading: ^{ns} $p > 0.05$, $* p \leq 0.05$, $** p \leq 0.01$

2.4.2 Crystallization in aqueous buffer

Crystallization of the samples in aqueous environment was also evaluated. Each powder sample was wetted with buffer (pH 7.4) and monitored with synchrotron radiation as a function of time. Representative diffraction patterns are shown in **Figure 2.6a to c**, from which the extent of crystallization was quantified (**Figure 2.6d**). Even at the very low polymer content of 4% w/w, the PAA and PHEMA ASDs were resistant to drug

crystallization with less than 12% crystalline content by 4 hours. The PVP ASD on the other hand crystallized rapidly (~90% crystalline content at 4 hours), with the rate of drug crystallization being very similar to that of neat amorphous ketoconazole. Similar results were obtained for ASDs having higher (10 and 20%) polymer contents, where drug crystallization was absent in the PAA and PHEMA ASDs, even beyond 4 hours, but the PVP ASDs crystallized (data not shown).

When the drug–polymer physical mixtures were evaluated (see **Figure 2.6d**), PAA was more effective than PHEMA in inhibiting drug crystallization in solution, even though for both polymers, the extent of suppression was much less than in the corresponding ASD. PVP, however, did not suppress drug crystallization as a physical mixture.

The crystallization inhibition results complement the observations from the dissolution tests, in that, PAA and PHEMA were better at stabilizing the drug, than PVP. For the water-soluble polymers (PAA and PVP), strong drug–polymer interactions that persist in solution, would possibly prevent the dissolved drug from crystallizing, and thereby contribute to sustaining the level of supersaturation. For ASDs formulated with hydrogels (eg. PHEMA), however, the diffusion-controlled drug release mechanism would be more relevant in sustaining supersaturation.

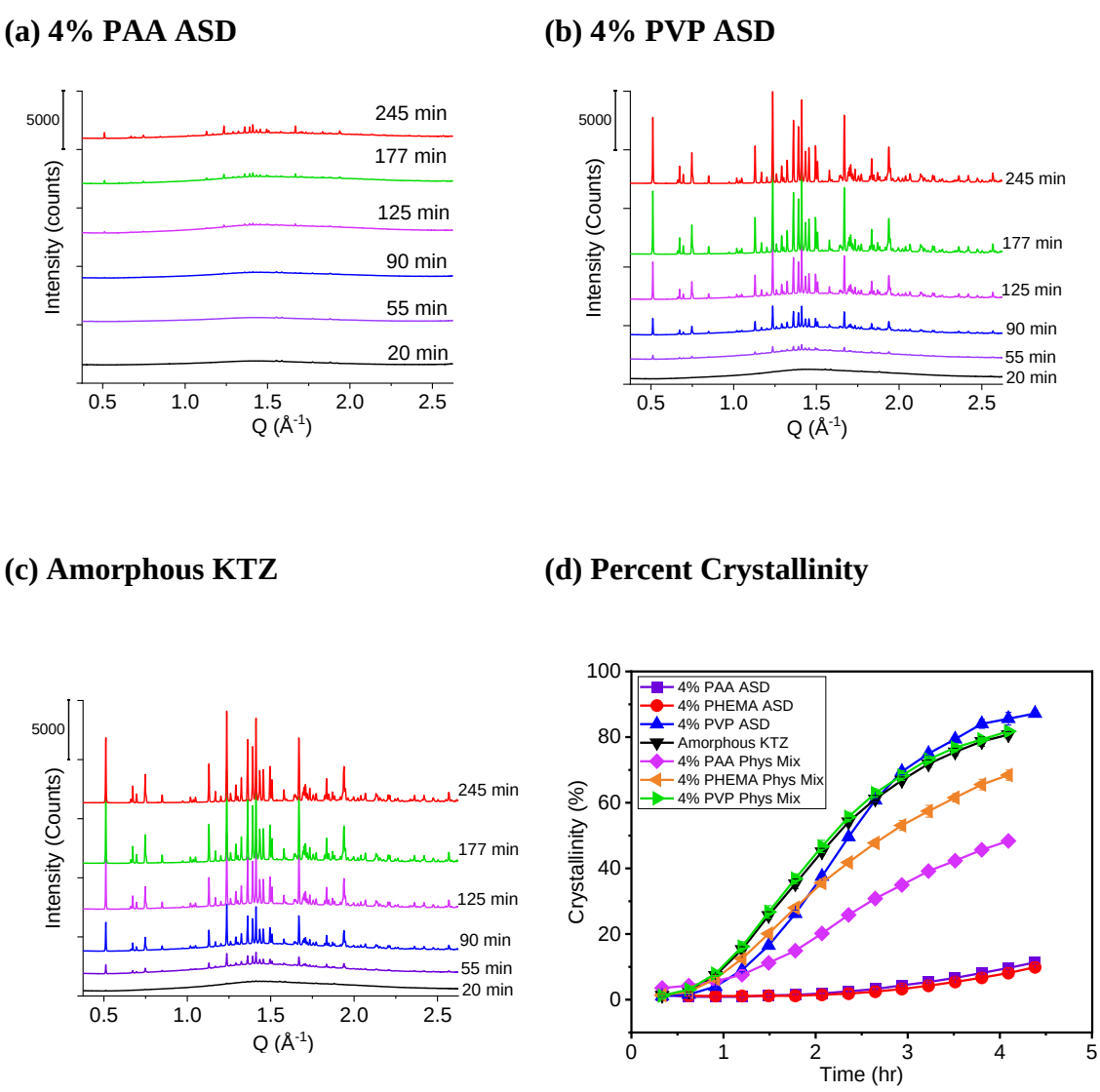

Figure 2.6. (a-c) Synchrotron X-ray diffraction patterns of powder samples, wetted with dissolution medium (phosphate buffer, pH 7.4 at ~25 °C) and monitored as a function of time. (a) KTZ + 4% PAA ASD, (b) KTZ + 4% PVP ASD, (c) neat amorphous KTZ. Each pattern has been offset on the vertical axis, for clarity. (d) Percent crystallinity as a function of time (mean ± SD; n = 3).

2.4.3 Drug–polymer interactions in solution

The potential interactions between KTZ and the water-soluble polymers, PAA and PVP, were investigated with solution proton NMR spectroscopy, as well as isothermal titration calorimetry. The low solubility of PHEMA in water resulted in weak signals, which made it impossible to investigate KTZ–PHEMA interactions. NMR spectra of the drug and polymers are described using the numbering scheme in **Figure 2.1**.

1D ^{1}H NMR

Figure 2.7a shows spectra of the KTZ–polymer mixtures, as well as the individual components. Peak assignments for the relevant KTZ protons are listed in **Table S1**. Peaks of KTZ protons were observed at chemical shifts of ~2 ppm (N-acetyl methyl protons), 3–5 ppm (piperazine, dioxolane and other aliphatic protons), 6–8 ppm (imidazolyl and phenyl groups) and >8 ppm (single resonance from the dichlorophenyl ring). The aliphatic proton peaks for neat PAA were between 1–3 ppm. The peak corresponding to the carboxylic acid proton of PAA, expected at ~12 ppm, did not appear, because of the rapid hydrogen-deuterium exchange in D_2O. The spectrum of neat PVP showed the peaks of the vinyl backbone and the pyrrolidone functional group (1.5–4 ppm). The spectral region between 6 and 9 ppm of both polymers, PAA and PVP, had no peaks, and could therefore be used to characterize the behavior of KTZ in the presence of either polymer (see the highlighted area in **Figure 2.7a**).

In the presence of PAA, some of the peaks from the aromatic ring systems of KTZ shifted downfield (**Figure 2.7b**; red dashed arrows). The most pronounced shifts were observed for the protons of the para-substituted phenyl ring of KTZ (H21/25 in **Figure 2.1a**) which moved from 7.06 ppm to 7.35 ppm in the presence of PAA. The peaks assigned to protons of the imidazole group (H10, H12, H13) also shifted downfield. Since neat KTZ was dissolved under acidic conditions (D_2O at pH 2.5), the basic nitrogen sites (N11 and N26) were protonated (see **Figure 2.1a**, and the green profile of **Figure S1b**). Yet, strong peak shifts were still observed, reflecting decreases in the electron densities around the hydrogen atoms, most likely induced by the electron-withdrawing carboxylic acids of PAA[96,97]. In many host-guest complexation systems, peak shifts of 0.1–0.5 ppm typically indicate strongly interacting systems[97]. Thus, both ion–dipole interactions between the positively charged NH groups of KTZ and the carboxylic acids of PAA, as well as hydrogen bonding between the oxygen atoms of KTZ (O19 or O34) and the carboxylic acid hydrogens of PAA, may be present. The 1D results therefore provided the first indication of interaction, between PAA and KTZ in aqueous solution. On the other hand, the KTZ proton peaks in the 6-9 ppm region, remained unaffected by the presence of PVP (**Figure 2.7b**, green dashed arrows).

(a)

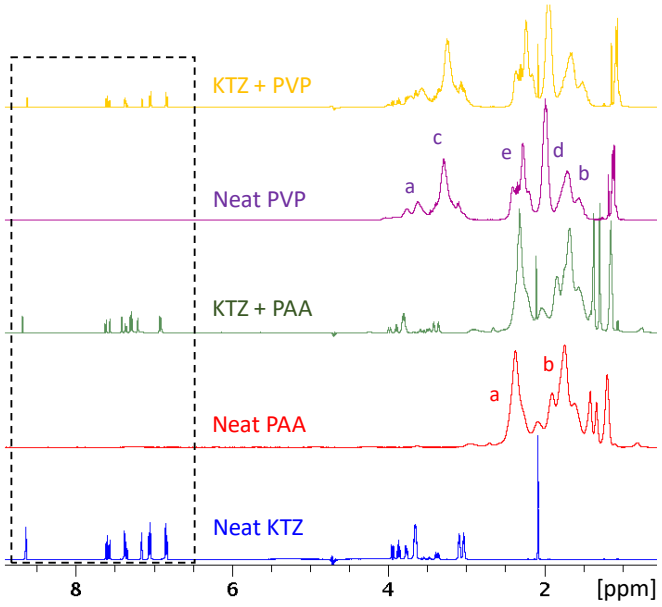

(b)

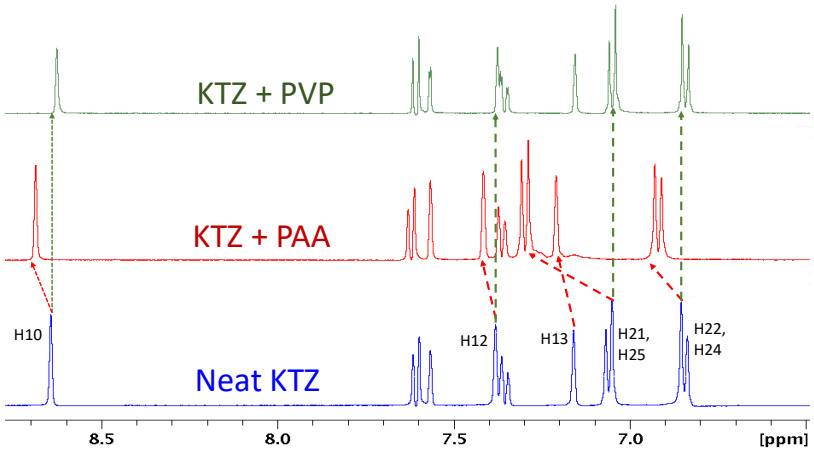

Figure 2.7. One-dimensional ^{1}H NMR spectra KTZ alone, and with polymers in D_2O at pH 2.5. (a) Overview of the entire chemical shift range. The (6.5 to 8.8 ppm) region indicated by a dashed box, is expanded in panel (b). Peak position changes for selected KTZ resonances caused by the polymer, have been pointed out with dashed arrows.

2D $^{1}H^{1}H$ NOESY

Two-dimensional (2D) nuclear Overhauser effect spectroscopy (NOESY) was used to probe the drug–polymer interactions in greater detail. Generally, for small molecules (M_w < 600 Daltons), a nuclear Overhauser effect (NOE) may be observed between protons that are less than 4 Å apart; for large molecules (M_w > ~1500 Daltons), NOEs are observed, when the protons are 5 Å apart[119,120]. The sign (or the phase) of the NOE, is also related to Brownian motion. In the free state, small molecules tumble rapidly in solution, giving positive NOEs. Conversely, large molecules tumble slowly, showing negative NOEs[119,120]. Thus, the observation of negative NOEs for a small molecule – in the presence of a macromolecule – provides a clear indication of interaction.

The 2D NOESY plot of neat KTZ in D_2O (at pH 2.5), is shown in **Figure 2.8**. Several off-diagonal peaks with positive signs (red) are observed, arising from cross-correlations between protons of the drug molecules. Of note, the diagonal peaks are negatively phased (blue). The plot of neat KTZ can be contrasted with those of neat PAA and PVP shown in **Figure S4**, which have cross-correlations, same-phased with the diagonal peaks. The controls confirm that neat KTZ tumbles rapidly while the neat polymers tumble slowly, as expected.

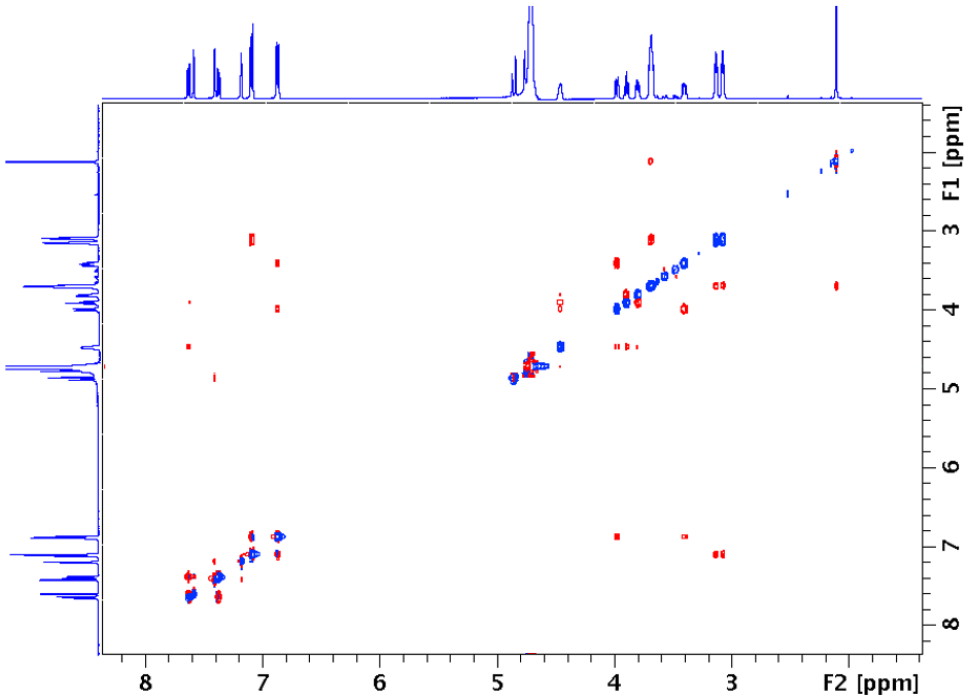

Figure 2.8. 2D $^{1}H^{1}H$ NOESY plot of KTZ alone in D_2O at pH 2.5. The drug-drug, off-diagonal cross-peaks are red, indicating they are opposite-phased to the diagonal (blue) peaks.

Figure 2.9 is the 2D NOESY spectrum of the KTZ-PAA mixture. Cross peaks (circled in red for clarity), between the aromatic proton peaks of KTZ (H21/25 & H22/24; H12, 13; H3, 5, 6) and those of the aliphatic backbone of PAA (Ha, and to a lesser extent, Hb), indicate the spatial proximity of the KTZ and PAA molecules. The cross peaks have the same phase as the diagonal peaks (negative; blue, in the color scheme), indicating that, in the presence of PAA, the tumbling of the drug molecules is reduced. These results collectively suggest that the polymer and drug molecules are intercalated.

It should be noted that dipolar cross correlations only reflect the spatial proximity of protons. Thus, it is not possible based on the NOESY spectra alone, to unequivocally identify the functional groups of the drug and polymer that interact. Since the aliphatic backbone of PAA is spatially close to the aromatic regions of KTZ, hydrophobic drug–polymer associations may be present. It is also possible that the interaction occurs between the imidazole nitrogen of KTZ and the carboxylic acid of PAA, but result in the hydrophobic regions being close to each other and manifesting as cross peaks.

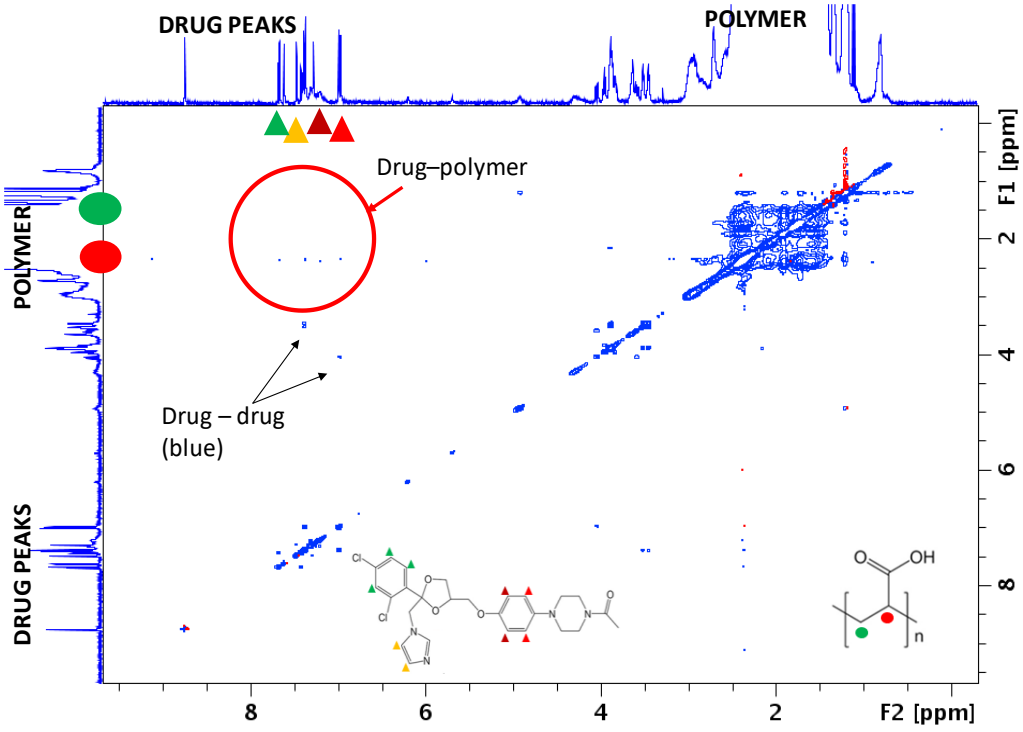

Figure 2.9. 2D $^{1}H^{1}H$ NOESY plot of a mixture of KTZ and PAA in D_2O. Cross peaks (circled in red) between the aromatic proton peaks of KTZ and the aliphatic proton peaks of PAA indicate drug–polymer intermolecular interactions. All (off-diagonal) cross peaks are blue, same-phased with the diagonal peaks.

In contrast, no cross peaks are observed between the protons of KTZ and PVP (**Figure 2.10**). Instead, only intramolecular (i.e. drug-drug or polymer-polymer) cross-correlations are observed. Moreover, the drug-drug and the polymer-polymer cross peaks maintain their positive (red; compare with **Figure 2.8**) and negative (blue; compare with **Figure S4b**) phases respectively, indicating that the tumbling of KTZ molecules is unaffected by PVP.

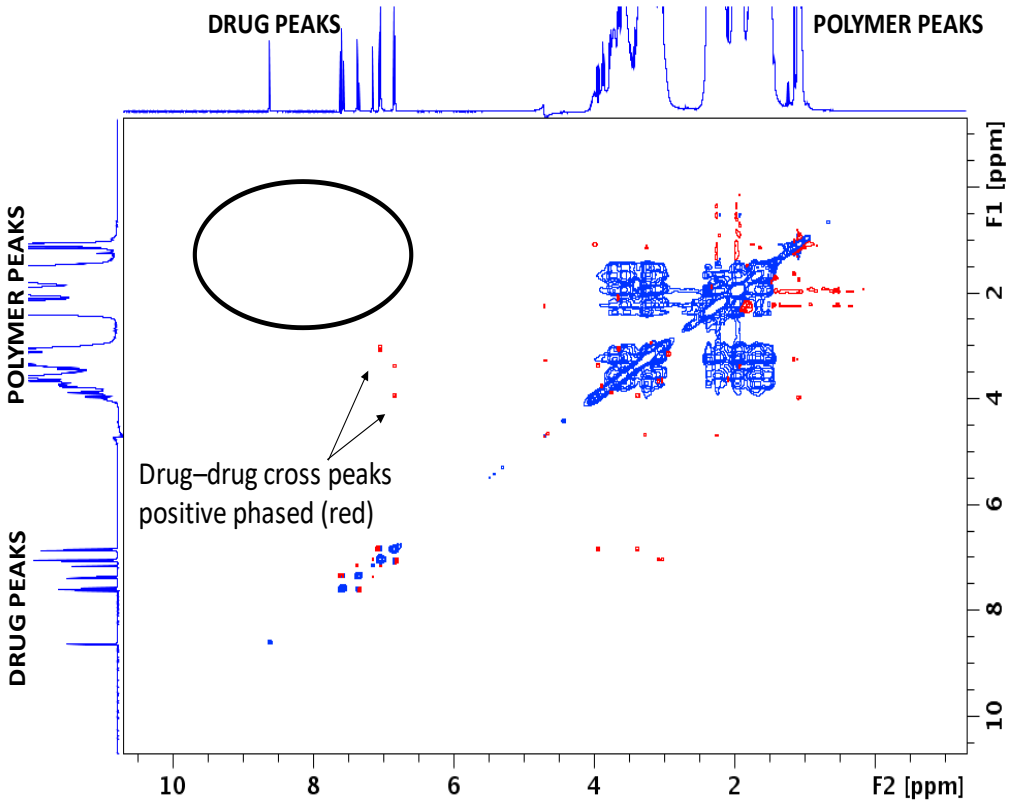

Figure 2.10. 2D $^{1}H^{1}H$ NOESY plot of a mixture of KTZ and PVP in D_2O at pH 2.5. No drug–polymer cross peaks are observed in the circled region. Only drug-drug (red; some pointed out) or polymer-polymer (blue) cross peaks can be identified.

2D ^{1}H DOSY

2D ^{1}H NMR diffusion ordered spectroscopy (DOSY) is another useful tool for investigating molecular interactions in solution[97,121]. The technique enables spectroscopic "separation" of the diffusion coefficients of individual components of a mixture. Small molecule drugs, diffuse faster than bulky polymers[97]. Interaction of the drug with the polymer should in principle, result in reduced drug diffusivity. However, such an interaction should have a negligible effect on the polymer diffusion coefficient, because of the bulky nature of the polymer. The change in the self-diffusion coefficient of the small molecule is thus considered a direct measure of molecular association and aggregation[97,121,122].

Representative 2D DOSY plots of the drug–polymer mixtures, and the controls (KTZ alone, PAA alone, and PVP alone), all prepared in D_2O at pH 2.5, are presented in the supplementary information (**Figure S5**). The corresponding diffusion coefficient values (D-values) are listed in **Table S2**. The diffusion coefficient of KTZ alone, 3.5×10^{-10} m^2s^{-1}, is in good agreement with the values of other similar small molecule drugs in D_2O[123,124]. The neat polymers, PAA and PVP, have similar diffusion values (~1.7×10^{-10} m^2s^{-1}), reflecting the similarity in their molecular weights and shape (1800 $gmol^{-1}$ and 2500 $gmol^{-1}$ for PAA and PVP respectively, both linear with ~24 monomers per chain). The polymer diffusion values are also consistent with the literature[96,109].

To gauge the magnitude of the influence of the drug–polymer interaction on the movement of the different species in solution, the measured D-values are normalized with the D-value of neat KTZ (D_0). The resulting (D/D_0) values are presented in **Figure 2.11** with the neat drug having a value of 1, and the neat polymers having values of ~0.5. In the presence of PAA, the normalized D-value of KTZ is ~0.58, indicating that the drug movement is slowed down by the polymer. The extent of reduction of drug diffusivity in the polymer solution, is likely correlated with solubility enhancement due to the polymer[124]. In the presence of PVP, however, the diffusion coefficient of KTZ is similar to that of the neat drug (D/D_0 = 0.91), indicating that the polymer has a negligible effect on drug diffusion, and further corroborating the absence of drug–polymer interactions. As expected, the diffusivity of PAA or PVP, in the respective drug–polymer mixtures, remain unchanged, compared to the neat polymers.

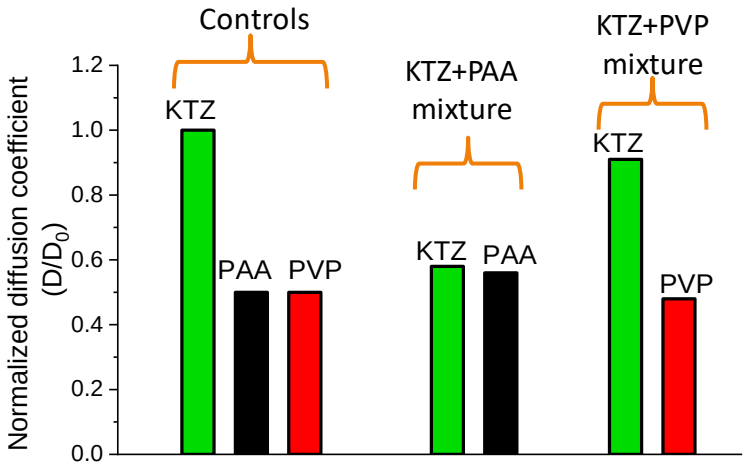

Figure 2.11. Normalized diffusion coefficients of the neat drug (KTZ alone), neat polymers (PAA or PVP alone), and the drug or polymer in the drug–polymer mixtures.

Isothermal titration calorimetry (ITC)

Figure 2.12a shows the raw ITC power compensation signals for the titration of KTZ into PAA. An exothermic signal of ~6 µcal/sec, is initially registered. The magnitudes of the peaks progressively decrease with sequential titration of drug into polymer solution, until the end of the experiments, when the signal is ~1 µcal/sec. A separate control experiment, comprising titration of KTZ into the blank solvent (pH 1.1 buffer), was performed (labeled as KTZ control; **Figure 2.12c**) to obtain the dilution heats, which are of much smaller magnitude. The pH values of the drug solution, the polymer solutions and blank buffer were within 0.2 units of each other. The drug dilution heats observed are therefore not attributed to a mismatch in pH of the syringe and cell contents, but presumably from the entropic gain when drug molecules from the highly concentrated syringe solution spread through the buffer in the sample cell. The drug dilution background heats could also indicate some form of aggregation such as dimerization of the drug molecules in solution, even though this is not expected in the case of ketoconazole. In a second blank experiment, the heat of dilution of the polymer was also measured by titrating buffer from the syringe into the polymer solution in the sample cell (labeled PAA control; **Figure 2.12d**). The heat of dilution of both polymer solutions, measured in this way, are negligible.

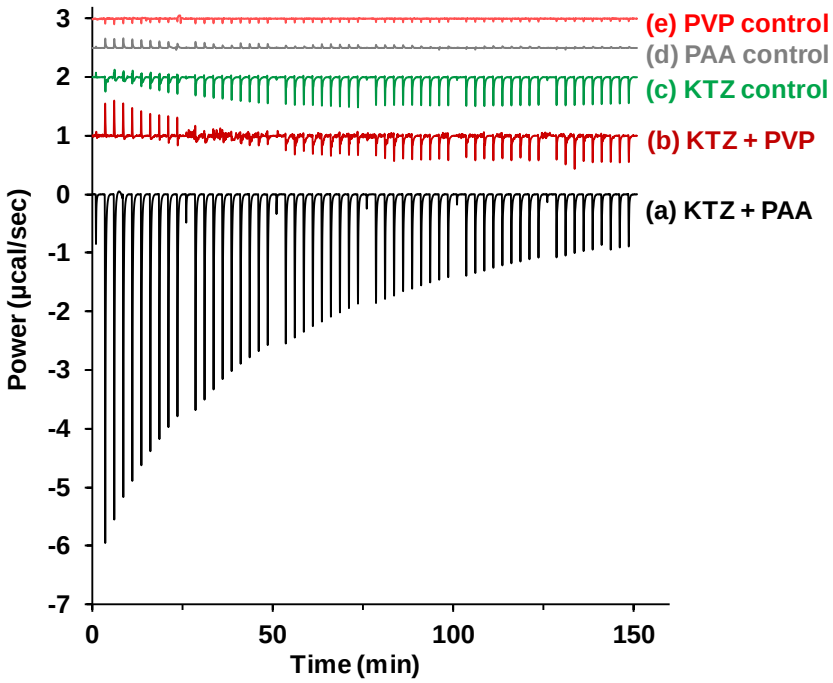

Figure 2.12. Isothermal titration calorimetry power compensation signals, obtained from sequential injections of (a) 40 mM KTZ into 3 mM PAA, (b) 40 mM KTZ into 3 mM PVP (c) 40 mM KTZ into plain buffer (pH 1.1), (d) plain buffer into 3mM PAA (e) plain buffer into 3 mM PVP. For clarity, b, c, d and e have been offset by 1, 2, 2.5 and 3 units respectively on the vertical axis.

The peaks recorded following each stepwise injection of KTZ into PAA were integrated, normalized with respect to the moles of drug added per injection, and then plotted as a function of the drug-to-polymer molar ratio in the sample cell. This representation is commonly referred to as the differential binding curve (**Figure 2.13a**). The shape of the curve obtained for the titration of KTZ into PAA, is typical for binding interactions with weak affinity (K_a < 10^4 M^{-1})[105,125]. Similar profiles have been reported for drug-cyclodextrin interactions[126] as well as protein-carbohydrate interactions[127]. In standard

practice, a thermodynamic binding model is fitted to the differential binding data to provide additional insight into the ligand-macromolecular interaction mechanism[128]. A good fit was obtained using an independent sites analysis approach, with one independent set of sites and an additional term that accounts for the contribution from drug dilution (see supporting information)[106,128]. The stoichiometry parameter, n, was fixed to 1, an approach that can be used for analyzing data with weak binding affinity, to increase the confidence in the other fit parameters[125,129,130]. The resulting fit to the binding isotherm, is shown in **Figure 2.13a**, and the corresponding thermodynamic binding signature is plotted in **Figure 2.13b**. The data analysis shows an association constant (K_a) of 43.3 ± 0.4 M^{-1}, with a negative overall enthalpy change (ΔH = -2.69 ± 0.02 kcal/mol) indicating an enthalpy-driven interaction. The enthalpic contribution from the drug dilution, is negligible (ΔH_{dil}~0.1 kcal/mol).

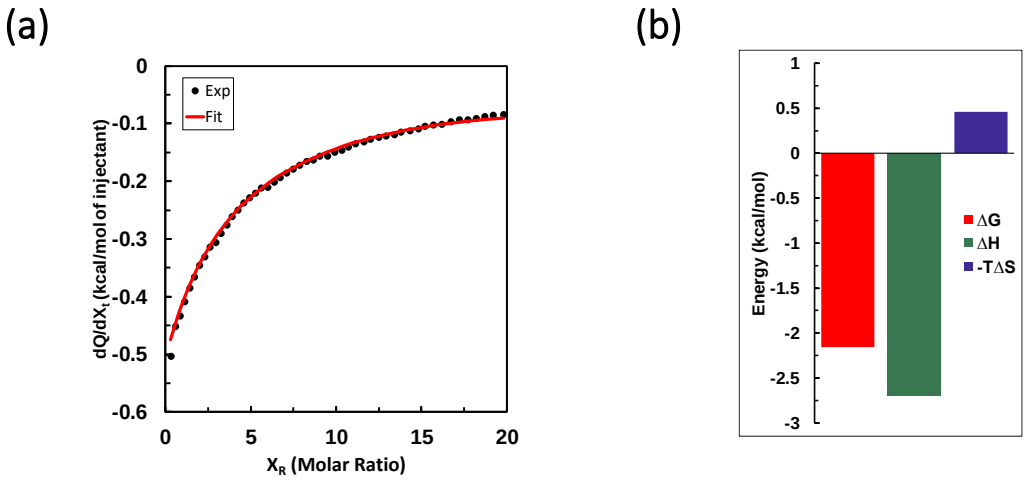

Figure 2.13. Isothermal titration calorimetry results. (a) Integrated heat as a function of drug-to-polymer molar ratio, for the titration of 40mM KTZ into 3mM PAA. The standard one-set-of-sites binding model was fitted to the experimental data (exp). (b) "Binding"

signature plot (overall change in free energy, enthalpy, and entropy factor) for the KTZ-PAA titration.

The overall enthalpy change extracted from ITC experiments, provides a measure of the energy content of bonds broken and formed in the interaction process. In general, polar interactions tend to contribute favorably to the enthalpic component, the major contribution being from hydrogen bonds, whereas entropically favored interactions tend to be more hydrophobic. Thus, the binding signature suggests polar interactions such as hydrogen bonding or ion-dipole interactions, most likely between the imidazole groups of KTZ and the carboxylic acids of PAA, being present. The interaction is spontaneous and favorable due to the negative change in free energy (ΔG = -2.3 kcal/mol).

The ITC profile obtained for the titration of KTZ into PVP (**Figure 2.12b**) however, starts with very weak endothermic peaks (~0.5 µcal/sec), which become exothermic when the drug-to-polymer molar ratio is greater than 5. The exothermic signals of the KTZ-PVP interaction, are of the same magnitude as the signal for the titration of KTZ into the blank buffer (~0.5 µcal/sec). Subtraction of the heat of KTZ dilution, from the KTZ-PVP titration, results in a largely featureless differential enthalpy curve which cannot be fitted with any of the standard binding models.

2.4.4 Possible mechanisms of interaction in aqueous solution

Together, the NMR and ITC experiments clearly show that interactions between KTZ and PAA exist in aqueous solution, which are stronger than interactions, if any, between KTZ

and PVP. Because KTZ is weakly basic, with ionizable functional groups, the ionization states of both the drug and the polymer will influence the type of interaction occurring in aqueous solution. In acidic buffer (<pH 2.5), the imidazolyl group of KTZ is fully protonated assuming a net positive charge, whilst the carboxylic acids of PAA (pKa ~ 4.5), though protonated, remain uncharged. In neutral medium where the dissolution experiments were conducted, the charges are reversed; KTZ becomes substantially neutral (~10% protonated) while PAA gains a net negative charge due to deprotonation of the carboxylic acid groups. Thus, in either acidic or neutral medium, ion-dipole interactions between the drug and polymer would very likely be present. Additionally, multiple avenues exist for hydrogen bonding between KTZ and PAA, which could contribute to the overall interaction strength. The thermodynamic interaction signature from the ITC experiments also point to enthalpy-driven, polar interactions being dominant. It is therefore reasonable to infer that strong interactions in the solid state translate to aqueous solution, explaining, at least in part, the sustained duration of supersaturation in the dissolution experiments.

It is noteworthy, that the KTZ-PAA ASDs outperformed the KTZ-PVP ASDs when the polymer contents were low (4-20% w/w polymer); at 40% polymer content, the dissolution profiles of the ASDs, regardless of polymer type, were not statistically different (see **Figure 2.5**). This suggests that for water-soluble polymers, the strong drug–polymer interactions may contribute substantially to sustaining the level of supersaturation at low

polymer content. Other factors such as steric hindrance to precipitation, due to the bulkiness of the polymer, become equally important, at higher polymer contents.

Finally, we will briefly address the relevance of our work to the *in vivo* situation, specifically following oral administration. We will consider KTZ–PAA as the model system. The highly acidic gastric fluid will favor the solubility of KTZ. As the dissolved ASD transitions to the intestine, drug crystallization would likely be prevented, if the drug–polymer interaction persists. Even though soluble drug–polymer complexes can, in principle, inhibit release of free drug, the low association constant (K_a) obtained for the KTZ–PAA system, suggests that drug release and subsequent drug absorption, would not be inhibited.

2.5 SIGNIFICANCE

This study provides mechanistic insights into the factors that affect the dissolution of ASDs, providing a basis for rational polymer selection. When a polymer that can form strong (e.g. ionic) interactions with the drug is selected, stable ASDs can be prepared at low polymer loadings. This could accomplish multiple goals of (i) reducing the pill burden (ii) preventing solid state drug crystallization in the dosage form and (iii) improving the dissolution performance of the ASDs. To determine the extent of generalizability of the hypothesis, a wider range of drug–polymer systems needs to be studied. The next step would be to investigate if the dissolution enhancement observed *in vitro* due to strong interactions, translates to enhanced bioavailability *in vivo*.

2.6 CONCLUSIONS

In our earlier work, we showed that strong interactions (ionic, as well as hydrogen bonding) between ketoconazole (KTZ) and polyacrylic acid (PAA), resulted in pronounced reduction in both the molecular mobility and the crystallization propensity of the amorphous solid dispersion (ASD), in the dry, "solid" state. Weak dipole-dipole interactions between KTZ and polyvinylpyrrolidone (PVP) however resulted in an ASD that crystallized more rapidly. In this work, using 2D nuclear Overhauser effect spectroscopy, diffusion ordered spectroscopy and isothermal titration calorimetry, we demonstrated the existence of KTZ-PAA interactions in aqueous solution. The solution-state interaction translated to prolonged duration of supersaturation, reflecting resistance to drug crystallization in aqueous media. Conversely, no evidence of KTZ-PVP interactions were observed in aqueous solution. The sustainment of supersaturation with PVP was much less pronounced. The results suggest that in this system, and possibly for other weakly basic drugs, the *interactions* that stabilize ASDs in the solid state, can also be relevant and important in sustaining the level of supersaturation in solution.

2.7 ACKNOWLEDGEMENTS

This project was funded by the National Science Foundation (grant number NSF-CMMI-1662046) and partially supported by the William and Mildred Peters endowment fund. KKAE acknowledges the Bighley Graduate Student Fellowship. The research used resources of the Advanced Photon Source, a US Department of Energy (DOE) Office of

Science User Facility, operated for the DOE Office of Science by Argonne National Laboratory, under contract number DE-AC02-06CH11357. Dr. Wenquian Hu and Dr. Andrey Yakovenko (beamline 17-BM-B) are acknowledged for their help. The authors are grateful to Dr. Courtney Aldrich, University of Minnesota, for granting access to an ITC-200 microcalorimeter (NIH shared instrumentation grant S10-OD017982) and to Dr. Anant Paradkar, University of Bradford, for granting access to a USP dissolution apparatus IV. We also thank Dr. Letitia Yao (NMR), Dr. Michelle Miller (NMR), Evan Alexander (ITC) and Dr. Shivprasad Deshmukh (dissolution tests) for their help with experiments, and Dr. Eva Munoz and Dr. Juan Sabin for their help with fitting of the ITC data.

2.8 SUPPLEMENTARY INFORMATION

(a)

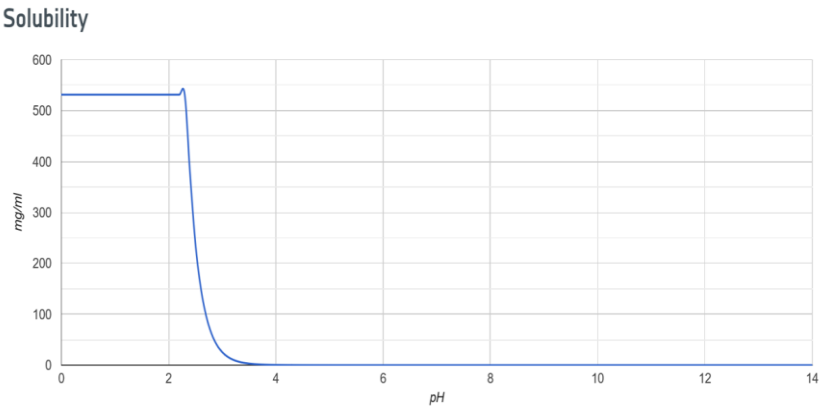

(b)

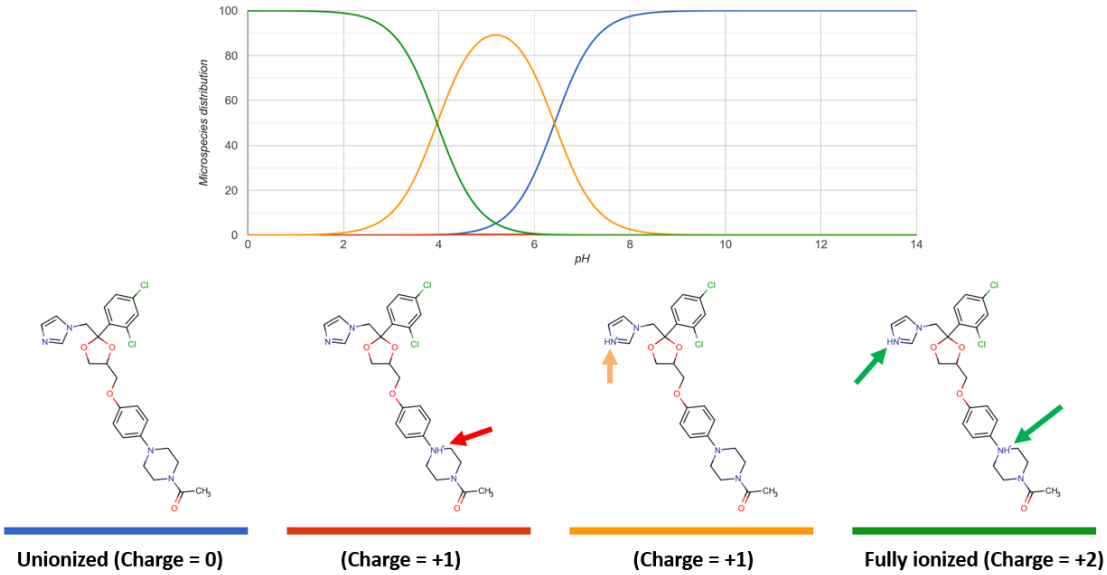

Figure S2.1. (a) Solubility of ketoconazole as a function of pH. (b) Microspecies distribution of ketoconazole at different aqueous solution pH values. Protonated regions are pointed out. Calculations (and output figures) were performed in Chem 3D ultra®.

Dissolution Experiments

(a) KTZ-PHEMA ASDs

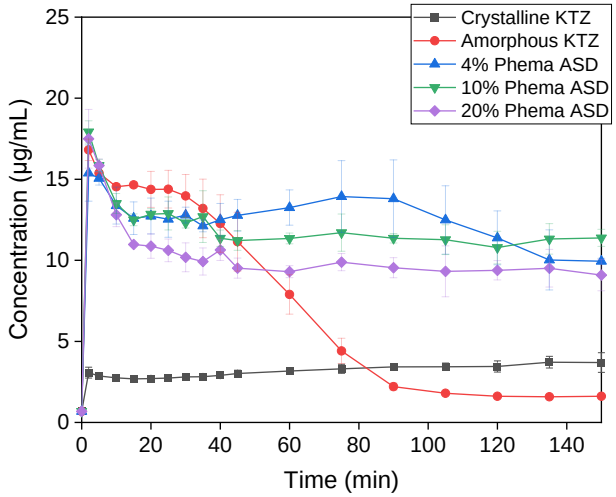

(b) KTZ-PHEMA Physical Mixtures

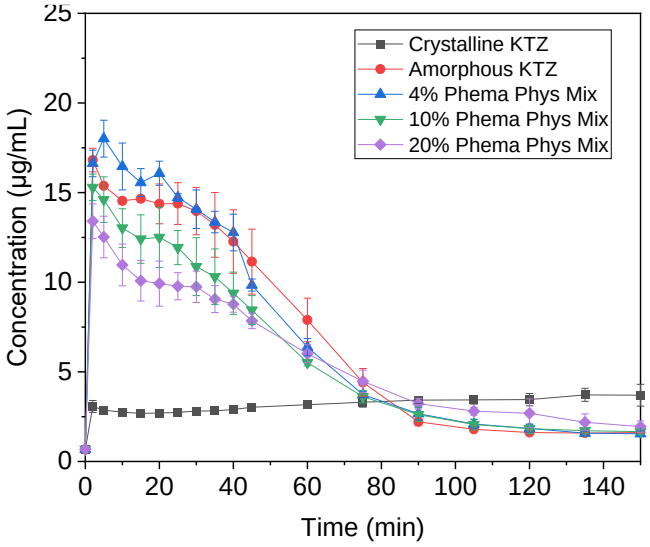

Figure S2.2. Dissolution profiles of crystalline KTZ, amorphous KTZ, and (a) ASDs or (b) Physical Mixtures, formulated with PHEMA, at polymer contents ranging between 4 and 40% w/w (mean ± standard dev; n = 3). Experiments were in performed in pH 7.4 phosphate buffer at 37°C.

Dissolution Experiments

(a)

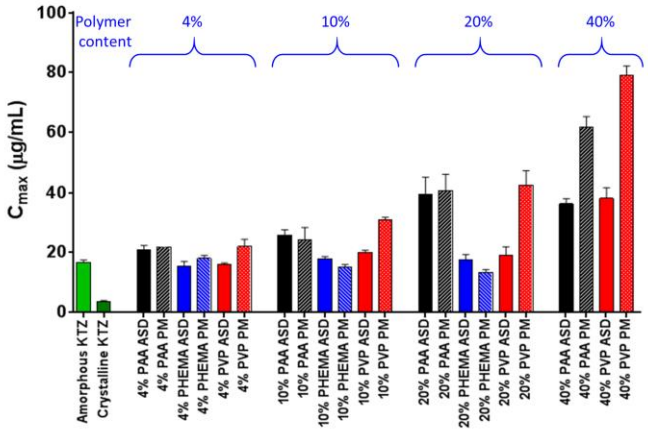

(b)

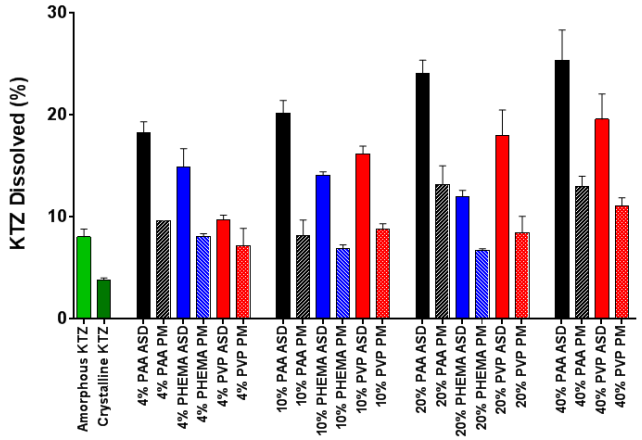

Figure S2.3. **(a)** Maximum dissolved drug concentration (C_{max}) values, **(b)** cumulative percent drug dissolved*, obtained from dissolution profiles of amorphous solid dispersions (ASDs) and physical mixtures (PMs), prepared with different polymers (PAA, PHEMA or PVP) at polymer contents ranging between 4 and 40% w/w. Values for crystalline and amorphous KTZ are included for comparison.

*KTZ Dissolved % = ($AUC_{0\rightarrow150min}$ × Flow rate)/Nominal drug weight × 100

1D proton NMR

Table S2.1. NMR peak assignments for KTZ in D_2O, acidified to pH 2.5. Based on structure numbering scheme of **Figure 2.1**.

Assignment	**Group**	**Chemical shift (ppm)**
H3	Dichlorophenyl ring	doublet at 7.58
H5	Dichlorophenyl ring	doublet of doublets at 7.38
H6	Dichlorophenyl ring	doublet at 7.62
H8	CH_2 link	AB quartet at 4.75, 4.85
H10	Imidazole ring	single resonance at 8.68
H12	Imidazole ring	triplet at 7.16
H13	Imidazole ring	triplet at 7.38
H15	Dioxolane	multiplet within 3.85 and 4.00
H16	Dioxolane	doublet of doublets at 3.38 and 3.77
H18	CH_2 (methoxy) link	~4 (doublet of doublets)
H21, H25	Para substituted phenyl ring	AA'BB' centered at 7.06
H22, H24	Para substituted phenyl ring	AA'BB' centered at 6.85
H27, H31	Piperazine ring	pair of triplets at 3.04 and 3.09
H28, H30	Piperazine ring	overlapping pair of doublets of doublets within 3.64 and 3.67
H33	N-acetyl methyl	2.09

Nuclear Overhauser Effect Spectroscopy (NOESY)

(a) Neat PAA

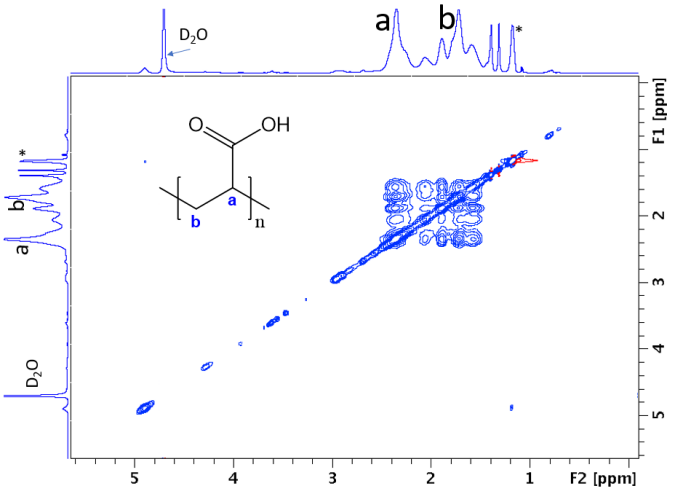

(b) Neat PVP

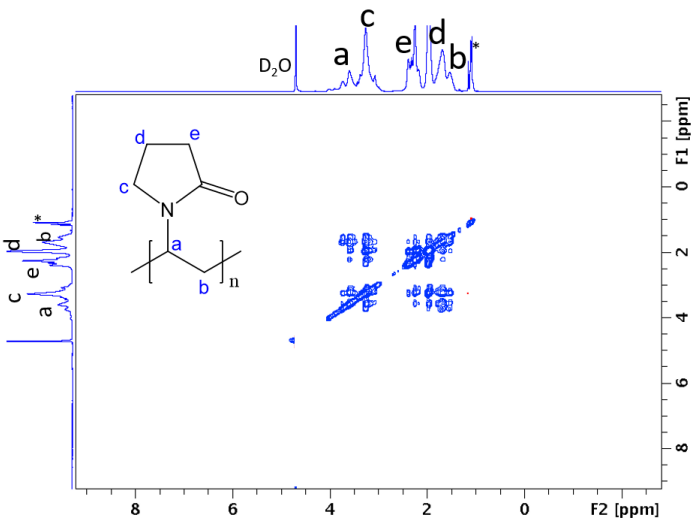

Figure S2.4. 2D $^{1}H^{1}H$ NOESY spectra of (a) neat PAA and (b) neat PVP. Cross peaks are same-phased with the diagonal peaks (blue, negative sign). *Possibly from leached syringe material.

Diffusion Ordered Spectroscopy (DOSY)

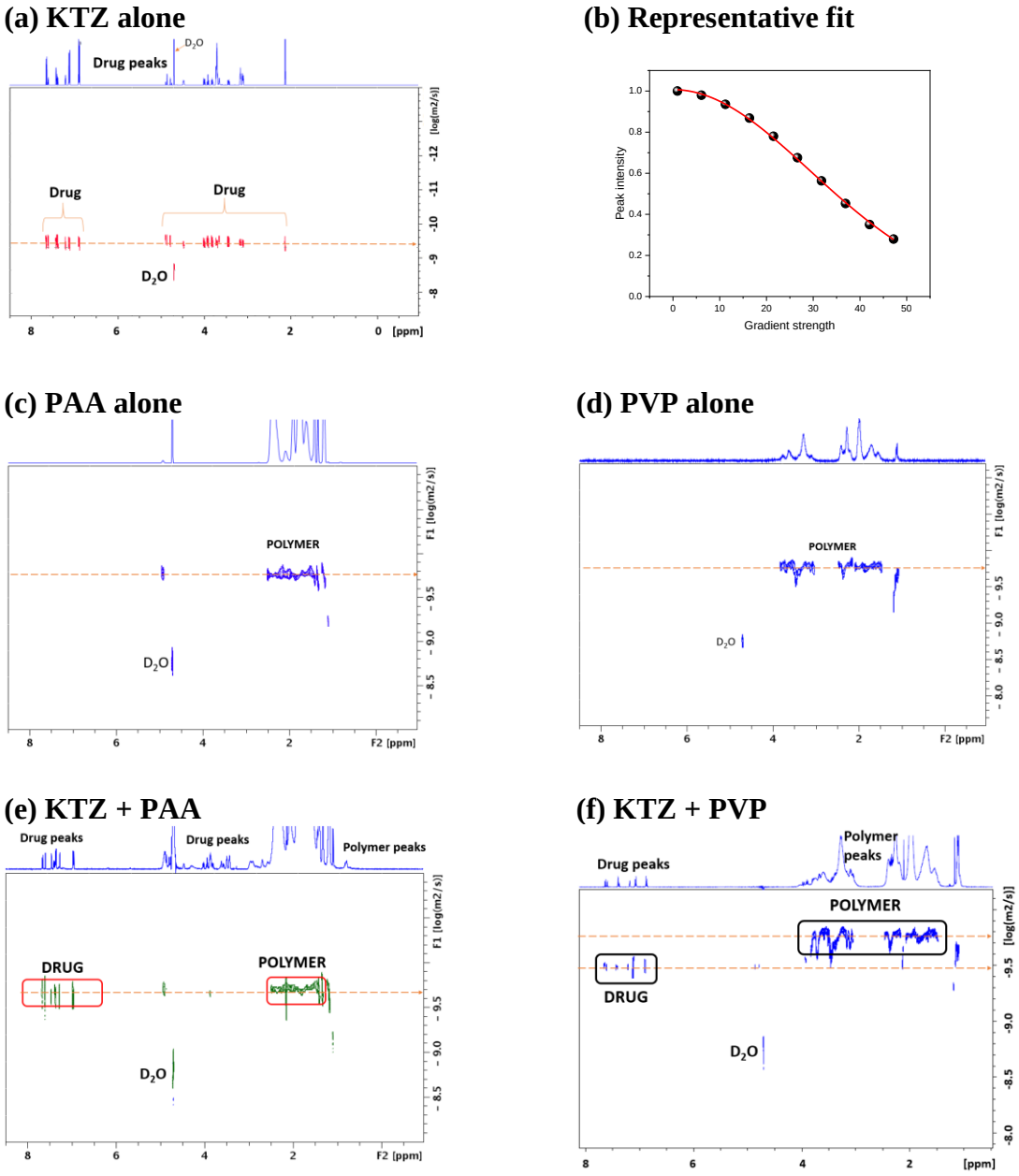

Figure S2.5 (a, c-f). Representative 2D DOSY plots of the neat drug (KTZ), the neat polymers (PAA or PVP), and the drug+polymer mixtures. The solvent was D_2O at pH 2.5. **(b)** Representative fit of equation (2.2) to the peak intensity vs gradient strength data.

The DOSY results are displayed as a 2D matrix with the conventional 1D chemical shift spectrum plotted on the horizontal (top) axis, and the diffusion coefficients plotted along the perpendicular (right) axis. Diffusion peaks on each horizontal dashed line correlate with signals in the chemical shifts dimension, and are attributed to a specific molecular species[121].

Table S2.2. Diffusion coefficients of neat KTZ, PAA and PVP (lines 1 to 3), and the drug or polymer in the drug+polymer mixtures (lines 4 to 7). Experiments were performed in D_2O at pH 2.5

#	Sample	D (m^2s^{-1}) × 10^{-10} *	D/D_0
1	KTZ alone	3.548	1.00
2	PAA Alone	1.778	0.50
3	PVP Alone	1.769	0.50
4	KTZ in (KTZ + PAA) mixture	2.042	0.58
5	PAA in (KTZ + PAA) mixture	1.995	0.56
6	KTZ in (KTZ + PVP) mixture	3.236	0.91
7	PVP in (KTZ + PVP) mixture	1.715	0.48
8	D_2O	17.780	5.01

*Standard errors from fit of equation (2.2) to the intensity vs gradient strength data, on the order of 1×10^{-12} m^2s^{-1} for all samples.

Isothermal Titration Calorimetry (ITC)

$$[Drug] + [Polymer] \overset{K_a}{\leftrightarrow} [Drug \cdot Polymer] \tag{S2.1}$$

$$\frac{dQ}{d[X]_t} = \Delta H^o V_0 \left[\frac{1}{2} + \frac{1 - X_R - r}{2\sqrt{(1 + X_R + r)2 - 4X_R}}\right] + Q_{dil} \tag{S2.2}$$

Equation (S2.1) assumes as simple 1:1 interaction between the drug and polymer, with an association constant K_a. In equation (S2.2), Q is the heat recorded, $[X]_t$ is the molar concentration of injectant at time t, $\Delta H^o$is the molar enthalpy change, V_0 is the initial volume of the sample cell, X_R is the mole ratio of drug to polymer in the sample cell, and Q_{dil} is the molar enthalpy of dilution, an adjustable parameter included to account for the dilution of drug in the solvent. The term r is defined as:

$$\frac{1}{r} = nK_a[M]_t \tag{S2.3}$$

where n is the stoichiometric ratio and $[M]_t$ is the molar concentration of polymer at time t. The Gibbs free energy change (ΔG), enthalpy change (ΔH) and entropy change (ΔS), can be calculated from the fundamental thermodynamic relation:

$$\Delta G = -RTlnK_a = \Delta H - T\Delta S \tag{S2.4}$$

where R is the universal gas constant, and T is temperature.

In the standard one-sites model, n, the stoichiometry number, represents the average number of drug binding sites per mole of macromolecule in the solution, with the assumption that all sites are identical and independent. In standard ITC fitting, the stoichiometry number can be obtained from the fit. However, for isotherms with weak affinity, (commonly termed low "c" data), the stoichiometry number can be fixed at 1, to reduce the number of variables, and increase the confidence in the fitted enthalpy change parameter. A global fit of the individual isotherms obtained before concatenation (see methods section for additional details) was performed, and the thermodynamic signature obtained was consistent with the values from the linear fit.

3 Analytical Ultracentrifugation for the Characterization of Drug–Polymer Interactions in Aqueous Solution

3.1 OVERVIEW

We present a new approach for characterizing drug–polymer interactions in aqueous media, using sedimentation velocity analytical ultracentrifugation (AUC). We investigated the potential interaction of ketoconazole (KTZ), a poorly water-soluble drug, with polyacrylic acid (PAA) and polyvinyl caprolactam–polyvinyl acetate–polyethylene glycol graft copolymer (Soluplus®) in aqueous buffers. The effect of the polymer on the sedimentation coefficient of the drug, was the observable metric. The drug alone, when subjected to AUC, exhibited a very narrow sedimentation peak at 0.2 Svedberg (S), in agreement with the expectation for a monomeric drug with a molar mass <1000 Dalton. Conversely, the neat polymers showed broad profiles with higher sedimentation coefficients, reflecting their larger more heterogeneous size distributions. The sedimentation profiles of the drug–polymer mixtures were expectedly different from the profile of the neat drug. With KTZ-Soluplus®, a complete shift to faster sedimentation times (indicative of interaction) was observed, while with KTZ-PAA, a split peak indicated the existence of the drug in both free and interacting states. The sedimentation profile of carbamazepine, a second model drug, in the presence of hydroxypropyl methyl cellulose acetate succinate (HPMCAS, another polymer), revealed multiple "populations" of drug–polymer species, very similar to the sedimentation profile of neat HPMCAS. The interactions probed by AUC, were compared with the results from isothermal titration calorimetry. *In vitro* dissolution tests performed on amorphous solid dispersions prepared with the same drug–polymer pairs, suggested that the interactions may play a role in prolonging drug supersaturation. The results show the possibility of characterizing drug–polymer interactions in aqueous solution with high hydrodynamic resolution, addressing a major challenge frequently encountered in the mechanistic investigations of the dissolution behavior of amorphous solid dispersions.

Keywords: Sedimentation Velocity Analytical Ultracentrifugation, Amorphous Solid Dispersions, Drug–polymer Interactions, Dissolution

3.2 INTROUDUCTION

When given orally, a solid drug must first dissolve in the gastrointestinal fluid, before being absorbed into the bloodstream[3]. Unfortunately, about 80% of drugs in the development pipeline are crystalline hydrophobic compounds, with poor aqueous solubility[4,131]. Therefore, a key focus in pharmaceutical science research is to develop strategies that could overcome this solubility challenge[5]. One approach is to formulate amorphous solid dispersions (ASDs), wherein the drug is mixed with a polymer, at the molecular level, to form a homogeneous phase[4,5,12].

One major consideration in formulating an ASD into a solid dosage form, is to prevent drug crystallization during the shelf life of the product. Strong intermolecular interactions between the drug and polymer (particularly ionic and hydrogen bonding interactions) can result in ASDs which are physically stable for timescales of pharmaceutical interest[52,61,89]. When the ASD is taken by the patient, supersaturated drug concentrations may be achieved in the gastrointestinal fluid[12]. To realize the solubility advantage, drug crystallization should also be prevented for a period, long enough to allow absorption to occur[2]. A widely held view is that an optimum strength of drug–polymer interaction in solution, is required to maintain the desired level of supersaturation[14,94,132]. If the interaction is too weak, the drug may rapidly crystallize from solution. If the interaction is too strong, it is possible that the drug–polymer complex may not dissociate and, in spite of being in solution, the drug may be unavailable for absorption. Adequate characterization of the *nature* and *strength* of drug–polymer interactions in aqueous solutions therefore aids, both in

understanding and interpreting, the *in vitro* drug dissolution profiles[14]. Analytical methods that can provide molecular-level information on the formation, composition, structure, size and stability of the drug–polymer complexes are thus required.

Techniques for characterizing interactions between heterogenous species in solution include vibrational spectroscopy (e.g. infrared, Raman), fluorescence and nuclear magnetic resonance (NMR) spectroscopy and isothermal titration calorimetry[78]. One dimensional (1D) vibrational spectroscopic techniques utilize shifts and general changes in characteristic vibrational bands of functional groups of the drug or polymer to indicate hydrogen bonding or ionic interactions[15,89]. The congested nature of 1D spectra, with numerous overlapping vibrational modes, poses a significant challenge in making unambiguous peak assignments[89]. Moreover, the broad infrared absorbance band from water, especially in the 3000 cm^{-1} region, occludes signals from functional groups of interest, making it impossible to observe spectral changes of drugs in aqueous solutions[15,89,133,134]. Even though Raman spectroscopy is transparent to water, the signals from poorly soluble drugs tend to be very weak with high fluorescence backgrounds.

As an advancement over 1D spectroscopy, two-dimensional (2D) NMR methods provide more reliable information on drug–polymer interactions. In 2D nuclear Overhauser effect spectroscopy (NOESY), resonances are spread along multiple axes, giving a frequency correlation spectrum[120]. If the drug and polymer are within 5 Å of each other in solution, cross peaks will develop indicating interactions[94,96,135]. Interactions in solution can also be

indirectly probed with diffusion measurements (*via* the principle of co-diffusion).[97,121,122] A reduction in drug diffusivity in the presence of a polymer, is often indicative of interaction. Of the several solute diffusion measurement techniques (e.g. dynamic light scattering, fluorescence correlation spectroscopy, asymmetric flow field flow fractionation, or NMR diffusion), only two-dimensional diffusion ordered spectroscopy (2D DOSY) has been successfully adapted for this application. DOSY allows simultaneous spectroscopic separation of the diffusion coefficients of heterogeneous species in solution (in a sense, reminiscent of chromatography)[96,98,135].

A significant barrier to the use of all these techniques stems from the weak signal of the drug–polymer systems in aqueous media. NMR in particular, inherently has a lower sensitivity than many other spectroscopic methods[136]. Similarly, the need for very high drug concentrations almost entirely precludes the use of isothermal titration calorimetry (ITC)[105]. While organic solvents can be used, interactions probed in such systems, do not reflect interactions in aqueous solution[137]. Other techniques that can address the challenge of poor signal sensitivity in aqueous media, must therefore be explored.

Analytical ultracentrifugation (AUC) is a powerful fractionation-based technique, used extensively to characterize the hydrodynamic and thermodynamic properties of biomacromolecules (e.g. proteins), colloidal systems, and nanoparticles[138–140]. AUC measures sedimentation or diffusion coefficients, from which the size, density, and shape of heterogeneous species in solution can be obtained[141]. Detection systems based on UV-

visible absorbance, fluorescence, or interference optics, make this technique amenable to a wide range of applications. The high sensitivity of the detection systems is particularly valuable for analytes with low aqueous solubility. Although AUC is suitable for the study of most macromolecules, the technique suffers low patronage in the investigation of synthetic polymers[142,143]. There are no reports on the sedimentation behavior of pharmaceutically-relevant (mostly synthetic) polymers typically used in ASD formulations. It is also not known, whether the interaction of such polymers with small molecule drugs in aqueous solution, can be adequately measured with AUC.

In this work, we highlight an opportunity to semi-quantitatively characterize drug–polymer interactions in aqueous solution, using sedimentation velocity analytical ultracentrifugation (AUC). The drug sedimentation coefficient, in the presence and absence of the polymer, is the metric. The free drug (in this context, small molecule with low density and molar mass less than 1,000 Da), will hardly sediment. In comparison, the bulky polymer (> 10,000 Da) should sediment rapidly. We hypothesize that when the drug interacts with the polymer, the sedimentation rate of the complexed drug changes, and approaches the sedimentation behavior of the neat polymer. The drug movement in the presence of the polymer can be monitored, if the UV-vis spectrum of the drug exhibits pronounced absorption in a wavelength region where the polymer does not absorb. This new AUC-based method would be analogous to the co-diffusion method used for characterizing drug–polymer interactions in two-dimensional DOSY[96,98].

We tested this method with two model hydrophobic drugs – carbamazepine (CBZ, an anti-epileptic) and ketoconazole (KTZ, an anti-fungal) – and three polymers. The structures are shown in **Figure 3.1**, and the reasons for selecting each drug–polymer pair are given in Section 3.3.1.

Our main objective was to evaluate the potential utility of sedimentation velocity analytical ultracentrifugation (AUC) to characterize drug–polymer interactions in aqueous media. We also compared the results of the AUC method, to interactions probed *via* isothermal titration calorimetry (ITC). Finally, the possible effects of the interactions on the *in vitro* dissolution performance of amorphous solid dispersions were discussed.

3.3 EXPERIMENTAL SECTION

3.3.1 Selection of model systems

Three drug–polymer pairs were used in this study: (i) ketoconazole (KTZ) and poly acrylic acid (PAA), (ii) ketoconazole and Soluplus® and (iii) carbamazepine (CBZ) and hydroxypropyl methyl cellulose acetate succinate (HPMCAS). The structures are shown in **Figure 3.1**.

In amorphous solid dispersions, the carboxylic acid groups of PAA, a linear polymer, were shown to interact with the imidazole nitrogen of KTZ[52]. The strong (ionic and hydrogen bonding) interactions translated to a pronounced resistance to drug crystallization, following storage of the KTZ-PAA dispersions in both the glassy and supercooled

states[93,100]. Our preliminary investigations (using 2D H^1H^1 NOESY and 2D DOSY) also showed that the drug–polymer interactions persisted in aqueous media[144,145]. Soluplus®, the second model polymer, is a commercial polyvinyl caprolactam—polyvinyl acetate—polyethylene glycol graft co-polymer that was specifically designed with amphiphilic groups for ASD formulation[50,146]. It forms micelles in water, conferring the ability to enhance the solubility of hydrophobic compounds[146]. Having no ionizable functional groups, ionic interactions with KTZ would be unlikely. Hydroxy propyl methyl cellulose acetate succinate (HPMCAS, the third polymer), is widely used in amorphous solid dispersion formulations and facilitates the formation of stable supersaturated solutions[14,147]. Interaction of HPMCAS with CBZ in the dry solid form, was recently characterized[148]. Furthermore, with NMR (2D NOESY and saturation transfer difference) experiments, it was shown that hydrophobic-driven associations between CBZ and HPMCAS exist in aqueous buffers[94]. The interaction was correlated with a reduction in carbamazepine recrystallization from supersaturated solutions[149]. The three drug–polymer pairs, KTZ–PAA, KTZ–Soluplus and CBZ–HPMCAS, were therefore expected to provide different types of interactions in solution.

3.3.2 Materials

Carbamazepine (Sigma, USA), ketoconazole (Laborate Pharmaceuticals, Haryana, India) Soluplus® (BASF, USA), HPMCAS, HF grade (Ashland, USA) and PAA (Sigma, USA) were used as received (**Figure 3.1**). All reagents and chemicals used to prepare the buffers and the amorphous solid dispersions, were of analytical grade.

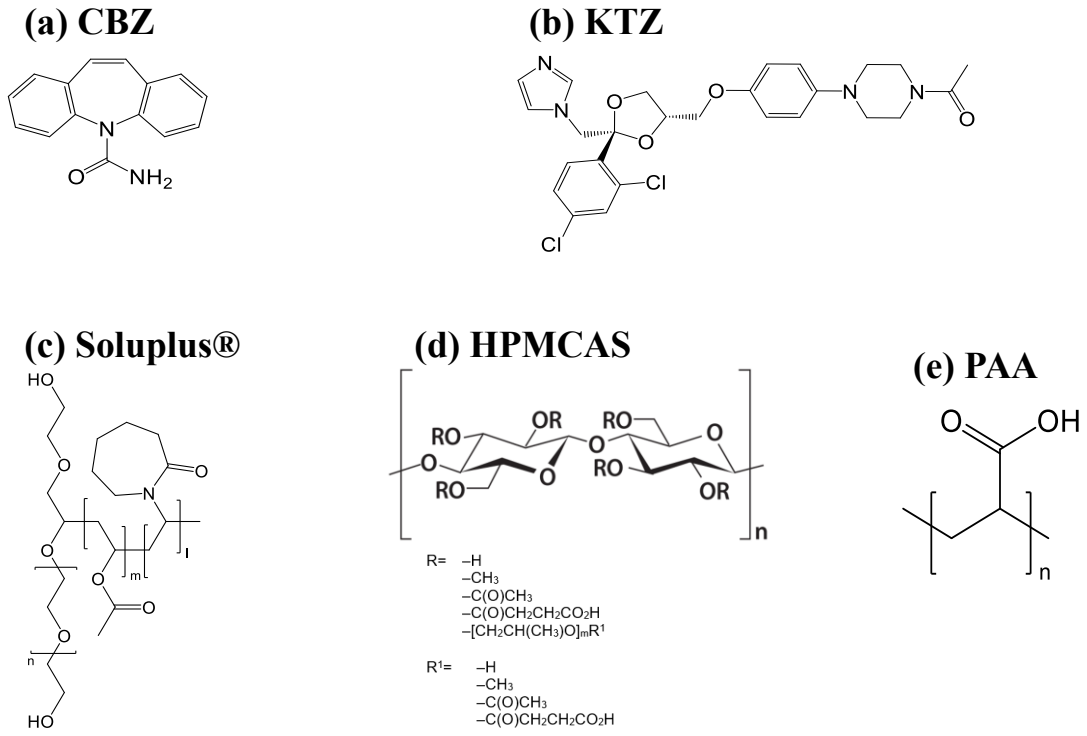

Figure 3.1. Structures and average molecular weights (M_w) of the drugs and polymers. **(a)** carbamazepine (CBZ), 236 Da, **(b)** ketoconazole (KTZ), 531 Da, **(c)** polyvinyl caprolactam—polyvinyl acetate—polyethylene glycol graft co-polymer (Soluplus®), 115,000 Da (ref[146]), **(d)** hydroxypropyl methyl cellulose acetate succinate (HPMCAS), 17,000 Da (ref[150]), **(e)** polyacrylic acid (PAA), 1,033,000 Da.

3.3.3 Preparation of amorphous solid dispersions

Amorphous solid dispersions (ASDs) with 33% w/w drug loading were prepared by solvent evaporation. For each system, the drug and polymer were individually dissolved in appropriate organic solvents (KTZ, Soluplus®, PAA and HPMCAS-HF in methanol; CBZ in ethanol). The solutions were combined and the solvent rapidly evaporated, at 50 ℃ under reduced pressure (IKA-HB10 digital system rotary evaporator, Werke GmbH and Co., Staufen, Germany). The solid dispersions were further dried at room temperature for 24 hours to remove any residual solvent, lightly ground using a mortar and pestle in a glovebox (RH < 5%), sifted (250 µm pore size) and stored at -20 ℃ in desiccators containing anhydrous calcium sulfate, before use. All ASDs prepared were found to be amorphous when characterized by powder X-ray diffractometry [model D8 ADVANCE; Bruker AXS, Madison, WI, using Cu Kα radiation (40 kV × 40 mA) over an angular range of 5−35° 2θ with a step size of 0.05° and a dwell time of 0.5 s].

3.3.4 Preparation of buffers and solutions

Phosphate buffer (pH 6.8; 50 mM monobasic potassium phosphate and 22.4 mM sodium hydroxide) and hydrochloric acid buffer (pH 1.1; 106 mM hydrochloric acid and 50 mM potassium chloride) and were used. Separate stock solutions of drug (up to 1 mg/mL) and polymer (~15 mg/mL) were prepared by dissolving an accurately weighed amount of material in the buffer followed by filtration (0.45 µm pore filter). Aliquots of the stock solutions were pipetted into a vial and diluted with buffer to obtain solutions with the

required final compositions for ITC and AUC experiments (details in **Table 3.1**). The pH of all samples (drug solutions, polymer solutions or their mixtures) did not differ by more than ±0.1 units of the required value.

3.3.5 UV-Vis spectroscopy

UV/visible absorbance spectra were recorded in the 200-600 nm range (Cary 100 Bio, Agilent Technologies), using a quartz cuvette with a path length of 1 cm.

3.3.6 Analytical ultracentrifugation

Concentrations of solutions (i.e. neat drug, neat polymer, and drug–polymer mixtures), as well as solvents used in each case, are summarized in **Table 3.1**. Concentrations were chosen such that an optical density of ~0.6 would be obtained, at the desired wavelength of detection for the AUC experiments.

Table 3.1. Solvents and solution concentrations used in the AUC experiments.

Sample	**pH of solvent**	**[Drug alone], mg/mL**	**[Polymer alone], mg/mL**	**[(Drug) + Polymer mixture], mg/mL**	**Drug : Polymer ratio (by weight)**
Ketoconazole and PAA	1.1	0.25	0.5000	(0.25) + 0.50	1:2
Ketoconazole and Soluplus®	1.1	0.25	0.0625	(0.16) + 0.33	1:2
Carbamazepine and HPMCAS	6.8	0.04	4.0000*	(0.04) + 4.00	1:100
*Experiments at lower polymer concentrations yielded qualitatively similar profiles.					

KTZ, PAA and Soluplus experiments were performed at the Center for Analytical Ultracentrifugation of Macromolecular Assemblies at the University of Texas Health Science Center at San Antonio, using an analytical ultracentrifuge (Optima AUC, Beckman Coulter, Indianapolis IN) equipped with multi-wavelength UV-visible detection (absorbance optics). Samples were placed into Epon centerpieces with quartz windows, and measured at 20°C, 45000 rpm, in an An50Ti rotor. CBZ and HPMCAS experiments were performed at the Canadian Center for Hydrodynamics at the University of Lethbridge, Alberta, Canada. Samples were placed into titanium centerpieces (Nanolytics Instruments, Potsdam, Germany) with sapphire windows and measured at 20°C, 60000 rpm, in an An60Ti rotor. Approximately 500 scans were collected for each wavelength. Data analyses were carried out with standard models implemented in the UltraScan III® software[151,152], using the two-dimensional spectrum analysis (2DSA)[153], coupled with Monte Carlo analysis[154], and the parametrically constrained spectrum analysis (PCSA)[155]. Briefly, these methods model sedimentation velocity data with linear combinations of finite element solutions of the Lamm equation[156] to obtain sedimentation and diffusion coefficients (s and D values respectively). The 2DSA-Monte Carlo analysis was used to obtain an unconstrained sedimentation/diffusion profile of the hydrodynamic parameter space. Due to the lack of constraint, for experiments with low signal, there was a possibility that the 2DSA algorithm occasionally would fit the noise in the experimental data, leading to artifactual results. The PCSA analysis would further constrain the fitted data, reducing noise contributions, and also detect size-vs-anisotropy trends for polymerizing systems, should they exist. Computationally intensive calculations were carried out on high-

performance supercomputing platforms. Sedimentation coefficient values were standardized to water at 20 °C ($s_{20,w}$). The profiles were normalized by dividing each data point in the original distribution by the maximum dC/ds data point, so that the peak maximum for each distribution was equal to 1.

3.3.7 Isothermal titration calorimetry (ITC)

KTZ solution (20 mg/mL) was prepared in buffer (pH 1.1 ± 0.1), and filtered (0.45 µm PTFE), immediately before each ITC experiment. Solutions of PAA (5 mg/mL) and Soluplus® (5 mg/mL), were also prepared in the same buffer (pH 1.1 ± 0.1).

A microcalorimeter (Microcal^{TM} Auto-ITC$_{200}$ system, Malvern Instruments, MA) which has a 200 uL sample cell and an identical reference cell, was used. The drug solution in the syringe, was sequentially injected into the polymer solution within the sample cell, with a constant stirring rate of 750 rpm. The temperature was maintained at 25 °C. The first injection was a 0.4 µL aliquot to remove the effect of solute diffusion across the syringe tip during the equilibration period. Subsequently, 4 µL injections were made into the sample cell. The duration of each injection was 20 s, and the time interval between successive injections was 180 s. The run time was extended by performing experiments in an automated "continued injection" mode, wherein, when full, 30 uL of solution was withdrawn from the sample cell, to make room for more sequential injections of the titrant. This process of withdrawing solution from the sample cell and continuing the titrations was repeated for up to four experiments. Individual experiments were concatenated using the

Microcal origin® concat (add-on) software. Data processing, integration and analysis was done with the Affinimeter® software[106].

3.3.8 Powder *in vitro* dissolution

Dissolution tests under non-sink conditions were performed with a USP Apparatus II (Varian 705 DS, Agilent Technologies, Santa Clara, CA). Each sample, containing 250 mg of drug, was dispersed in 250 mL of dissolution medium (pH 6.8 buffer) set at 37 °C and stirred with a paddle speed of 100 rpm. Aliquots (2 mL) were withdrawn at each time point, filtered (0.45 µm pore size, Whatman® PP) and diluted appropriately with methanol. The drug concentration in the filtrate, was determined by high performance liquid chromatography (HPLC; Nexera XR® system, Shimadzu, Japan).

Chromatographic separation was performed using a reversed-phase column (Zorbax® Eclipse XDB-C18, 4.6 x 150 mm, 5 µm, Agilent, USA). The mobile phase consisted of 2.55 g of tetrabutylammonium hydrogen sulfate dissolved in 750 mL of water and diluted to 1000 mL with acetonitrile. The flow rate was 1 mL/min at 30 °C. Injection volumes, detection wavelengths and retention times were respectively; 20 µL, 223 nm, 4 min for KTZ and 5 µL, 230 nm, 14 min for CBZ. Drug concentrations were calculated from linear calibration curves generated over a concentration range of 4 - 400 µg/mL.

3.4 RESULTS AND DISCUSSION

In general, upon dissolution of an amorphous solid dispersion, the three main species that may exist in solution are: (i) free drug, (ii) free polymer, and (iii) various types of drug–polymer aggregates or complexes[14]. Both free and complexed drug contribute to the total drug concentration measured via *in vitro* dissolution tests[14]. Any technique that can independently monitor the differing rates of solute transport (e.g. diffusion, sedimentation) and/or the relative amounts of each of these species in solution can, in principle, provide a measure of the drug–polymer interactions. This formed the basis for the experimental design.

In a typical sedimentation velocity AUC experiment, the dissolved solute within a sample cell, is exposed to a high centrifugal field, induced by the spinning of the centrifuge rotor. The solute transport is tracked by an optical detection system (in this case, UV multi-wavelength absorbance optics) that measures the concentration change of the sample, as a function of time and sample cell radius (see supporting information). The procedure for selecting UV absorbance wavelengths, which allows the sedimentation coefficient (*s*-value) distribution of different species in solution to be monitored, is explained in the next section.

3.4.1 Wavelength selection for analytical ultracentrifugation

Utilizing absorbance optics, the first step involved examination of the UV absorbance profiles of the (i) neat drugs (ii) neat polymers and (iii) drug–polymer mixtures. The main

consideration was to identify a wavelength region where the neat drug has a strong absorbance, but where the neat polymer does not absorb. The spectra of the samples are shown in **Figure 3.2**. Solution compositions and buffers used as solvent are listed in **Table 3.1**.

Carbamazepine exhibits pronounced absorbance at wavelengths < 250 nm, as well as a peak at 270 nm (**Figure 3.2a**, blue-dashed profile). The AUC optics can be tuned to any wavelength at which the drug absorbs, to observe the sedimentation of the neat drug. The neat polymer HPMCAS, on the other hand, only absorbs significantly at wavelengths < 250 nm (**Figure 3.2a**, violet dashed line profile), such that its sedimentation can only be monitored at wavelengths < 250 nm. In the 250–330 nm wavelength region, the absorbance of the neat drug is much higher than the absorbance of the neat polymer, such that the polymer does not contribute significantly to the absorbance of the drug–polymer mixture. The AUC optics can therefore be tuned to any wavelength in the 250–330 nm range, to observe the migration of the drug in the presence of the polymer. The UV profiles of ketoconazole and the polymers, PAA and Soluplus®, exhibit qualitatively similar characteristics (**Figure 3.2b**).

By monitoring the sedimentation profile of the drug–polymer mixture at a wavelength where only the neat drug absorbs, the sedimentation experiment becomes selective for the drug and any drug–polymer complexes formed. If the neat polymer sediments faster than the neat drug, any increase in the sedimentation coefficient of the drug within the polymer

matrix, will provide evidence of drug–polymer interactions. This is the principle upon which the drug–polymer interactions were monitored. It should be noted, however, that the sedimentation profile of the free polymer within the mixture cannot be monitored.

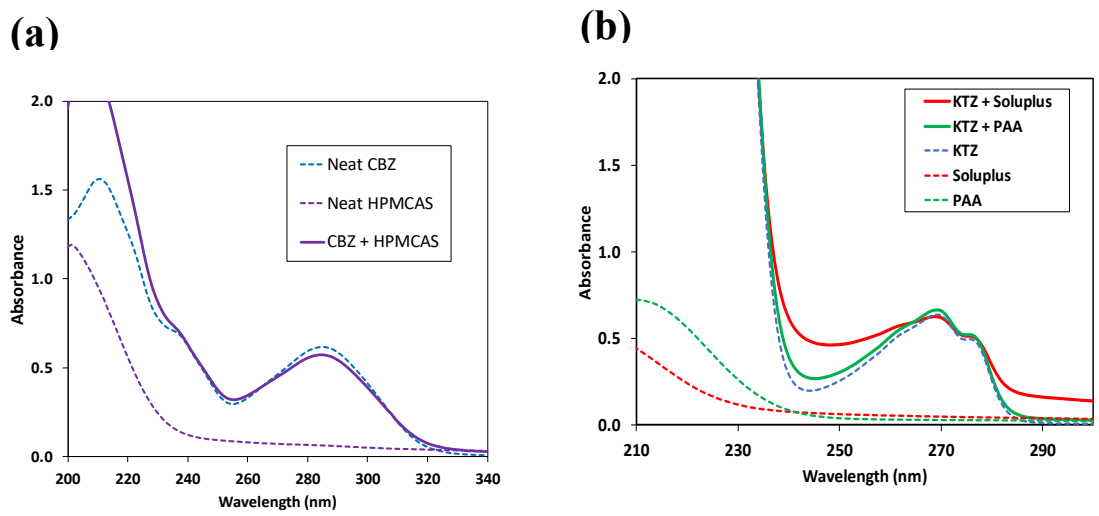

Figure 3.2. UV absorbance spectra of neat drugs, neat polymers, and (drug + polymer) mixtures. (a) carbamazepine alone, HPMCAS alone and the (CBZ + HPMCAS) mixture. (b) Ketoconazole alone, PAA alone, Soluplus® alone, the (KTZ + PAA) mixture and the (KTZ + Soluplus®) mixture. Solute concentrations and solvent systems are listed in **Table 3.1**.

3.4.2 Sedimentation profiles of neat drugs and polymers

Sedimentation profiles of the neat drugs and neat polymers are presented in **Figure 3.3**. The corresponding experimental raw data plots, as well as the fitting residuals, which were mostly randomly distributed, are provided in the supplementary information **(Figure S3.1 to Figure S3.5;** see AUC experimental methods for details of data analyses). When either CBZ (**Figure 3.3a**, M_w = 236 Da) or KTZ (**Figure 3.3b,** M_w = 531 Da) was examined

alone, a very narrow sedimentation peak at 0.2 S was observed. Posaconazole, another drug with a slightly higher molecular weight (M_w = 701 Da), also showed a sedimentation coefficient at 0.2 S (data not shown). The identical sedimentation profiles are in excellent agreement with the expectation that monomeric molecules with low molecular weights (<1000 Dalton) hardly sediment, and are at the limit of detectability by analytical ultracentrifugation[141].

The neat polymers, however, had very different sedimentation profiles. PAA, a linear polymer, was present in solution as a heterogeneous mixture sedimenting between 0 and 50 S (**Figure 3.3c**). The high molecular weight (1,031,000 Da), long chains (~14,300 monomers per chain) and high dispersity index of 7.9, contribute to the broad, skewed sedimentation coefficient distribution. The larger aggregates between 10 and 50 S are likely from chain entanglement[109]. Soluplus®, with molecular weight an order of magnitude lower than that of PAA, had a narrower, more homogeneous size distribution (from 0-4 S) and a negligible number of larger aggregates (**Figure 3.3d**). Soluplus® is amphiphilic, and the concentration examined was well above the reported critical micelle concentration of 0.0076 mg/mL[146].

The sedimentation profile of neat HPMCAS however showed five well-defined peaks, from 0 to 2 S (**Figure 3.3e**). The molecular weight (~17,000 Da) is significantly lower than that of PAA or Soluplus®, resulting in a narrower range of s-values. The sharpness of the peaks however suggests that in solution, HPMCAS migrates as discrete, light species

which is a rather surprising observation. Of note, all polymer solutions were measured at sufficiently low concentrations to avoid non-ideal sedimentation[83,157,158]. Because of the amphiphilic nature of HPMCAS, a widely-held view is that any higher order structures in solution will be due to colloidal aggregation or gelation[14,147]. Friesen *et al,* using cryogenic transmission electron microscopy, characterized a range of nanometer-sized structures (mainly 10-20 nm polymer colloids, and a few 70-300 nm nanoaggregates) formed by HPMCAS in aqueous buffer (pH 6.8)[14]. They posited that because HPMCAS is partially ionized at pH 6.8, the charge on the polymer allows the colloids to remain stable, while minimizing the formation of much larger aggregates[14]. Ricarte *et al* however suggested that the large species, also observed with light scattering measurements over a wide concentration range (0.01 to 9 mg/mL), were from chain coupling (i.e. covalently cross-linked chains) and not from colloidal aggregation[159]. Both scenarios could result in the discrete sedimenting fractions observed in this study. It is also possible, that the different combinations of acetyl and succinoyl substituents of the cellulose backbone (the R and R^1 groups of **Figure 3.1d**), result in polymer fractions that sediment at different speeds. If the latter explanation holds, the sedimentation profiles of neat polymer solutions manufactured to different specifications may be characteristic, allowing use of the technique as a quality control measure. Clearly, this interesting sedimentation profile warrants further investigation.

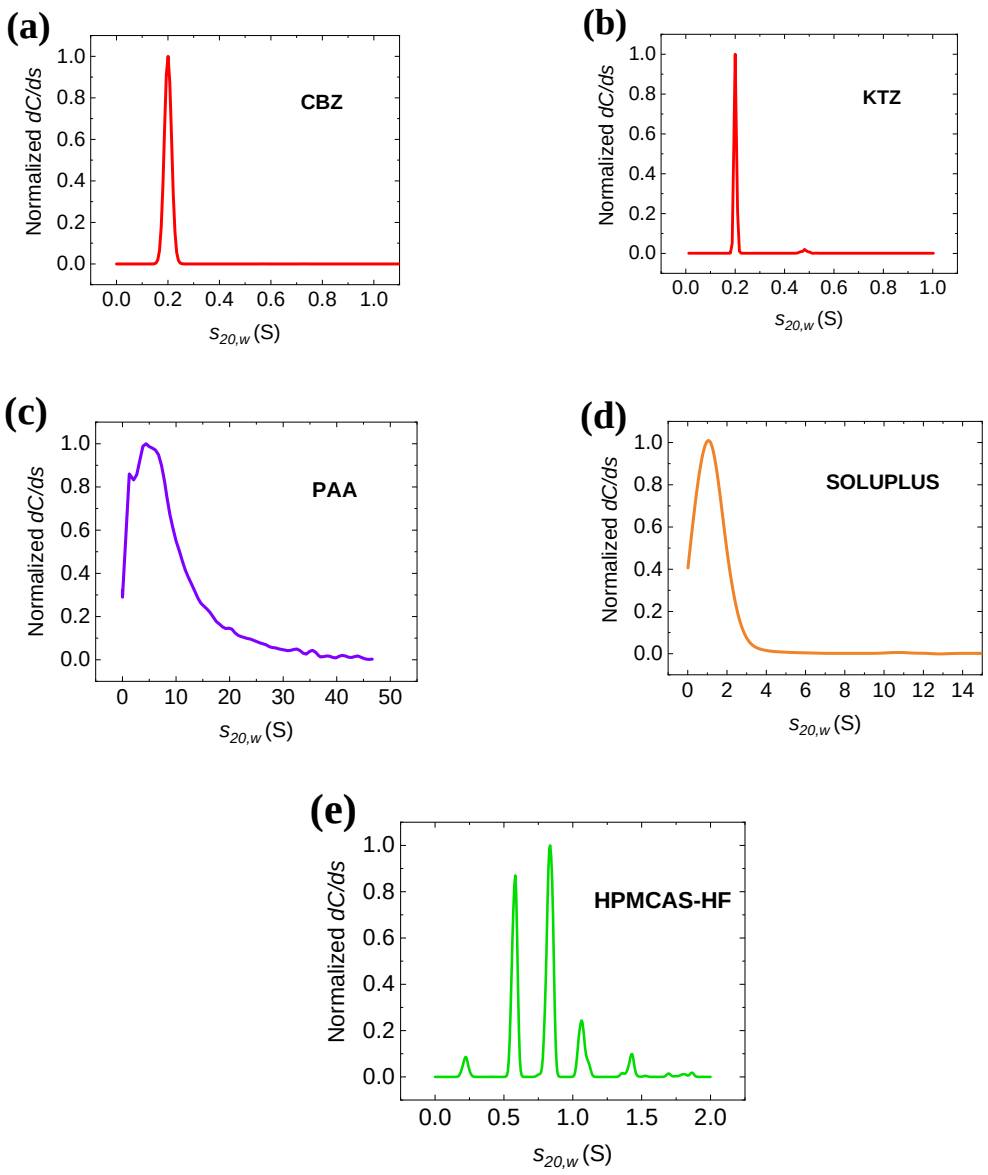

Figure 3.3. Sedimentation profiles of the neat drugs and neat polymers. (a) CBZ alone, observed at 315 nm, (b) KTZ alone, observed at 262 nm (c) PAA alone observed at 215 nm, (d) Soluplus® alone observed at 215 nm and, (e) HPMCAS alone observed at 220 nm. Solution concentrations and solvent systems are listed in **Table 3.1**.

3.4.3 Sedimentation profiles of drug–polymer mixtures

Sedimentation profiles of the drug–polymer mixtures, each overlaid with the profile of the corresponding neat drug, are presented in **Figure 3.4**. Experimental raw data for each sample, as well as the fitting residuals, have also been provided in the supplementary information (**Figure S3.6 to Figure S3.8**). For each sample, shifts to higher sedimentation coefficient values (s-values) were observed, which can be attributed to drug–polymer interactions.

The KTZ-Soluplus® mixture (**Figure 3.4a**, bottom profile) showed a complete shift in s-value, suggesting that the drug molecules migrate at the same rate (in a single distribution) in the presence of the polymer. For the KTZ-PAA mixture, a split peak was observed; the first peak at 0.2 S, which matches the peak position of neat KTZ, and the second peak centered at 0.3 S, a faster sedimentation rate compared to the neat drug (**Figure 3.4b**). This observation suggests a mixture of free (30%, at 0.2 S) and "interacting" (70%, at 0.3 S) drug fractions respectively, at the concentration level evaluated.

The sedimentation profile of the CBZ-HPMCAS system shows four peaks, in the 0 to 2 S region (**Figure 3.4c**, green bottom profile). Evidently, this profile is very different from the single sharp peak of the neat drug, and more closely resembles the profile of neat HPMCAS (**Figure 3.4c**, middle profile). The first peak of the drug–polymer mixture appears at 0.3 S (~ 0.1 S shift in s-value, when compared to the neat drug) indicating that there is no free drug fraction. The three additional peaks of the drug–polymer mixture,

which appear at 0.6, 1.1 and 1.7 S, match the peak positions of the neat polymer. The peak positions and corresponding peak areas for all the drug–polymer pairs, are listed in **Table 3.2**. If the multiple peaks of neat HPMCAS indeed result from the diverse substituent units of the cellulose backbone, this observation would mean that CBZ preferentially partitions into different polymer fractions. The ability to quantify with high resolution, the different fractions of drug–polymer complexes, is indeed a key advantage of the analytical ultracentrifugation technique.

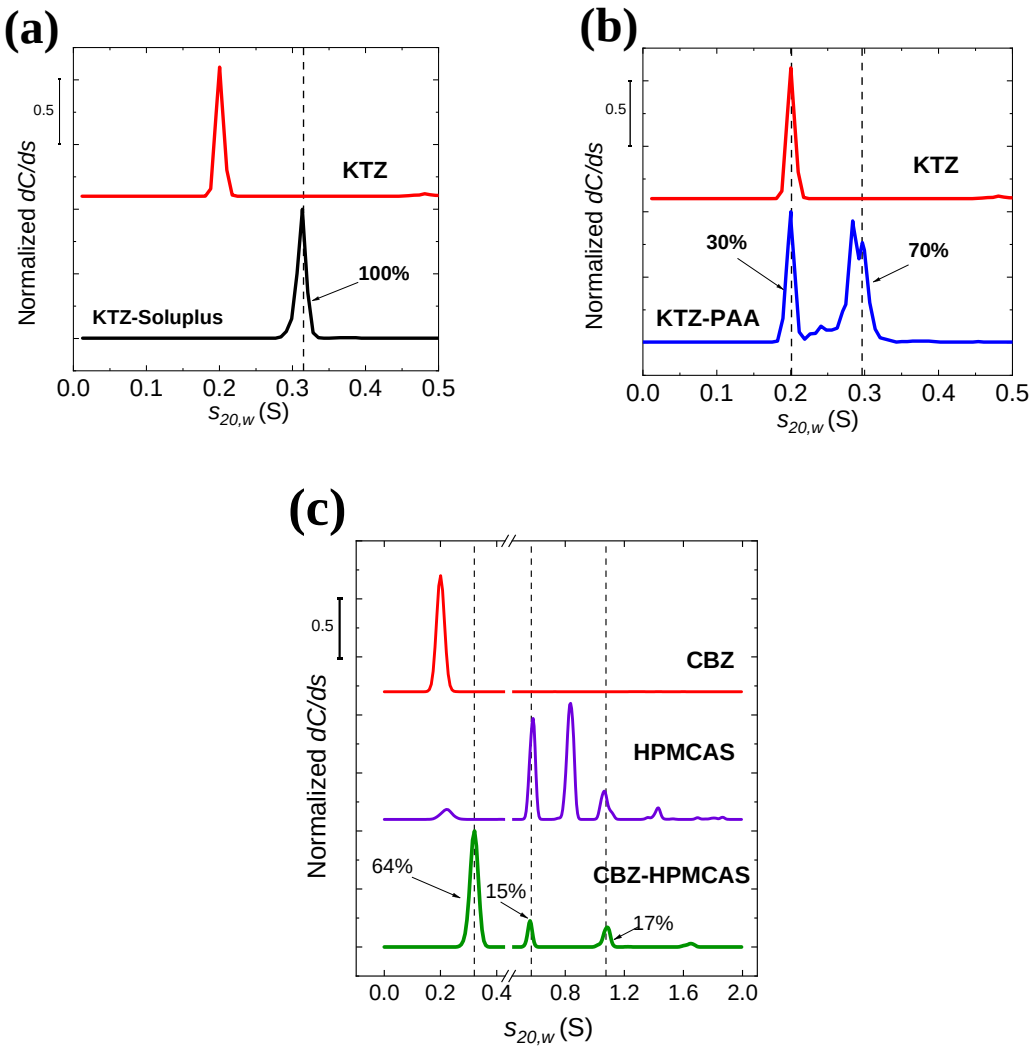

Figure 3.4. Sedimentation profiles of drug–polymer mixtures. **(a)** KTZ-Soluplus observed at 262 nm, stacked with KTZ alone. **(b)** KTZ-PAA observed at 262 nm, stacked with KTZ alone. **(c)** CBZ-HPMCAS observed at 315 nm, stacked with CBZ alone and HPMCAS alone. The peak positions of drug–polymer mixtures are indicated with dashed vertical lines. The percentage abundance of different fractions are pointed out with arrows (see **Table 3.2**).

Table 3.2. Peak positions and peak areas for the neat drugs, the neat polymers and the drug–polymer mixtures.

Component	Sedimentation Coefficient ($s_{20,w}$, S)	Abundance (%)
Neat CBZ (or KTZ)	0.2	100.0
Neat Soluplus®	1.2	100.0
Neat PAA	4.4	100.0
Neat HPMCAS	0.2	3.3
	0.6	32.7
	0.8	46.3
	1.1	12.0
	1.4	4.2
	1.8	1.5
CBZ + HPMCAS*	0.3	63.9
	0.6	15.1
	1.1	17.4
	1.7	3.6
KTZ + Soluplus®*	0.3	100.0
KTZ + PAA*	0.2	30.7
	0.3	69.3

*The shifted peaks, when measured in the presence of the polymer, were baseline resolved from the peaks observed for the neat drug. A 50-iteration Monte Carlo analysis (see Section 3.3.6 for details) did not detect any variation in the results.

3.4.4 General inference from AUC results

Overall, the AUC results suggest that the drugs form very weak associations with the polymers, that are much weaker than binding interactions conventionally probed by sedimentation velocity AUC, such as ligand-protein, or protein-protein interactions[138,160]. This inference is made because the magnitude of the shift in sedimentation coefficient of the drug–polymer mixture (relative to the drug alone), is rather small. If the drug were tightly bound to the polymer, the sedimentation pattern of the drug–polymer mixture would have mirrored the sedimentation pattern of the neat polymer. The CBZ-HPMCAS system

gives closest support of this expectation. However, for the KTZ-polymer systems, only subtle shifts in drug sedimentation coefficient were observed, indicating that a weight average *free*- versus *interacting*-drug sedimentation is favored by the free state. The weak shifts in the *s*-value, make it impossible to perform additional analyses of the sedimentation data, which could have allowed extraction of other thermodynamic information. Nonetheless, the percent abundance of the various species, obtained from the peak areas, allows for semi-quantitative rank-ordering of the interaction strengths.

3.4.5 Isothermal titration calorimetry (ITC)

Isothermal Titration Calorimetry (ITC) provided an avenue to assess the energetics of the drug–polymer interactions in aqueous solution. Generally, ITC experiments require very high ligand (the drug in this case) concentrations so as to obtain data sets optimal for the reliable determination of thermodynamic parameters[105]. This condition is typically not met for drugs with poor aqueous solubility. However, we took advantage of the pH-dependent aqueous solubility of KTZ. Being a weak base (pKa values of 6.5 and 2.9), KTZ is practically insoluble at pH > 4, but highly soluble in acidic buffers (pH < 2.5; 20°C)[107]. A solution with a high drug concentration (~20 mg/mL) could thus be prepared in acidic solvent, making it possible to perform ITC experiments. Conversely, because the aqueous solubility of CBZ is very low (<0.22 mg/mL) at all pH values, ITC experiments with CBZ in HPMCAS could not be performed.

Figure 3.5a shows the power compensation signals for the titration of KTZ into PAA. Exothermic peaks were initially registered, which progressively decreased in magnitude as the drug was titrated into the polymer solution. The control experiments, comprising titration of drug solution into the blank buffer, or the titration of buffer into polymer solution (respectively labeled as KTZ, and PAA in **Figure 3.5a**) yielded negligible heats.

The peaks obtained for the titration of drug into polymer, were integrated to obtain the heat change (ΔQ) at each injection and then plotted as a function of the drug-to-polymer ratio in the sample cell (**Figure 3.5c**). The shape of the curve obtained for KTZ-PAA, is typical for binding interactions with weak affinity (association constants less than 10^4 M^{-1})[105,125]. An overall enthalpy change of -10.2 kcal/g was obtained when the data was analyzed with an independent sites fitting method[106], indicating an enthalpy-driven interaction. The titration of KTZ into Soluplus (**Figure 3.5b**) however showed very weak peaks (~0.5 µcal/sec), of the same magnitude as the peaks from the drug dilution experiment, resulting in a flat, featureless binding isotherm (**Figure 3.5c**).

The ITC experiments (*via* the shape of the binding isotherm) confirm the inference from the AUC experiments, that drug–polymer interactions are generally very weak. The KTZ-PAA exothermic heats are most likely from electrostatic interactions between the carboxylic acids of the polymer (pKa 4.5) and the ionizable imidazole groups of the drug (see **Figure 3.1**). Soluplus on the other hand, has no ionizable functional groups or hydrogen bond donors (except the end groups). Thus, (ionic or hydrogen bonding)

interactions of KTZ with Soluplus would be unlikely, providing a reasonable explanation for the observation that there were no heats released or absorbed.

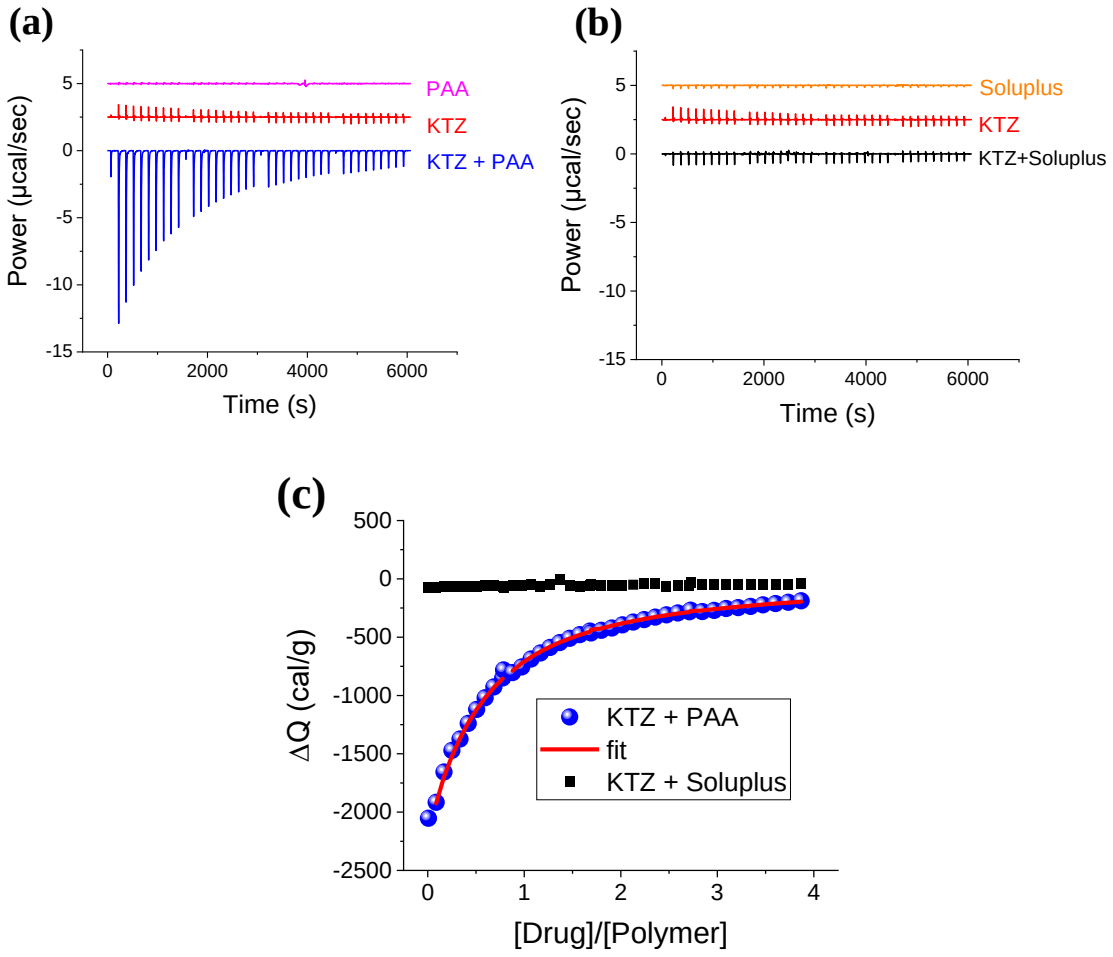

Figure 3.5. ITC raw data measured during the stepwise injection of KTZ (20 mg/mL) into (a) 5 mg/mL PAA (b) 5 mg/mL Soluplus. The solvent was pH 1.1 buffer. Each panel also has the profile for the titration of drug into plain buffer (labeled as KTZ, offset by 2.5 units on the vertical axis for clarity) and the profile for titration of buffer into polymer solution (labeled PAA or Soluplus, offset by 5 units). (c)Overlay of the integrated heat data (ΔQ per gram of drug injected) as a function of the drug-to-polymer ratio in the sample cell (concentrations expressed in mg/mL).

3.4.6 Dissolution of amorphous solid dispersions

The *in vitro* performance of amorphous solid dispersions (ASDs) prepared by solvent evaporation, was evaluated with powder dissolution studies, conducted in pH 6.8 buffer, under non-sink conditions. The dissolution profiles are in **Figure 3.6**, and the results are summarized in **Table 3.3**. The maximum concentration of the neat crystalline drugs recovered in solution were just about the same as the equilibrium solubility values reported in the literature (220 µg/mL for CBZ[161], and 3 µg/mL for KTZ[107] at 37°C, pH 6.8).

The ASDs, each at a nominal drug concentration of 1000 µg/mL, resulted in substantially higher dissolved drug concentration levels, compared to the neat crystalline drugs. For the KTZ-PAA ASD (**Figure 3.6a**), a rapid surge in drug concentration was observed ($C_{max} \approx$ 390 µg/mL) followed by a sharp decline to ~55 µg/mL, presumably the result of drug crystallization. In contrast, a gradual rise in drug concentration was observed for the KTZ-Soluplus® ASD, with a substantially lower C_{max} value (~140 µg/mL) even though the maximum level of supersaturation was sustained for a longer duration. The profile of the carbamazepine-HPMCAS ASD (**Figure 3.6b**), showed complete drug release within the first 20 minutes, with the supersaturation sustained for 24 hours.

The composite effect of the extent and duration of supersaturation was quantified, by normalizing the area under the dissolution profile of each ASD, with the area under the curve of the corresponding crystalline drug. The resulting dissolution enhancement factors

are presented in **Table 3.3**. The dissolution enhancement of the PAA dispersion, despite the rapid surge in drug concentration, was about the same as the enhancement from the Soluplus® dispersion, over the physiologically relevant time frame (up to 8 hours, ~5-fold enhancement), and even when extended to a 24-hour period (~10-fold enhancement). A five-fold dissolution enhancement was obtained for the CBZ-HPMCAS dispersion in 24 hours. It is worth noting that the nominal drug concentration for the CBZ-HPMCAS ASD in the dissolution vessel (1000 µg/mL), was only 4.5 times higher than the CBZ crystalline solubility. Dissolution experiments performed using a higher quantity of the ASD (nominal drug concentration of 2200 µg/mL, 10 times the crystalline solubility) yielded a qualitatively similar profile, with no decline in dissolved drug concentration beyond 24 hours (data not shown).

3.4.7 Possible effects of interaction strength on supersaturation

The polymers used in this study are hydrophilic. Thus, the initial rate of drug release from their ASDs will most likely be controlled by the rate at which the polymer dissolves in the dissolution medium[16,162,163]. Rapid polymer dissolution results in immediate liberation of the amorphous drug, generating supersaturated solutions, as observed for the KTZ-PAA and CBZ-HPMCAS dispersions. Additionally, PAA creates an acidic microenvironment, favorable for the dissolution of the basic drug, KTZ[114]. The slower initial drug release rate from the KTZ-Soluplus dispersion however suggests that, despite its hydrophilic nature, the polymer possibly formed a "gel-like" matrix, from which the amorphous drug slowly diffused.

Once the drug is released in solution, however, it is likely that drug–polymer interactions will play a more substantial role in sustaining the level of supersaturation[16]. When the polymer remains associated with the dissolved drug, nucleation and crystal growth (the two stages of crystallization) can be prevented[16]. It is reasonable to expect that the duration of supersaturation will be related to the fraction of drug molecules that remains associated with the polymer in solution, and this information can be obtained from the AUC sedimentation profiles.

If the drug–polymer interaction strengths revealed by AUC were to be rank-ordered, CBZ-HPMCAS (**Figure 3.4c**; 100% of drug molecules associated with the polymer, with strong shifts in *s*-value) would be considered the strongest interacting system, followed by KTZ-Soluplus (**Figure 3.4a**; 100% of drug molecules associated with polymer, but not as strong a shift in *s*-value). The KTZ-PAA system (**Figure 3.4b**) would be considered the weakest interacting, since 30% of the drug remained free.

Interestingly, the duration of maximum supersaturation observed for the dissolution profiles of the amorphous solid dispersions, appear to follow a similar trend. In the CBZ-HPMCAS ASD, supersaturation was sustained far beyond 24 hrs; for KTZ-Soluplus, supersaturation was sustained for up to 6 hours, and for KTZ-PAA, supersaturation was sustained for just ~2 hours. The similarity in the trends may be merely coincidental, since the conditions for the analytical ultracentrifugation experiments were not identical to the

conditions for the *in vitro* dissolution tests. Particularly, while the dissolution tests were performed in a neutral medium (pH 6.8), the AUC experiments for the ketoconazole systems were performed under acidic conditions (pH 1.1, in order to increase the signal strength and ensure solution stability). Furthermore, the ionization behavior of both ketoconazole and PAA are pH dependent[107,109], which could potentially affect the drug–polymer interaction strengths and dissolution profiles. Ketoconazole in acidic solvent is positively charged, but substantially uncharged in neutral conditions. PAA, on the other hand, remains uncharged with a somewhat globular conformation in acidic solvent, but negatively charged with a more extended conformation in neutral solvent[109]. It would therefore be speculative, to unequivocally attribute the trends in dissolution profiles observed in the current study, solely to the interaction strengths probed by the AUC technique. Nonetheless, analytical ultracentrifugation adds a new dimension, i.e. sedimentation metrics and other hydrodynamic parameters, to investigations aimed at unravelling the impact of drug–polymer interactions on dissolution enhancement. With other systematic studies performed on a wider range of drug–polymer systems, a clearer picture is likely to emerge about the relevance of the nature and the strength of interactions on the dissolution enhancement of amorphous solid dispersions.

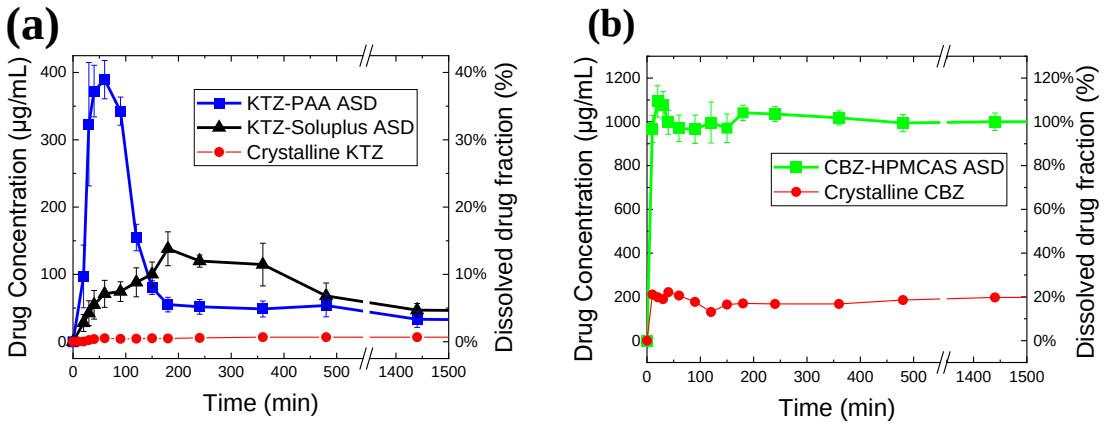

Figure 3.6. *In vitro* powder dissolution profiles of amorphous solid dispersions, each at 33 %w/w drug loading. (a) KTZ-PAA ASD and KTZ-Soluplus® ASD (b) CBZ-HPMCAS ASD. Data points (with bars) are the arithmetic means of three replicate runs (with standard deviations).

Table 3.3. Dissolution test results (±standard deviation, n=3).

	Sample	C_{max} (µg/mL)	t_{max} (min)	Area under curve, $t_{0\rightarrow 8hr}$ (µg/mL·min)	Dissolution enhancement factor*, $t_{0\rightarrow 8hr}$	Area under curve, $t_{0\rightarrow 24hr}$ (µg/mL·min)	Dissolution enhancement factor*, $t_{0\rightarrow 24hr}$
1	CBZ Crystalline	221	40	82722	**1.0**	266533	**1.0**
2	CBZ-HPMCAS ASD	1093 (±71)	20	480567 (±15721)	**1.8 (±0.1)**	1438455 (±48398)	**5.4 (±0.2)**
3	KTZ Crystalline	7	360	2602	**1.0**	9163	**1.0**
4	KTZ-Soluplus® ASD	138 (±25)	180	46197 (±7985)	**5.1 (±0.9)**	101449 (±19675)	**11.1 (±2.1)**
5	KTZ-PAA ASD	389 (±28)	60	53579 (±4843)	**5.8 (±0.5)**	95380 (±12106)	**10.4 (±1.3)**

*Dissolution enhancement factor = (area under curve of sample)/ (area under curve of crystalline drug)

3.5 CONCLUSIONS

We have presented a novel approach for characterizing drug–polymer interactions in aqueous solution, using sedimentation velocity analytical ultracentrifugation (AUC) with multi-wavelength UV detection. The uniqueness and strength of the technique stem from the ability to track the sedimentation behavior of the drug, in the presence and absence of the polymer. We analyzed drug–polymer pairs that were expected to present different types of interactions in aqueous solution, based on their physicochemical properties. In each case, the sedimentation coefficient (s-value) of the drug–polymer complex increased, compared to the sedimentation of the neat drug, suggesting drug–polymer interactions.

The results reveal several advantages of using AUC to provide fundamental information on drug–polymer association patterns. Firstly, there is the possibility of teasing out and quantifying the *free* versus *interacting* fractions of drug, in the drug–polymer mixtures. Higher interacting-drug fractions are very likely to increase the duration of supersaturation. Secondly, for polymers with multi-modal sedimentation profiles, there is the possibility of quantifying the amount of drug that partitions into different polymer "populations". The latter will be particularly beneficial for characterizing functionalized polymers designed to interact with specific parts of drug molecules; an approach commonly used for controlled-release purposes. Thirdly, for poorly-soluble drugs which possess strong chromophores, the high sensitivity of ultraviolet absorption makes it possible to investigate interactions directly in aqueous buffers, without the need for organic cosolvents, or extrinsic tags and labels. Finally, the sedimentation profiles of the neat polymers in this study were unique,

indicating that AUC protocols could be refined and adopted for routine quality control testing of pharmaceutical polymers. With adequate scientific attention, analytical ultracentrifugation could be a versatile tool for physicochemical characterization of amorphous solid dispersions.

3.6 ACKNOWLEDGEMENTS

This work was supported by the William and Mildred Peters endowment fund 1701-11392-20662-UMF0003766-2108004 (to R.S.), an NSF-GOALI grant NSF-CMMI-1662039 (to R.S.), NIH grant GM120600 (to B.D.) and NSF grant NSF-ACI-1339649 (to B.D.). Supercomputer calculations were performed on Comet at the San Diego Supercomputing Center (support through NSF/XSEDE grant TG-MCB070039N to B.D.) and on Lonestar-5 at the Texas Advanced Computing Center (supported through UT grant TG457201 to B.D.). Isothermal titration calorimetry experiments were performed using an ITC-200 microcalorimeter, funded by the NIH Shared Instrumentation Grant S10-OD017982. K.K.A.E. acknowledges the Bighley Graduate Student Fellowship. We thank Beckman-Coulter, Indianapolis, for the use of an Optima AUC instrument and for supporting this research financially. We also thank Dr. Courtney Aldrich for granting access to the ITC-200 microcalorimeter, and Akash Bhattacharya and Amy Henrickson, for helpful discussions.

3.7 SUPPORTING INFORMATION

Brief Theory of Analytical ultracentrifugation

An analytical ultracentrifuge is simply a high-speed (up to 60,000 rev/min) centrifuge, with an appropriate detecting system for simultaneously recording solute migration. In sedimentation velocity AUC experiments, high centrifugal forces (up to 250000 g) cause the solute to migrate from the meniscus to the base of the AUC cell. The migration of molecules as a function of time is characterized by the sedimentation coefficient, expressed in the unit of seconds, and usually reported in Svedbergs (S), where 1 S = 10^{-13} seconds. The sedimentation coefficient (s), is governed by the famous Svedberg equation,

$$s = \frac{M(1 - \overline{v} \cdot \rho_s)}{N \cdot f} \tag{3.1}$$

where M is the molar mass, $\overline{v}$ the partial specific volume of the solute, ρ_s the density of the solvent, f is the friction coefficient and N Avogadro's number. A hydrodynamic radius, r, can be derived from the diffusion coefficient, D, measured in a velocity experiment, in combination with the Stokes-Einstein relationship:

$$f = \frac{RT}{ND} = 6\pi\eta r \tag{3.2}$$

where R is the universal gas constant, T is the temperature in Kelvin, and η is the viscosity of the solvent. Therefore:

$$r = \frac{RT}{6\pi\eta ND} \tag{3.3}$$

Additional details of the theory of Analytical Ultracentrifugation can be found in literature references[83,164–166].

Sedimentation velocity analytical ultracentrifugation raw data
NEAT POLYMERS

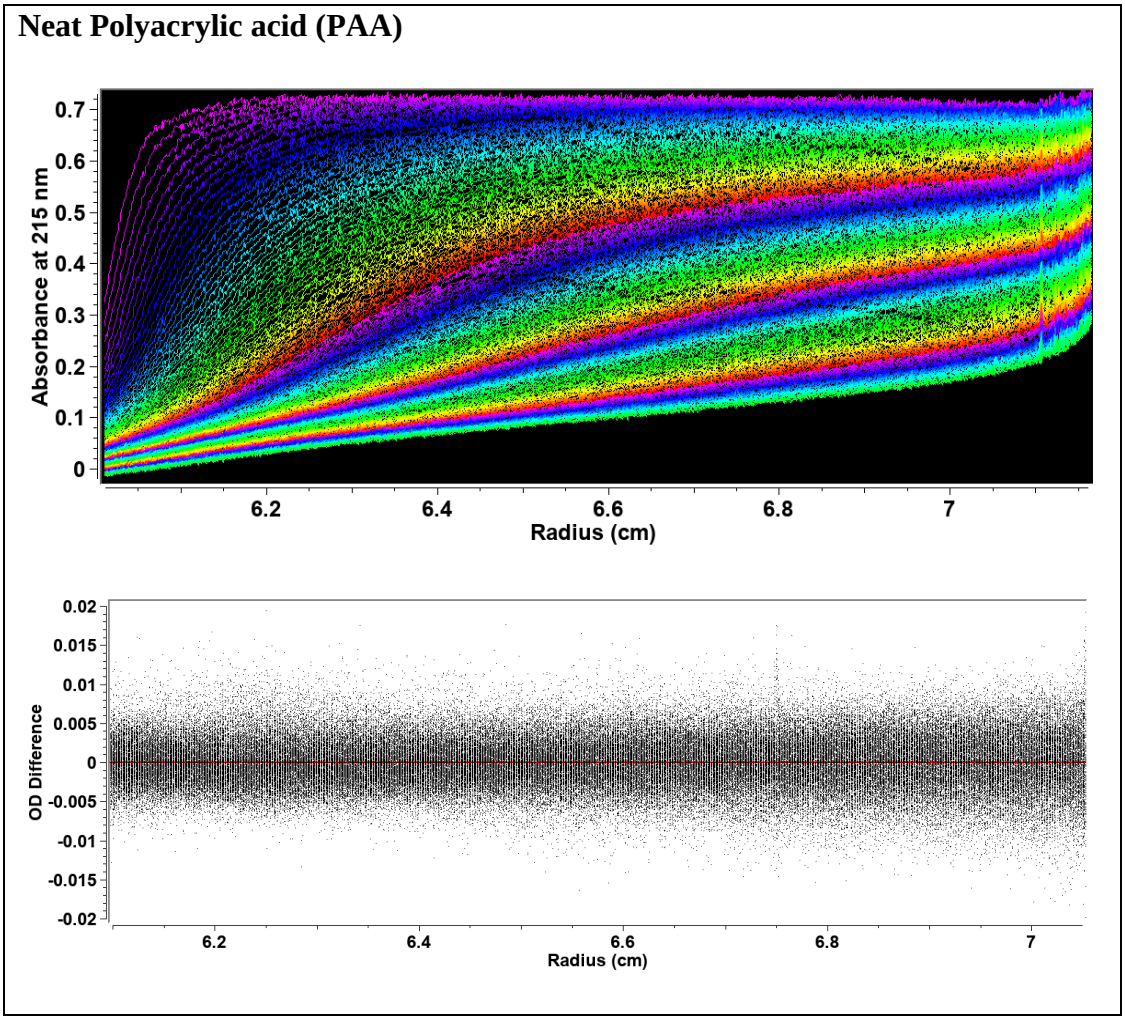

Figure S3.1. Sedimentation velocity analytical ultracentrifugation raw data for neat polyacrylic acid. Top: Experimental data. Bottom: residuals of the fit

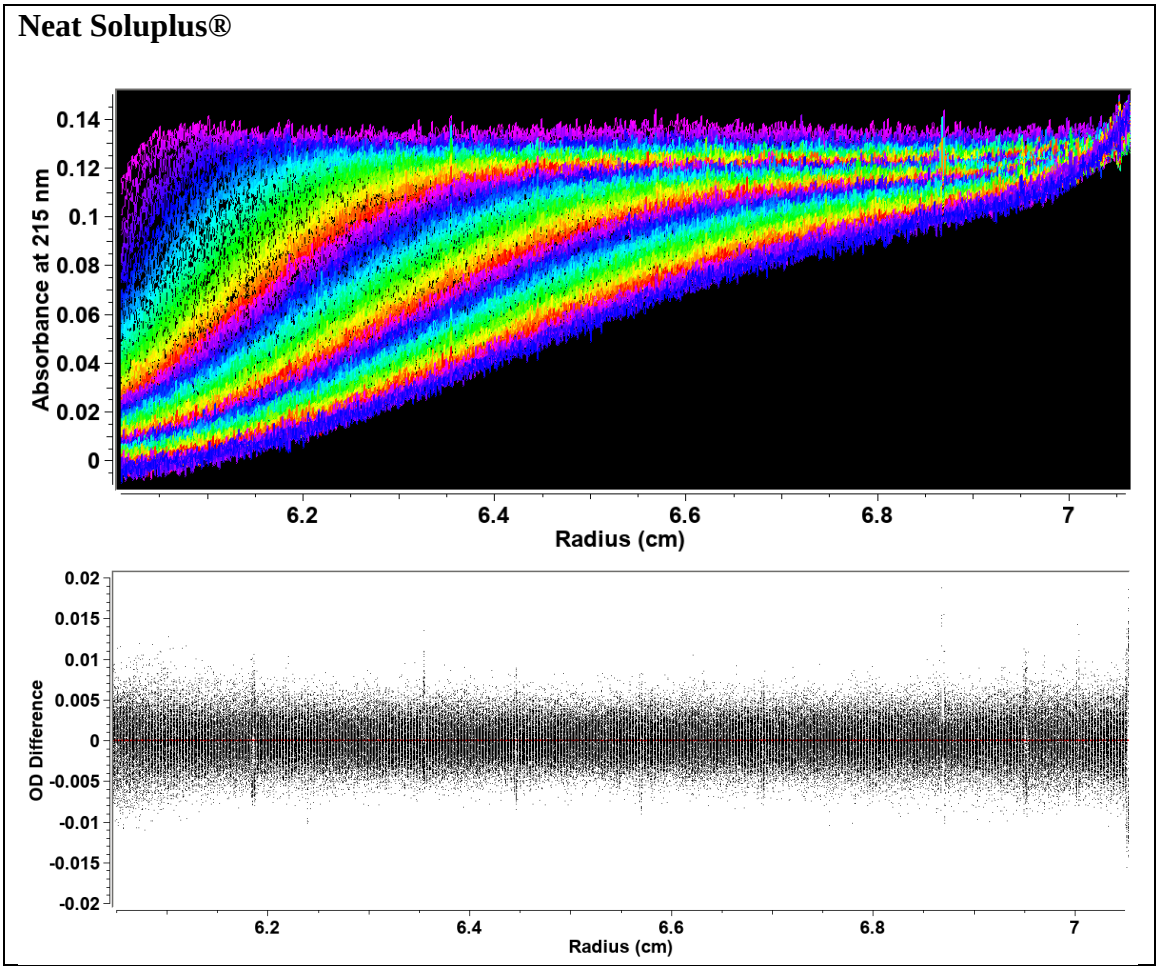

Figure S3.2. Sedimentation velocity analytical ultracentrifugation raw data for neat Soluplus®. Top: Experimental data. Bottom: residuals of the fit.

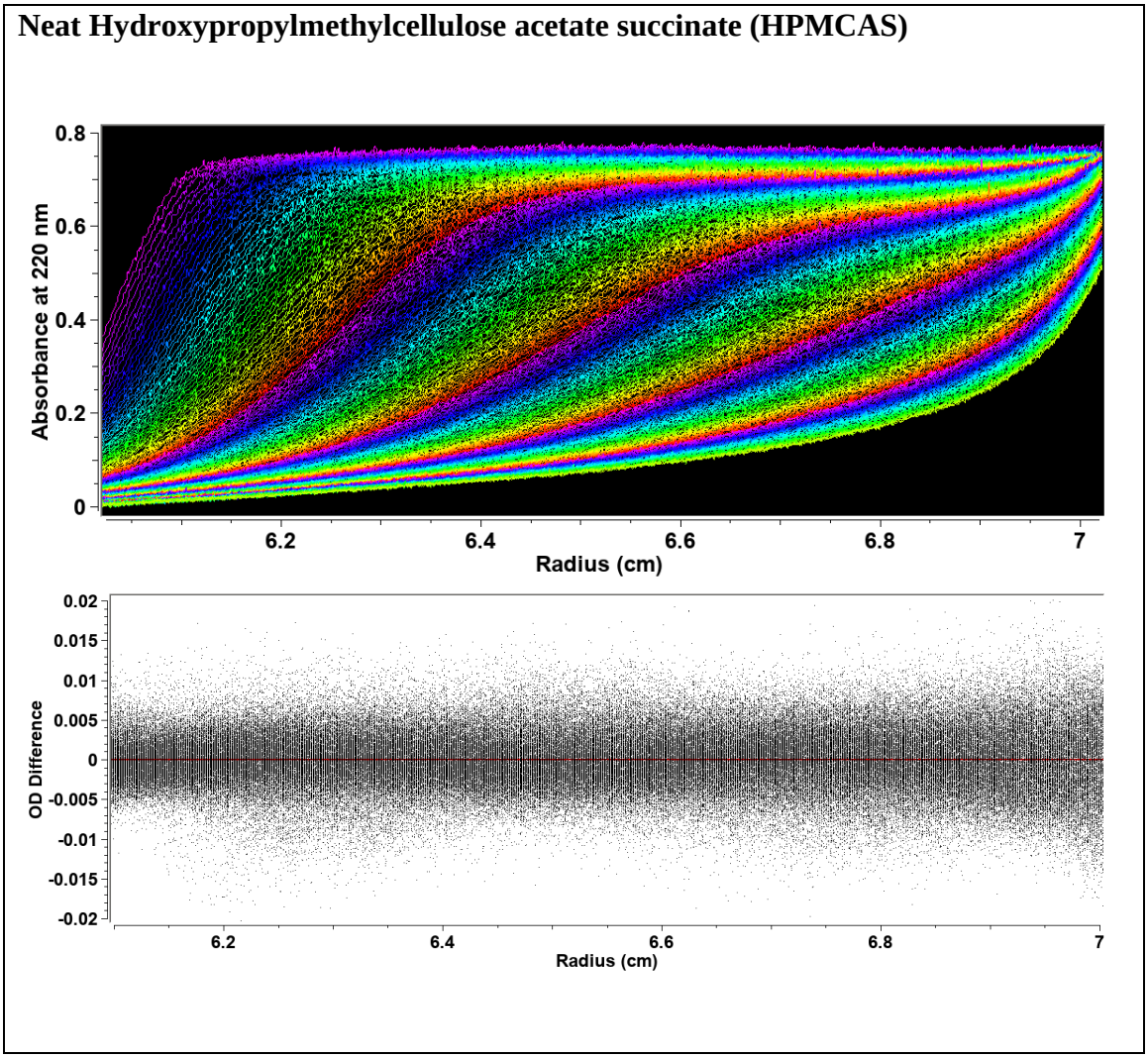

Figure S3.3. Sedimentation velocity analytical ultracentrifugation raw data for neat hydroxypropylmethylcellulose acetate succinate (HPMCAS). Top: Experimental data. Bottom: residuals of the fit.

Sedimentation velocity analytical ultracentrifugation raw data
NEAT DRUGS

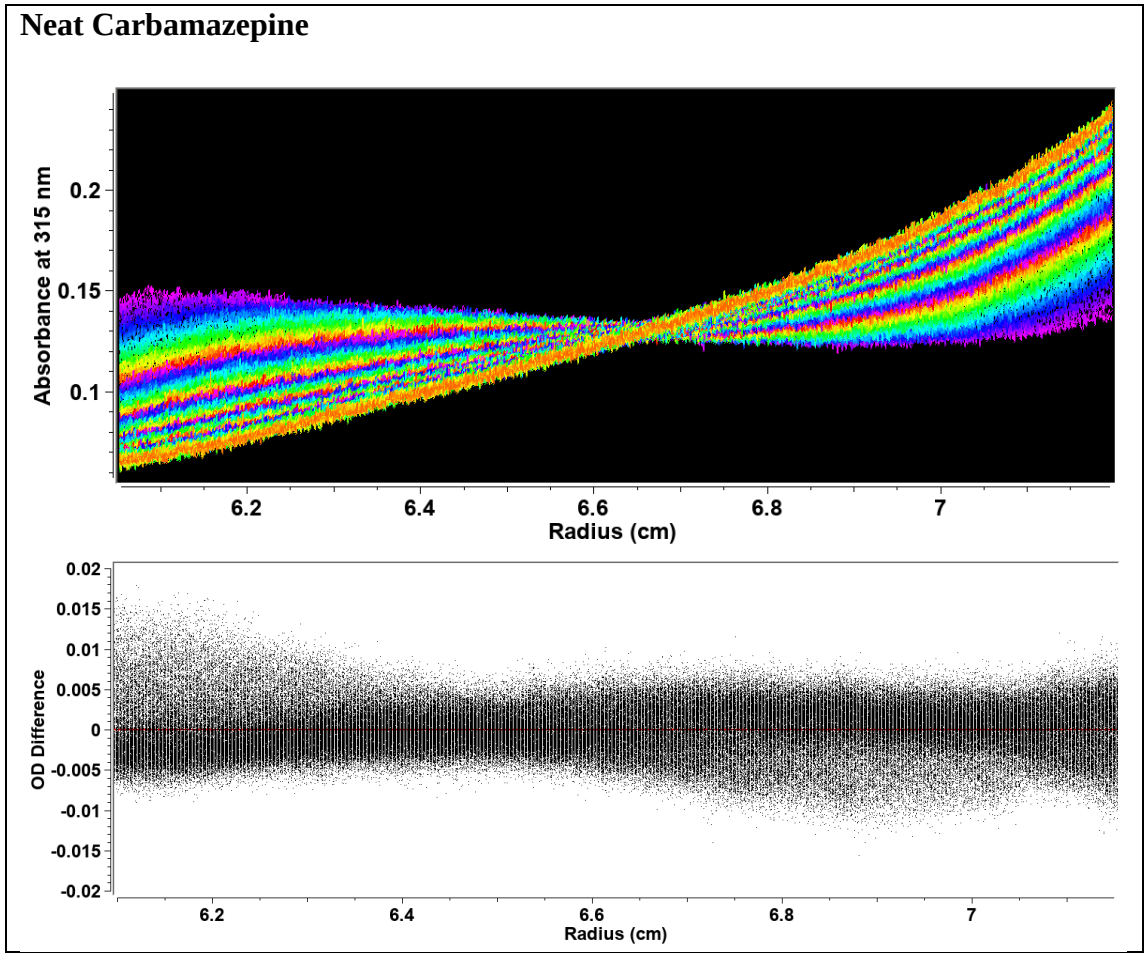

Figure S3.4. Sedimentation velocity analytical ultracentrifugation raw data for neat carbamazepine. Top: Experimental data. Bottom: residuals of the fit.

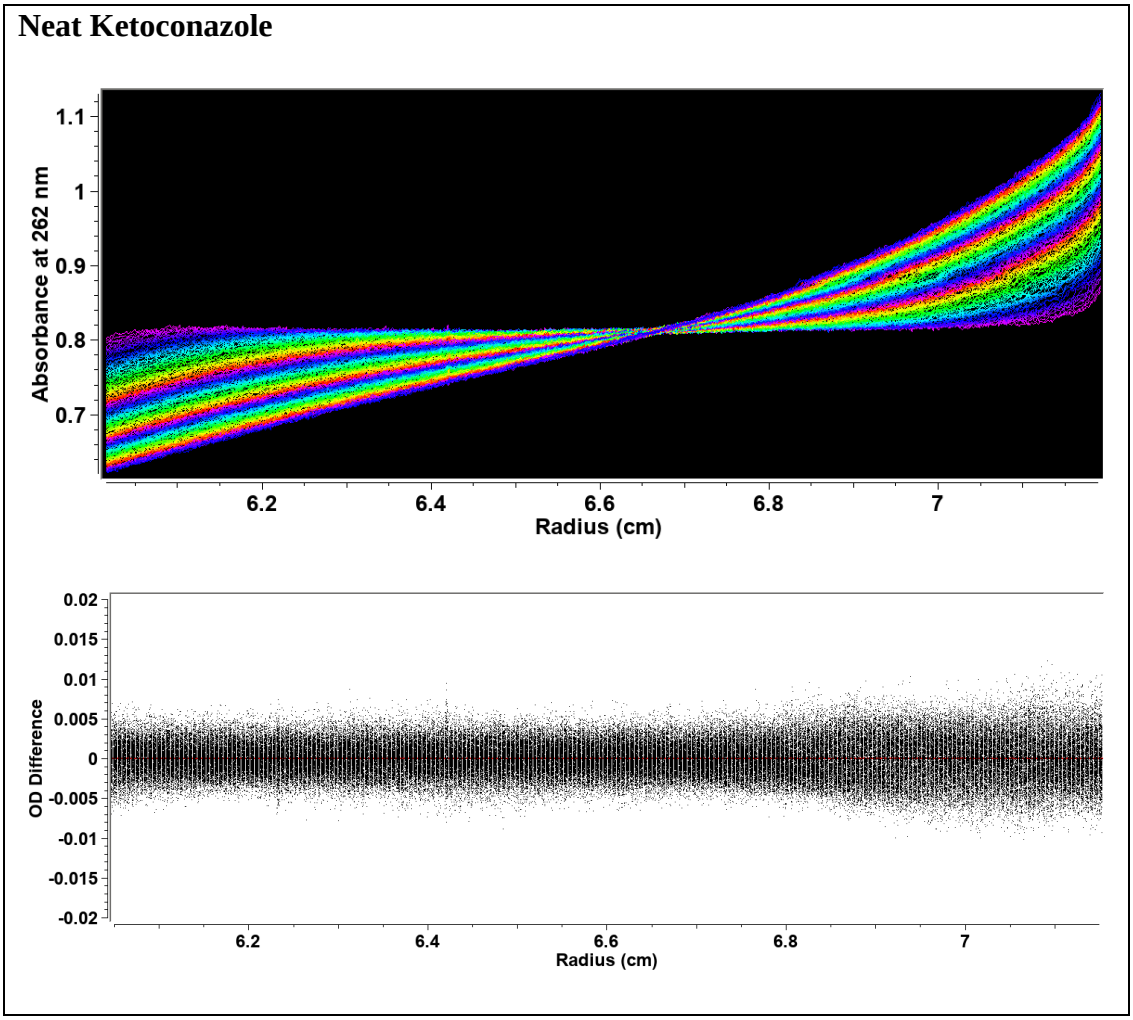

Figure S3.5. Sedimentation velocity analytical ultracentrifugation raw data for neat ketoconazole. Top: Experimental data. Bottom: residuals of the fit.

Sedimentation velocity analytical ultracentrifugation Raw Data
DRUG + POLYMER MIXTURES

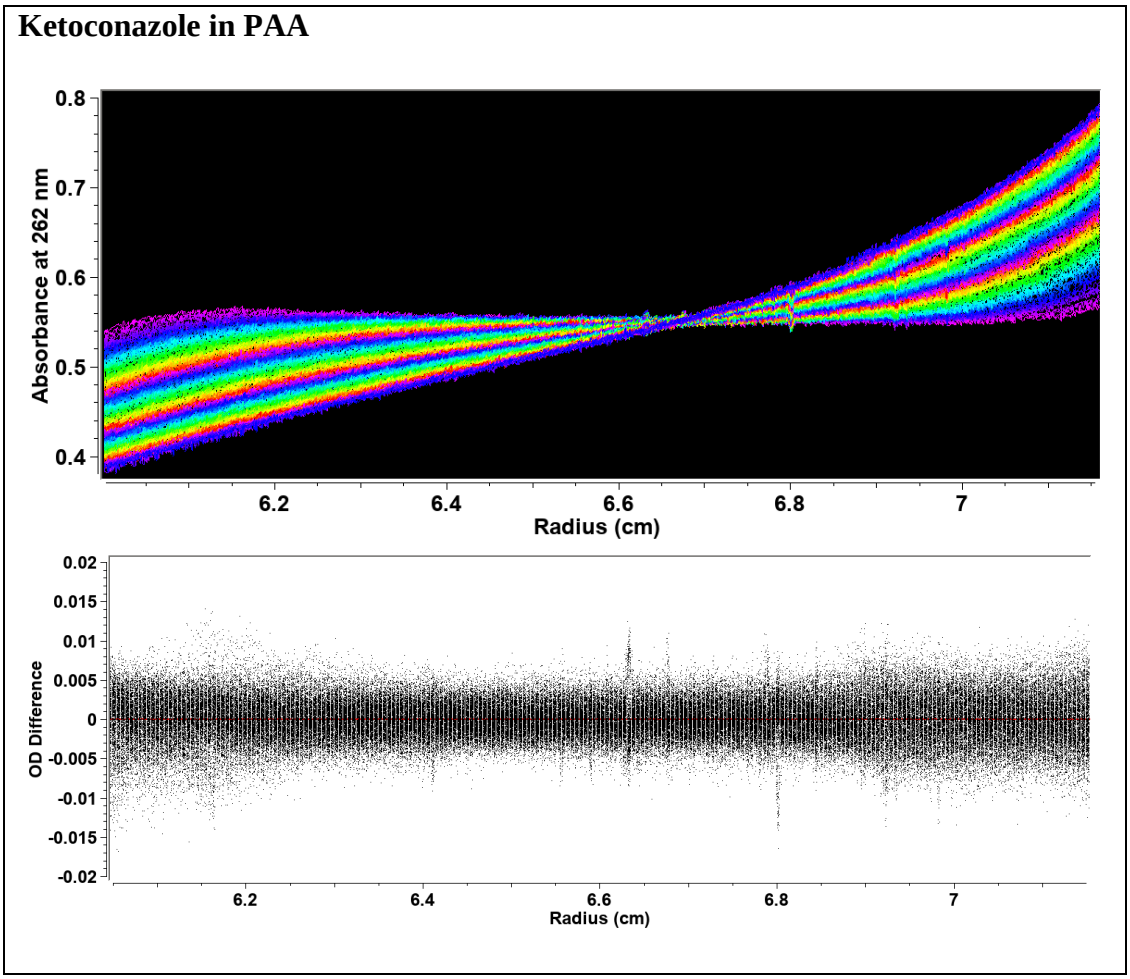

Figure S3.6. Sedimentation velocity analytical ultracentrifugation raw data for ketoconazole in polyacrylic acid. Top: Experimental data. Bottom: residuals of the fit.

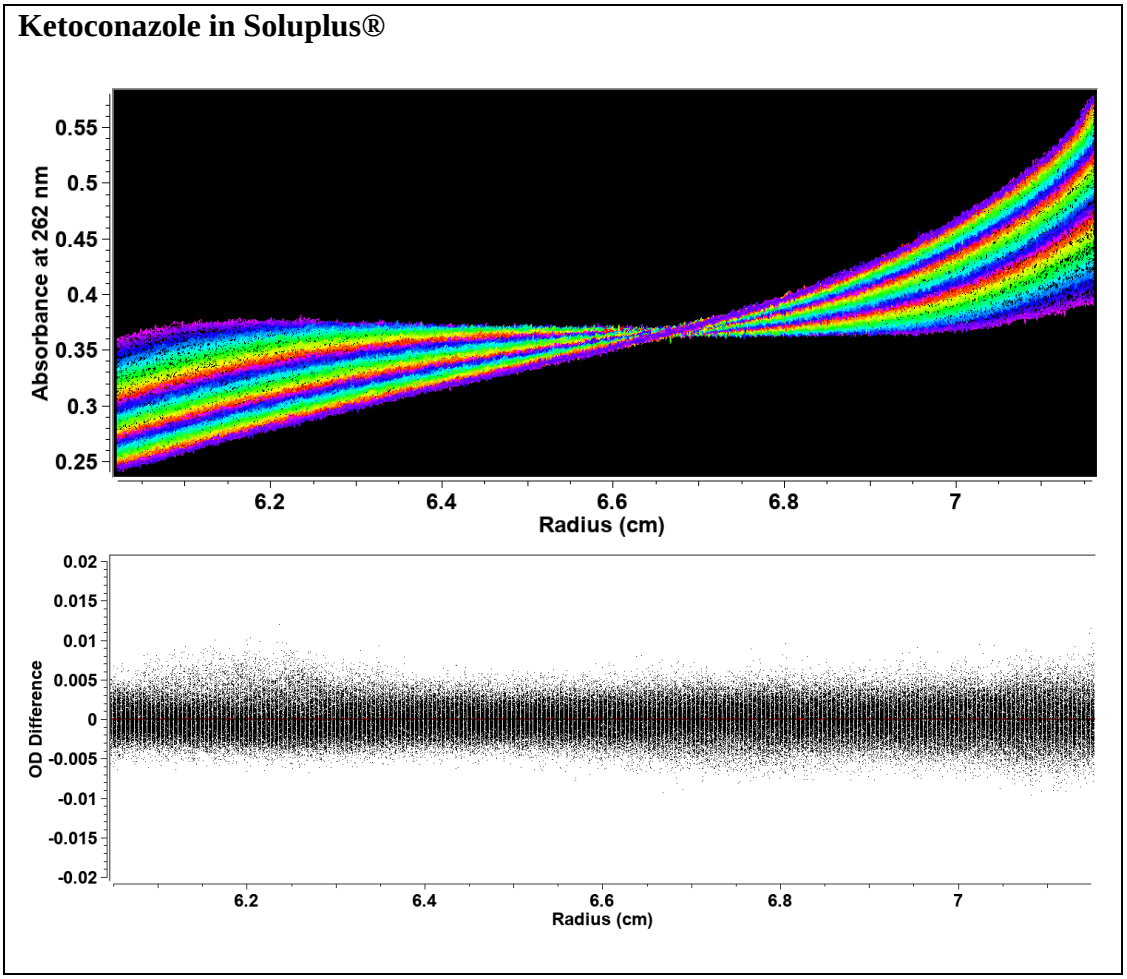

Figure S3.7. Sedimentation velocity analytical ultracentrifugation raw data for ketoconazole in Soluplus®. Top: Experimental data. Bottom: residuals of the fit.

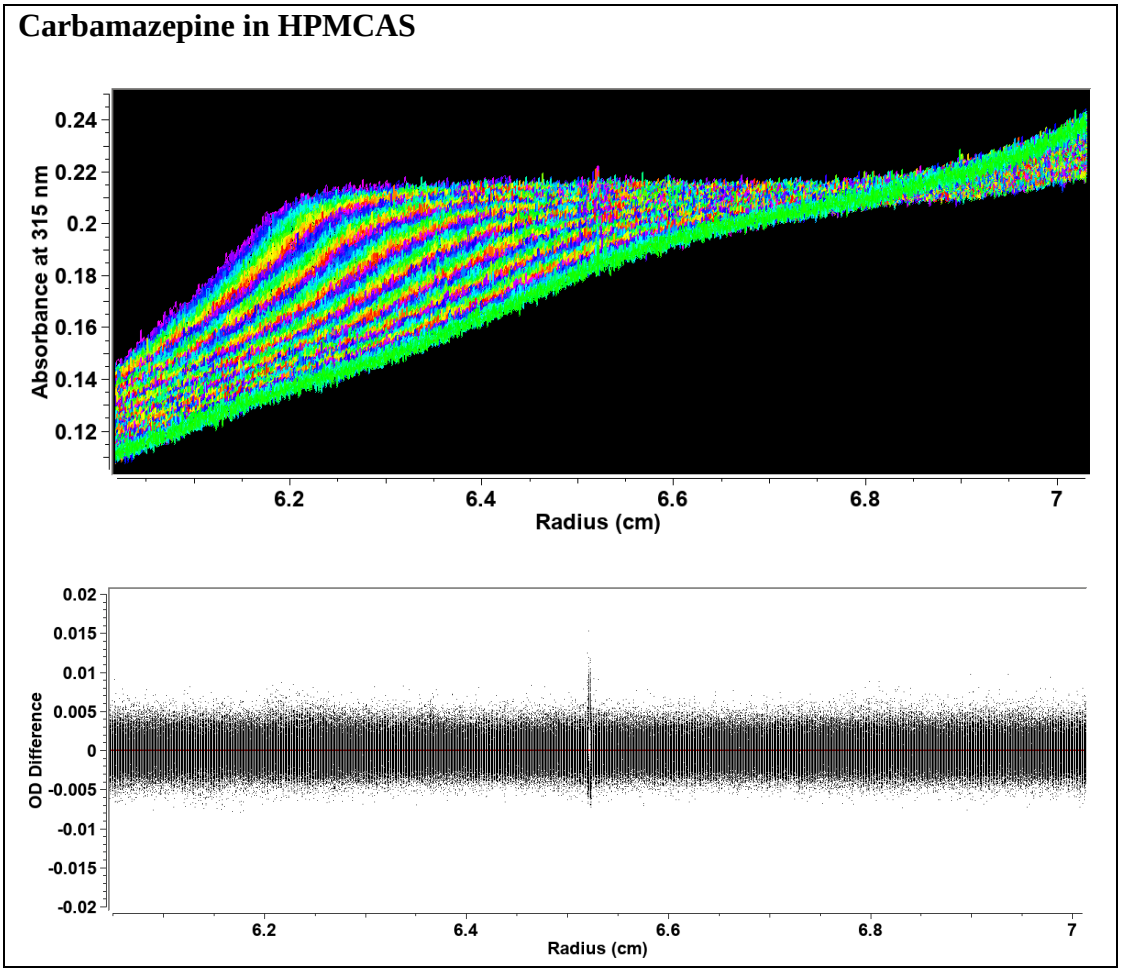

Figure S3.8. Sedimentation velocity analytical ultracentrifugation raw data for carbamazepine in HPMCAS. Top: Experimental data. Bottom: residuals of the fit.

4 Effect of Glycerol on the Order of the Mesophase Transitions of Supercooled Itraconazole.

4.1 OVERVIEW

Itraconazole, an antifungal drug, is a thermotropic liquid crystal that exhibits nematic (N) and smectic A (SmA) phases, when cooled from the melt. By means of high-resolution adiabatic scanning calorimetry (ASC), we have obtained the temperature dependence of the heat capacity as well as the enthalpy (including latent heats) of the nematic to smectic A (N-SmA) and the isotropic to nematic (I-N) phase transitions. The N-SmA transition is weakly first-order, with substantial pretransitional heat capacity increases. The critical exponent α obtained from power law fits to the heat capacity data, is 0.50 ± 0.05, suggesting that the N-SmA transition must be very close to a tricritical point. Indeed, with this character, the small molecule dopant glycerol (in binary mixtures with ITZ), causes interesting changes to the mesomorphic phase sequence and to the order of the phase transitions. With increasing glycerol content, the temperature width of the nematic phase systematically reduces, until a critical concentration, at which the nematic phase disappears, leading to a direct isotropic-smectic A (I-SmA) transition. The I-SmA transitions of the ITZ-glycerol mixtures show stronger first-order character with substantial latent heats and wide two-phase regions, when compared to the (N-SmA and I-N) transitions of neat itraconazole. The ability of glycerol to drive the ITZ transitions to stronger first-order character indicates a possible coupling of the additive concentration to the smectic order parameter, which leads to the development of highly ordered, stable smectic structures.

4.2 INTRODUCTION

Liquid crystals (LCs), have properties intermediate between crystalline solids and isotropic liquids. The rich variety of intermediate phases make LCs excellent model systems for testing general concepts of phase transitions and critical phenomena. In particular, the first-order (discontinuous) or second-order (continuous) character of the transitions, and the universality class of critical exponents have been, and are being, the object of investigations.

Two of the most common mesophases are the nematic (N) and the smectic-A (SmA) phases[167]. In the nematic phase, rod-like molecules align parallel to each other, with their long axes all pointing approximately in the same direction. In the smectic phase, the molecules maintain the orientational order and are further organized into layers.

The nematic to smectic A (N-SmA) transition is one of the most extensively studied. Since the order in the SmA phase can be described in terms of a two-component complex order parameter, the N-SmA transition can be expected to be in the 3D–XY universality class[36,37]. Experiments have however shown non-universal critical behavior in some systems. According to the molecular field theory of McMillan and Kobayashi[31,38], as well as by de Gennes[36,37], the N-SmA transition could be either first- or second-order in nature, depending on the nematic range (i.e. the temperature width of the nematic phase). A narrow nematic range indicates a strong coupling between the N and SmA order parameters, resulting in a first-order N-SmA transition. Conversely, a wide nematic range

(weak coupling) gives a continuous transition. Halperin, Lubensky and Ma, via their HLM theory, however suggested that the coupling between the director fluctuations and the smectic order parameter makes the N-SmA transition always weakly first-order[168]. The isotropic-nematic (I-N) transition, usually described in terms of the Landau-de Gennes mean-field theory, or based on the Maier-Saupe theory, should be weakly first order[36,37].

Due to the wide range of complex phases that can be encountered within LC systems, as well as the different theoretical predictions about the nature of the mesomorphic transitions, experimental determination of the order of phase transitions, provides a pathway to understand the behavior of these systems. To establish the order of a phase transition, the true latent heat (or absence of latent heat) must be measured. With differential scanning calorimetry (DSC), the most popular calorimetric technique, it is possible to locate the different LC phases with sufficiently wide temperature ranges, and to qualitatively characterize the magnitude of the thermal features associated with the transitions. DSC is however not ideally suited for confirming the order of phase transitions. This is because the latent heat and the pretransitional increase in the specific heat near a phase transition are lumped together into one thermal event (peak)[33]. Distinguishing between true latent heats and pretransitional (fluctuation induced) enthalpy variations is almost impossible, thereby making it difficult to distinguish between first- and second-order transitions[33].

Adiabatic Scanning Calorimetry (ASC), by maintaining thermal equilibrium, continuously measures the enthalpy (H) and the heat capacity (C_p) as a function of temperature.

Continuous determination of $H(T)$, serves as a unique approach for confirming the order of phase transitions. An enthalpy 'jump', indicative of latent heat (ΔH_L), is a characteristic feature of a first-order (discontinuous) transition. Second-order (continuous) transitions show no discontinuities in the enthalpy ($\Delta H_L = 0$)[20,33]. However, the heat capacity, which is the temperature derivative of the enthalpy [$(C_p = (\partial H/\partial T)_P$], exhibits a discontinuous jump (mean-field behavior), or a divergence (critical fluctuation behavior). Information on the pre-transitional heat capacity is also needed to analyze relevant thermal aspects of critical fluctuations[33]. With ASC, the critical behavior of different LC classes, have been studied.

Compounds (having or lacking liquid crystalline order) are added to LCs, forming binary mixtures, as a means of either (i) extending the working ranges of the mesophase transitions or (ii) exploring unusual phase sequences. It has been observed that non-mesogenic solutes broaden the I-N transition temperature leading to the subsequent formation of two-phase regions[34]. As an example, the I-N transition temperature of 5CB (a compound of the alkylcyanobiphenyl homologous series) increases, when doped with molecularly rigid carboxylic acids, but decreases when the carboxylic acid dopants have flexible aliphatic chains[169]. The transition temperatures shift without any effects on the magnitude of the total enthalpy change of the I-N transition[169]. In the case of N-SmA transitions, non-mesogenic solutes can cause a change in the order of the transition (from second- to first-order), by coupling to the order paramters[170]. Conversely, nanoparticles dispersed in liquid crystals can induce a decoupling mechanism of the order parameters, leading to a change

in the critical behavior of the bulk material[171]. The unusual phase sequences that result from LC mixtures, find practical use in LC devices for display and telecommunication applications[172–174].

Itraconazole (ITZ), a pharmaceutical compound indicated for treatment of fungal infections, is a known thermotropic LC[175]. ITZ exhibits nematic and smectic phases, when cooled from the isotropic melt, with a nematic range of ~16 °C. Itraconazole is a rather unusual glassy LC, being one of the few compounds for which the smectic order can be eliminated by cooling from the isotropic phase with an appropriate rate[176]. Also, effects of addition of polymers on the smectic order of ITZ have been reported, for three different classes of polymers[177]. The polymer either disrupts the smectic order, resulting in a uniform isotropic mixture, or remains separated from the smectic domains[177]. The critical behavior of the mesophase transitions in ITZ, however, has not been studied. There is also a general interest, to know how other pharmaceutical additives affect the mesophase transitions in ITZ.

The goal of this work is therefore, to investigate the effect of glycerol, a small-molecule plasticizer[72], on the phase transitions of itraconazole. In the pharmaceutical sciences, glycerol is of interest, because it is sometimes incorporated into amorphous formulations, to aid processing[51]. Meanwhile, in the liquid crystal literature, glycerol is a typical protic solvent, used to supply mobility to amphiphilic molecules, in lyotropic LC systems[178,179]. Furthermore, when thermotropic mesogens were functionalized with glycerol (propane-

2,3-diol attachments to the mesogen's aromatic core), novel thermotropic mesophases were obtained[180]. Thus, glycerol has the potential to induce unusual effects in the mesomorphic sequence of ITZ. We have investigated the thermal behavior in itraconazole, with the glycerol concentration ranging from 1 to 40% w/w. DSC studies were conducted with the goal of generating the phase diagram. We have also performed a detailed analysis of the critical behavior of the N-SmA transition of ITZ and investigated the effect of glycerol on the order of the mesophase transitions, using adiabatic scanning calorimetry.

4.3 EXPERIMENTAL METHODS

4.3.1 Materials

Itraconazole (Bepharm Limited, Shanghai, China; purity ~98%) and glycerol (Sigma Aldrich, USA, purity ≥99.5%) were used as received. All other reagents and chemicals were of analytical grade and purchased from Sigma Aldrich.

4.3.2 Sample preparation

Amorphous itraconazole (glass without smectic order) was prepared by melting the crystalline drug at 180 °C and rapidly cooling by dipping the melt in liquid nitrogen. To prepare ITZ-glycerol mixtures, crystalline ITZ was dissolved in dichloromethane at 50 °C with sonication, glycerol was dissolved in methanol and the two solutions were mixed. The solvent was rapidly evaporated at 50 °C under reduced pressure, in a rotary evaporator (IKA-HB10 digital system, Werke GmbH and Co. Germany) at 250 rpm, and lightly ground using a mortar and pestle, to obtain a free-flowing powder. The powder samples

were further dried at room temperature under vacuum for 24 hours, to remove any residual solvent, and kept in desiccators containing anhydrous calcium sulfate at -20 °C, until further use.

4.3.3 Differential scanning calorimetry (DSC)

A differential scanning calorimeter (Q2000, TA Instruments, New Castle, DE) equipped with a refrigerated cooling accessory unit was used. The instrument was calibrated (temperature, heat capacity and enthalpy) with tin, indium, and sapphire. An accurately weighed sample was hermetically sealed in an aluminum pan (T-zero®, TA instruments) and subjected to a modulated temperature program, under dry nitrogen gas purge (50 mL/min). The temperature modulation used was ±0.212 °C every 40 s, with an underlying heating rate of 2 °C/min.

The sample was heated from room temperature (~20 °C) to 180 °C, held for ~1 minute to ensure complete melting, cooled back to room temperature and reheated to the melting temperature. Both the heating and cooling rates were 2 °C/min.

DSC data analysis was performed with Universal Analysis® software (TA Instruments). In the text, glass transition temperatures (T_g) are reported as the midpoint of the baseline shift (step-change) in the reversing heat flow signals. Phase transition temperatures are evaluated from the peak positions of the endothermic or exothermic reversing heat flow

signals. Enthalpy change values are the peak areas of the reversing heat flow endo or exotherms.

4.3.4 Adiabatic scanning calorimetry (ASC)

High-resolution enthalpy and heat capacity data were obtained with a novel Peltier-element-based implementation of the adiabatic scanning calorimetry concept (pASC). The modes of operation are described in detail elsewhere[181,182]. An accurately weighed sample (~50 mg) was placed in a 120 µl stainless steel medium-pressure DSC crucible (Mettler-Toledo GmbH, Switzerland). The sample was heated from room temperature to ~190 °C, held for ~1 minute to ensure complete melting, and rapidly cooled back to room temperature. The resulting glass was again reheated rapidly to ~60 °C, after which a very slow average scan rate (on the order of 50 mK/min; details in the text) was imposed while the ASC data were collected in the 60-100 °C region. This sequence was necessary (i) to ensure the samples did not crystallize during the run, and (ii) to ensure a standardized thermal history for the samples.

4.4 BRIEF THEORY OF ADIABATIC SCANNING CALORIMETRY

Adiabatic scanning calorimetry measures with high resolution, the heat capacity and enthalpy near critical points in soft matter systems (e.g. liquid mixtures and liquid crystals)[167,183]. A constant, known heating or cooling power is applied to the sample cell (differently from imposing a constant rate, as done in DSC-type calorimeters) with an adiabatic shield that follows the temperature evolution of the sample cell. During a run, the

sample temperature $T(t)$ is recorded as a function of time t, and the heat capacity $C_p(T)$ as a function of temperature is calculated *via* the ratio of the known constant power P and the changing temperature rate $\dot{T} = \mathrm{d}T/\mathrm{d}t$:

$$C_p(T) = \frac{P}{\dot{T}} \tag{4.1}$$

This leads to a continuous heat capacity curve. The heat capacity of the addenda $C_{add}(T)$, obtained in a separate calibration experiment, is subtracted from $C_p(T)$ in order to obtain the heat capacity of the bare sample. The result is divided by the sample mass to arrive at the specific heat capacity of the sample. The same $T(t)$ data and the known constant power P directly result in the continuous enthalpy curve $H(T)$, since

$$H(T) - H(T_0) = \int_{t_0}^{t(T)} P dt = P(t - t_0), \tag{4.2}$$

where $H(T_0)$ is the enthalpy of the system at the starting time t_0 of the experiment. The constant power results in the simple solution of the integral. The enthalpy of the sample is obtained after subtraction of the enthalpy of the addenda obtained from the calibration experiment. Further division by the sample mass results in the specific enthalpy.

In an ASC run, the power P is kept constant in equation (4.1) and the resulting *changing* rate $\dot{T}$ is measured. This is exactly the opposite of what is done in DSC; in DSC, a predetermined constant rate (usually large for resolution reasons) is applied, and the *changing* power $P(t)$ is measured (differentially). Also, in ASC, at a transition, the rate reduces almost effectively to zero, which ensures thermal and thermodynamic equilibrium. In DSC however, it becomes more and more challenging to deliver (at the right

temperature) the strongly increasing power needed to maintain the imposed temperature rate. This results in rounding off and overshooting phenomena.

An essential requirement of high-resolution ASC operating in a (slow) heating mode is the equality (mK or better) of the temperatures of the adiabatic shield and of the sample holder in very weak thermal contact with this adiabatic shield. The temperature of the adiabatic shield is maintained at the temperature of the sample holder by means of a proportional-integrating feedback loop that controls electrical heating of the shield. In cooling mode, a constant (preset) temperature difference between sample and shield must be maintained within the same stability limits. To achieve this, highly sensitive thermistors (placed on the sample holder and shield), requiring careful and extensive calibrations, have been used in the past. However, differences in the temperature coefficients of the thermistors, made measurements over large temperature ranges very complicated. In the recent Peltier-element-based implementation, pASC, these problems are completely eliminated[181,182]. This is achieved by inserting a highly sensitive semi-conductor-material-based Peltier element, to detect (and next nullify) the temperature difference between sample and shield.

4.5 RESULTS AND DISCUSSION

4.5.1 General information on itraconazole

Itraconazole (ITZ) is a crystalline powder, that melts at 168 °C[175,177]. When cooled from the melt, the isotropic (I) liquid transforms, first to a nematic (N) phase, and then to a smectic A (SmA) phase, before vitrifying. The LC transitions are reversible upon

reheating. The isotropic melt is light yellow and transparent. However, a visible color-change (white, opaque) occurs at the I-N transition temperature, which is retained upon vitrification. Phase assignments based on differential scanning calorimetry and X-ray diffractometry, have been reported in the literature[175,177,184,185].

4.5.2 Effect of glycerol on the mesophase transitions

Glycerol was incorporated into itraconazole, *via* the solvent evaporation technique, commonly used to make amorphous solid dispersions. Homogeneous itraconazole-glycerol mixtures were prepared up to a glycerol content of 40% w/w, beyond which the material became sticky and visibly phase-separated. The binary mixtures with glycerol content <30% w/w were free-flowing powders.

To systematically characterize the phase transitions, under a "standardized" thermal history, each solvent-evaporated formulation was first melted *in situ*, in the DSC pan, cooled to room temperature at ~2 °C/min, and reheated at the same rate. Representative reheating scans of select compositions are shown in **Figure 4.1**, with the corresponding transition temperatures and enthalpies listed in **Table 4.1**. A phase diagram constructed based on the DSC results, is presented in **Figure 4.2**.

The mesophase transition temperatures for neat itraconazole, are pointed out in the topmost scan of **Figure 4.1a**. The glass (T_g), nematic-to-smectic A (T_{N-SmA}), and isotropic-to-nematic (T_{I-N}) transitions, occur at ~ 59, 74 and 90 °C respectively. These transition

temperature and enthalpy change values (**Table 4.1**, 0% glycerol) are in agreement with the literature values[175,184,185].

As the glycerol content increases from 0 to 2% w/w, the temperature of the nematic-to-smectic A transition (T_{N-SmA} ≈74 °C, for neat itraconazole) does not change appreciably, indicating that the smectic state is not destabilized by the additive. The isotropic-to-nematic transition temperature (T_{I-N} ≈90 °C, in neat itraconazole) however, systematically shifts to lower values. At glycerol concentrations ≥ 5% w/w, the nematic phase completely disappears, indicating a direct isotropic → smectic A (I-SmA) transition. The I-SmA transition is also temperature-invariant, with increasing glycerol concentration (**Figure 4.1b; Table 4.1**, 5-40% glycerol).

The enthalpy changes of the mesophase transitions are also affected by the additive. As the glycerol content increases from 0% to 2% w/w, the enthalpy change of the nematic-to-smectic transition (ΔH_{N-SmA}) increases, whilst that of the nematic-to-isotropic transition (ΔH_{I-N}) decreases (**Table 4.1**). The I-SmA transition endotherms (observed in compositions with ≥ 5% w/w glycerol), are however noticeably pronounced. Of note, the ΔH_{I-SmA} at any composition, is much higher, than the sum of ΔH_{I-N} and ΔH_{N-SmA} (observed at glycerol concentrations ≤ 2% w/w).

Generally, condensation from the isotropic to the nematic phase (I-N) requires calamitic molecules to reorient with their molecular axes approximately parallel to the nematic

director. This typically manifests as a larger change in enthalpy, than transition from the nematic to the smectic A phase (N-SmA), which only requires longitudinal displacement of the molecules to form layers (in fact only weak density modulations along the director)[20,33]. Direct transition from the isotropic to the smectic A phase (I-SmA), on the other hand, typically goes along with a pronounced enthalpy change[33,39]. This is because, in order to complete the I-SmA transition, a significant increase in orientational as well as translational order must occur almost simultaneously.

Often, when a mesogenic material possesses intermediate phases, the individual enthalpy changes of the low-ordered phases sum up to the total enthalpy change for the higher ordered phase[39]. Thus, the enthalpy change of the I-N and N-SmA phases are expected to sum up to the total enthalpy change of the I-SmA transition. However, as shown in **Table 4.1**, the ΔH_{I-SmA} values are substantially higher. This unusual finding indicates that the ITZ molecules become exceptionally well-ordered, with 5-10% glycerol being the most favorable composition.

4.5.3 Effect of glycerol on the glass transition temperature

The glass transition temperature (T_g) decreases only slightly, as the glycerol content increases (**Figure 4.1**; **Figure 4.2**; **Table 4.1**). Glycerol, due to its low T_g (~ -83 °C), is usually a potent plasticizer of amorphous pharmaceuticals. To assess the extent of plasticization, the experimentally determined T_g values, are compared with the values

predicted by the Gordon-Taylor (GT) additivity rule for binary mixtures[64,74,186,187] (equation (4.3)).

$$T_{gx} = \frac{T_{g1}w_1 + K(T_{g2}w_2)}{w_1 + Kw_2} \tag{4.3}$$

The subscripts 1 and 2 represent the components itraconazole and glycerol respectively, and w is the weight fraction of each component. K is a constant, calculated with the Simha–Boyer rule[74]

$$K \cong \frac{\rho_1 T_{g1}}{\rho_2 T_{g2}} \tag{4.4}$$

where ρ_1 and ρ_2 are the densities of itraconazole (1.4 g/cm^3) and glycerol (1.26 g/cm^3) respectively.

The GT relation assumes perfect volume additivity at T_g and no interactions between the two components[187]. As shown in **Figure 4.3**, a consistent positive deviation from the trend predicted by the GT equation, is observed for mixtures, indicating a reduction in the net free volume and hence, a more efficient packing of the itraconazole molecules.[188]

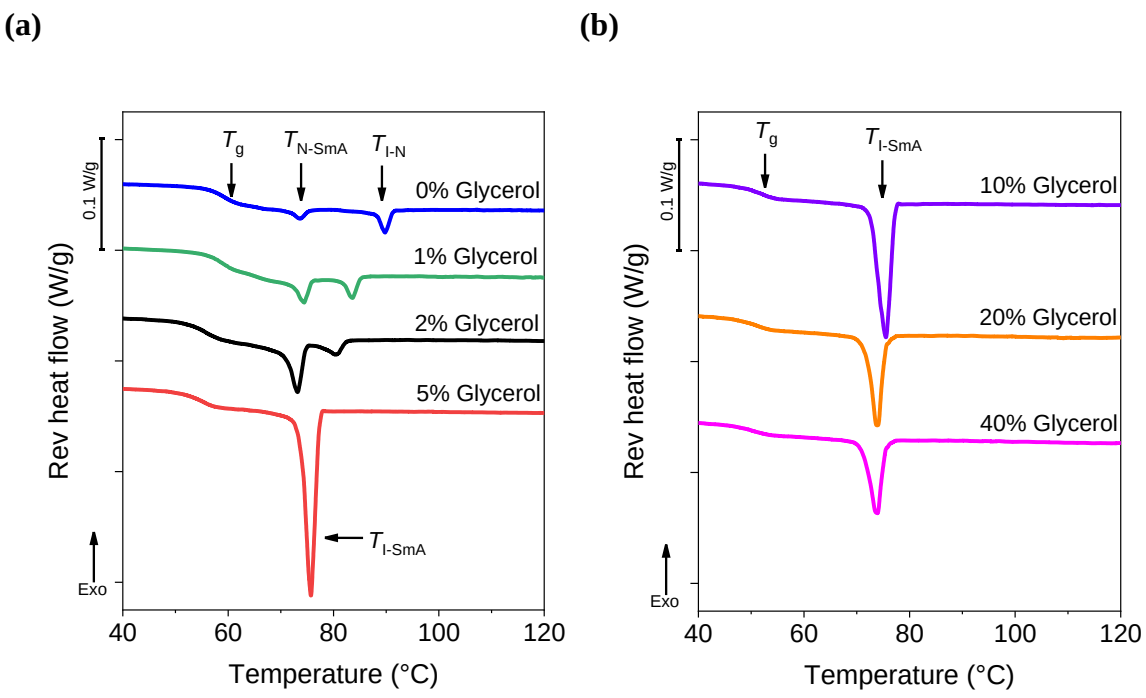

Figure 4.1. DSC heating curves of itraconazole-glycerol binary mixtures of different compositions. The glycerol content (w/w) is given above each curve. (a) 0 to 5% glycerol, and (b) 10 to 40% glycerol. Each sample was heated from room temperature (~20 °C) to 180 °C, held for 1 minute, and cooled back to room temperature. The sample was then reheated to 180 °C. Both the heating and cooling rates were 2 °C/min. Only the final heating curves over the temperature range of interest, are shown.

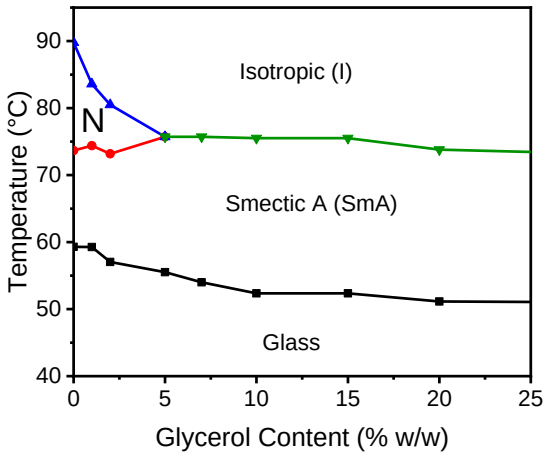

Figure 4.2. Phase diagram generated from the DSC results (**Figure 4.1**;**Table 4.1**). Solid lines are drawn to assist in assessing the trends. N=nematic phase.

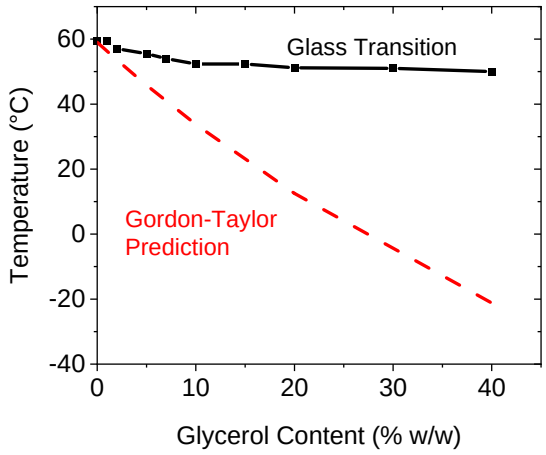

Figure 4.3. Experimental glass transition temperatures (T_g) of itraconazole-glycerol binary mixtures, compared with the values predicted using the Gordon-Taylor equation.

Table 4.1. Transition temperatures (T, °C) and associated enthalpies (ΔH, J/g) determined from the reversible heat flow signals of modulated DSC reheating scans (at 2 °C/min). Each value is an average of three replicate runs with standard deviations in parentheses. The McMillan ratios (T_{N-SmA}/T_{I-N}) are included for the samples with 0 to 2% glycerol content.

Glycerol Content (w/w)	**Isotropic – Nematic**		**Nematic– Smectic A**		**Isotropic – Smectic A**		**Smectic A – Glass**	$\frac{T_{N-SmA}}{T_{I-N}}$
	T, °C	ΔH, J/g	T, °C	ΔH, J/g	T, °C	ΔH, J/g	T_g, °C	
0%	89.8 (0.1)	1.6 (0.2)	73.7 (0.3)	0.6 (0.1)	--	--	59.3 (0.6)	0.955
1%	83.7 (0.0)	1.2 (0.1)	74.4 (0.1)	1.9 (0.2)	--	--	59.3 (0.5)	0.973
2%	80.0 (1.7)	0.9 (0.3)	73.2 (0.1)	3.7 (0.2)	--	--	55.6 (0.8)	0.980
5%	--	--	--	--	75.3 (0.4)	11.7 (1.3)	55.5 (0.5)	--
7%	--	--	--	--	75.9 (0.0)	9.8 (0.5)	55.2 (2.9)	--
10%	--	--	--	--	75.5 (0.5)	10.1 (1.1)	52.4 (0.9)	--
20%	--	--	--	--	73.1 (0.7)	8.0 (0.8)	51.2 (0.2)	--
30%	--	--	--	--	73.1 (0.6)	7.8 (0.3)	51.5 (0.2)	--
40%	--	--	--	--	73.9 (0.2)	5.7 (0.2)	50.0 (0.7)	--

4.5.4 The order of the transitions

In the context of this investigation, three types of phase transitions are relevant: the isotropic-nematic (I-N), the nematic-smectic A (N-SmA) and the isotropic-smectic A (I-SmA). For purely geometrical reasons (regarding molecular orientation), the I-N transition must be first-order (with the possible exception at a single critical point induced by an

external parameter)[37]. On the same grounds (because orientational order is also present in the SmA phase), the I-SmA transition should be first-order.

There are no obvious reasons, however, for the N-SmA transition to be first- or second-order. Extensive calorimetric investigations of the N-SmA transition have been carried out[33]. It has been found that the temperature range of the nematic phase (i.e. the temperature width between the I-N and N-SmA transitions) plays an important role. Compounds with narrow nematic ranges are more likely to exhibit first-order N-SmA transitions, while second-order transitions are encountered for compounds with wide nematic ranges[31,36–38]. This behavior is often qualitatively characterized by the McMillan phenomenological parameter, $r = T_{SmA-N}/T_{N-I}$ (ratio of absolute temperatures)[31]. According to McMillan's model the N-SmA transition is first-order for $r > 0.87$, but second-order for values below 0.87. Experimentally, first-order transitions have only been observed for McMillan ratios close to 1, typically above 0.95[33,41]. From the variation in McMillan parameter and differences in total transition enthalpies (ΔH in **Table 4.1**), there is some indication for differences in the order of the transition for the itraconazole samples having different glycerol contents. Therefore, in the following sections, we analyze Adiabatic Scanning Calorimetry (ASC) data to establish the nature of the N-SmA transition of the itraconazole samples with different glycerol contents.

4.5.5 ASC results for neat itraconazole

Figure 4.4a shows an overview of the temperature dependence of the specific heat capacity C_p and the specific enthalpy H from well below the smectic A (SmA) to well into the isotropic (I) phase. For the sake of clear contrast, a large, linearly temperature-dependent enthalpy background has been subtracted from the measured enthalpy values. Indeed, for a constant heat capacity, the enthalpy increase is linearly dependent on temperature. Subtracting such (often irrelevant) contribution allows a more detailed study of fine phase transition effects. Furthermore, a careful inspection of the enthalpy and heat capacity, as well as higher order derivatives, allows the temperature width of the (impurity induced) two-phase region to be located, and the true latent heats to be separated from (often substantial) pretransitional effects. This treatment was applied to all the samples, and the transition temperatures and latent heats are summarized in **Table 4.2**. The transition temperatures and total enthalpy changes (ΔH) measured by adiabatic scanning calorimetry, for all the samples (**Table 4.2**) are in agreement with the corresponding values obtained *via* DSC (**Table 4.1**).

We first describe the N-SmA transition for neat itraconazole. In **Figure 4.4**b, the temperature scale of the $H(T)$ data is expanded (within 2 °C temperature range), to show the detailed behavior very close to the N-SmA transition. A linear change in enthalpy with an almost constant effective heat capacity (constant slope) can be identified between the two dashed vertical lines, over a temperature interval of 0.15 ± 0.03 °C. This allows a small but finite latent heat of 0.095 ± 0.010 J/g, to be identified, indicating that the N-SmA

transition is weakly first-order. Similar analyses of the $H(T)$ data were performed around the isotropic-to-nematic (I-N) transition. A larger latent heat of 0.27 ± 0.02 J/g can be separated from the total enthalpy change (see **Table 4.2**), confirming a stronger first-order nature, for the I-N transition. It is clear (from the profiles in **Figure 4.4**), that for both transitions (N-SmA and I-N), there are large pretransitional contributions to the total enthalpy changes. These aspects will be discussed in a separate section.

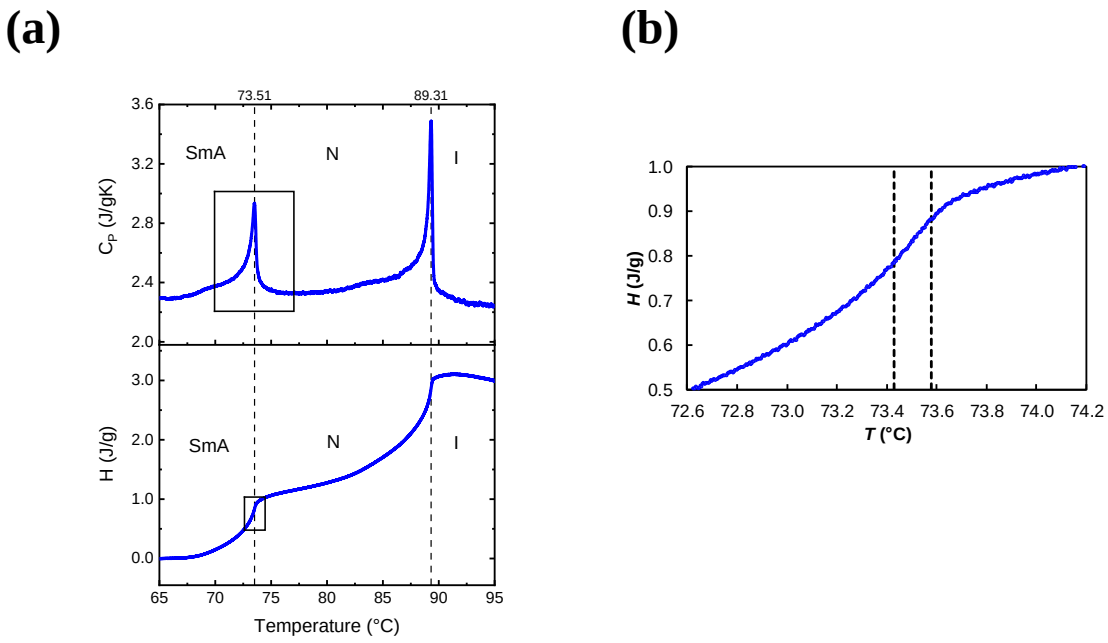

Figure 4.4. (a) ASC data for neat itraconazole, covering the N-SmA and the I-N transitions. The upper panel displays the specific heat capacity and the bottom panel the specific enthalpy as a function of temperature. Dashed lines are the mesophase transition temperatures. A linear temperature-dependent background, $2.3(T - T_{ref})$, with T_{ref} an arbitrary reference temperature, has been subtracted from the direct enthalpy results. (b) A blow-up of the small square in the bottom panel of **Figure 4.4a**. The vertical dashed lines indicate a two-phase region (between T=73.43 °C and T=73.58 °C).

Table 4.2. Adiabatic scanning calorimetry results for itraconazole with different glycerol contents. The transition temperature (T, °C), total enthalpy change over the transition (ΔH, J/g), and true latent heat (ΔH_L, J/g) are measured during a heating run with constant power, resulting in slow average scanning rate, on the order of 50 mK/min for full measuring ranges. For a complete definition of all the terms, see reference[167,181,182].

Glycerol Content (w/w)	**Isotropic – Nematic**			**Nematic–Smectic A**			**Isotropic – Smectic A**			$\frac{T_{N-SmA}}{T_{I-N}}$
	T (°C)	ΔH (J/g)	ΔH_L (J/g)	T (°C)	ΔH (J/g)	ΔH_L (J/g)	T (°C)	ΔH (J/g)	ΔH_L (J/g)	
0%	89.31 ±0.03	1.61 ±0.05	0.27 ±0.02	73.51 ±0.03	0.76 ±0.05	0.095 ±0.010	--	--		0.956
2%	80.41 ±0.02	0.87 ±0.05	0.13 ±0.03	72.71 ±0.05	3.2 ±0.2	0.61 ±0.03	--	--		0.978
5%	--	--	--		--		75.6 ±0.1	11.8 ±0.5	4.8 ±0.2	

4.5.6 ASC results for the ITZ-glycerol mixtures

Figure 4.5a (similar to **Figure 4.4**) gives an overview of the temperature dependence of the specific heat capacity C_p and the specific enthalpy H from well below the smectic A (SmA) to well in the isotropic phase, for the ITZ + 2% glycerol mixture. Compared to neat ITZ, the I-N transition occurs at a lower temperature (80.4 °C), whilst the N-SmA transition temperature (72.7 °C) remains almost unaffected, resulting in a much narrower nematic range (i.e. $T_{I-N} - T_{N-SmA}$ = 7.7 °C). Both transitions are clearly first-order, with substantial (true) latent heats (see **Table 4.2**; 2% glycerol). Additionally, some pretransitional specific heat capacity increases and minor supercooling are observed.

When the glycerol content is increased to 5% w/w, however, only one strongly first-order transition, with substantial total enthalpy increase and a large true latent heat over a wide

two-phase region, is observed (see **Figure 4.5b** and **Table 4.2**). The I-SmA transition also shows some pretransitional heat capacity increase in the SmA phase.

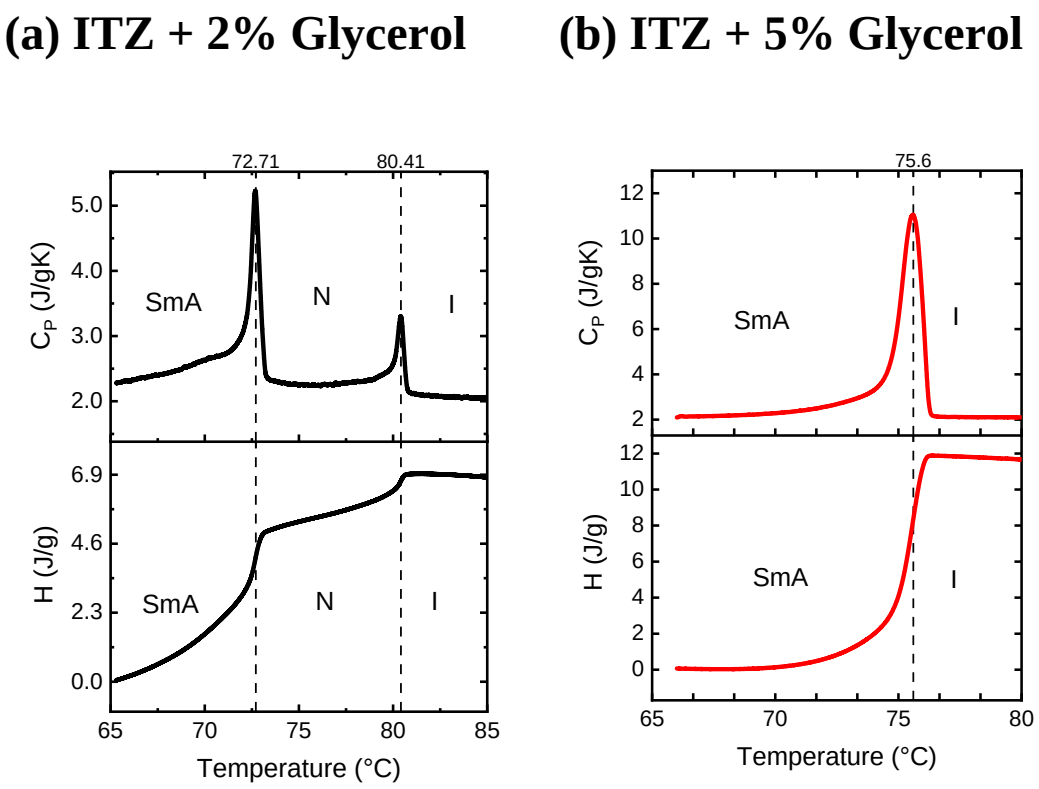

Figure 4.5. ASC results for ITZ-glycerol mixtures from the smectic A to the isotropic phase. The upper panel shows the specific heat capacity and the bottom panel the specific enthalpy as a function of temperature. For the sake of clarity, a linear temperature-dependent background has been subtracted from the direct enthalpy results. (a) ITZ + 2% w/w glycerol; background $2.7(T - T_{ref})$. (b) ITZ + 5% w/w glycerol; background $2.2(T - T_{ref})$. T_{ref} is an arbitrary reference temperature.

4.5.7 Critical exponent analysis of the N-SmA transition

Second-order (continuous) phase transitions are characterized by large fluctuations, which, for a properly defined order-parameter, diverge in size to infinity. This size divergence can be described by a power law, with a characteristic critical exponent depending on the universality class of the phase transition[189]. The limiting behavior of the specific heat capacity at a second-order transition, can also be described by means of a power law of the form:

$$C_p = A|\tau|^{-\alpha} + B \tag{4.5}$$

with $\tau = (T - T_c)/T_c$. The parameter A is the critical amplitude, α is the critical exponent, T_c is the critical temperature (T and T_c in kelvin) and B is the background term. The different coefficients in equation (4.5) must be derived from (non-linear) least-squares fitting of experimental data. However, the fact that ASC scans result directly in an enthalpy $H(T)$ curve (see equation(4.2)) allows substantial simplification. One can define the following quantity:

$$C = \frac{H - H_c}{T - T_c} \tag{4.6}$$

which corresponds to the slope of the chord connecting $H(T)$ at T, with H_c at T_c. It can easily be shown, that C has a power law behavior of the form[33,167]:

$$C = \frac{A}{1 - \alpha}|\tau|^{-\alpha} + B \tag{4.7}$$

Both C_p and C have the same critical exponent, and either equation (4.5) or (4.7) can be used in fitting data to arrive at important values for the critical exponent α and amplitude A. However, by considering the difference $(C - C_p)$, above or below T_c, the (unimportant) background term drops out, resulting in:

$$C - C_p = \frac{\alpha A}{1-\alpha}|\tau|^{-\alpha} \tag{4.8}$$

Taking the logarithm on both sides of equation (4.8) gives:

$$\log(C - C_p) = \log\left(\frac{\alpha A}{1-\alpha}\right) - \alpha \log|\tau| \tag{4.9}$$

As a result, one obtains a straight line with a negative slope immediately giving the critical exponent α.

In **Figure 4.6**, data for the two quantities C and C_p are given for the N-SmA transition of neat itraconazole. The corresponding logarithmic plot [see equation (4.9)] is given in **Figure 4.7**. From the detailed analysis of the enthalpy and heat capacity curves, and their higher derivatives, we arrived at a two-phase region of 150 ± 30 mK and a small latent heat of 0.095 ± 0.010 J/g. Since the power law description breaks down in the two-phase region, only data outside that region are used in **Figure 4.6** and **Figure 4.7**. From the limiting slope of the data (for $\log|\tau| < -2.5$) in **Figure 4.7**, a value for α of 0.50 ± 0.05 can be estimated above and below the transition. The deviations from the straight line observed

for log $|\tau|$ > -2.5, can be ascribed to higher order correction terms, relevant away from the transition, which have been neglected in equations (4.5) and (4.7).

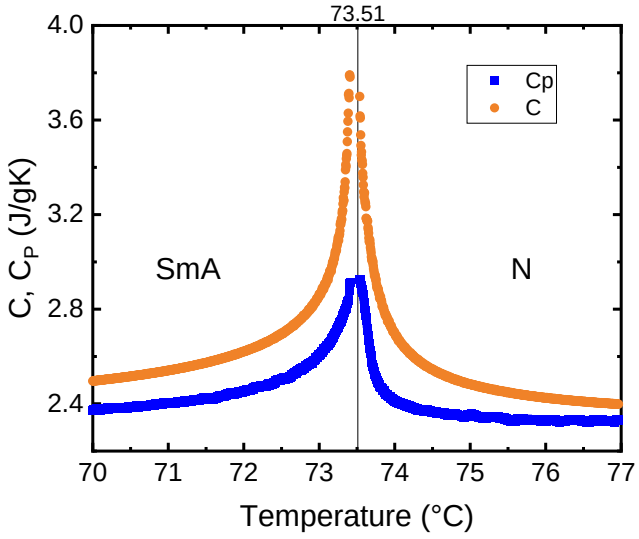

Figure 4.6. Adiabatic scanning calorimetry results above and below the N-SmA transition of neat itraconazole. The lower (blue) curves are the specific heat capacity C_p values, a blow up of the square in the top panel of **Figure 4.4a.** The upper (orange) curves are results for the quantity C defined in equation (4.6).

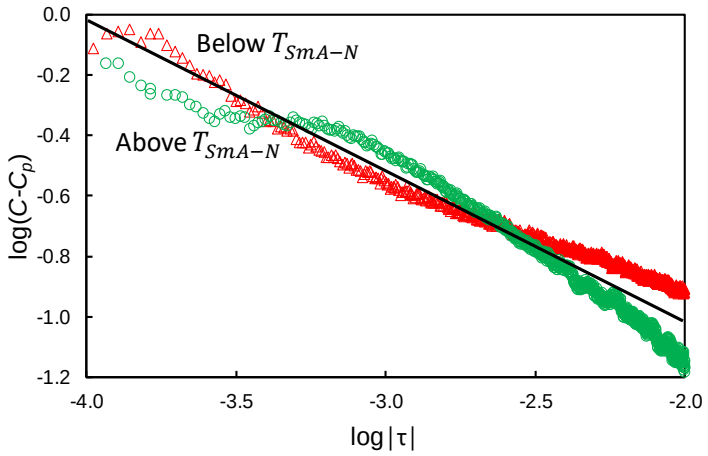

Figure 4.7. Adiabatic scanning calorimetry results for the N-SmA transition of neat itraconazole. Double logarithmic plot of the difference $(C - C_p)$ expressed in J/gK, as a function of the reduced temperature difference $|\tau|$. Red triangles are for $T < T_c$ and green circles for $T > T_c$. The average limiting slope of the black solid line, is consistent with α=0.50 ± 0.05.

Although the N-SmA transition in neat itraconazole is weakly first-order, the small value of the latent heat and the consistency of the obtained value of critical exponent α with the tricritical value α = 0.5, indicates the N-SmA transition is close to a tricritical point.

For the mixture of itraconazole with 2% of glycerol, although a N-SmA transition (with a much smaller nematic range) is observed, a substantial true latent heat (0.61 ± 0.03 J/g), in addition to pretransitional contributions, is also present for this transition. Moreover, the transition is broadened over several tenths of a degree, not allowing a similar critical exponent analysis as for neat itraconazole. Nevertheless, the substantial latent heat, the narrower nematic range and a McMillan parameter closer to 1 (**Table 4.2**; 2% glycerol),

are fully consistent with the overall picture of the nature of the nematic-to-smectic A transitions.

For the isotropic-to-nematic (I-N) transitions observed for neat itraconazole and itraconazole + 2% glycerol, as well as for the isotropic-to-smectic A (I-SmA) transition for itraconazole + 5% glycerol, sizeable true latent heats (with wide two-phase regions) and pretransitional contributions are observed (see **Table 4.2**). Unfortunately, the widths of the two-phase regions do not allow a reliable analysis of the pretransitional contributions.

4.5.8 Implications of the critical behavior

The critical exponent analysis and the extracted magnitudes of the latent heats confirm the general picture concerning the three transitions investigated. The N-SmA transition in ITZ, being close to a tricritical point, is easily driven from a weakly first-order transition, to a (strongly) first-order transition, most likely due to a coupling of the concentration of glycerol to the nematic and smectic order parameters. The invariance of the resulting I-SmA transition temperature to increasing glycerol concentration, the exceptionally large total enthalpy change, and the large latent heats of the I-SmA transition, all point to ITZ-glycerol mixtures having highly ordered, rigid smectic layers. Structural, molecular orientation, and molecular interaction studies from scattering and spectroscopy experiments, will be needed to provide additional insight into the smectic ordering process of the binary mixtures, and to arrive at the most likely packing arrangement. This will be the subject of a different manuscript.

4.6 SIGNIFICANCE

Glassy liquid crystals are versatile materials, with wide range of applications from displays, to organic electronics. This study demonstrates that glycerol (and by extension, other similar small-molecule plasticizers, such as water or ethylene glycol) can be incorporated at very low concentrations to modulate the thermotropic phase sequence and to increase the stability of the smectic-A layers. In the model compound studied, this wide range of tunability is linked to the fact that the N-SmA transition is close to a tricritical point. A coupling of the concentration of glycerol to the smectic order parameter, drives the N-SmA transition from a weak to a strong first-order character. Beyond a critical additive concentration, the nematic phase can be eliminated. This relatively simple approach of incorporating a small molecule plasticizer via solvent evaporation, into a glassy thermotropic LC, presents an opportunity to systematically modulate phase behavior in smectic phases. Since the smectic phase possesses a lower free energy level than the amorphous phase, pharmaceutical thermotropic LCs with stabilized smectic phases may be more resistant to crystallization, while offering adequate dissolution enhancement, when compared to the corresponding crystalline drug. The stabilized smectic phase therefore presents an alternate formulation approach for improving the bioavailability of pharmaceutical compounds with poor aqueous solubility.

4.7 CONCLUSIONS

We have investigated the effects of glycerol, a small molecule dopant, on the phase behavior of the thermotropic liquid crystal, itraconazole. A phase diagram was constructed from DSC heating curves, by varying the concentration of glycerol from 1 to 40% w/w. When cooled from the melt, the isotropic liquid of neat itraconazole transitions to the nematic (N) state, and then to the smectic A (SmA) state, before vitrifying.

With increasing glycerol content, the I-N transition shifts to lower temperatures without substantial modification of the N-SmA transition temperature. At glycerol contents ≥5% w/w, however, the nematic phase disappears, indicating a direct I-SmA transition. The I-SmA transition enthalpy is significantly larger than the individual I-N and N-SmA transition enthalpies.

We also performed heat capacity and enthalpy measurements around the phase transitions, with high resolution adiabatic scanning calorimetry. The N-SmA transition in neat itraconazole shows the characteristics of a weakly first-order transition, with a small latent heat of 0.095 ± 0.010 J/g. From a detailed analysis of the critical pretransitional behavior, an effective heat capacity critical exponent of 0.50 ± 0.05 is obtained, in agreement with predictions of the Landau-de Gennes mean-field theory for tricritical behavior.

As expected, the I-N transition in ITZ is found to be first-order with a larger latent heat. The transitions observed in the ITZ-glycerol binary mixtures, however, show stronger first-

order character (when compared to those in neat ITZ), with sizeable true latent heats, and pre-transitional contributions.

4.8 ACKNOWLEDGEMENTS

This project was funded by the National Science Foundation (grant award number NSF-CMMI-1662039). The support of the William and Mildred Peters endowment fund is acknowledged. KKAE acknowledges the Bighley Graduate Student Fellowship. We also thank Dr. Jorge Vinals and Dr. Satyendra Kumar for enlightening discussions.

5 Stabilization of the Smectic Phase of Itraconazole: Implications on Crystallization Propensity and Dissolution Performance.

5.1 OVERVIEW

Itraconazole (ITZ) is an antifungal compound with thermotropic liquid crystalline properties. Upon cooling from the melt, neat itraconazole transitions from the isotropic liquid (I) to the nematic (N) and then to the smectic A (SmA) phase, before being vitrified. The objective of this study was to investigate the effects of low concentrations of glycerol, a small molecule additive, on the mesophase sequence and structural packing of ITZ. With increasing glycerol content, the temperature range of the nematic phase systematically decreased, with little destabilization of the N-SmA phase transition temperature. At glycerol contents ≥ 5% w/w, the nematic phase disappeared, and the ITZ-glycerol samples transitioned directly from the isotropic liquid to the smectic A state. The I-SmA transitions exhibited strong first-order character, marked by unusually large enthalpy change values. There was a rapid rise in smectic order as determined by variable temperature synchrotron X-ray diffractometry, a sharp discontinuity in lateral correlation lengths, and a hysteresis upon thermal cycling. The smectic order parameter, which characterizes the quality of smectic layering, was tunable within a considerable range, with near-perfect smectic layers formed for glycerol contents ≥ 5% w/w. Alpha relaxation times of unaligned samples, measured with dielectric spectroscopy, progressively increased with increasing glycerol content in the isotropic, but not in the smectic phase, indicating that glycerol did not accelerate mobility in the smectic phase. Interestingly, drug crystallization was not observed in the ITZ-glycerol samples for up to 2 years, at pharmaceutically relevant storage temperatures (25-45 °C). Further, the dissolution performance of the ITZ-glycerol sample

was better than that of neat amorphous itraconazole (lacking smectic order), but comparable to the performance of an amorphous solid dispersion. The results suggest that the stabilized smectic state, can offer the dual advantage of good physical stability with adequate dissolution and possibly bioavailability.

Keywords: phase transition; itraconazole; dielectric spectroscopy; thermotropic liquid crystal, dissolution, physical stability, amorphous solid dispersion

5.2 INTRODUCTION

As the number of poorly water-soluble pharmaceutical compounds under development increases, formulation strategies that can enhance the apparent aqueous solubility of the drugs, with adequate physical stability, become increasingly important. Attention has been given to amorphous solid dispersions, which are homogeneous, molecular-level drug-polymer mixtures: the disordered (isotropic) state can result in apparent drug solubility, much higher than the solubility of the corresponding, fully ordered crystalline form[8]. Liquid crystals (LCs) are partially ordered materials, with properties intermediate between the properties of crystalline solids and isotropic liquids. The intermediate mesomorphic states are thermodynamically stable at defined temperatures and pressures[28], and can cause mechanical, structural, electrical and optical responses, useful in diverse fields such as organic electronics, thermal sensors and agriculture.[29] The pharmaceutical benefits of this class of compounds have, however, not been adequately explored[42].

LCs can be divided into two broad classes based on their structure, composition and method of preparation as (i) thermotropic liquid crystals, whose mesophases are formed by heating the crystalline solid or cooling the isotropic melt, and (ii) lyotropic liquid crystals, formed when amphiphilic compounds are dissolved in protic solvents, under appropriate conditions of solvent concentration and temperature[28]. The majority of pharmaceutical LCs form lyotropic phases, and, because of their ability to interact with phospholipids, typically find use as topical preparations[22]. Thermotropic LC drugs are relatively less

common[22,42]. Nonetheless, because they possess positional and/or orientational order, thermotropic LC drugs could be more stable physically, than the corresponding fully disordered amorphous forms. Additionally, the higher Gibbs free energy of mesophases, compared with the crystalline solid, should in principle lead to higher apparent solubility of mesophases. From the drug-delivery viewpoint, thermotropic LCs can therefore provide a good balance of physical stability and increased bioavailability.

Itraconazole (ITZ; **Figure 5.1a**), indicated in the treatment of fungal infections, is a thermotropic LC that forms nematic (N) and smectic-A (SmA) mesomorphic phases, upon cooling from the isotropic (I) melt[175]. In the nematic phase, the rod-like ITZ molecules align parallel to each other, with their long axes all pointing approximately in the same direction. In the smectic phase, the molecules maintain the orientational order and are further organized into layers[167]. Depending on the cooling rate from the melt, ITZ glasses of varying molecular order can be produced: with quench-cooling, smectic ordering can be arrested, resulting in nearly isotropic glasses, whilst slow cooling leads to glasses with organized smectic layers[176,190]. The degree of smectic order can alternatively be varied with compression pressure[191], and the depth of smectic layer spacings can be modulated based on substrate temperature during vapor deposition[192].

Apart from the different degrees of molecular order that can be induced by different preparation methods, some unexpected effects of water (a ubiquitous plasticizer) on the physical stability of itraconazole have been documented. Su[190] reported the appearance of

a sharp peak in the small angle region ($q = 0.4$ Å^{-1}) of the X-ray diffraction pattern of itraconazole, upon storage at 40 °C/75% RH. The peak persisted for up to two months, without subsequent drug recrystallization[190]. Mugheirbi *et al*[193] investigated further, and confirmed that the sharp low-angle peak, indicative of smectic ordering, developed with sorption of 2.5% w/w water (1:1 drug:water mole ratio). The glass transition temperature (T_g) of ITZ was, however, not substantially depressed with increasing water content[193]. Our preliminary studies also revealed a similar effect with glycerol (**Figure 5.1b**) as additive[24]. With up to 10% w/w glycerol content, drug crystallization was not observed in the ITZ-glycerol binary mixtures stored at 40 °C/0% RH, for more than two months, in agreement with Su's observations. Neat ITZ is known to be a slow-crystallizing, stable glass former[194]. Nonetheless, since very low levels of plasticizers invariably cause rapid crystallization in many stable glass formers[57,187,195], the physical stability of ITZ with such high plasticizer contents, is an unusual property, warranting detailed investigations of the underlying mechanisms.

Because the low angle X-ray diffraction peak of ITZ denotes the layered structure of the smectic phase[176,193,196], we hypothesized that additives with fast dynamics (such as water or glycerol), even at very low concentrations, accelerate the development of smectic order in amorphized ITZ. The smectic phase, being at a higher free energy level than the fully ordered 3D crystalline state, would offer higher drug solubility and thereby better dissolution, than the crystalline form. To test this hypothesis, we first investigated the phase behavior of ITZ-glycerol mixtures. Glycerol offered one main advantage over water,

in that, having a lower vapor pressure and higher boiling point than water, the ITZ-glycerol systems could be easily melt-quenched and characterized, with precise control over the plasticizer content. Furthermore, to aid processing, glycerol and other small-molecule plasticizers are included in amorphous formulations[51]. The current investigations could therefore shed light on some of the mechanisms of additive-induced phase transitions that may be encountered in rod-like pharmaceutical compounds.

The first part of our study was recently reported, where we determined the critical behavior of the N-SmA transition of ITZ, as well as the effect of glycerol on the order of the mesophase transitions, using high-resolution adiabatic scanning calorimetry (ASC)[24]. Here, to understand the mechanisms by which glycerol modulates the mesophase sequence, we have characterized the structural features and molecular mobility of the ITZ-glycerol binary mixtures with synchrotron X-ray diffractometry (s-XRD) and dielectric spectroscopy (DES), respectively. Long-term stability studies in the glassy state, as well as *in vitro* powder dissolution experiments, have also been performed.

(a) **(b)**

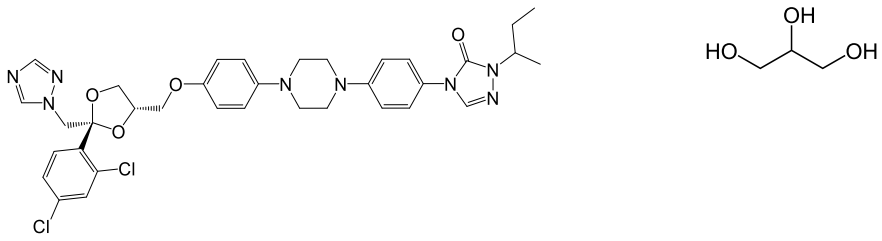

Figure 5.1. Structures of the model compounds. (a) Itraconazole; molecular length, ~30 Å. (b) Glycerol; ~6.4 Å. Molecular lengths were determined from the most extended conformers after energy optimization, using Chem 3D Ultra®.

5.3 EXPERIMENTAL METHODS

5.3.1 Materials

Itraconazole (Bepharm Limited, Shanghai, China), glycerol (Sigma Aldrich, USA), and polyacrylic acid (PAA, 1800 g/mol, Sigma Aldrich, USA) were used as received. All other reagents and chemicals were of analytical grade and purchased from Sigma Aldrich.

5.3.2 Sample Preparation

Amorphous itraconazole, considered to be without smectic order, was prepared by melting the crystalline drug at 180°C and quenching, by dipping the melt in liquid nitrogen. The ITZ-glycerol, and ITZ-PAA samples were prepared by solvent-evaporation, followed by melt-quenching. Crystalline ITZ was dissolved in dichloromethane (at 50°C with sonication), glycerol or PAA was dissolved in methanol, and the two solutions were mixed. The solvent was rapidly evaporated under reduced pressure at 50°C, 250 rpm, in a rotary evaporator (IKA-HB10 digital system, Werke GmbH and Co. Germany). The resulting mass was ground in a mortar and pestle, to obtain a free-flowing powder. The powder samples were further dried under vacuum and at room temperature for 24 hours, to remove residual solvent, and kept in desiccators containing anhydrous calcium sulfate at -20°C, until further use.

5.3.3 Differential Scanning Calorimetry (DSC)

A differential scanning calorimeter (Q2000, TA Instruments, New Castle, DE) equipped with a refrigerated cooling accessory unit was used. Temperature, heat capacity and enthalpy calibrations were performed with tin, indium, and sapphire respectively. An accurately weighed sample (~15 mg) was hermetically sealed in an aluminum pan (T-zero®, TA instruments) and subjected to a temperature program, under dry nitrogen gas purge (50 mL/min). A heating rate of 2 °C/min was used with a temperature modulation of ±0.212 °C every 40 s.

Each sample was heated from room temperature (~20 °C) to 180 °C, held for ~1 minute to ensure complete melting, and cooled back to room temperature. The sample was then reheated to the melting temperature. Both the heating and cooling rates were 2 °C/min.

DSC data analyses were performed with the Universal Analysis® software (TA Instruments). Glass transition temperatures (T_g) are reported as the midpoint of the step-change (baseline shift) in the reversing heat flow signal. Phase transition temperatures were evaluated from the peak positions of the exothermic or endothermic reversing heat flow signals. Enthalpy change values are the peak areas of the reversing heat flow endotherms.

5.3.4 Variable Temperature Synchrotron X-ray diffractometry

High resolution, rapid acquisition powder diffraction experiments were carried out at beamline 17-BM-B of the Advanced Photon Source, Argonne National Laboratory, IL, USA. A monochromatic X-ray beam (incident beam energy 27.3 keV; wavelength 0.45390 Å; beam diameter 300 μm) was used in transmission mode, with a two-dimensional area detector (PaxScan 4343, Varex Imaging). The scattering wavevector (q) scale was calibrated with LaB_6 (SRM 660c; NIST) and silver behenate.

An accurately weighed quantity of each sample (~10–30 mg, depending on density) was tightly packed and hermetically sealed in an aluminum pan generally used for DSC analysis (T-zero, TA Instruments®). The pan was mounted vertically on a custom-made polyether ether ketone (PEEK) holder, at a sample-to-detector distance of 1200 mm. The path length of the X-ray beam through the sample in the pan was 3 mm. Temperature was controlled with a stream of nitrogen gas (Cryostream 800 plus®, Oxford Cryosystems, with precision better than 0.1 K) pointed to the top of the aluminum pan. A fine-wire thermocouple was placed in direct contact with the bottom of the sample pan to record the actual sample temperature, *via* a temperature input device (USB-TC01, National Instruments). The accuracy of the temperature readings was verified by monitoring the crystal-to-melt transition temperatures (T_m, indicated by the disappearance of all characteristic XRD peaks) of crystalline ibuprofen (T_m~76°C) and crystalline itraconazole (T_m~168°C) in the same sample configuration. A nominal ramp rate of 2° C/min set on the Cryostream

corresponded to an actual steady-state rate of 1.67 °C/min measured by the thermocouple attached to the sample pan.

Two-dimensional (2D) diffraction images were recorded in 30 second intervals. Ten frames were summed up to make up each scan, with an exposure time of 1 second per scan. The 2D raw images were azimuthally integrated to obtain one-dimensional scattering intensity (I) versus scattering wavevector ($q = 4\pi sin\,\theta/\lambda$; θ is the angle of incidence and λ is the wavelength) plots, using the GSAS II software[197]. Unless otherwise stated in the text, each low-angle liquid crystalline peak (at $q \approx$ 0.2, 0.4 and 0.6 Å^{-1}) from the 1D patterns, was fitted with a single Pseudo-Voigt (the sum of a Gaussian and Lorentzian peak, weighted by a fourth parameter) function on a linear background, using Jade® software (Materials Data Inc, CA), to obtain peak areas, full width at half maximum ($fwhm$) values, and layer spacings ($d = 2\pi/q$). Wide angle peaks (discussed in the text) were deconvoluted by fitting two pseudo-Voigt profiles, each centered at $q \approx$ (1.3 and 1.6) Å^{-1}, respectively. The skew of the two sub-peaks was unified, whilst the peak positions, widths, $fwhm$, and heights were left as free parameters. Diffraction patterns of the empty DSC pan and silver behenate packed in the DSC pan, were used for background correction and beam intensity normalization, respectively.

5.3.5 Dielectric Spectroscopy

Approximately 50 mg of each sample was placed on a gold-plated stainless-steel electrode (20 mm diameter) and heated on a hotplate until complete melting was achieved. The melt

was spread evenly as a thin film, separated with three 50 μm glass fiber spacers, covered with a second electrode, and rapidly quenched on a cold metal block (pre-cooled at -20°C).

Measurements at ambient pressure were performed with a broadband dielectric spectrometer (Alpha-AK high performance frequency analyzer, Novocontrol Technologies, Germany), which uses a Quatro system liquid nitrogen cryostat to maintain the sample temperature with stability better than 0.1 K. The complex dielectric permittivity (ε^*), consisting of real (ε') and imaginary (ε'') components, was measured at multiple fixed temperatures within the frequency (f) range of 10^{-2} to 10^6 Hz. Dielectric spectra obtained in the supercooled region (at $T > T_g$) were analyzed with the Havriliak-Negami (HN) function[198] (equation (5.1)) with an additional term describing the dc conductivity (σ):

$$\varepsilon^*(\omega) = \varepsilon_\infty + \frac{\Delta\varepsilon}{(1 + (i\omega\tau_{HN})^{\alpha_{HN}})^{\beta_{HN}}} + \frac{\sigma}{\varepsilon_0\omega} \tag{5.1}$$

In the HN function, τ_{HN} is the characteristic relaxation time, α_{HN} and β_{HN} are the shape parameters accounting for symmetric and asymmetric broadening of the spectrum respectively, ω is the angular frequency ($\omega = 2\pi f$) and $\Delta\varepsilon$ is the dielectric strength given by $\Delta\varepsilon = \varepsilon_0 - \varepsilon_\infty$ where ε_0 is the low frequency limit ($\omega \to 0$) of $\varepsilon'(\omega)$ and ε_∞ is the high frequency limit ($\omega \to \infty$) of $\varepsilon'(\omega)$.

For neat itraconazole, the temperature dependence of α relaxation times (τ_α) at $T > T_g$ was modeled with the Vogel-Fulcher-Tamman (VFT) equation[45]:

$$\tau_\alpha = \tau_0 exp\left(\frac{DT_0}{T - T_0}\right) \tag{5.2}$$

where τ_0, T_0 and D are fitting parameters: τ_0 is the relaxation time of the unrestricted material, D is the strength parameter, an indicator of the kinetic fragility of the material, and T_0 is the temperature of zero mobility (theoretical Kauzmann temperature).

The temperature dependence of τ_α for samples with >2% glycerol content (details discussed in text), was fitted to the Arrhenius equation[45]:

$$\tau_\alpha = \tau_\infty exp\left(\frac{E_a}{k_B T}\right) \tag{5.3}$$

where τ_∞ is the pre-exponetial factor representing the high temperature limit of the relaxation rate, E_a is the energy barrier (activation energy) for the relaxation process, and k_B is the Boltzmann constant.

5.3.6 Infrared Spectroscopy

Infra-red spectra of the dry powder samples were obtained with a spectrometer (Vertex 70, Bruker, Ettlingen, Germany; equipped with a globar mid-IR source) using an attenuated total reflectance (ATR) accessory (single reflection germanium crystal) and a DLaTGS detector. For each measurement, 64 scans were acquired in the 4000–400 cm^{-1} range, with a 4 cm^{-1} resolution.

5.3.7 Nuclear Magnetic Resonance Spectroscopy

Solid-state NMR spectra were acquired at the Minnesota NMR Center with a Bruker spectrometer operating at a ^1H Larmor frequency of 700 MHz and equipped with 3.2 mm MAS probe. All spectra were acquired at 25 °C using the Hartmann-Hahn cross

polarization (CP) experiment at 12 kHz MAS rate. The CP contact time was set to 3 ms, the recycle delay was set to 3 s, and ^{15}N acquisition time was set to 10 ms with 100 kHz spectral width. During CP, ^{15}N and ^{1}H RF amplitudes were set to 35 and 59 kHz respectively. SPINAL decoupling was used during acquisition with 83.33 kHz ^{1}H RF amplitude. A total of 15,000 to 35,000 scans were used for acquiring each sample.

5.3.8 Powder Dissolution

Dissolution tests were performed with a USP Apparatus II (Varian 705 DS, Agilent Technologies, Santa Clara, CA). Each sample, containing 100 mg of drug (powdered and sifted through a 250 µm pore-size sieve) was dispersed in 250 mL of dissolution medium (0.1 N HCl) at 37 °C and stirred at a paddle speed of 100 rpm. Aliquots (3 mL) were withdrawn at each time point, filtered (0.45 µm pore size, Whatman® GHP), and diluted appropriately with 0.1 N HCl. The drug concentration in the filtrate was determined *via* UV spectroscopy (Cary 100 Bio, Agilent Technologies) at the wavelength of maximum absorption (~254 nm), using a calibration curve of crystalline itraconazole dissolved in methanol and serially diluted with 0.1 N HCl.

5.4 RESULTS AND DISCUSSION

5.4.1 Calorimetric investigations

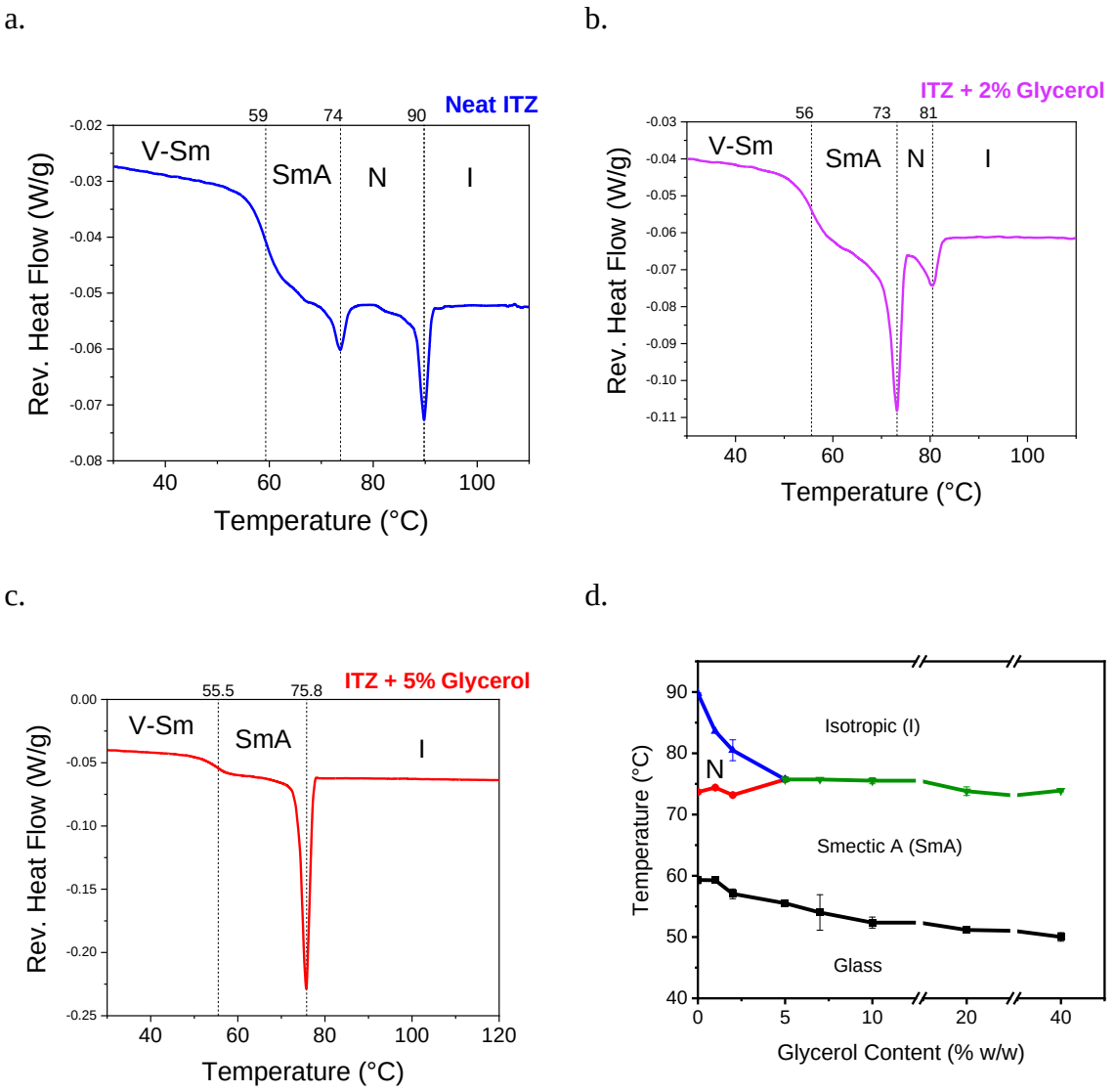

Figure 5.2. DSC curves obtained from the second heating of (a) Neat ITZ, (b) ITZ + 2% glycerol and (c) ITZ + 5% glycerol. Mesophase transition temperatures are indicated by the dashed lines. Each sample was cooled from the melt to -20 °C and reheated to 180 °C. Both the heating and cooling rates were 2 °C/min. Only the final heating curves over the temperature range of interest, are shown. Figure (d) shows the phase diagram, constructed from the mesophase transition temperatures. Data replotted from reference[24].

Figure 5.2a shows the DSC heating scan of neat itraconazole that has been cooled from the melt, and reheated. The isotropic (I), nematic (N), smectic (SmA) and vitrified smectic (V-Sm) phases have been labeled. The mesophase transition temperatures (indicated with dashed lines) and enthalpies (not given), agreed with the values reported in the literature[175,177,184,185]. The mesophase transitions are reversible. The transition names adopted in this text will therefore reflect mesophase sequences encountered upon cooling from the melt.

Glycerol was incorporated into ITZ via solvent evaporation, followed by melt-quenching. Of note, the resulting free-flowing powders are thermotropic, not lyotropic, LC systems. With 2% glycerol content (**Figure 5.2b**), the isotropic to nematic (I-N) transition shifted to a lower temperature, even though the nematic to smectic A (N-SmA) transition temperature remained relatively unaffected, resulting in a much narrower nematic range. With 5% glycerol, however, the nematic phase completely disappeared, resulting in a direct isotropic-to-smectic A (I-SmA) transition (**Figure 5.2c**). Other ITZ-glycerol mixtures with higher glycerol contents (>5%) also exhibited the direct I-SmA transition, as shown in the phase diagram (**Figure 5.2d**). The glass transition temperature, also plotted on the phase diagram, was not substantially depressed (when compared to predictions from the free volume additivity rule for binary mixtures[74]) with increasing glycerol content[24].

An extensive discussion of the thermal behavior of the ITZ-glycerol samples, has been presented earlier[24], with two major conclusions. First, the systematic decrease in the I-N transition temperature of ITZ (due to incorporation of glycerol), can be partly explained by the critical behavior of the N-SmA transition of neat ITZ. A heat capacity critical exponent of 0.5 was obtained by ASC, indicating that the N-SmA transition of neat ITZ is close to a tricritical point. Thus, the impurity (i.e. glycerol) concentration, could be easily coupled to the order parameter of the mesogen (ITZ), driving the transition from a weak first-order N-SmA to a much stronger first-order I-SmA transition. Second, since the enthalpy change of the I-SmA transition for the samples containing ≥5% w/w of glycerol is much larger than the sum of the enthalpy changes of the I-N and the N-SmA transitions of neat ITZ, it can be reasonably inferred that the resulting smectic structures for the ITZ-glycerol mixtures will be highly ordered, and consequently, very stable.

5.4.2 Structural Analysis by Synchrotron X-Ray Diffractometry

The structural features associated with the changes in the mesophase transitions were investigated in detail using high resolution synchrotron powder X-ray diffractometry. The samples were unaligned, evidenced by the uniform rings in the 2D scattering images (see **Figure S5.1**).

Neat itraconazole

The one-dimensional (1D) pattern of neat itraconazole, quenched (with liquid nitrogen) from the melt, shows a major diffuse maximum at q = 1.3 Å^{-1}, commonly referred to as the

amorphous halo, as well as three minor diffuse maxima (small "humps") equally spaced in the small angle region (**Figure 5.3a**). The lack of Bragg peaks at small angles, confirms that neat itraconazole melted and rapidly quenched, lacks smectic order. When slowly cooled from the melt, however, the diffraction pattern (**Figure 5.3b**), has two sharp Bragg peaks at q = 0.21 and 0.42 Å^{-1}, in addition to the wide-angle peak centered at q ~ 1.34 Å^{-1}. The appearance of the small angle Bragg peaks is classic evidence of a lamellar structure[28]. The fundamental scattering peak (q = 0.21 Å^{-1}) indicates a layer spacing ($d = 2\pi/q$) of ~30 Å. The layer spacing agrees with the molecular length of itraconazole (~30 Å), suggesting a smectic A structure. This result confirms earlier reports, that smectic ordering in itraconazole develops at slow cooling rates[176,192].

Itraconazole-Glycerol Samples

The XRD patterns of the itraconazole-glycerol mixtures, however, have three sharp, well-defined Bragg peaks at $q \approx$ 0.21, 0.42 and 0.63 Å^{-1} (**Figure 5.3c** and **d**). No other peaks in the q < 0.1 Å^{-1} region were observed, when we investigated with a diffractometer having a wider q-range (data not shown). The $q \approx$ 0.6 Å^{-1} peak (absent in the neat ITZ samples) being equidistant to the first two, is likely an additional higher-order peak[28]. The intensities of all the Bragg peaks increase significantly with increasing glycerol content.

An important observation from the XRD patterns is that, while very slow cooling from the melt was required to induce the small angle LC peaks in neat itraconazole, all three LC peaks appeared in the glycerol-containing samples right after solvent evaporation, and

persisted upon melt-quenching. Intense low-angle peaks indicate well-ordered layers, with large coherence lengths, and a narrow distribution of directors[28]. The sharpness of the peaks is related to the extent to which the smectic layer structure extends periodically over large distances[28]. It is qualitatively very clear, therefore, that glycerol, in a concentration-dependent manner, remarkably increases both the orientational and translational order of ITZ. Two key parameters that characterize the structure of smectic liquid crystals – the translational order parameter and the smectic layer spacings[28] – will be discussed in the next section.

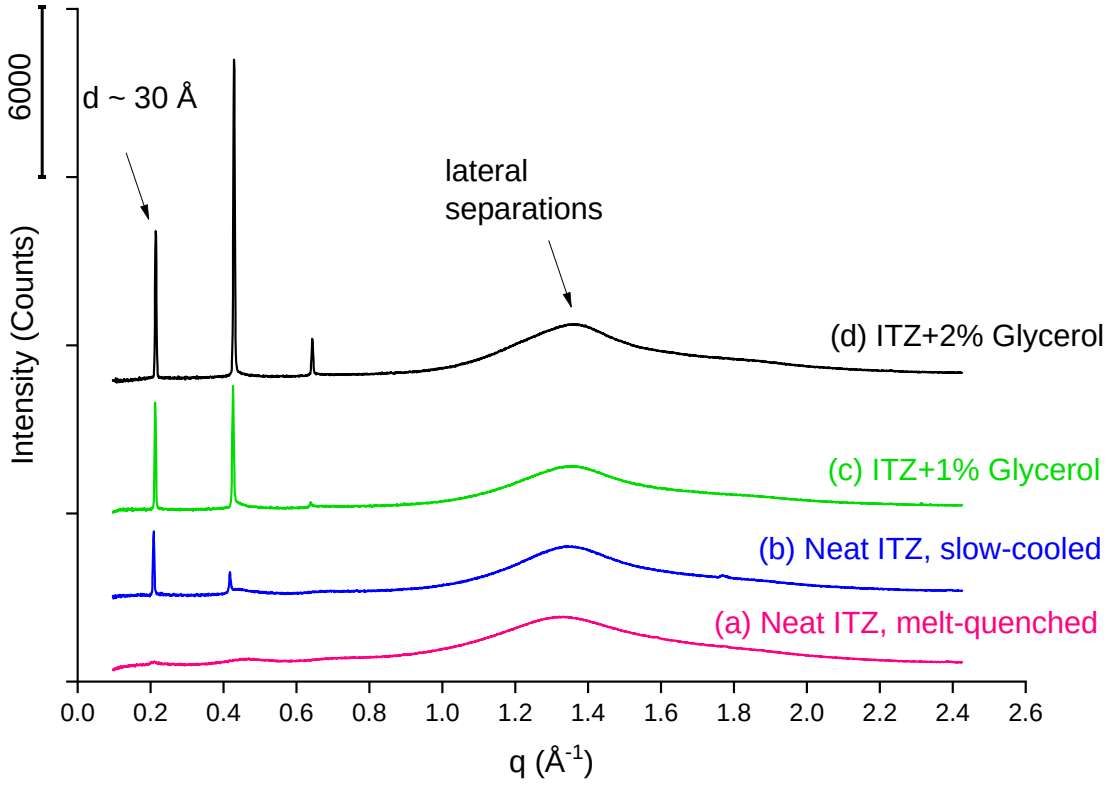

Figure 5.3. 1D synchrotron powder diffraction patterns of unaligned samples, at ambient temperature ($T \approx 30$ °C). (a) Neat itraconazole, rapidly cooled from the melt (melt-quenched). (b) Neat itraconazole, slowly cooled from the melt. (c) ITZ + 1% glycerol. (d) ITZ + 2% glycerol. Each pattern has been offset on the vertical axis for clarity.

5.4.2.1 Temperature variation of the small angle peaks (Evolution of smectic order)

The translational order parameter Σ, introduced by McMillan[30–32], is defined as the amplitude of a density wave that originates from the one-dimensional periodic layers, and may take values between 0 (for a system with no layer structure) and 1 (for a system with perfect layering, in the absence of thermal fluctuations). From X-ray scattering experiments, Σ can be obtained by comparing the fundamental (001) smectic layer peak intensity observed at a certain temperature, $I(T)$, with the theoretical 001-peak intensity which would result from the same smectic structure having perfect one-dimensional translational order (I_0)[30,199].

$$\frac{I(T)}{I_0} = \Sigma^2 \tag{5.4}$$

Kapernaum and Giesselmann[30], assuming a power-law dependence of Σ on reduced temperature, proposed a procedure to obtain I_0 from the temperature-dependence of I.

$$I(T) = I_0 \left[1 - \left(\frac{T}{T_c}\right)\right]^{2\beta} \tag{5.5}$$

Equation (5.5) is fitted to the temperature-dependent experimental integrated peak intensities (peak areas), with three adjustable parameters – I_0 defined above, T_c the transition temperature in kelvin (or in the case of first-order transitions, the superheating limit of the smectic phase) and β, the order parameter exponent. We applied this method to probe Σ, using synchrotron radiation. Diffraction patterns were acquired, without field alignment, as each sample was cooled (at ~ 2 °C/min) from the melt. For selected formulations, the heat-cool cycle was repeated around the phase transition point.

Figure 5.4a shows the area of the $q \sim 0.2$ Å^{-1} peak, as a function of temperature, for neat itraconazole. As the sample was cooled from the melt, the peak appeared at ~75 °C, increased gradually until ~55 °C, and decreased from 55 °C to 30 °C. The peak area stops increasing when the material falls out of equilibrium, as the smectic order becomes frozen in the glassy state. The slight decrease in smectic order below 55 °C, may be due to tension caused by the larger thermal expansion of ITZ relative to the container[176]. The rise in smectic order up to the temperature at which the maximum peak intensity occurred, was well-described by the empirical power-law expression (equation (5.5)). The exponent of the fit (2β=0.51) and the transition temperature (~76 °C) were in reasonable agreement with the literature values[176,196]. The itraconazole sample with 1% glycerol content (**Figure 5.4b**) also exhibited a similar behavior, with a steady rise in smectic order. The exponent of the power-law fit (2β=0.45) was however lower than the exponent obtained for neat itraconazole, indicating that smectic order rises more rapidly in the ITZ+1% glycerol sample. The heating curve retraced the cooling curve at the high temperature region, around the transition point (data not shown).

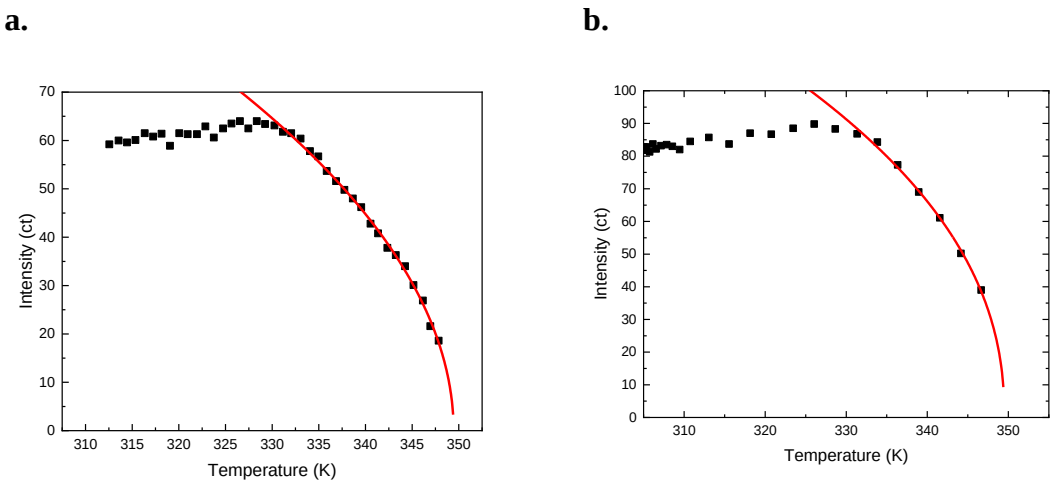

Figure 5.4. Temperature dependence of the integrated intensity (peak area) of the $q \approx 0.2$ Å^{-1} peak for (a) neat itraconazole, (b) ITZ + 1% glycerol. The curves are fits of equation (5.5) to the high-temperature (>50 °C) data. Fit parameters are listed in Table 5.1.

The samples with higher glycerol contents (from 2 to 20%) however, showed very rapid increases in the intensities of all the three low angle peaks (q =0.21, 0.42, and 0.63 Å^{-1}), at the transition points. **Figure 5.5** is a representative example at 5% glycerol content. Additionally, a hysteresis (~3 °C gap) developed around the mesophase transition temperature upon thermal cycling, even though the heating and cooling curves perfectly overlapped at low temperatures (T < 65 °C). The hysteresis was reproducible with multiple thermal cycles (data not shown) and therefore not due to macroscopic phase separation[39,200]. The sharp discontinuity in peak intensities is a characteristic feature of strong first-order phase transitions[30,34]. As shown earlier from the DSC curves, itraconazole containing 5% w/w glycerol (**Figure 5.2c**) transitions directly from the isotropic to the smectic A phase (I-SmA). The I-SmA transition is expected to be a first-order transition, based on the Landau-de Gennes theory and other molecular models[35].

Indeed, from our earlier investigation, we obtained a latent heat of 4.8 ± 0.2 J/g, using adiabatic scanning calorimetry (ASC)[24], in perfect agreement with the prevailing theories. A wide "impurity-induced" two-phase region was also identified with ASC[24] which, together with the effect of minor supercooling, explains the hysteresis loop observed in the variable-temperature X-ray diffraction experiments[200]. To compare, a much smaller latent heat (0.095 ± 0.010 J/g) was measured for the N-SmA transition of neat itraconazole, indicating its weaker first-order nature and explaining the relatively gradual rise in smectic order. The temperature variation of the area of the fundamental (001) peak, for all samples, upon cooling from the melt, are overlaid in **Figure 5.6**.

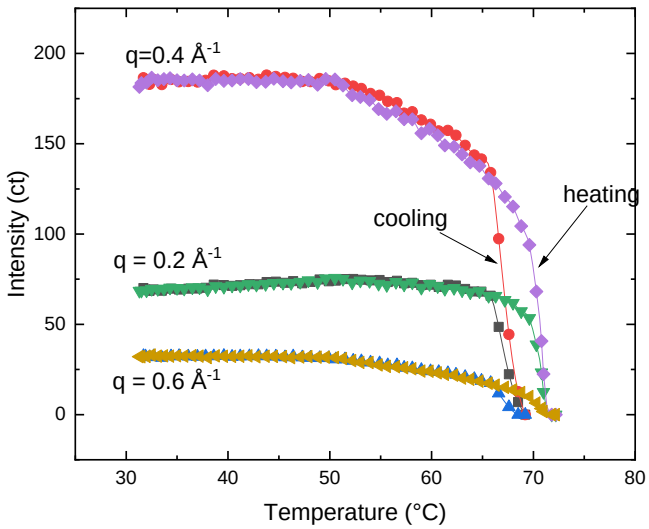

Figure 5.5. Temperature dependence of the integrated intensities (peak areas) of the three low angle Bragg peaks ($q \approx 0.2, 0.4, 0.6$ Å^{-1}) of the itraconazole sample containing 5% glycerol. The red, black, and blue symbols are data points obtained upon cooling the isotropic melt; the violet, green and yellow symbols are data taken from the subsequent reheating cycle. Data points are connected with solid lines, to assist in visualizing the trends.

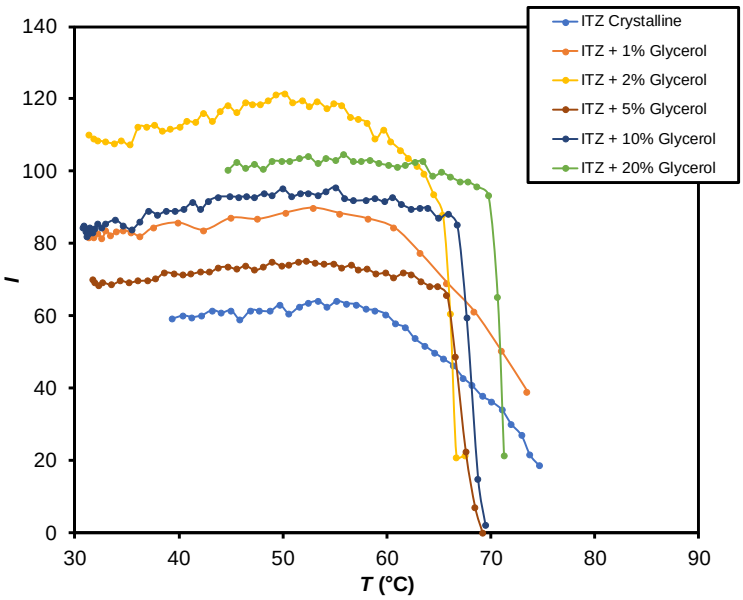

Figure 5.6. Integrated intensity (peak area, I) of the $q \approx 0.2$ Å^{-1} peak as a function of temperature during cooling, for neat ITZ (labelled as ITZ crystalline) and itraconazole formulations with different glycerol contents. Solid lines are drawn to assist in visualizing the trends.

The translational order parameter (Σ) values calculated from equation (5.4) are plotted in **Figure 5.6b**, as a function of reduced temperature. Fitted curves for the samples with higher glycerol contents are presented in the supplementary information (**Figure S5.3**), and the corresponding fit parameters are given in **Table 5.1**. The maximum order achieved for neat ITZ, and the sample containing 1% glycerol, were 0.47 and 0.52 respectively, both within the typical range of Σ values, for other smectic A materials[30,201]. The samples containing ≥2% glycerol however had order parameters greater than 0.8, significantly higher than values reported for many compounds[30,202]. By simply varying the concentration of glycerol, it was possible to systematically tune the smectic order, with near-perfect

smectic layers formed at glycerol contents ≥5% w/w. The high Σ values independently confirm that the smectic layers form spontaneously[30,201,202]. More importantly, such high translational order parameter values, together with the large latent heat and enthalpy change values (obtained from ASC and DSC respectively) further indicate that the highly-ordered smectic structures should be very stable.

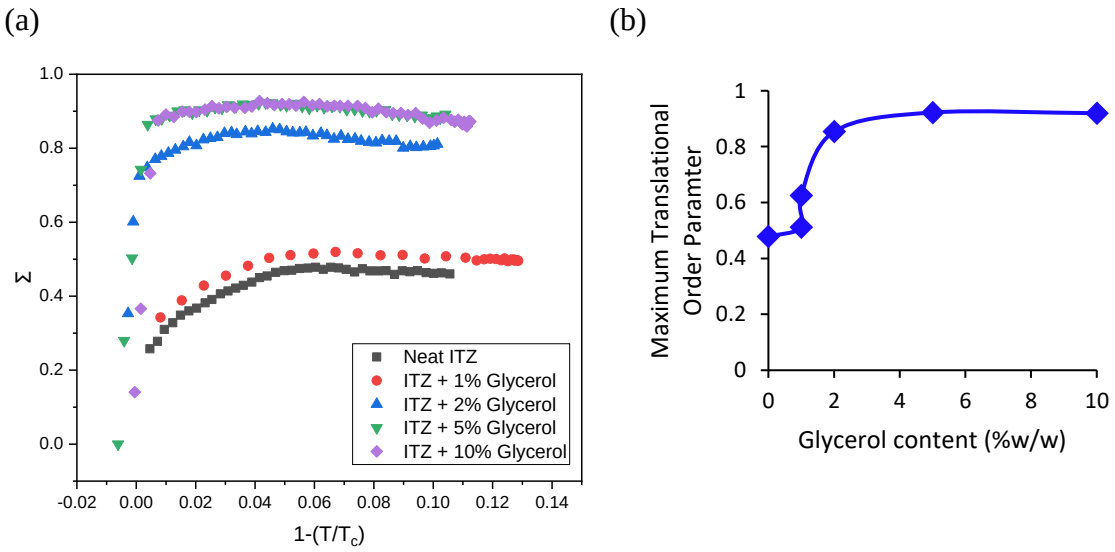

Figure 5.7. (a) Translational order parameter Σ, calculated from equation (5.4), as a function of reduced temperature, for ITZ samples with different glycerol contents. Values of parameters returned from the fits, are listed in Table 5.1. (b) Maximum translational order parameter, Σ_{max}, as a function of glycerol content. Data points are connected to assist in visualizing the trend.

Table 5.1. Values of the parameters I_0, β and T_c obtained from fits of equation (5.5) to the peak areas for the itraconazole samples with different glycerol contents. Errors of the fit parameters are in parentheses.

Glycerol Content (w/w)	Phase directly above SmA	Order of the I-SmA or N-SmA transition*	I_0	T_c (K)	β	Fit range**	$T_{\Sigma_{max}}$ ***	I_{max}	Σ_{max}
0%	N	Weak first-order	280 (17)	349.4 (0.3)	0.25 (0.01)	328-348	328	64	0.48
1%	N	First-order	333 (52)	349.5 (1.1)	0.22 (0.02)	331-346	331	87	0.51
1%	N	First-order	230 (34)	348.1 (1.1)	0.16 (0.02)	326-346	326	90	0.62
2%	N	First order	167 (7)	338.9 (0.8)	0.05 (0.01)	323-339	323	122	0.85
5%	I	Strong first-order	88 (3)	340.3 (1.3)	0.02 (0.01)	324-339	324	75	0.92
10%	I	Strong first-order	111 (8)	342.5 (3.9)	0.02 (0.01)	327-339	327	94	0.92

For all samples, I_0, β and T_c were left as free (adjustable) parameters. For the samples with ≥5% glycerol content, wide two-phase regions were observed, resulting in the first-order transition temperature T_0 being separated from T_c by a few degrees. *Based on latent heats extracted from ASC[24]. **Temperature range of data that was fitted. *** Temperature at which the maximum peak area I_{max}, and thus the maximum smectic order, Σ_{max}, occurs.

5.4.2.2 Temperature variation of the smectic layer spacings

For all samples, (i.e. neat itraconazole, or itraconazole/glycerol binary mixtures), the layer spacings ($d = 2\pi/q$), and the corresponding full width at half maximum ($fwhm$) values for all three low angle peaks ($q \approx 0.2, 0.4, 0.6$ Å^{-1}) remained unchanged with increasing glycerol content; the peak positions did not vary with temperature, either. The temperature invariance (or glycerol-concentration invariance) of the smectic layer spacing, gives two main indications. First, the molecule director does not become tilted, with respect to the layer normal, as would have been the case if the smectic A phase were to switch to a

different smectic phase. As an example, in the SmC phase, the layer spacing reduces due to the tilting of the molecules within the layers. Second, glycerol does not exclusively occupy the tail ends of the ITZ molecules; the layers are thus not separated.

5.4.2.3 The Wide Angle Peak

The diffuse wide-angle peak (the "amorphous" halo) was at the same position ($q \approx 1.3$ Å^{-1}), in neat itraconazole samples, having or lacking liquid crystalline order (**Figure 5.3**). Thus, the 1D diffraction patterns of the nematic phase are not easily distinguished from the patterns of the isotropic phase[28]. It is also evident from **Figure 5.3**, that the wide-angle peak is not perfectly symmetrical. Rather, apart from the main halo centered at $q \sim 1.3$ Å^{-1} (d-spacing of ~4.8 Å) there is a "shoulder" that suggests a weaker second halo centered at about q ~1.7 Å^{-1} (d ~ 3.7 Å). An example of the wide-angle peak deconvolution is shown in **Figure S5.2**. The origin of the wide-angle peaks have been the subject of earlier investigations[196,203]. With pair distribution function analysis, it was shown that peaks in the 4-7 Å region, corresponded to second and higher atom-atom nearest neighbor distances[196,203]. The sub-peak at $q \sim 1.3$ Å^{-1} is therefore more likely related to the average side-to-side separation of the close-packed molecules (or the width, w_0, of the itraconazole molecule, $w_0 = 2\pi/q$)[28]. The peak is broad because the positional correlations extend over short distances[28]. The positional correlation length, ξ, is inversely related to the width of the wide-angle peak (i.e., ξ is related to the full width at half maximum, *fwhm* value; $\xi = 2\pi/fwhm$).

The wide-angle peaks of the ITZ-glycerol samples did not vary significantly (either in intensity or position) with increasing glycerol content, at room temperature. The implications of this observation will be discussed in subsequent sections.

5.4.2.4 Temperature variation of the wide-angle peak

The wide-angle peak (the "amorphous" halo) for each sample was deconvoluted into two sub-peaks, by fitting two pseudo-Voigt functions (see **Figure S5.2** for a sample fit). As we pointed out earlier, the sub-peak at $q \approx 1.3$ Å^{-1}, is more likely related to the average side-to-side (lateral) separation of the close-packed ITZ molecules. The lateral spacings ($d = 2\pi/q$) and the corresponding correlation lengths ($\xi = 2\pi/fwhm$) for the different compositions, are plotted as a function of temperature, in **Figure 5.8**.

Upon cooling from the melt, the average lateral separation of the molecules, for each sample (with or without glycerol), decreased from ~5.1 Å (at 140 °C) to ~4.6 Å (at 30 °C), as shown in **Figure 5.8a**. The correlation lengths increased from ~11 Å in the isotropic phase, to ~19 Å in the smectic phase (**Figure 5.8b**). Major differences were however observed at the mesophase transition temperatures. For neat itraconazole, as well as itraconazole with 1% glycerol, there was a gradual change in the lateral spacing, as well as the correlation lengths, around the temperature of transition to the smectic phase. However, for the samples with glycerol content ≥ 2%, both parameters (d and ξ) changed abruptly at the mesophase transition temperatures. The step change was more pronounced as the glycerol content increased. The abrupt discontinuity in d and ξ at the transition point for

samples with higher glycerol contents, provides independent confirmation that the mesophase transitions become strongly first-order.

Another observation that provides information on the structural packing arrangement is that, at $T < 50°C$, the position of the main wide-angle peak (corresponding lateral spacing 4.8 Å) remained the same for all samples, regardless of the glycerol content (see **Figure 5.8a**; the *d* values between 40 and 50 °C are all ~4.65 Å). This indicates that glycerol did not disrupt the lateral separation of the close packed ITZ molecules. The positional correlation lengths, on the other hand, systematically increased with increasing glycerol content. For example, in **Figure 5.8b**, at 40°C, the correlation length increased from ~17 Å (neat ITZ) to ~20 Å (ITZ + 10% glycerol), in a glycerol concentration-dependent manner. This shows that as the glycerol content increases, the smectic clusters become longer and more highly ordered.

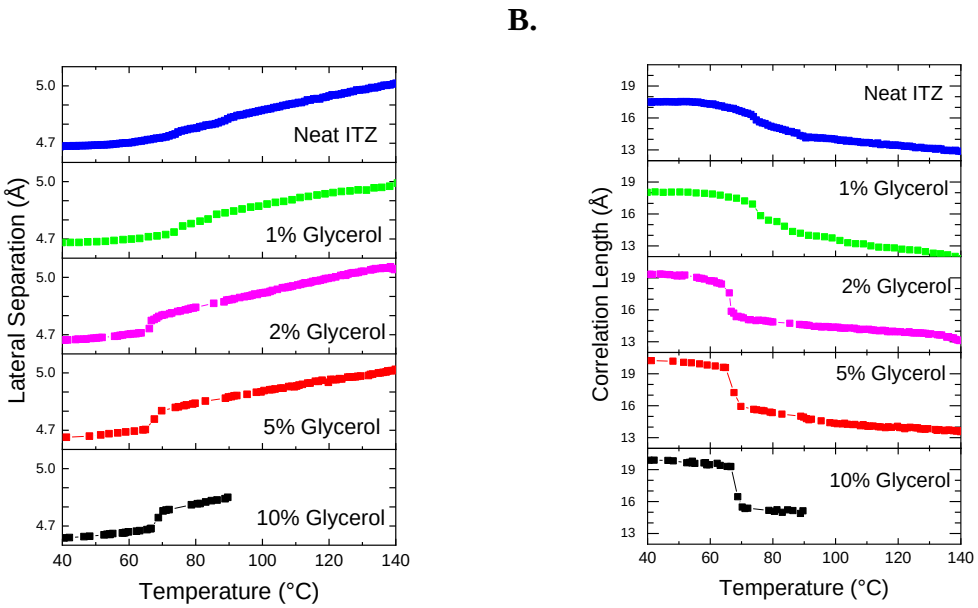

Figure 5.8. Temperature dependence of the (a) average lateral separation ($d = 2\pi/q$) and (b) average bulk correlation length ($d = 2\pi/fwhm$), of the wide-angle peak (sub peak at q~1.3 Å^{-1}) of ITZ with different glycerol contents. Data were obtained as each sample was cooled from the melt.

5.4.3 Drug-plasticizer interactions

The formation of a periodic smectic structure, is driven by interactions between the highly polarizable aromatic cores of mesogens (core-core interactions)[30–32]. An additive that has a high affinity for the host molecule can, in principle, weaken the core-core interactions, thereby disrupting the smectic layers. Itraconazole has electronegative atoms distributed along the rigid molecular core. With glycerol being a ubiquitous hydrogen bond donor, multiple avenues exist for establishment of itraconazole-glycerol hydrogen bonds in the lateral direction, with at least two possible consequences. On the one hand, glycerol, via weak H-bonding, could act as a molecular cross-link that "glues" the itraconazole molecules in the lateral direction resulting in a stable smectic arrangement. On the other

hand, strong ITZ-glycerol interactions could disrupt the core-core (ITZ-ITZ) hydrogen bonding interactions, leading to disruption of the smectic arrangement. We assessed the hydrogen bonding between itraconazole and glycerol using FTIR and NMR spectroscopy.

Figure 5.9 shows the FTIR spectra of itraconazole with and without glycerol. The sharp peak at 1700 cm^{-1} is attributed to the stretching vibration of the carbonyl group of itraconazole. Peaks at 1614 and 1451 cm^{-1} correspond to C-N and C=N stretching vibrations respectively, and peaks at 1230 and 1040 cm^{-1} are most likely from the C-O stretching vibrations. When hydrogen-bonded to glycerol, the C=O, C=N, or C-O stretching peaks of itraconazole would be expected to broaden or to be down-shifted. As shown in **Figure 5.9**, the addition of glycerol did not bring about any significant changes. N-H stretch vibrations, indicative of hydrogen bonding, are typically observed in the 3000-3500 cm^{-1} region. However, O-H stretching vibrations (from glycerol) which also occur in the same region, interfere with the weak N-H absorption band. The possibility of N-H hydrogen bonding was thus investigated using ^{15}N solid-state NMR. As shown in **Figure 5.10**, the NMR spectra of ITZ with and without glycerol are similar, suggesting the absence of hydrogen bonding between ITZ and glycerol.

The NMR and FTIR data indicate that hydrogen bonding, if any, between ITZ and glycerol, will not be strong enough to disrupt the "core-core" (ITZ-ITZ) intermolecular attractive forces that stabilize the smectic layers in the lateral direction. Thus, any glycerol molecules

wedged between the ITZ molecules laterally will more likely strengthen the link between the drug molecules, leading to more rigid smectic layers.

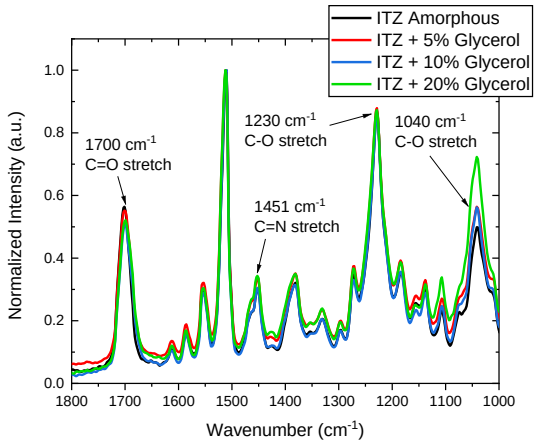

Figure 5.9. FTIR spectrum of neat ITZ, overlaid with spectra of ITZ-glycerol mixtures. Absorbance values of each spectrum have been normalized with the peak maximum at 1515 cm^{-1}. Characteristic bands of interest have been pointed out.

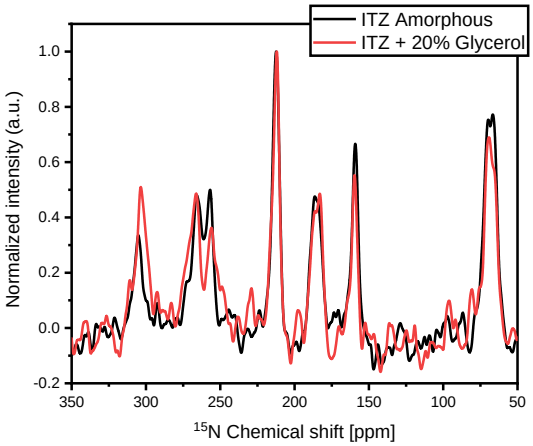

Figure 5.10. Overlay of ^{15}N solid-state NMR spectra. Intensities for each spectrum are normalized to the maximum intensity value (~212 ppm). An overlay of ^{13}C spectra is presented in the supporting information.

5.4.4 Molecular Mobility

Dielectric spectroscopy provides a direct indication of molecular mobility through the measurement of relaxation times (τ). In rod-like liquid crystals possessing large dipole moments, two main relaxation mechanisms are generally expected that can be related to reorientation about the long and short molecular axes[45,204]. Molecular rotations about the long axes are faster, and result in a broad prominent loss peak, commonly referred to as the α-relaxation peak. The α-relaxation process, an effect of the cooperative motions of the molecules, is considered to be responsible for the glass transition. The relaxation mode at the lower frequency (termed the α'-relaxation[185] or the δ-mode[45,204]) can be assigned to rotational fluctuations of the molecule about its short axis (end-over-end rotation). Above the clearing temperature, the two processes may collapse into one broad loss peak.

Figure 5.11(a-c) shows the dielectric loss curves as a function of frequency, measured at multiple temperatures above T_g. The α-relaxation peak is observed within the frequency window. The slow relaxation mode (the α'-peak), though prominent in neat ITZ, was absent in the ITZ-glycerol mixtures (data not shown). Thus, only the faster motions, which indicate precession around the long molecular axes, will be assessed from the dielectric data.

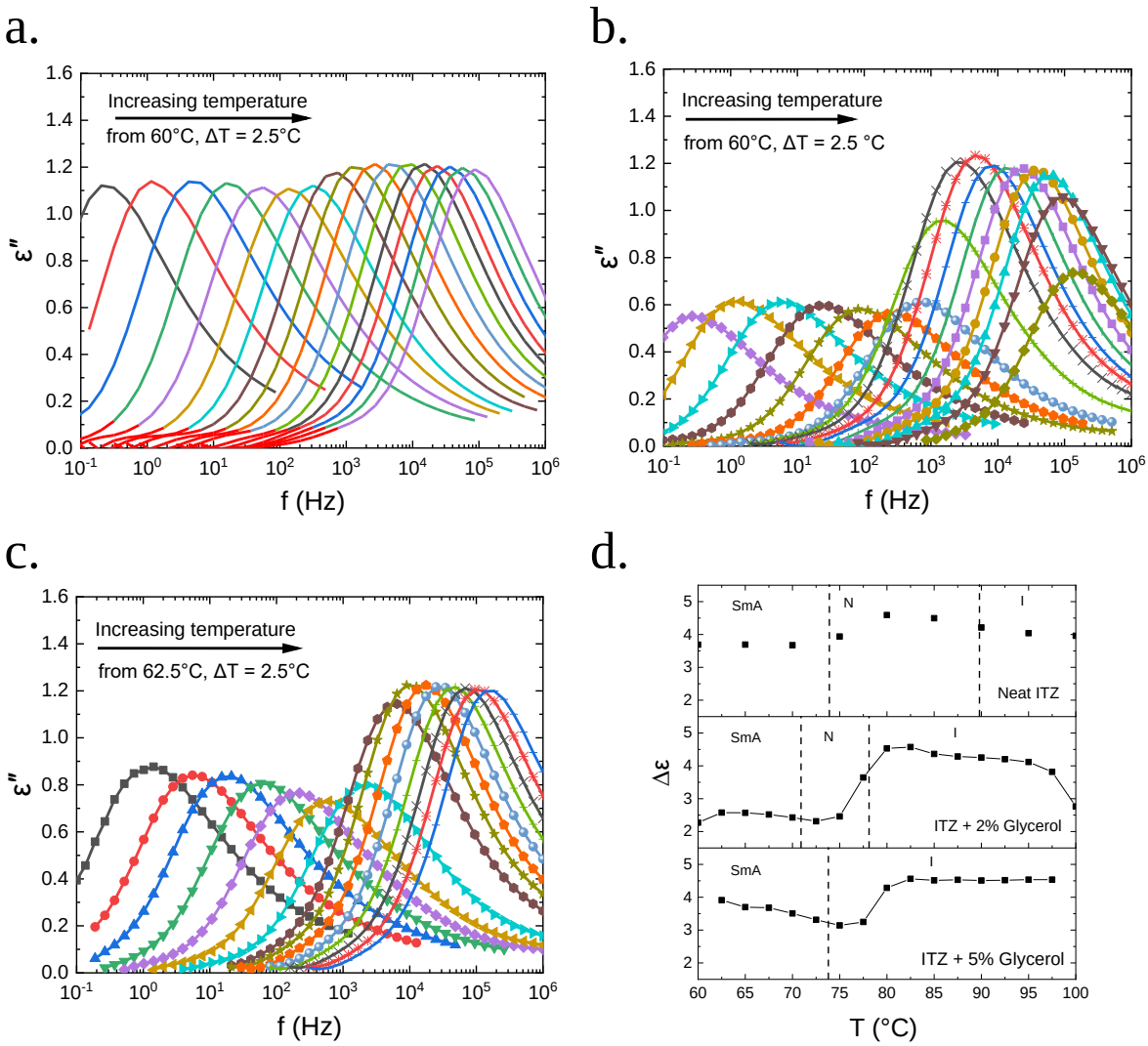

Figure 5.11. Panels a-c show the dielectric loss (ε'') *vs* frequency (f) data, measured at multiple temperatures above the glass transition temperature, on unaligned samples. (a) Neat ITZ (b) ITZ + 2% glycerol, and (c) ITZ + 5% glycerol. For clarity, the DC conductivity contribution has been subtracted. In panel d, the dielectric strength ($\Delta\varepsilon$) is plotted as a function of temperature, for the three samples. The data points are connected by lines, to assist in visualizing the trends. The dashed vertical lines are mesophase transition temperatures observed by DSC, for each composition.

For each sample, the α-peak shifts to higher frequencies with increasing temperature, reflecting an increase in molecular mobility. It is also very clear in **Figure 5.11a**, that the maximum dielectric response, the ε_{max} value, changes abruptly at ~76 °C. This temperature is within the vicinity of the smectic-nematic (SmA-N) phase transition of neat ITZ. The ε_{max} gives an indication of the dielectric strength ($\Delta\varepsilon = \varepsilon_0 - \varepsilon_\infty$; terms defined in the experimental section). The temperature dependence of $\Delta\varepsilon$ is thus shown in **Figure 5.11d**. The dielectric strength is generally considered an indicator of the total number of dipoles participating in the reorientation process. It is clear from **Figure 5.11b** and **c,** that in the smectic phase, the ε_{max} values for the samples containing glycerol, are substantially reduced, when compared to neat ITZ. The suppression of the dielectric strength in the ITZ-glycerol samples, shows that molecular movements in the smectic phase are restricted by the presence of glycerol.

Each dielectric loss spectrum was fitted with the Havriliak Negami function to obtain the characteristic relaxation time, τ. The temperature-dependence of the relaxation times, for each sample, are presented in **Figure 5.12**. The behavior of neat itraconazole (black circles) is well described by the Vogel-Fulcher-Tamman (VFT) function, the fit parameters (τ_0= 1.8×10^{-11} s, E_a=0.08272 eV, T_0=295.2 K) being in agreement with the literature values[184,185,205]. The ITZ-glycerol mixtures however exhibited a different behavior. For each composition, two linear trends in relaxation times with differing slopes can be identified, suggesting two separate activated processes. The two activated processes can be attributed mainly to dipole reorientation in the smectic and the isotropic phases, since

from the DSC analysis, samples with >2%w/w glycerol lacked the nematic phase. Activation energies for the smectic phase are higher, indicating a greater barrier to dipole reorientation, a high degree of order, as well as an increase in local viscosity[45]. The sharp discontinuity in α relaxation times for samples with >2% w/w glycerol, is another clear indication of the strongly first-order character of the I/SmA transition, in agreement with the general observations from the X-ray diffraction and calorimetry data.

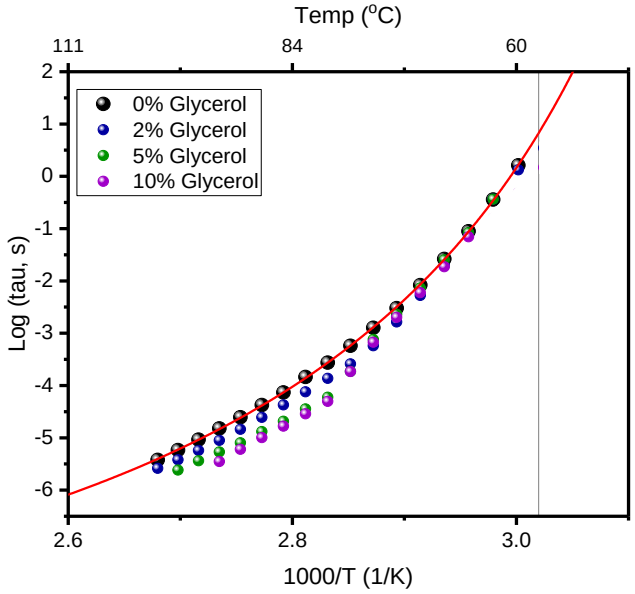

Figure 5.12. Temperature-dependence of α relaxation times for unaligned samples of itraconazole, containing different concentrations of glycerol. The vertical line is the DSC T_g of neat ITZ.

The effect of glycerol on the molecular mobility is evident from **Figure 5.12**. At high temperatures (T > ~72 °C), with increasing glycerol content, there is a systematic decrease in α-relaxation times (increase in mobility). The decrease in α-relaxation times in the isotropic phase, is therefore attributed to the plasticizing effect of glycerol. In the smectic

phase (at T < 72 °C), however, the α-relaxation times for all samples overlap, indicating that the glycerol content does not appreciably influence molecular mobility. As indicated earlier, for rod-like molecules, τ_α signifies rotation about the molecule's long axes. Thus, in the smectic phase, glycerol does not accelerate the rotational movements about the long molecular axis.

5.4.5 Most probable molecular packing model

To understand, at least qualitatively, the structural packing, we consider information from the molecular mobility, synchrotron x-ray diffraction and spectroscopy experiments, together. Because the smectic layer spacing does not change with increasing glycerol content (indicated by the invariance of fundamental (001) X-ray diffraction peak position), it is unlikely that glycerol exclusively occupies the tail ends of the rod-like ITZ molecules. On the other hand, the average lateral spacing of the close-packed molecules (indicated by the wide-angle peak position) does not change significantly with increasing glycerol content either, indicating that glycerol does not separate the ITZ molecules laterally. The invariance of the dielectric spectroscopy alpha relaxation times in the smectic temperature range as the glycerol content increases, show that glycerol does not lubricate the interstitial spaces of the ITZ molecules, but rather strengthens the ITZ-ITZ "core-core" interactions. The most likely scenario, therefore, is that glycerol – possibly via a mechanism similar to the hydrophobic effect – drives the formation of very long, highly-ordered, rigid smectic-A clusters having near-perfect periodicity over several layers, similar to the well-known cybotactic clusters[206].

5.4.6 Effect of smectic layer stabilization on the crystallization tendency below T_g

To evaluate their long-term physical stability, neat itraconazole, as well as the binary mixtures with 2% and 5% glycerol, melt-quenched and pulverized, were filled into DSC pans under dry conditions (0% RH), hermetically sealed, and stored at different temperatures below T_g (25 to 45 °C). Crystallization was monitored periodically with synchrotron radiation.

The 1D X-ray pattern of freshly melt-quenched neat itraconazole did not have liquid crystalline Bragg peaks in the low-angle region (see **Figure 5.3a**). However, with time, the peaks at $q \approx 0.2$ and 0.4 A^{-1} started to appear (see **Figure S5.5** for a representative example at 45 °C). The intensities and sharpness of the peaks increased with storage time, indicating a gradual increase in the degree of smectic order. The positions of the two low angle peaks, however, did not change with time, indicating that the smectic A state persisted at all temperatures for the entire storage duration. Also, characteristic crystalline ITZ peaks did not develop when freshly melt-quenched neat amorphous ITZ was stored at different temperatures below 45 °C, for up to 2 years (**Figure 5.13a**). Itraconazole is a stable glass former and has been classified as a slow crystallizer[194]. The gradual molecular rearrangement from the isotropic, towards the smectic state, under isothermal storage conditions, strongly indicates, that the partially ordered smectic phase is a thermodynamically-stable, equilibrium state. In the glassy region, it is likely that the

smectic phase represents a “local minimum” in the free energy landscape, when compared to the “global minimum” of the three-dimensional crystalline phase[207,208].

The sharp small-angle liquid crystalline peaks ($q \approx 0.2$, 0.4 and 0.6 A^{-1}) were present in the XRD patterns of the freshly prepared binary mixtures containing 2 and 5% w/w glycerol (see **Figure 5.3d**). The positions and intensities of the low angle peaks did not change with time, under isothermal storage conditions (for a representative example, see **Figure S5.6**; ITZ + 5% glycerol, stored at 45 °C). The samples with 2 and 5% w/w glycerol content, also did not crystallize when stored below 45 °C, for up to 2 years (**Figure 5.13b**). The remarkable physical stability of the ITZ-glycerol samples is somewhat counterintuitive, since plasticizers, even at very low concentrations, reduce the glass transition temperature, and invariably accelerate crystallization in amorphous pharmaceuticals. For example, ketoconazole is classified as a slow crystallizer just like itraconazole[194]. However, when prepared with 2% glycerol, the KTZ-glycerol binary mixture crystallized rapidly within 2 days, at 20 °C[57] (the T_g of KTZ decreased from 45 to 30°C). The most likely explanation for the itraconazole situation is that, once the plasticizer accelerates the development of smectic order, the ITZ-glycerol mixtures become more resistant to crystallization because the smectic state is also a thermodynamically stable equilibrium state.

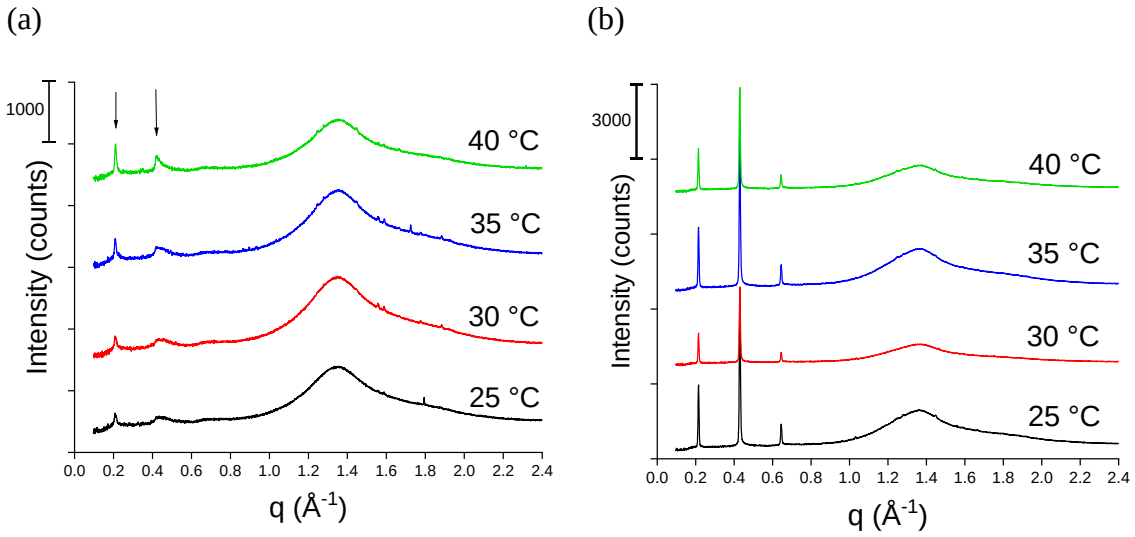

Figure 5.13. Synchrotron XRD patterns obtained after each sample had been stored for 2 years, at the different temperatures indicated. (a) Neat amorphous ITZ, freshly melt-quenched; the two LC peaks at 0.21 and 0.42 $Å^{-1}$, that developed by 2 years, have been pointed out. Minor peaks between 1.5 and 2.0 $Å^{-1}$ are from the aluminum pan. (b) ITZ+2% glycerol.

5.4.7 Effect of smectic layer stabilization on dissolution performance

Finally, to assess the potential impact of the stabilized smectic layers on drug release from a solid oral dosage form, *in vitro* powder dissolution tests were performed. As earlier indicated, amorphous ITZ prepared by rapidly cooling the neat drug from the melt (i.e. melt-quenching), is considered to be free of smectic order. On the other hand, the ITZ+10% glycerol sample, with a translational order parameter >0.9 at room temperature (see **Figure 5.7b**), has the drug molecules existing as highly-ordered smectic layers. The dissolution behaviors of the two samples, were compared to that of an amorphous solid dispersion (ASD) of ITZ prepared with the polymer, polyacrylic acid (PAA). The

ITZ+10% PAA ASD was also considered to be free of smectic order since there was no endotherm associated with the N-SmA transition, in the DSC scan of the ASD[177].

As shown in **Figure 5.14**, drug release from the ITZ+10% glycerol sample was rapid, with the supersaturation level, sustained for the entire duration of the experiment (4 h). It is also clear, that the dissolution performance of the glycerol-containing sample is better than that of neat amorphous ITZ. The smectic phase is the most solid-like mesophase of ITZ. Thus, the substantially high content of smectic layers in the glycerol-containing sample should, in principle, confer a Gibb's free energy level, lower than the energy level of the isotropic phase, but higher than the energy level of the crystalline phase. The rapid drug dissolution rate and sustained supersaturation of the glycerol-containing sample can therefore be attributed to the combined effects of the hydrophilic nature of glycerol and the high free energy of the smectic state. More importantly, since the dissolution performance of the ITZ-glycerol sample is comparable to – or perhaps, marginally better than – the performance of the ASD containing an equal amount of a hydrophilic polymeric additive (**Figure 5.14**, ITZ+10% PAA ASD), the results strongly suggest that the stabilized smectic phase offers a viable avenue to enhancing the bioavailability of poorly water-soluble drugs.

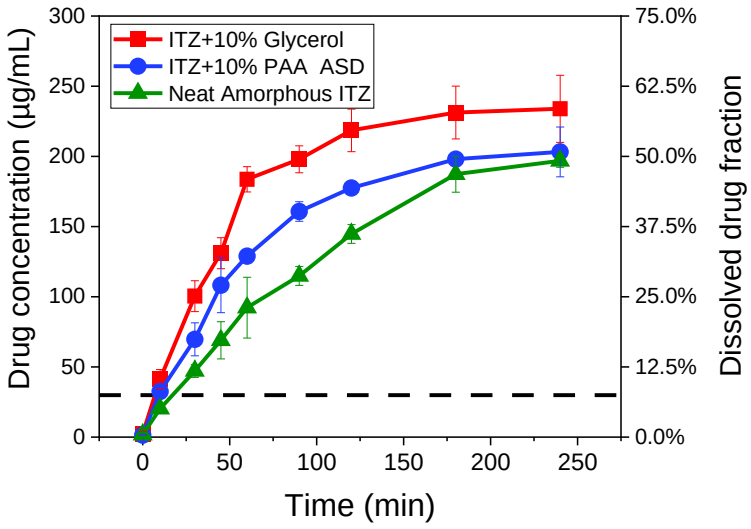

Figure 5.14. *In vitro* dissolution profiles of powder samples in 0.1 N HCl, at 37 °C. (1) Itraconazole + 10% glycerol, possessing highly ordered smectic layers, $\Sigma > 0.9$. (2) Itraconazole + 10% polyacrylic acid amorphous solid dispersion, mostly free of smectic order, and (3) Neat amorphous itraconazole, melt-quenched, and mostly free of smectic order. The horizontal dashed line represents the solubility of crystalline itraconazole, measured under the same conditions.

5.5 SIGNIFICANCE

It is well known that plasticizers generally accelerate molecular mobility and thereby crystallization (i.e. to the 3D crystalline structure) of amorphous compounds[209]. In this work, we have shown the unusual effect of glycerol, selectively accelerating the development of smectic order in thermotropic liquid crystal itraconazole, and consequently stabilizing the mesophase. The highly ordered smectic arrangement may offer the two-pronged advantage of good physical stability with increased dissolution performance. As

more mesogenic APIs are identified, other additive-induced unusual phase sequences might be reported, with a clearer picture emerging about the pharmaceutical relevance of these partially ordered states. It may very well turn out that plasticizers, at low concentrations, are stabilizers for a wide range of mesogenic APIs.

5.6 CONCLUSIONS

In our earlier work, we investigated the effects of glycerol on the phase behavior of itraconazole (ITZ), a thermotropic liquid crystal. A phase diagram was constructed, based on differential scanning calorimetry transition temperatures. Detailed investigations on the critical behavior (and the order) of the transitions were also performed with adiabatic scanning calorimetry[24]. With increasing glycerol content, the nematic temperature range of neat ITZ was systematically reduced, and eventually eliminated, resulting in direct I-SmA transition.

In this report, we investigated the structural packing arrangement, molecular mobility, physical stability and dissolution performance of the ITZ-glycerol mixtures. Consistent with the observations from calorimetry, synchrotron X-ray diffraction experiments revealed that the ITZ-glycerol mixtures had exceptionally well-ordered smectic A layers. The smectic order parameter, which characterizes the quality of smectic layering, could be systematically varied from 0.47 (neat ITZ) to as high as 0.92 (ITZ+5% glycerol), without a change in the type of smectic arrangement (i.e. the smectic A state persisted). Information from a range of complementary techniques (dielectric, infrared and NMR spectroscopy, as

well as synchrotron X-ray diffractometry) confirmed that the ITZ-glycerol binary mixtures formed rigid smectic clusters in the vitrified state, which were stable when the samples were stored, for up to 2 years, at pharmaceutically relevant temperatures. The binary mixtures also achieved and sustained much higher drug concentration levels than the neat drug, when powder dissolution tests were performed.

5.7 ACKNOWLEDGEMENTS

This project was funded by the National Science Foundation (grant number NSF-CMMI-1662046) and partially supported by the William and Mildred Peters endowment fund. KKAE acknowledges the Bighley Graduate Student Fellowship. The research used resources of the Advanced Photon Source, a US Department of Energy (DOE) Office of Science User Facility, operated for the DOE Office of Science by Argonne National Laboratory, under contract number DE-AC02-06CH11357. Dr. Wenquian Hu and Dr. Andrey Yakovenko (beamline 17-BM-B) are acknowledged for their help. The authors are grateful to Dr. Jan Thoen and Dr. Jorge Vinals for enlightening discussions.

5.8 SUPPORTING INFORMATION

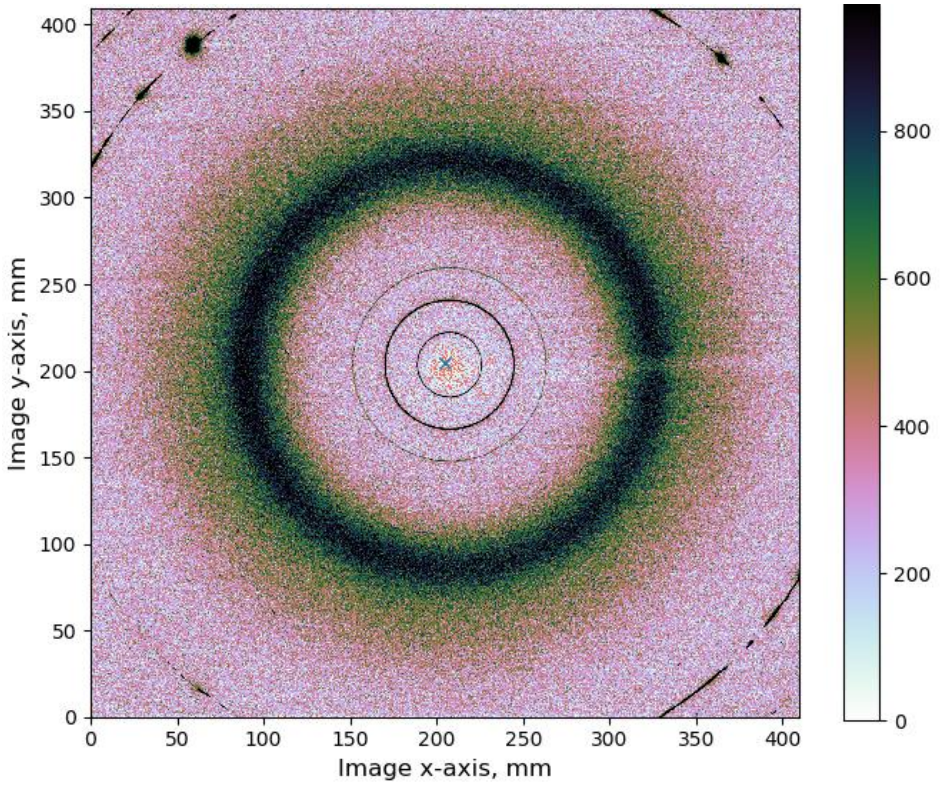

Figure S5.1. Representative 2D synchrotron diffraction image of an ITZ + 5% glycerol sample, collected at ~30°C. The sample was unaligned, resulting in uniform diffraction rings. The three inner rings are characteristic of the smectic layers. The diffuse ring, commonly referred to as the amorphous halo, indicates the lateral spacing of the close-packed ITZ molecules. The two outermost incomplete rings are from the aluminum sample pan.

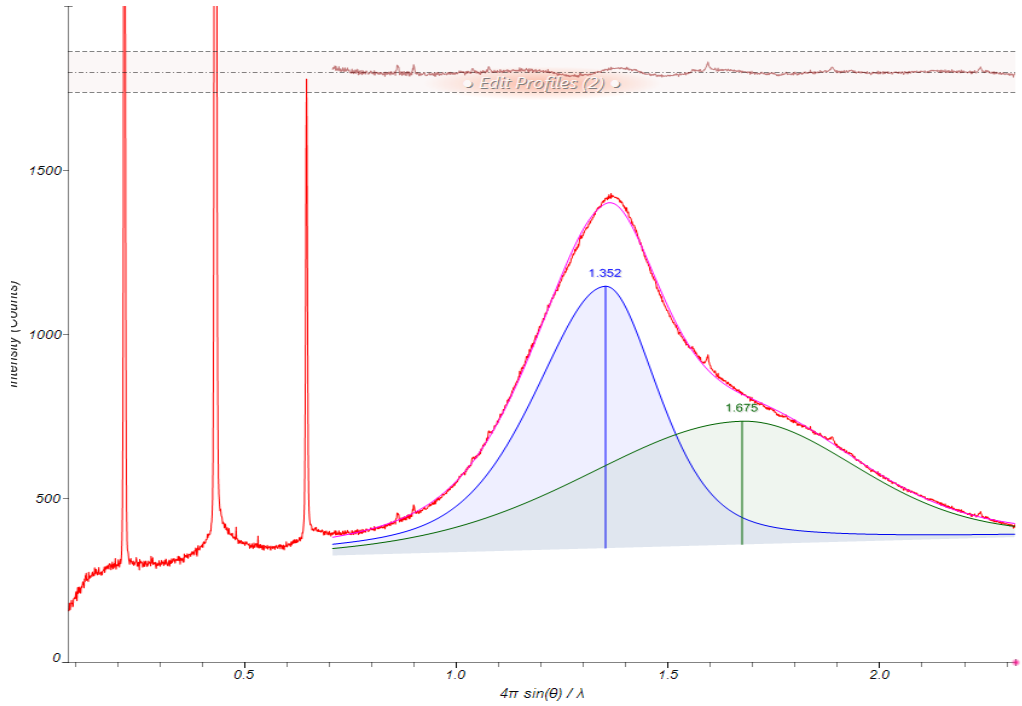

Figure S5.2. Representative fit, showing the deconvolution of the diffuse wide-angle peak (q from 0.7 to 2.3 Å^{-1}) of itraconazole containing glycerol (5% w/w), into two sub-peaks. The red curve is the experimental data profile. The blue and green shaded areas are the sub-peaks. The pink trace is the combined fitted profile, with the corresponding fitting residuals shown at the top.

(a)

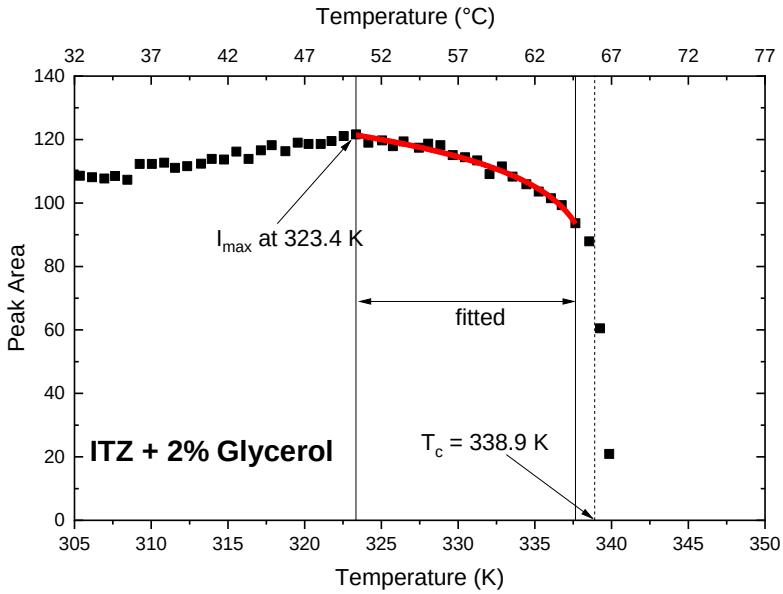
Temperature (°C)
32 37 42 47 52 57 62 67 72 77
140 120 100 80 60 40 20 0
Peak Area
I_{max} at 323.4 K
fitted
ITZ + 2% Glycerol
T_c = 338.9 K
305 310 315 320 325 330 335 340 345 350
Temperature (K)

(b)

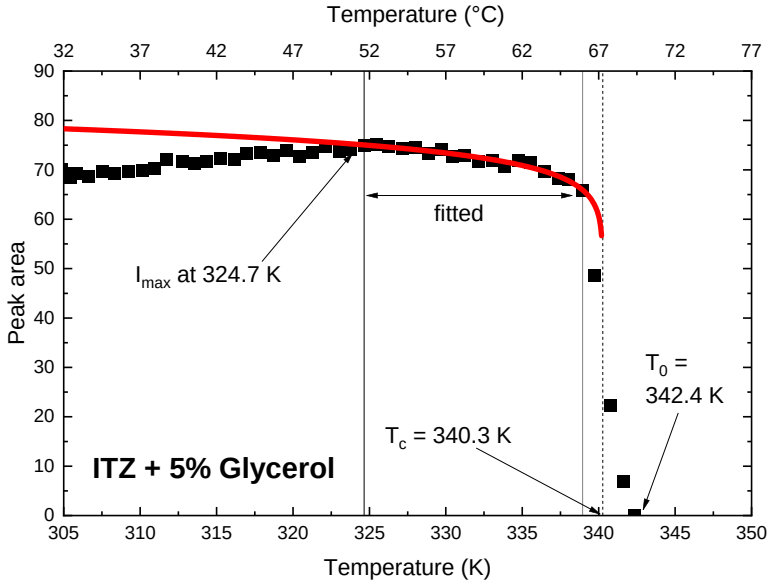
Temperature (°C)
32 37 42 47 52 57 62 67 72 77
90 80 70 60 50 40 30 20 10 0
Peak area
fitted
I_{max} at 324.7 K
T_0 = 342.4 K
T_c = 340.3 K
ITZ + 5% Glycerol
305 310 315 320 325 330 335 340 345 350
Temperature (K)

(c)

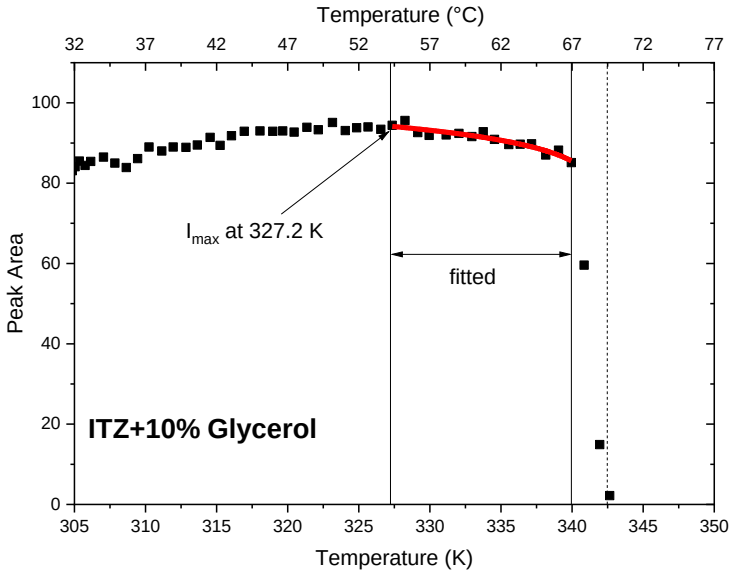

Figure S5.3. Temperature dependence of the area of the $q \approx 0.2$ Å^{-1} peak for (a) ITZ+2% glycerol, (b) ITZ+5% glycerol, and (c) ITZ+10% glycerol. The red curves are fits of equation (5.5) to the data in the high-temperature region (>50 °C). The range of data included in the fitting is indicated by solid vertical lines. T_c , indicated by the dashed vertical line, is separated by a few degrees from T_0, the first-order transition temperature, which is a characteristic behavior of strong first-order transitions[30]. Fit parameters are listed in Table 5.1.

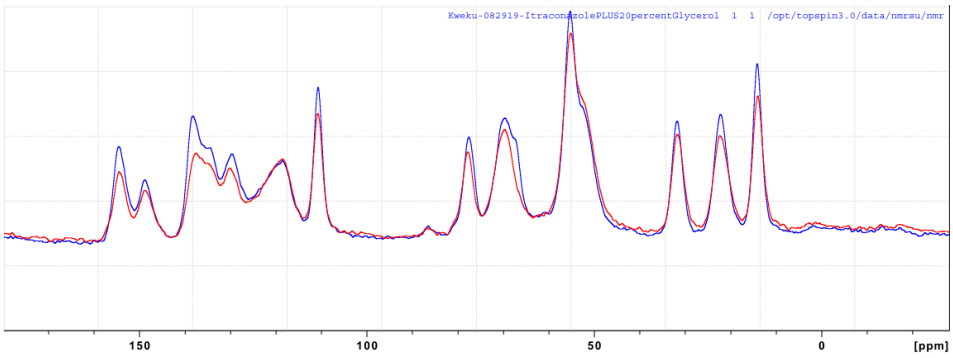

Figure S5.4. Overlay of one-dimensional ^{13}C NMR spectra for neat ITZ (blue) and ITZ + 20% glycerol (red). No significant differences are observed between the spectra.

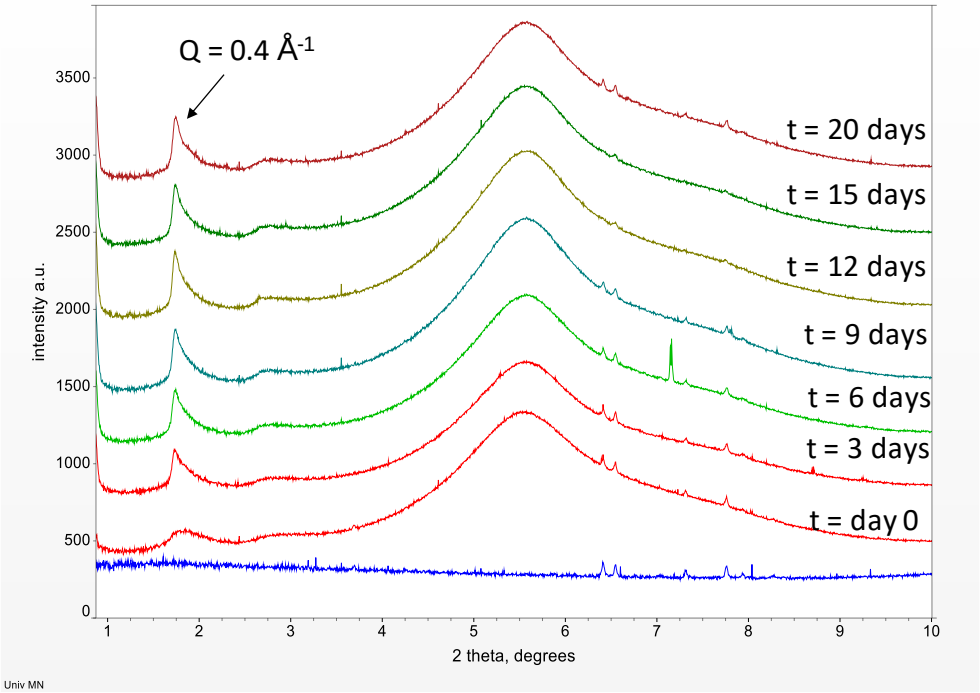

Figure S5.5 Synchrotron XRD patterns of neat amorphous itraconazole (rapidly quenched from the melt), held isothermally at 45 °C for various storage durations, *t*. The gradual development of smectic order, is indicated by the appearance and sharpening of the liquid crystalline peak at q=0.4 $Å^{-1}$ (pointed out). The peak at q=0.2 $Å^{-1}$ was not captured in its entirety. The bottom blue pattern is that of an empty pan, showing the pan peaks.

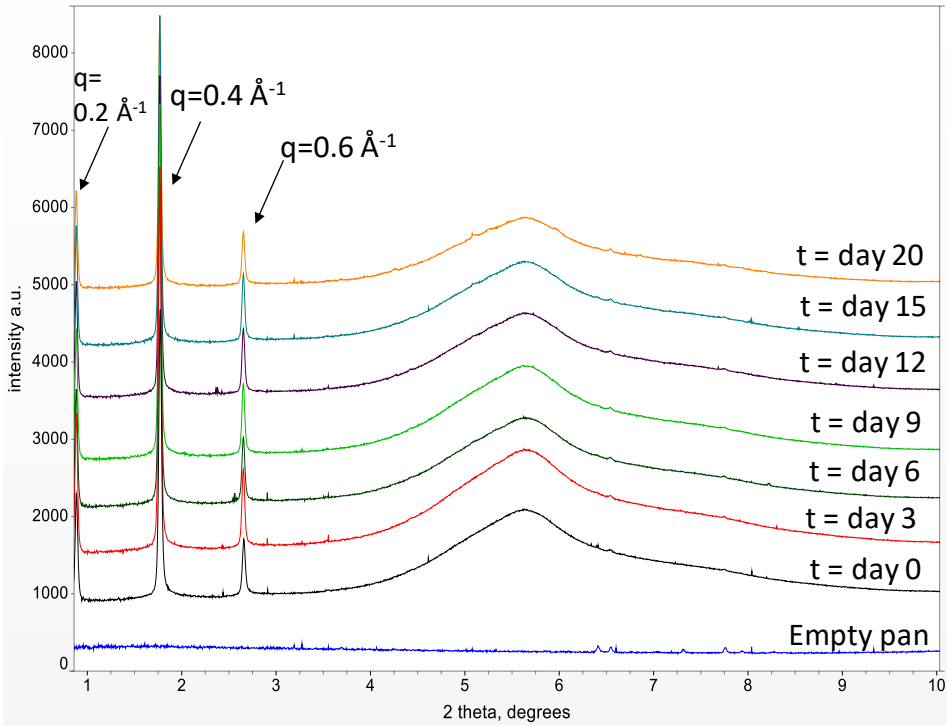

Figure S5.6 Synchrotron XRD patterns of ITZ+5% glycerol samples, held isothermally at 45 °C for various storage durations, t. The characteristic LC peaks remain at their original positions, indicating that smectic A state persists. The peak at q=0.2 $Å^{-1}$ was not captured in its entirety. The bottom blue pattern is that of an empty pan, showing the pan peaks.

6 CONCLUSIONS AND RECOMMENDATIONS FOR FUTURE RESEARCH

In ***Chapter 2***, we investigated the influence of drug–polymer interactions on the dissolution performance of amorphous solid dispersions, using ketoconazole (KTZ) and three polymers, PAA, PVP and PHEMA, as model compounds. With three techniques – NOESY, DOSY, and ITC – we identified, confirmed and quantified KTZ–PAA interactions in the aqueous medium. The interaction was linked to an increased duration of supersaturation.

This study can be extended to a wider variety of drug–polymer systems, in order to draw a more generalized conclusion. Drug–polymer interactions have been characterized in the solid state in many model systems. For example, nifedipine interacts with PVP via strong hydrogen bonding, but not with PAA[63]. Indomethacin (weakly acidic), also interacts with PVP, but not with PAA or poly(ethylene glycol)[58,61]. In our preliminary studies, we determined the crystallization propensities of the nifedipine and indomethacin ASDs mentioned above, in aqueous buffers. Consistent with our working hypothesis, the crystallization trends reported in the solid state, were also observed in aqueous media. Dissolution profiles of these and other systems can be determined, and the interactions

monitored using either analytical ultracentrifugation, or high-resolution NMR. The next step would be to assess the *in vivo* behavior of the ASDs.

In ***Chapter 3***, we explored the use of analytical ultracentrifugation (AUC) for characterizing drug–polymer interactions in aqueous solution. We showed how differences in UV absorbance profiles of drugs and polymers can enable the sedimentation behavior of the drug to be monitored, within the polymer matrix. The UV detection method was able to address the problem of poor signal sensitivity, generally encountered when the model drugs are dissolved in water. Also, consistent with our expectations, shifts in sedimentation coefficient values (s-values) of the drug–polymer mixtures were observed, indicative of interactions. The major problem, however, was that the s-value shifts were not very strong, reflecting the weak nature of the interactions, and thereby limiting the utility of AUC in this regard. We expect the AUC technique to be more suitable for characterizing drug–polymer interactions that are much stronger than the interactions probed in the current study. This study can thus be repeated, with a focus on polymers designed to have substantial hydrophobic content which will very likely interact more strongly with the typical small molecule drugs, in water.

When suitable drug–polymer pairs have been identified, it would be worthwhile comparing interactions probed by the AUC technique, to interactions probed by diffusion ordered spectroscopy (DOSY). Both techniques measure diffusion coefficients, and it would be helpful to know the extent of agreement between the two techniques. While the diffusion

data from AUC are easier to interpret, compared to the complex NMR peak assignments that are a prerequisite for DOSY analyses, NMR spectrometers are more readily available/accessible than analytical ultracentrifuges.

In spite of the limitations in characterizing drug–polymer interactions, the AUC technique can be very useful for routine characterization of the hydrodynamic behavior of pharmaceutical polymers. This was evident from the unique sedimentation profiles that were obtained for the different polymers. The model-free physical parameters that can be obtained simultaneously from AUC analyses, are often important input parameters for mathematical models that describe the dissolution behavior of ASDs[83,210,211]. Such parameters can be obtained in a single experiment, when viscosity and partial specific volume measurements are available.

In ***Chapters 4 and 5***, we investigated the mechanism by which glycerol modified the mesogenic properties of itraconazole (ITZ). The temperature range of the nematic phase of ITZ systematically reduced, until a critical glycerol concentration, where the ITZ-glycerol binary mixtures transitioned directly from the Isotropic liquid (I) to the smectic A (SmA) state. The I-SmA transition was confirmed to be a strong first-order transition, in agreement with standard liquid crystalline (LC) theories and the ITZ-glycerol mixtures were found to be very stable.

It will be useful to investigate if glycerol can similarly accelerate the development of smectic order in a wider variety of LCs (both pharmaceutical and non-pharmaceutical compounds). Unusual phase sequences may be observed, which may result in other useful material properties. Posaconazole, saperconazole, pramiconazole, and terconazole are structurally similar to itraconazole. It has already been suggested that posaconazole does not have smectic phases, even though it does have nematic-like characteristics[212]. Saperconazole on the other hand does have the same mesomorphic sequence as itraconazole, albeit with different temperature ranges[213]. It will be interesting to know if glycerol can induce smectic order in posaconazole, or stabilize the smectic phase of saperconazole.

Apart from glycerol, other additives may similarly modulate the phase behavior of pharmaceutical LCs. Preliminary experiments conducted using polyalcohols with different lengths of carbon chains – ethylene glycol (2C), erythritol (4C), xylitol (5C), and sorbitol (6C) – showed that the smectic state was similarly potentiated by these additives, even though the phase sequences were different. The effect of the molecular length – and thereby the flexibility – of the additive on the LC phase transition sequences, as well as the translational and orientational order parameters, can be investigated using the protocols applied in this thesis.

When additives are used to induce (and possibly isolate) intermediate LC phases, the physical stability and the dissolution of the LC phases can be less ambiguously

investigated. This would strengthen the hypothesis that mesomorphic phases provide an alternative route for physical stability enhancement, with improved dissolution performance.

Co-amorphous systems are emerging as an alternative way of delivering two or more BCS Class II active pharmaceutical ingredients (APIs). When either of the APIs is mesogenic, attempts at co-amorphization could easily result in liquid crystalline host-guest effects. The effects of the other small-molecule drugs (having or lacking mesogenic properties), on thermotropic LCs can be investigated. This will help formulation scientists understand how any unique packing arrangements that result from such binary mixtures+, affect the physical stability, dissolution behavior, and other critical quality attributes of the drugs.

7 BIBLIOGRAPHY

(1) Lipinski, C. A.; Lombardo, F.; Dominy, B. W.; Feeney, P. J. Experimental and Computational Approaches to Estimate Solubility and Permeability in Drug Discovery and Development Settings. *Adv. Drug Deliv. Rev.* **1997**, *23* (96), 3–25. https://doi.org/10.1016/S0169-409X(00)00129-0.

(2) Chessari, G.; Woodhead, A. J. From Fragment to Clinical Candidate—a Historical Perspective. *Drug Discov. Today* **2009**, *14* (13–14), 668–675. https://doi.org/10.1016/j.drudis.2009.04.007.

(3) Amidon, G. L.; Lennernäs, H.; Shah, V. P.; Crison, J. R. A Theoretical Basis for a Biopharmaceutic Drug Classification: The Correlation of in Vitro Drug Product Dissolution and in Vivo Bioavailability. *Pharm. Res. An Off. J. Am. Assoc. Pharm. Sci.* **1995**, *12* (3), 413–420. https://doi.org/10.1023/A:1016212804288.

(4) Babu, N. J.; Nangia, A. Solubility Advantage of Amorphous Drugs and Pharmaceutical Cocrystals. *Cryst. Growth Des.* **2011**, *11* (7), 2662–2679. https://doi.org/10.1021/cg200492w.

(5) Williams, H. D.; Trevaskis, N. L.; Charman, S. A.; Shanker, R. M.; Charman, W. N.; Pouton, C. W.; Porter, C. J. H. Strategies to Address Low Drug Solubility in Discovery and Development. *Pharmacol. Rev.* **2013**, *65* (1), 315–499. https://doi.org/10.1124/pr.112.005660.

(6) Serajuddin, A. T. M. Salt Formation to Improve Drug Solubility. *Advanced Drug Delivery Reviews*. 2007. https://doi.org/10.1016/j.addr.2007.05.010.

(7) Schultheiss, N.; Newman, A. Pharmaceutical Cocrystals and Their Physicochemical Properties. *Cryst. Growth Des.* **2009**, *9* (6), 2950–2967. https://doi.org/10.1021/cg900129f.

(8) Newman, A.; Knipp, G.; Zografi, G. Assessing the Performance of Amorphous Solid Dispersions. *J. Pharm. Sci.* **2012**, *101* (4), 1355–1377. https://doi.org/10.1002/jps.23031.

(9) Rekharsky, M. V.; Inoue, Y. Complexation Thermodynamics of Cyclodextrins.

Chem. Rev. **1998**, *98* (5), 1875–1918. https://doi.org/10.1021/cr970015o.

(10) Rumondor, A. C. F.; Dhareshwar, S. S.; Kesisoglou, F. Amorphous Solid Dispersions or Prodrugs: Complementary Strategies to Increase Drug Absorption. *J. Pharm. Sci.* **2016**. https://doi.org/10.1016/j.xphs.2015.11.004.

(11) Taylor, L. S.; Zhang, G. G. Z. Physical Chemistry of Supersaturated Solutions and Implications for Oral Absorption. *Adv. Drug Deliv. Rev.* **2016**, *101*, 122–142. https://doi.org/10.1016/j.addr.2016.03.006.

(12) Leuner, C.; Dressman, J. Improving Drug Solubility for Oral Delivery Using Solid Dispersions. *Eur. J. Pharm. Biopharm.* **2000**, *50* (1), 47–60. https://doi.org/10.1016/S0939-6411(00)00076-X.

(13) Overview, S. S. D. A.; Friesen, D. T.; Shanker, R.; Crew, M.; Smithey, T.; Curatolo, W. J.; Nightingale, J. A. S.; Curatolo, W. J.; Nightingale, J. A. S. Spray-Dried Dispersions : An Overview. **2008**, *5* (6), 1003–1019.

(14) Friesen, D. T.; Shanker, R.; Crew, M.; Smithey, D. T.; Curatolo, W. J.; Nightingale, J. A. S. Hydroxypropyl Methylcellulose Acetate Succinate-Based Spray-Dried Dispersions: An Overview. *Mol. Pharm.* **2008**, *5* (6), 1003–1019. https://doi.org/10.1021/mp8000793.

(15) Chen, Y.; Liu, C.; Chen, Z.; Su, C.; Hageman, M.; Hussain, M.; Haskell, R.; Stefanski, K.; Qian, F. Drug-Polymer-Water Interaction and Its Implication for the Dissolution Performance of Amorphous Solid Dispersions. *Mol. Pharm.* **2015**, *12* (2), 576–589. https://doi.org/10.1021/mp500660m.

(16) Craig, D. Q. . The Mechanisms of Drug Release from Solid Dispersions in Water-Soluble Polymers. *Int. J. Pharm.* **2002**, *231* (2), 131–144. https://doi.org/10.1016/S0378-5173(01)00891-2.

(17) Zhou, D.; Zhang, G. G. Z.; Law, D.; Grant, D. J. W.; Schmitt, E. A. Physical Stability of Amorphous Pharmaceuticals: Importance of Configurational Thermodynamic Quantities and Molecular Mobility. *J. Pharm. Sci.* **2002**, *91* (8), 1863–1872. https://doi.org/10.1002/jps.10169.

(18) Bhugra, C.; Pikal, M. J. Role of Thermodynamic, Molecular, and Kinetic Factors in Crystallization from the Amorphous State. *J. Pharm. Sci.* **2008**, *97* (4), 1329–1349. https://doi.org/10.1002/jps.21138.

(19) Grzybowska, K.; Capaccioli, S.; Paluch, M. Recent Developments in the Experimental Investigations of Relaxations in Pharmaceuticals by Dielectric Techniques at Ambient and Elevated Pressure. *Adv. Drug Deliv. Rev.* **2016**, *100*, 158–182. https://doi.org/10.1016/j.addr.2015.12.008.

(20) Kumar, S. *Liquid Crystals: Experimental Study of Physical Properties and Phase Transitions*; Kumar, S., Ed.; Cambridge University Press: Cambridge, 2001.

(21) Stevenson, C. L.; Bennett, D. B.; Lechuga-Ballesteros, D. Pharmaceutical Liquid Crystals: The Relevance of Partially Ordered Systems. *J. Pharm. Sci.* **2005**, *94* (9), 1861–1880. https://doi.org/10.1002/jps.20435.

(22) Bunjes, H.; Rades, T. Thermotropic Liquid Crystalline Drugs. *J. Pharm. Pharmacol.* **2005**, *57* (7), 807–816. https://doi.org/10.1211/0022357056208.

(23) Ghebremeskel, A. N.; Vemavarapu, C.; Lodaya, M. Use of Surfactants as Plasticizers in Preparing Solid Dispersions of Poorly Soluble API: Selection of Polymer–Surfactant Combinations Using Solubility Parameters and Testing the Processability. *Int. J. Pharm.* **2007**, *328* (2), 119–129. https://doi.org/10.1016/j.ijpharm.2006.08.010.

(24) Amponsah-Efah, K. K.; Glorieux, C.; Thoen, J.; Suryanarayanan, R. Effect of Glycerol on the Order of the Mesophase Transitions of Supercooled Itraconazole. *J. Mol. Liq.* **2020**, *320*, 114222. https://doi.org/10.1016/j.molliq.2020.114222.

(25) Wunderlich, B. A Classification of Molecules, Phases, and Transitions as Recognized by Thermal Analysis. *Thermochim. Acta* **1999**, *340*, 37–52. https://doi.org/10.1016/S0040-6031(99)00252-X.

(26) Kawakami, K.; Pikal, M. J. Calorimetric Investigation of the Structural Relaxation of Amorphous Materials: Evaluating Validity of the Methodologies. *J. Pharm. Sci.* **2005**, *94* (5), 948–965. https://doi.org/10.1002/jps.20298.

(27) Badrinarayanan, P.; Zheng, W.; Li, Q.; Simon, S. L. The Glass Transition Temperature versus the Fictive Temperature. *J. Non. Cryst. Solids* **2007**, *353* (26), 2603–2612. https://doi.org/10.1016/j.jnoncrysol.2007.04.025.

(28) *Handbook of Liquid Crystals*; Demus, D., Goodby, J., Gray, G. W., Spiess, H.-W., Vill, V., Eds.; Wiley-VCH: Weinheim, 1998.

(29) Kato, T.; Uchida, J.; Ichikawa, T.; Sakamoto, T. Functional Liquid Crystals towards the Next Generation of Materials. *Angew. Chemie Int. Ed.* **2018**, *57* (16), 4355–4371. https://doi.org/10.1002/anie.201711163.

(30) Kapernaum, N.; Giesselmann, F. Simple Experimental Assessment of Smectic Translational Order Parameters. *Phys. Rev. E* **2008**, *78* (6), 062701. https://doi.org/10.1103/PhysRevE.78.062701.

(31) McMillan, W. L. Simple Molecular Model for the Smectic A Phase of Liquid Crystals. *Phys. Rev. A* **1971**, *4* (3), 1238–1246. https://doi.org/10.1103/PhysRevA.4.1238.

(32) McMillan, W. L. X-Ray Scattering from Liquid Crystals. I. Cholesteryl Nonanoate and Myristate. *Phys. Rev. A* **1972**, *6* (3), 936–947. https://doi.org/10.1103/PhysRevA.6.936.

(33) Thoen, J. Thermal Investigations of Phase Transitions in Thermotropic Liquid Crystals. *Int. J. Mod. Phys. B* **1995**, *09* (18n19), 2157–2218. https://doi.org/10.1142/S0217979295000860.

(34) Mukherjee, P. K.; Khan, B. C. Nematic to Smectic-A Phase Transition in Mixture of Liquid Crystal and Nonmesogenic Impurities: Existence of Tricritical Point. *Liq. Cryst.* **2019**, *46* (7), 1060–1066. https://doi.org/10.1080/02678292.2018.1555722.

(35) Mukherjee, P. K. Isotropic to Smectic-A Phase Transition: A Review. *J. Mol. Liq.* **2014**, *190*, 99–111. https://doi.org/10.1016/j.molliq.2013.11.001.

(36) de Gennes, P. G. An Analogy between Superconductors and Smectics A. *Solid State Commun.* **1972**, *10* (9), 753–756. https://doi.org/10.1016/0038-1098(72)90186-X.

(37) de Gennes, P. G.; Prost, J. *The Physics of Liquid Crystals*, Second.; Oxford University Press, 1993.

(38) Kobayashi, K. K. On the Theory of Translational and Orientational Melting with Application to Liquid Crystals. *Phys. Lett. A* **1970**, *31* (3), 125–126. https://doi.org/10.1016/0375-9601(70)90186-6.

(39) Sigdel, K. P.; Iannacchione, G. S. Study of the Isotropic to Smectic-A Phase Transition in Liquid Crystal and Acetone Binary Mixtures. *J. Chem. Phys.* **2010**, *133* (17), 174501. https://doi.org/10.1063/1.3502112.

(40) Wen, X.; Garland, C. W.; Shashidhar, R.; Barois, P. Calorimetric Study of the Smectic-Ad - Smectic-A2 Critical Point in a Binary Mixture of Homologs. *Phys. Rev. B* **1992**, *45* (10), 5131–5139. https://doi.org/10.1103/PhysRevB.45.5131.

(41) Denolf, K.; Van Roie, B.; Glorieux, C.; Thoen, J. Effect of Nonmesogenic Impurities on the Order of the Nematic to Smectic-A Phase Transition in Liquid Crystals. *Phys. Rev. Lett.* **2006**, *97* (10), 1–4. https://doi.org/10.1103/PhysRevLett.97.107801.

(42) Shalaev, E.; Wu, K.; Shamblin, S.; Krzyzaniak, J. F.; Descamps, M. Crystalline Mesophases: Structure, Mobility, and Pharmaceutical Properties. *Adv. Drug Deliv. Rev.* **2016**, *100*, 194–211. https://doi.org/10.1016/j.addr.2016.04.002.

(43) Ngai, K. L.; Paluch, M. Classification of Secondary Relaxation in Glass-Formers Based on Dynamic Properties. *J. Chem. Phys.* **2004**, *120* (2), 857–873. https://doi.org/10.1063/1.1630295.

(44) Ngai, K. L.; Magill, J. H.; Plazek, D. J. Flow, Diffusion and Crystallization of Supercooled Liquids: Revisited. *J. Chem. Phys.* **2000**, *112* (4), 1887–1892. https://doi.org/10.1063/1.480752.

(45) Dunmur, D.; Toriyama, K. Dielectric Properties. In *Handbook of Liquid Crystals Set*; Wiley-VCH Verlag GmbH: Weinheim, Germany, 2008; pp 231–252. https://doi.org/10.1002/9783527619276.ch7da.

(46) Lunkenheimer, P.; Wehn, R.; Schneider, U.; Loidl, A. Glassy Aging Dynamics.

Phys. Rev. Lett. **2005**, *95* (5), 055702. https://doi.org/10.1103/PhysRevLett.95.055702.

(47) Casalini, R.; Roland, C. M. Aging of the Secondary Relaxation to Probe Structural Relaxation in the Glassy State. *Phys. Rev. Lett.* **2009**, *102* (3), 035701. https://doi.org/10.1103/PhysRevLett.102.035701.

(48) Liu, H.; Taylor, L. S.; Edgar, K. J. The Role of Polymers in Oral Bioavailability Enhancement; a Review. *Polymer (Guildf).* **2015**, *77*, 399–415. https://doi.org/10.1016/j.polymer.2015.09.026.

(49) Mosquera-Giraldo, L. I.; Borca, C. H.; Parker, A. S.; Dong, Y.; Edgar, K. J.; Beaudoin, S. P.; Slipchenko, L. V.; Taylor, L. S. Crystallization Inhibition Properties of Cellulose Esters and Ethers for a Group of Chemically Diverse Drugs: Experimental and Computational Insight. *Biomacromolecules* **2018**, *19* (12), 4593–4606. https://doi.org/10.1021/acs.biomac.8b01280.

(50) Shamma, R. N.; Basha, M. Soluplus®: A Novel Polymeric Solubilizer for Optimization of Carvedilol Solid Dispersions: Formulation Design and Effect of Method of Preparation. *Powder Technol.* **2013**, *237*, 406–414. https://doi.org/10.1016/j.powtec.2012.12.038.

(51) LaFountaine, J. S.; McGinity, J. W.; Williams, R. O. Challenges and Strategies in Thermal Processing of Amorphous Solid Dispersions: A Review. *AAPS PharmSciTech* **2016**, *17* (1), 43–55. https://doi.org/10.1208/s12249-015-0393-y.

(52) Mistry, P.; Mohapatra, S.; Gopinath, T.; Vogt, F. G.; Suryanarayanan, R. Role of the Strength of Drug–Polymer Interactions on the Molecular Mobility and Crystallization Inhibition in Ketoconazole Solid Dispersions. *Mol. Pharm.* **2015**, *12* (9), 3339–3350. https://doi.org/10.1021/acs.molpharmaceut.5b00333.

(53) Miyazaki, T.; Yoshioka, S.; Aso, Y.; Kojima, S. Ability of Polyvinylpyrrolidone and Polyacrylic Acid to Inhibit the Crystallization of Amorphous Acetaminophen. *J. Pharm. Sci.* **2004**, *93* (11), 2710–2717. https://doi.org/10.1002/jps.20182.

(54) Mehta, M.; McKenna, G. B.; Suryanarayanan, R. Molecular Mobility in Glassy Dispersions. *J. Chem. Phys.* **2016**, *144* (20), 204506. https://doi.org/10.1063/1.4950768.

(55) Kothari, K.; Ragoonanan, V.; Suryanarayanan, R. Influence of Molecular Mobility on the Physical Stability of Amorphous Pharmaceuticals in the Supercooled and Glassy States. *Mol. Pharm.* **2014**, *11* (9), 3048–3055. https://doi.org/10.1021/mp500229d.

(56) Bhardwaj, S. P.; Arora, K. K.; Kwong, E.; Templeton, A.; Clas, S.; Suryanarayanan, R. Mechanism of Amorphous Itraconazole Stabilization in Polymer Solid Dispersions: Role of Molecular Mobility. **2014**. https://doi.org/10.1021/mp5004515.

(57) Fung, M. H.; Suryanarayanan, R. Use of a Plasticizer for Physical Stability Prediction of Amorphous Solid Dispersions. *Cryst. Growth Des.* **2017**, *17* (8), 4315–4325. https://doi.org/10.1021/acs.cgd.7b00625.

(58) Mohapatra, S.; Samanta, S.; Kothari, K.; Mistry, P.; Suryanarayanan, R. Effect of Polymer Molecular Weight on the Crystallization Behavior of Indomethacin Amorphous Solid Dispersions. *Cryst. Growth Des.* **2017**, acs.cgd.7b00096. https://doi.org/10.1021/acs.cgd.7b00096.

(59) Yang, Z.; Han, C. D. Rheology of Miscible Polymer Blends with Hydrogen Bonding. *Macromolecules* **2008**, *41* (6), 2104–2118. https://doi.org/10.1021/ma7025385.

(60) Song, Y.; Yang, X.; Chen, X.; Nie, H.; Byrn, S.; Lubach, J. W. Investigation of Drug-Excipient Interactions in Lapatinib Amorphous Solid Dispersions Using Solid-State NMR Spectroscopy. *Molecular Pharmaceutics*. 2015, pp 857–866. https://doi.org/10.1021/mp500692a.

(61) Yuan, X.; Xiang, T.-X.; Anderson, B. D.; Munson, E. J. Hydrogen Bonding Interactions in Amorphous Indomethacin and Its Amorphous Solid Dispersions with Poly(Vinylpyrrolidone) and Poly(Vinylpyrrolidone-Co-Vinyl Acetate) Studied Using (13)C Solid-State NMR. *Mol. Pharm.* **2015**, *12* (12), 4518–4528. https://doi.org/10.1021/acs.molpharmaceut.5b00705.

(62) Matsumoto, T.; Zografi, G. Physical Properties of Solid Molecular Dispersions of Indomethacin with Poly(Vinylpyrrolidone) and Poly(Vinylpyrrolidone-Co-Vinyl-Acetate) in Relation to Indomethacin Crystallization. *Pharmaceutical Research*. 1999, pp 1722–1728. https://doi.org/10.1023/A:1018906132279.

(63) Kothari, K.; Ragoonanan, V.; Suryanarayanan, R. The Role of Drug-Polymer Hydrogen Bonding Interactions on the Molecular Mobility and Physical Stability of Nifedipine Solid Dispersions. *Mol. Pharm.* **2015**, *12* (1), 162–170. https://doi.org/10.1021/mp5005146.

(64) Gordon, M.; Taylor, J. S. Ideal Copolymers and the Second-Order Transitions of Synthetic Rubbers. I. Noncrystalline Copolymers. *Rubber Chem. Technol.* **2011**, *26* (2), 323–335. https://doi.org/10.5254/1.3539818.

(65) Konno, H.; Taylor, L. S. Influence of Different Polymers on the Crystallization Tendency of Molecularly Dispersed Amorphous Felodipine. *J. Pharm. Sci.* **2006**, *95* (12), 2692–2705. https://doi.org/10.1002/jps.20697.

(66) Shamblin, S. L.; Huang, E. Y.; Zografi, G. The Effects of Co-Lyophilized Polymeric Additives on the Glass Transition Temperature and Crystallization of Amorphous Sucrose. *J. Therm. Anal.* **1996**, *47* (5), 1567–1579. https://doi.org/10.1007/BF01992846.

(67) Wellscheid, R.; Wust, J.; Jungnickel, B.-J. The Competition between Crystallization and Demixing in Polymer Blends. IV. Detection of Composition Inhomogeneities around Growing Spherulites. *J. Polym. Sci. Part B Polym. Phys.* **1996**, *34* (2), 267–275. https://doi.org/10.1002/(SICI)1099-0488(19960130)34:2<267::AID-POLB7>3.0.CO;2-Q.

(68) Kalivianakis, P.; Jungnickel, B. J. Crystallization-Induced Composition Inhomogeneities in PVDF/PMMA Blends. *J. Polym. Sci. Part B Polym. Phys.* **1998**. https://doi.org/10.1002/(SICI)1099-0488(19981130)36:16<2923::AID-POLB7>3.0.CO;2-R.

(69) *Handbook of Plasticizers*, Third.; Wypych, G., Ed.; ChemTec Publishing: Toronto, 2017.

(70) Mehta, M.; Kothari, K.; Ragoonanan, V.; Suryanarayanan, R. Effect of Water on Molecular Mobility and Physical Stability of Amorphous Pharmaceuticals. *Mol. Pharm.* **2016**, *13* (4), 1339–1346. https://doi.org/10.1021/acs.molpharmaceut.5b00950.

(71) Roussenova, M.; Murith, M.; Alam, A.; Ubbink, J. Plasticization, Antiplasticization,

and Molecular Packing in Amorphous Carbohydrate-Glycerol Matrices. *Biomacromolecules* **2010**, *11* (12), 3237–3247. https://doi.org/10.1021/bm1005068.

(72) Marcilla, A.; Beltran, M. Mechanisms of Plasticizer Action. In *Handbook of Plasticizers*; Wypych, G., Ed.; ChemTec Publishing: Toronto, 2017; pp 119–134. https://doi.org/10.1016/B978-1-895198-97-3.50007-X.

(73) Doolittle, A. K. Mechanism of Solvent Action. Influence of Molecular Size and Shape on Termperature Dependence of Solvent Ability. *Ind. Eng. Chem.* **1946**, *38* (5), 535–540. https://doi.org/10.1021/ie50437a025.

(74) Fox, T. G.; Flory, P. J. On a General Relation Involving the Glass Temperature and Coefficients of Expansion Of. *Glas. Transit. J. Chem. Phys.* **1950**, *21* (March 1962), 1003. https://doi.org/10.1063/1.1699711.

(75) MARCILLA, A.; BELTRÁN, M. MECHANISMS OF PLASTICIZERS ACTION. In *Handbook of Plasticizers*; Elsevier, 2017; pp 119–134. https://doi.org/10.1016/B978-1-895198-97-3.50007-X.

(76) Huang, S.; Mao, C.; Williams, R. O.; Yang, C. Y. Solubility Advantage (and Disadvantage) of Pharmaceutical Amorphous Solid Dispersions. *J. Pharm. Sci.* **2016**, *105* (12), 3549–3561. https://doi.org/10.1016/j.xphs.2016.08.017.

(77) Guzmán, H. R.; Tawa, M.; Zhang, Z.; Ratanabanangkoon, P.; Shaw, P.; Gardner, C. R.; Chen, H.; Moreau, J.; Almarsson, Ö.; Remenar, J. F. Combined Use of Crystalline Salt Forms and Precipitation Inhibitors to Improve Oral Absorption of Celecoxib from Solid Oral Formulations. *J. Pharm. Sci.* **2007**, *96* (10), 2686–2702. https://doi.org/10.1002/jps.20906.

(78) Kamerzell, T. J.; Esfandiary, R.; Joshi, S. B.; Middaugh, C. R.; Volkin, D. B. Protein–Excipient Interactions: Mechanisms and Biophysical Characterization Applied to Protein Formulation Development. *Adv. Drug Deliv. Rev.* **2011**, *63* (13), 1118–1159. https://doi.org/10.1016/j.addr.2011.07.006.

(79) Chen, Y.; Pui, Y.; Chen, H.; Wang, S.; Serno, P.; Tonnis, W.; Chen, L.; Qian, F. Polymer-Mediated Drug Supersaturation Controlled by Drug–Polymer Interactions Persisting in an Aqueous Environment. *Mol. Pharm.* **2019**, *16* (1), 205–213. https://doi.org/10.1021/acs.molpharmaceut.8b00947.

(80) Frank, D. S.; Matzger, A. J. Effect of Polymer Hydrophobicity on the Stability of Amorphous Solid Dispersions and Supersaturated Solutions of a Hydrophobic Pharmaceutical. *Molecular Pharmaceutics*. 2019, pp 682–688. https://doi.org/10.1021/acs.molpharmaceut.8b00972.

(81) Vandecruys, R.; Peeters, J.; Verreck, G.; Brewster, M. E. Use of a Screening Method to Determine Excipients Which Optimize the Extent and Stability of Supersaturated Drug Solutions and Application of This System to Solid Formulation Design. *Int. J. Pharm.* **2007**. https://doi.org/10.1016/j.ijpharm.2007.05.006.

(82) Scott, D. J.; Schuck, P. A Brief Introduction to the Analytical Ultracentrifugation of Proteins for Beginners. In *Analytical Ultracentrifugation*; Scott, D. J., Harding, S. E., Rowe, A., Eds.; 2005; pp 1–25.

(83) Berkowitz, S. A.; Philo, J. S. Characterizing Biopharmaceuticals Using Analytical Ultracentrifugation. In *Biophysical Characterization of Proteins in Developing Biopharmaceuticals*; Elsevier, 2015; pp 211–260. https://doi.org/10.1016/B978-0-444-59573-7.00009-9.

(84) Bennett, R. C.; Keen, J. M.; Bi, Y.; Porter, S.; D??rig, T.; McGinity, J. W. Investigation of the Interactions of Enteric and Hydrophilic Polymers to Enhance Dissolution of Griseofulvin Following Hot Melt Extrusion Processing. *J. Pharm. Pharmacol.* **2015**, *67* (7), 918–938. https://doi.org/10.1111/jphp.12388.

(85) Franc, I.; Lipinski, A.; Feeney, P. J. Lipinski 1997 Drug Discovery.Pdf. **1997**, *23*. https://doi.org/10.1016/S0169-409X(96)00423-1.

(86) Butler, J. M.; Dressman, J. B. The Developability Classification System: Application of Biopharmaceutics Concepts to Formulation Development. *J. Pharm. Sci.* **2010**, *99* (12), 4940–4954. https://doi.org/10.1002/jps.22217.

(87) Baghel, S.; Cathcart, H.; Reilly, N. J. O. Polymeric Amorphous Solid Dispersions : A Review of Amorphization , Crystallization , Stabilization , Solid-State Characterization , and Aqueous Solubilization of Biopharmaceutical Classi Fi Cation System Class II Drugs. *J. Pharm. Sci.* **2016**, *105* (9), 2527–2544. https://doi.org/10.1016/j.xphs.2015.10.008.

(88) Khougaz, K.; Clas, S. Crystallization Inhibition in Solid Dispersions of MK-0591

and Poly(Vinylpyrrolidone) Polymers. *J. Pharm. Sci.* **2000**, *89* (10), 1325–1334. https://doi.org/10.1002/1520-6017(200010)89:10<1325::AID-JPS10>3.0.CO;2-5.

(89) Van Eerdenbrugh, B.; Taylor, L. S. Application of Mid-IR Spectroscopy for the Characterization of Pharmaceutical Systems. *Int. J. Pharm.* **2011**, *417* (1–2), 3–16. https://doi.org/10.1016/j.ijpharm.2010.12.011.

(90) Kestur, U. S.; Van Eerdenbrugh, B.; Taylor, L. S. Influence of Polymer Chemistry on Crystal Growth Inhibition of Two Chemically Diverse Organic Molecules. *CrystEngComm* **2011**, *13* (22), 6712–6718. https://doi.org/10.1039/c1ce05822c.

(91) Chen, Y.; Wang, S.; Wang, S.; Liu, C.; Su, C.; Hageman, M.; Hussain, M.; Haskell, R.; Stefanski, K.; Qian, F. Initial Drug Dissolution from Amorphous Solid Dispersions Controlled by Polymer Dissolution and Drug-Polymer Interaction. *Pharm. Res.* **2016**, *33* (10), 2445–2458. https://doi.org/10.1007/s11095-016-1969-2.

(92) Saboo, S.; Kestur, U. S.; Flaherty, D. P.; Taylor, L. S. Congruent Release of Drug and Polymer from Amorphous Solid Dispersions: Insights into the Role of Drug-Polymer Hydrogen Bonding, Surface Crystallization, and Glass Transition. *Mol. Pharm.* **2020**. https://doi.org/10.1021/acs.molpharmaceut.9b01272.

(93) Mistry, P.; Suryanarayanan, R. Strength of Drug–Polymer Interactions: Implications for Crystallization in Dispersions. *Cryst. Growth Des.* **2016**, *16* (9), 5141–5149. https://doi.org/10.1021/acs.cgd.6b00714.

(94) Ueda, K.; Higashi, K.; Yamamoto, K.; Moribe, K. Inhibitory Effect of Hydroxypropyl Methylcellulose Acetate Succinate on Drug Recrystallization from a Supersaturated Solution Assessed Using Nuclear Magnetic Resonance Measurements. *Mol. Pharm.* **2013**, *10* (10), 3801–3811. https://doi.org/10.1021/mp400278j.

(95) Morris, K. F.; Johnson, C. S. Diffusion-Ordered Two-Dimensional Nuclear Magnetic Resonance Spectroscopy. *J. Am. Chem. Soc.* **1992**, *114* (8), 3139–3141. https://doi.org/10.1021/ja00034a071.

(96) Hädener, M.; Gjuroski, I.; Furrer, J.; Vermathen, M. Interactions of Polyvinylpyrrolidone with Chlorin E6-Based Photosensitizers Studied by NMR and

Electronic Absorption Spectroscopy. *J. Phys. Chem. B* **2015**, *119* (36), 12117–12128. https://doi.org/10.1021/acs.jpcb.5b05761.

(97) Fielding, L. Determination of Association Constants (Ka) from Solution NMR Data. *Tetrahedron* **2000**, *56* (34), 6151–6170. https://doi.org/10.1016/S0040-4020(00)00492-0.

(98) Li, Z.; Johnson, L. M.; Ricarte, R. G.; Yao, L. J.; Hillmyer, M. A.; Bates, F. S.; Lodge, T. P. Enhanced Performance of Blended Polymer Excipients in Delivering a Hydrophobic Drug through the Synergistic Action of Micelles and HPMCAS. *Langmuir* **2017**, *33* (11), 2837–2848. https://doi.org/10.1021/acs.langmuir.7b00325.

(99) Arnaud, A.; Bouteiller, L. Isothermal Titration Calorimetry of Supramolecular Polymers. *Langmuir* **2004**, *20* (16), 6858–6863. https://doi.org/10.1021/la049365d.

(100) Mistry, P.; Amponsah-Efah, K. K.; Suryanarayanan, R. Rapid Assessment of the Physical Stability of Amorphous Solid Dispersions. *Cryst. Growth Des.* **2017**, *17* (5), 2478–2485. https://doi.org/10.1021/acs.cgd.6b01901.

(101) Nunes, C.; Mahendrasingam, A.; Suryanarayanan, R. Quantification of Crystallinity in Substantially Amorphous Materials by Synchrotron X-Ray Powder Diffractometry. *Pharm. Res.* **2005**, *22* (11), 1942–1953. https://doi.org/10.1007/s11095-005-7626-9.

(102) Whitehouse, L. W.; Menzies, A.; Dawson, B.; Cyr, T. D.; By, A. W.; Black, D. B.; Zamecnik, J. Mouse Hepatic Metabolites of Ketoconazole: Isolation and Structure Elucidation. *J. Pharm. Biomed. Anal.* **1994**, *12* (11), 1425–1441. https://doi.org/10.1016/0731-7085(94)00093-X.

(103) Redenti, E.; Ventura, P.; Fronza, G.; Selva, A.; Rivara, S.; Plazzi, P. V.; Mor, M. Experimental and Theoretical Analysis of the Interaction of (±)-Cis- Ketoconazole with β-Cyclodextrin in the Presence of (+)-L-Tartaric Acid. *J. Pharm. Sci.* **1999**, *88* (6), 599–607. https://doi.org/10.1021/js980468o.

(104) *Handbook of Proton-Nmr Spectra and Data*; Elsevier, 1987. https://doi.org/10.1016/B978-0-12-064511-4.50007-5.

(105) Freyer, M. W.; Lewis, E. A. Isothermal Titration Calorimetry: Experimental Design, Data Analysis, and Probing Macromolecule/Ligand Binding and Kinetic Interactions. *Methods Cell Biol.* **2008**, *84* (07), 79–113. https://doi.org/10.1016/S0091-679X(07)84004-0.

(106) Piñeiro, Á.; Muñoz, E.; Sabín, J.; Costas, M.; Bastos, M.; Velázquez-Campoy, A.; Garrido, P. F.; Dumas, P.; Ennifar, E.; García-Río, L.; et al. AFFINImeter: A Software to Analyze Molecular Recognition Processes from Experimental Data. *Anal. Biochem.* **2019**, *577*, 117–134. https://doi.org/10.1016/j.ab.2019.02.031.

(107) Dressman, J. B.; Reppas, C. In Vitro-in Vivo Correlations for Lipophilic, Poorly Water-Soluble Drugs. *Eur. J. Pharm. Sci.* **2000**, *11* (SUPPL. 2), 73–80. https://doi.org/10.1016/S0928-0987(00)00181-0.

(108) Paterson, S. M.; Brown, D. H.; Chirila, T. V.; Keen, I.; Whittaker, A. K.; Baker, M. V. The Synthesis of Water-Soluble PHEMA via ARGET ATRP in Protic Media. *J. Polym. Sci. Part A Polym. Chem.* **2010**, *48* (18), 4084–4092. https://doi.org/10.1002/pola.24194.

(109) Swift, T.; Swanson, L.; Geoghegan, M.; Rimmer, S. The PH-Responsive Behaviour of Poly(Acrylic Acid) in Aqueous Solution Is Dependent on Molar Mass. *Soft Matter* **2016**, *12* (9), 2542–2549. https://doi.org/10.1039/C5SM02693H.

(110) Bühler, V. *Kollidon® Polyvinylpyrrolidone Excipients for the Pharmaceutical Industry*, 9th Editio.; BASF SE, Pharma Ingredients and Services, 2008. https://doi.org/10.1016/B978-0-12-802182-8.00001-5.

(111) BASF. *Soluble Kollidon ® Grades*.

(112) Lubach, J. W.; Chen, J. Z.; Hau, J.; Imperio, J.; Coraggio, M.; Liu, L.; Wong, H. Investigation of the Rat Model for Preclinical Evaluation of PH-Dependent Oral Absorption in Humans. *Mol. Pharm.* **2013**, *10* (11), 3997–4004. https://doi.org/10.1021/mp400283j.

(113) Ilevbare, G. A.; Taylor, L. S. Liquid-Liquid Phase Separation in Highly Supersaturated Aqueous Solutions of Poorly Water-Soluble Drugs: Implications for Solubility Enhancing Formulations. *Cryst. Growth Des.* **2013**, *13* (4), 1497–1509. https://doi.org/10.1021/cg301679h.

(114) Fung, M.; Bērziņš, K.; Suryanarayanan, R. Physical Stability and Dissolution Behavior of Ketoconazole–Organic Acid Coamorphous Systems. *Mol. Pharm.* **2018**, *15* (5), 1862–1869. https://doi.org/10.1021/acs.molpharmaceut.8b00035.

(115) Sun, D. D.; Lee, P. I. Probing the Mechanisms of Drug Release from Amorphous Solid Dispersions in Medium-Soluble and Medium-Insoluble Carriers. *J. Control. Release* **2015**, *211*, 85–93. https://doi.org/10.1016/j.jconrel.2015.06.004.

(116) Sun, D. D.; Ju, T. R.; Lee, P. I. Enhanced Kinetic Solubility Profiles of Indomethacin Amorphous Solid Dispersions in Poly(2-Hydroxyethyl Methacrylate) Hydrogels. *Eur. J. Pharm. Biopharm.* **2012**, *81* (1), 149–158. https://doi.org/10.1016/j.ejpb.2011.12.016.

(117) Zahedi, P.; Lee, P. I. Solid Molecular Dispersions of Poorly Water-Soluble Drugs in Poly(2-Hydroxyethyl Methacrylate) Hydrogels. *Eur. J. Pharm. Biopharm.* **2007**, *65* (3), 320–328. https://doi.org/10.1016/j.ejpb.2006.10.025.

(118) Chiou, W. L.; Riegelman, S. Pharmaceutical Applications of Solid Dispersion Systems. *J. Pharm. Sci.* **1971**, *60* (9), 1281–1302. https://doi.org/10.1002/jps.2600600902.

(119) Butts, C. P.; Jones, C. R.; Towers, E. C.; Flynn, J. L.; Appleby, L.; Barron, N. J. Interproton Distance Determinations by NOE--Surprising Accuracy and Precision in a Rigid Organic Molecule. *Org. Biomol. Chem.* **2011**, *9* (1), 177–184. https://doi.org/10.1039/c0ob00479k.

(120) Macura, S.; Ernst, R. R. Elucidation of Cross Relaxation in Liquids by Two-Dimensional N.M.R. Spectroscopy. *Mol. Phys.* **2002**, *100* (1), 135–147. https://doi.org/10.1080/00268970110088983.

(121) Cohen, Y.; Avram, L.; Frish, L. Diffusion NMR Spectroscopy in Supramolecular and Combinatorial Chemistry: An Old Parameter - New Insights. *Angew. Chemie - Int. Ed.* **2005**, *44* (4), 520–554. https://doi.org/10.1002/anie.200300637.

(122) Cameron, K. S.; Fielding, L. NMR Diffusion Spectroscopy as a Measure of Host−Guest Complex Association Constants and as a Probe of Complex Size. *J. Org. Chem.* **2001**, *66* (21), 6891–6895. https://doi.org/10.1021/jo010081x.

(123) Ting, J. M.; Tale, S.; Purchel, A. A.; Jones, S. D.; Widanapathirana, L.; Tolstyka, Z. P.; Guo, L.; Guillaudeu, S. J.; Bates, F. S.; Reineke, T. M. High-Throughput Excipient Discovery Enables Oral Delivery of Poorly Soluble Pharmaceuticals. *ACS Cent. Sci.* **2016**, *2* (10), 748–755. https://doi.org/10.1021/acscentsci.6b00268.

(124) Saal, W.; Ross, A.; Wyttenbach, N.; Alsenz, J.; Kuentz, M. A Systematic Study of Molecular Interactions of Anionic Drugs with a Dimethylaminoethyl Methacrylate Copolymer Regarding Solubility Enhancement. *Mol. Pharm.* **2017**, *14* (4), 1243–1250. https://doi.org/10.1021/acs.molpharmaceut.6b01116.

(125) Turnbull, W. B.; Daranas, A. H. On the Value of *c* : Can Low Affinity Systems Be Studied by Isothermal Titration Calorimetry? *J. Am. Chem. Soc.* **2003**, *125* (48), 14859–14866. https://doi.org/10.1021/ja036166s.

(126) Segura-Sanchez, F.; Bouchemal, K.; Lebas, G.; Vauthier, C.; Santos-Magalhaes, N. S.; Ponchel, G. Elucidation of the Complexation Mechanism between (+)-Usnic Acid and Cyclodextrins Studied by Isothermal Titration Calorimetry and Phase-Solubility Diagram Experiments. *J. Mol. Recognit. 22* (3), 232–241. https://doi.org/10.1002/jmr.936.

(127) Dam, T. K.; Brewer, C. F. Thermodynamic Studies of Lectin-Carbohydrate Interactions by Isothermal Titration Calorimetry. *Chemical Reviews*. 2002, pp 387–429. https://doi.org/10.1021/cr000401x.

(128) Wiseman, T.; Williston, S.; Brandts, J. F.; Lin, L. N. Rapid Measurement of Binding Constants and Heats of Binding Using a New Titration Calorimeter. *Anal. Biochem.* **1989**, *179* (1), 131–137. https://doi.org/10.1016/0003-2697(89)90213-3.

(129) Tellinghuisen, J. Optimizing Experimental Parameters in Isothermal Titration Calorimetry. *J. Phys. Chem. B* **2005**, *109* (42), 20027–20035. https://doi.org/10.1021/jp053550y.

(130) Tellinghuisen, J. Isothermal Titration Calorimetry at Very Low C. *Anal. Biochem.* **2008**, *373* (2), 395–397. https://doi.org/10.1016/j.ab.2007.08.039.

(131) Thayer, A. M. Finding Solutions. *Chem. Eng. News* **2010**, *88* (22), 13–18. https://doi.org/10.1021/cen-v088n022.p013.

(132) Alonzo, D. E.; Zhang, G. G. Z.; Zhou, D.; Gao, Y.; Taylor, L. S. Understanding the Behavior of Amorphous Pharmaceutical Systems during Dissolution. *Pharm. Res.* **2010**, *27* (4), 608–618. https://doi.org/10.1007/s11095-009-0021-1.

(133) Qiu, S.; Lai, J.; Guo, M.; Wang, K.; Lai, X.; Desai, U.; Juma, N.; Li, M. Role of Polymers in Solution and Tablet-Based Carbamazepine Cocrystal Formulations. *CrystEngComm* **2016**, *18* (15), 2664–2678. https://doi.org/10.1039/c6ce00263c.

(134) Marsac, P. J.; Rumondor, A. C. F.; Nivens, D. E.; Kestur, U. S.; Lia, S.; Taylor, L. S. Effect of Temperature and Moisture on the Miscibility of Amorphous Dispersions of Felodipine and Poly(Vinyl Pyrrolidone). *J. Pharm. Sci.* **2010**, *99* (1), 169–185. https://doi.org/10.1002/jps.21809.

(135) Ting, J. M.; Tale, S.; Purchel, A. A.; Jones, S. D.; Widanapathirana, L.; Tolstyka, Z. P.; Guo, L.; Guillaudeu, S. J.; Bates, F. S.; Reineke, T. M. High-Throughput Excipient Discovery Enables Oral Delivery of Poorly Soluble Pharmaceuticals. *ACS Cent. Sci.* **2016**, *2* (10), 748–755. https://doi.org/10.1021/acscentsci.6b00268.

(136) Lee, J. H.; Okuno, Y.; Cavagnero, S. Sensitivity Enhancement in Solution NMR: Emerging Ideas and New Frontiers. *J. Magn. Reson.* **2014**, *241*, 18–31. https://doi.org/10.1016/j.jmr.2014.01.005.

(137) Meng, F.; Jing, Z.; Ferreira, R.; Ren, P.; Zhang, F. Investigating the Association Mechanism between Rafoxanide and Povidone. *Langmuir* **2018**, *34* (46), 13971–13978. https://doi.org/10.1021/acs.langmuir.8b03174.

(138) Bekdemir, A.; Stellacci, F. A Centrifugation-Based Physicochemical Characterization Method for the Interaction between Proteins and Nanoparticles. *Nat. Commun.* **2016**, *7*, 1–8. https://doi.org/10.1038/ncomms13121.

(139) Salveson, P. J.; Haerianardakani, S.; Thuy-Boun, A.; Yoo, S.; Kreutzer, A. G.; Demeler, B.; Nowick, J. S. Repurposing Triphenylmethane Dyes to Bind to Trimers Derived from Aβ. *J. Am. Chem. Soc.* **2018**, *140* (37), 11745–11754. https://doi.org/10.1021/jacs.8b06568.

(140) Karabudak, E.; Brookes, E.; Lesnyak, V.; Gaponik, N.; Eychmüller, A.; Walter, J.; Segets, D.; Peukert, W.; Wohlleben, W.; Demeler, B.; et al. Simultaneous Identification of Spectral Properties and Sizes of Multiple Particles in Solution with

Subnanometer Resolution. *Angew. Chemie - Int. Ed.* **2016**, *55* (39), 11770–11774. https://doi.org/10.1002/anie.201603844.

(141) Demeler, B.; Van Holde, K. E. Sedimentation Velocity Analysis of Highly Heterogeneous Systems. *Anal. Biochem.* **2004**, *335* (2), 279–288. https://doi.org/10.1016/j.ab.2004.08.039.

(142) Maechtle, W.; Borger, L. *Analytical Ultracentrifugation of Polymers and Nanoparticles*; Springer Laboratory; Springer-Verlag: New York, 2006. https://doi.org/10.1007/b137083.

(143) Raşa, M.; Schubert, U. S. Progress in the Characterization of Synthetic (Supramolecular) Polymers by Analytical Ultracentrifugation. *Soft Matter* **2006**, *2* (7), 561–572. https://doi.org/10.1039/b601666a.

(144) Amponsah-Efah, K. K.; Mistry, P.; Eisenhart, R.; Suryanarayanan, R. The Influence of Drug-Polymer Interactions on the Dissolution Performance of Amorphous Solid Dispersions. *Manuscr. under Rev.* **2020**.

(145) Amponsah-Efah, K. K.; Mistry, P.; Eisenhart, R.; Suryanarayanan, R. The Influence of Drug-Polymer Interactions on the Dissolution Performance of Amorphous Solid Dispersions. In *published abstract, Amercian Association of Pharmaceutical Scientists (AAPS) Annual Meeting,*; 2017.

(146) BASF. Soluplus - Technical Information. No. 03_090801e-04, 1–8.

(147) Curatolo, W.; Nightingale, J. A.; Herbig, S. M. Utility of Hydroxypropylmethylcellulose Acetate Succinate (HPMCAS) for Initiation and Maintenance of Drug Supersaturation in the GI Milieu. *Pharm. Res.* **2009**, *26* (6), 1419–1431. https://doi.org/10.1007/s11095-009-9852-z.

(148) Ishizuka, Y.; Ueda, K.; Okada, H.; Takeda, J.; Karashima, M.; Yazawa, K.; Higashi, K.; Kawakami, K.; Ikeda, Y.; Moribe, K. Effect of Drug-Polymer Interactions through Hypromellose Acetate Succinate Substituents on the Physical Stability on Solid Dispersions Studied by Fourier-Transform Infrared and Solid-State Nuclear Magnetic Resonance. *Mol. Pharm.* **2019**, *16* (6), 2785–2794. https://doi.org/10.1021/acs.molpharmaceut.9b00301.

(149) Ueda, K.; Higashi, K.; Yamamoto, K.; Moribe, K. The Effect of HPMCAS Functional Groups on Drug Crystallization from the Supersaturated State and Dissolution Improvement. *Int. J. Pharm.* **2014**, *464* (1–2), 205–213. https://doi.org/10.1016/j.ijpharm.2014.01.005.

(150) Fukasawa, M.; Obara, S. Molecular Weight Determination of Hypromellose Acetate Succinate (HPMCAS) Using Size Exclusion Chromatography with a Multi-Angle Laser Light Scattering Detector. *Chem. Pharm. Bull. (Tokyo).* **2004**, *52* (11), 1391–1393. https://doi.org/10.1248/cpb.52.1391.

(151) Demeler, B. UltraScan: A Comprehensive Data Analysis Software Package for Analytical Ultracentrifugation Experiments. In *Modern Analytical Ultracentrifugation: Techniques and Methods*; Scott, D. J., Harding, S. E., Rowe, A. J., Eds.; Royal Society of Chemistry, 2005; pp 210–230. https://doi.org/10.1039/9781847552617-00210.

(152) Demeler, B.; Gorbet, G. E. Analytical Ultracentrifugation Data Analysis with UltraScan-III. In *Analytical Ultracentrifugation*; Springer Japan: Tokyo, 2016; pp 119–143. https://doi.org/10.1007/978-4-431-55985-6_8.

(153) Brookes, E.; Cao, W.; Demeler, B. A Two-Dimensional Spectrum Analysis for Sedimentation Velocity Experiments of Mixtures with Heterogeneity in Molecular Weight and Shape. *Eur. Biophys. J.* **2010**, *39* (3), 405–414. https://doi.org/10.1007/s00249-009-0413-5.

(154) Demeler, B.; Brookes, E. Monte Carlo Analysis of Sedimentation Experiments. *Colloid Polym. Sci.* **2008**, *286* (2), 129–137. https://doi.org/10.1007/s00396-007-1699-4.

(155) Gorbet, G.; Devlin, T.; Hernandez Uribe, B. I.; Demeler, A. K.; Lindsey, Z. L.; Ganji, S.; Breton, S.; Weise-Cross, L.; Lafer, E. M.; Brookes, E. H.; et al. A Parametrically Constrained Optimization Method for Fitting Sedimentation Velocity Experiments. *Biophys. J.* **2014**, *106* (8), 1741–1750. https://doi.org/10.1016/j.bpj.2014.02.022.

(156) Demeler, B.; Saber, H. Determination of Molecular Parameters by Fitting Sedimentation Data to Finite-Element Solutions of the Lamm Equation. *Biophys. J.* **1998**, *74* (1), 444–454. https://doi.org/10.1016/S0006-3495(98)77802-6.

(157) Stafford, W. F. Analysis of Nonideal, Interacting, and Noninteracting Systems by Sedimentation Velocity Analytical Ultracentrifugation. In *Analytical Ultracentrifugation*; Springer Japan: Tokyo, 2016; pp 463–482. https://doi.org/10.1007/978-4-431-55985-6_23.

(158) Chaturvedi, S. K.; Sagar, V.; Zhao, H.; Wistow, G.; Schuck, P. Measuring Ultra-Weak Protein Self-Association by Non-Ideal Sedimentation Velocity. *J. Am. Chem. Soc.* **2019**, *141* (7), 2990–2996. https://doi.org/10.1021/jacs.8b11371.

(159) Ricarte, R. G.; Li, Z.; Johnson, L. M.; Ting, J. M.; Reineke, T. M.; Bates, F. S.; Hillmyer, M. A.; Lodge, T. P. Direct Observation of Nanostructures during Aqueous Dissolution of Polymer/Drug Particles. *Macromolecules* **2017**, *50* (8), 3143–3152. https://doi.org/10.1021/acs.macromol.7b00372.

(160) Zhang, J.; Pearson, J. Z.; Gorbet, G. E.; Cölfen, H.; Germann, M. W.; Brinton, M. A.; Demeler, B. Spectral and Hydrodynamic Analysis of West Nile Virus RNA–Protein Interactions by Multiwavelength Sedimentation Velocity in the Analytical Ultracentrifuge. *Anal. Chem.* **2017**, *89* (1), 862–870. https://doi.org/10.1021/acs.analchem.6b03926.

(161) Murphy, D.; Rodríguez-Cintrón, F.; Langevin, B.; Kelly, R. .; Rodríguez-Hornedo, N. Solution-Mediated Phase Transformation of Anhydrous to Dihydrate Carbamazepine and the Effect of Lattice Disorder. *Int. J. Pharm.* **2002**, *246* (1–2), 121–134. https://doi.org/10.1016/S0378-5173(02)00358-7.

(162) Sun, D. D.; Lee, P. I. Probing the Mechanisms of Drug Release from Amorphous Solid Dispersions in Medium-Soluble and Medium-Insoluble Carriers. *J. Control. Release* **2015**, *211*, 85–93. https://doi.org/10.1016/j.jconrel.2015.06.004.

(163) Sun, D. D.; Lee, P. I. Evolution of Supersaturation of Amorphous Pharmaceuticals: The Effect of Rate of Supersaturation Generation. *Mol. Pharm.* **2013**, *10* (11), 4330–4346. https://doi.org/10.1021/mp400439q.

(164) Schuck, P.; Zhao, H.; Brautigam, C. A.; Ghirlando, R. *Basic Principles of Analytical Ultracentrifugation*; CRC Press, 2016. https://doi.org/10.1201/b19028.

(165) Schuck, P.; Zhao, H. *Sedimentation Velocity Analytical Ultracentrifugation*; CRC Press: Boca Raton, FL : CRC Press, Taylor & Francis Group, [2017], 2017.

https://doi.org/10.1201/b21988.

(166) Hermans, J. J. An Introduction to Ultracentrifugation, T. J. Bowen, Wiley-Interscience, New York, 1971. 171 Pp. $6.95. *J. Polym. Sci. Part B Polym. Lett.* **1971**, *9* (8), 636–637. https://doi.org/10.1002/pol.1971.110090817.

(167) Thoen, J.; Marynissen, H.; Van Dael, W. Temperature Dependence of the Enthalpy and the Heat Capacity of the Liqud-Crystal Octylcyanobiphenyl (8CB). *Phys. Rev. A* **1982**, *26* (5), 2886–2905.

(168) Halperin, B. I.; Lubensky, T. C.; Ma, S. First-Order Phase Transitions in Superconductors and Smectic-A Liquid Crystals. *Phys. Rev. Lett.* **1974**, *32* (6), 292–295. https://doi.org/10.1103/PhysRevLett.32.292.

(169) Jirón, V.; Castellón, E. Increased Nematic–Isotropic Transition Temperature on Doping a Liquid Crystal with Molecularly Rigid Carboxylic Acids. *J. Phys. Chem. B* **2020**, *124* (5), 890–899. https://doi.org/10.1021/acs.jpcb.9b09567.

(170) Mukherjee, P. K. Effect of Nonmesogenic Solute on the Nematic-Smectic-A Phase Transition. *J. Chem. Phys.* **2002**, *116* (21), 9531–9536. https://doi.org/10.1063/1.1476314.

(171) Diez-Berart, S.; López, D. O.; de la Fuente, M. R.; Salud, J.; Pérez-Jubindo, M. A.; Finotello, D. Critical Behaviour in Liquid-Crystalline Phase Transitions: A Comparative Study of 9OCB in Bulk and Anopore Membranes. *Liq. Cryst.* **2010**, *37* (6–7), 893–901. https://doi.org/10.1080/02678291003798156.

(172) Pauluth, D.; Tarumi, K. Advanced Liquid Crystals for Television. *Journal of Materials Chemistry*. 2004. https://doi.org/10.1039/b400135b.

(173) Jones, J. C. The Fiftieth Anniversary of the Liquid Crystal Display. *Liq. Cryst. Today* **2018**, *27* (3), 44–70. https://doi.org/10.1080/1358314X.2018.1529129.

(174) Tschierske, C. Liquid Crystal Engineering - New Complex Mesophase Structures and Their Relations to Polymer Morphologies, Nanoscale Patterning and Crystal Engineering. *Chem. Soc. Rev.* **2007**, *36* (12), 1930–1970. https://doi.org/10.1039/b615517k.

(175) Six, K.; Verreck, G.; Peeters, J.; Binnemans, K.; Berghmans, H.; Augustijns, P.; Kinget, R.; Van den Mooter, G. Investigation of Thermal Properties of Glassy Itraconazole: Identification of a Monotropic Mesophase. *Thermochim. Acta* **2001**, *376* (2), 175–181. https://doi.org/10.1016/S0040-6031(01)00563-9.

(176) Teerakapibal, R.; Huang, C.; Gujral, A.; Ediger, M. D.; Yu, L. Organic Glasses with Tunable Liquid-Crystalline Order. *Phys. Rev. Lett.* **2018**, *120* (5), 1–5. https://doi.org/10.1103/PhysRevLett.120.055502.

(177) Kozyra, A.; Mugheirbi, N. A.; Paluch, K. J.; Garbacz, G.; Tajber, L. Phase Diagrams of Polymer-Dispersed Liquid Crystal Systems of Itraconazole/Component Immiscibility Induced by Molecular Anisotropy. *Mol. Pharm.* **2018**, *15* (11), 5192–5206. https://doi.org/10.1021/acs.molpharmaceut.8b00724.

(178) Carter, B. M.; Wiesenauer, B. R.; Hatakeyama, E. S.; Barton, J. L.; Noble, R. D.; Gin, D. L. Glycerol-Based Bicontinuous Cubic Lyotropic Liquid Crystal Monomer System for the Fabrication of Thin-Film Membranes with Uniform Nanopores. *Chem. Mater.* **2012**, *24* (21), 4005–4007. https://doi.org/10.1021/cm302027s.

(179) Kölbel, M.; Beyersdorff, T.; Tschierske, C.; Diele, S.; Kain, J. Thermotropic and Lyotropic Liquid Crystalline Phases of Rigid Aromatic Amphiphiles. *Chem. - A Eur. J.* **2000**, *6* (20), 3821–3837. https://doi.org/10.1002/1521-3765(20001016)6:20<3821::AID-CHEM3821>3.0.CO;2-8.

(180) Fuchs, P.; Tschierske, C.; Raith, K.; Das, K.; Diele, S. A Thermotropic Mesophase Comprised of Closed Micellar Aggregates of the Normal Type. *Angew. Chemie Int. Ed.* **2002**, *41* (4), 628–631. https://doi.org/10.1002/1521-3773(20020215)41:4<628::AID-ANIE628>3.0.CO;2-I.

(181) Thoen, J.; Leys, J.; Glorieux, C. Adiabatic Scanning Calorimeter. European Patent: EP 2 91328 B1(Sept. 02, 2015), US Patent: US 9.310.263 B2 (April 12, 2016).

(182) Leys, J.; Losada-Pérez, P.; Glorieux, C.; Thoen, J. Application of a Novel Type of Adiabatic Scanning Calorimeter for High-Resolution Thermal Data near the Melting Point of Gallium. *J. Therm. Anal. Calorim.* **2014**, *117* (1), 173–187. https://doi.org/10.1007/s10973-014-3654-1.

(183) Thoen, J.; Bloemen, E.; Marynissen, H.; Van Deal, W. High-Resolution

Calorimetric Investigations of Phase Transitions in Liquids. In *Proceedings of the 8th Symposium on Thermophysical Properties. American Society of Mechanical Engineers (ASME)*; New York, 1982; pp 422–428.

(184) Mapesa, E. U.; Tarnacka, M.; Kamińska, E.; Adrjanowicz, K.; Dulski, M.; Kossack, W.; Tress, M.; Kipnusu, W. K.; Kamiński, K.; Kremer, F. Molecular Dynamics of Itraconazole Confined in Thin Supported Layers. *RSC Adv.* **2014**, *4* (54), 28432–28438. https://doi.org/10.1039/c4ra01544d.

(185) Tarnacka, M.; Adrjanowicz, K.; Kaminska, E.; Kaminski, K.; Grzybowska, K.; Kolodziejczyk, K.; Wlodarczyk, P.; Hawelek, L.; Garbacz, G.; Kocot, A.; et al. Molecular Dynamics of Itraconazole at Ambient and High Pressure. *Phys. Chem. Chem. Phys.* **2013**, *15* (47), 20742–20752. https://doi.org/10.1039/c3cp52643g.

(186) Couchman, P. R.; Karasz, F. E. A Classical Thermodynamic Discussion of the Effect of Composition on Glass-Transition Temperatures. *Macromolecules* **1978**, *11* (1), 117–119. https://doi.org/10.1021/ma60061a021.

(187) Hancock, B. C.; Zografi, G. The Relationship Between the Glass Transition Temperature and the Water Content of Amorphous Pharmaceutical Solids. *Pharm. Res.* **1994**, *11* (4), 471–477. https://doi.org/https://doi.org/10.1023/A:1018941810744.

(188) Philp Chen, H.-M.; Ou, J. J.; Chen, S. H. Glassy Liquid Crystals as Self-Organized Films for Robust Optoelectronic Devices. In *Nanoscience with Liquid Crystals.*; Li, Q., Ed.; Springer International Publishing, 2014; pp 179–208. https://doi.org/10.1007/978-3-319-04867-3_6.

(189) Chaikin, P. M.; Lubensky, T. C. *Principles of Condensed Matter Physics*; Cambridge University Press, 1995. https://doi.org/10.1017/CBO9780511813467.

(190) Su, Z. The Investigation of Pharmaceutical Liquid Crystals: Formation, Stability and Phase Behavior, Purdue University, 2011.

(191) Heczko, D.; Kaminska, E.; Tarnacka, M.; Jurkiewicz, K.; Dulski, M.; Bebeneck, A.; Garbacz, G.; Kaminski, K.; Paluch, M. Varying Thermodynamic Conditions as a New Way to Tune the Molecular Order in Glassy Itraconazole. *J. Mol. Liq.* **2019**, *286*.

(192) Gujral, A.; Gómez, J.; Jiang, J.; Huang, C.; O'Hara, K. A.; Toney, M. F.; Chabinyc, M. L.; Yu, L.; Ediger, M. D. Highly Organized Smectic-like Packing in Vapor-Deposited Glasses of a Liquid Crystal. *Chem. Mater.* **2017**, *29* (2), 849–858. https://doi.org/10.1021/acs.chemmater.6b04877.

(193) Mugheirbi, N. A.; Fleischer, K.; Tajber, L. A Rare Case of Mesomorphic Behavior–Molecular Reorientation of Itraconazole Liquid Crystal Induced by a Hygrothermal Treatment. *Cryst. Growth Des.* **2016**, *16* (3), 1329–1336. https://doi.org/10.1021/acs.cgd.5b01464.

(194) Baird, J. A.; Van Eerdenbrugh, B.; Taylor, L. S. A Classification System to Assess the Crystallization Tendency of Organic Molecules from Undercooled Melts. *J. Pharm. Sci.* **2010**, *99* (9), 3787–3806. https://doi.org/10.1002/jps.22197.

(195) Mehta, M.; Suryanarayanan, R. Accelerated Physical Stability Testing of Amorphous Dispersions. *Mol. Pharm.* **2016**, *13* (8), 2661–2666. https://doi.org/10.1021/acs.molpharmaceut.6b00218.

(196) Benmore, C. J.; Mou, Q.; Benmore, K. J.; Robinson, D. S.; Neuefeind, J.; Ilavsky, J.; Byrn, S. R.; Yarger, J. L. A SAXS-WAXS Study of the Endothermic Transitions in Amorphous or Supercooled Liquid Itraconazole. *Thermochim. Acta* **2016**, *644*, 1–5. https://doi.org/10.1016/j.tca.2016.10.004.

(197) Toby, B. H.; Von Dreele, R. B. GSAS-II: The Genesis of a Modern Open-Source All Purpose Crystallography Software Package. *J. Appl. Crystallogr.* **2013**, *46* (2), 544–549. https://doi.org/10.1107/S0021889813003531.

(198) Havriliak, S.; Negami, S. A Complex Plane Analysis of α-Dispersions in Some Polymer Systems. *Journal of Polymer Science Part C: Polymer Symposia*. 2010, pp 99–117. https://doi.org/10.1002/polc.5070140111.

(199) Leadbetter, A. J.; Norris, E. K. Distribution Functions in Three Liquid Crystals from X-Ray Diffraction Measurements. *Mol. Phys.* **1979**, *38* (3), 669–686. https://doi.org/10.1080/00268977900101961.

(200) Imry, Y.; Wortis, M. Influence of Quenched Impurities on First-Order Phase Transitions. *Phys. Rev. B* **1979**, *19* (7), 3580–3585. https://doi.org/10.1103/PhysRevB.19.3580.

(201) Seddon, J. M. Structural Studies of Liquid Crystals by X-Ray Diffraction. In *Handbook of Liquid Crystals Set*; Wiley-VCH Verlag GmbH: Weinheim, Germany, 2008; pp 635–679. https://doi.org/10.1002/9783527619276.ch8ca.

(202) Sims, M. T.; Abbott, L. C.; Goodby, J. W.; Moore, J. N. Shape Segregation in Molecular Organisation: A Combined X-Ray Scattering and Molecular Dynamics Study of Smectic Liquid Crystals. *Soft Matter* **2019**, *15* (38), 7722–7732. https://doi.org/10.1039/C9SM01527B.

(203) Benmore, C. J. Advanced X-Ray Analytical Methods to Understand Structure, Properties, and Risk. In *Discovering and Developing Molecules with Optimal Drug-Like Properties*; Templeton, A. C., Byrn, S. R., Haskell, R. J., Prisinzano, T. E., Eds.; AAPS Advances in the Pharmaceutical Sciences Series; Springer New York: New York, NY, 2015; Vol. 15, pp 263–283. https://doi.org/10.1007/978-1-4939-1399-2_9.

(204) Brás, A. R.; Dionísio, M.; Huth, H.; Schick, C.; Schönhals, A. Origin of Glassy Dynamics in a Liquid Crystal Studied by Broadband Dielectric and Specific Heat Spectroscopy. *Physical Review E - Statistical, Nonlinear, and Soft Matter Physics*. 2007. https://doi.org/10.1103/PhysRevE.75.061708.

(205) Bhardwaj, S. P.; Arora, K. K.; Kwong, E.; Templeton, A.; Clas, S.-D.; Suryanarayanan, R. Correlation between Molecular Mobility and Physical Stability of Amorphous Itraconazole. *Mol. Pharm.* **2013**, *10* (2), 694–700. https://doi.org/10.1021/mp300487u.

(206) Zhang, C.; Gao, M.; Diorio, N.; Weissflog, W.; Baumeister, U.; Sprunt, S.; Gleeson, J. T.; Jákli, A. Direct Observation of Smectic Layers in Thermotropic Liquid Crystals. *Phys. Rev. Lett.* **2012**, *109* (10), 107802. https://doi.org/10.1103/PhysRevLett.109.107802.

(207) Emelyanenko, A. V.; Khokhlov, A. R. Simple Theory of Transitions between Smectic, Nematic, and Isotropic Phases. *J. Chem. Phys.* **2015**, *142* (20), 204905. https://doi.org/10.1063/1.4921684.

(208) Heuer, A. Energy Landscapes. Applications to Clusters, Biomolecules and Glasses. By David J. Wales. *Angew. Chemie Int. Ed.* **2005**, *44* (12), 1756–1757. https://doi.org/10.1002/anie.200485197.

(209) MARCILLA, A.; BELTRÁN, M. MECHANISMS OF PLASTICIZERS ACTION. In *Handbook of Plasticizers*; Elsevier, 2012; pp 119–133. https://doi.org/10.1016/B978-1-895198-50-8.50007-2.

(210) Ralston, G. Introduction to Analytical Ultracentrifugation. **1993**, xi, 87p. https://doi.org/CENT-1069TCH9.15-A.

(211) Wischerhoff, E. Characterization of Polymers and Particles by Analytical Ultracentrifugation Analytical Ultracentrifugation.

(212) Adrjanowicz, K.; Kaminski, K.; Wlodarczyk, P.; Grzybowska, K.; Tarnacka, M.; Zakowiecki, D.; Garbacz, G.; Paluch, M.; Jurga, S. Molecular Dynamics of the Supercooled Pharmaceutical Agent Posaconazole Studied via Differential Scanning Calorimetry and Dielectric and Mechanical Spectroscopies. *Mol. Pharm.* **2013**, *10* (10), 3934–3945. https://doi.org/10.1021/mp4003915.

(213) Chen, Z.; Yu, J.; Teerakapibal, R.; Meerpoel, L.; Richert, R.; Yu, L. Organic Glasses with Tunable Liquid-Crystalline Order through Kinetic Arrest of End-over-End Rotation: The Case of Saperconazole. *Soft Matter* **2020**. https://doi.org/10.1039/c9sm02180a.